学位論文

Tidal sensitivity of tectonic tremors and frictionally heterogeneous fault model

（深部低周波微動の潮汐応答性と摩擦不均質断層モデル）

平成 28 年 12 月　博士（理学）申請

東京大学大学院理学系研究科

地球惑星科学専攻

矢部　優

Abstract

Several modes of shear slip on the fault have been recognized since modern research on earthquakes began in Meiji era. Regular earthquakes repeatedly brought devastating hazard to Japanese society for many times. Geodetic measurements revealed the ground deformation lasting for many years after large regular earthquakes, called afterslip. Tsunami sometimes hits the coast without large ground shaking, which is categorized as tsunami earthquake. Furthermore, recent dense seismic and geodetic observation networks revealed a new type of shear slip on the plate interface named slow earthquakes, which have a different scaling relation from regular earthquakes. Ground deformation lasts for several years accompanying tiny seismic signals both in high frequency and low frequency. The discovery of slow earthquake in 21st century forced us to realize that shear slip behavior on the plate interface is much more diverse than expected. Understanding its physical mechanism is important not only for the pure earthquake science, but also for the sake of exploring the possibility of probabilistic hazard forecasting. For this purpose, I have worked on data analysis of slow earthquakes during my PhD course. Many parameters characterizing slow earthquake activity have been quantified. Correlations between these parameters should provide constraints on the physical mechanism of shear-slip diversity. I have also conducted numerical simulation of seismic rupture as a first step to construct the unified seismic source model, which can explain diverse slip behavior.

Slow earthquake activity varies among subduction zones and even within an individual subduction zone. The spatial heterogeneity of tectonic tremor activities, which is a high-frequency seismic signal of slow earthquake, has been quantified in various ways mainly in Nankai and Cascadia subduction zones. In this thesis, three parameters are focused; duration, amplitude, and tidal sensitivity of tectonic tremors. As a result, it has been confirmed that tremor occurrence rate is exponentially sensitive to tidal stress in the entire slow earthquake zone as observed by previous studies, which implies that the plate interface is governed by the rate and

state friction law. Furthermore, tidal sensitivity of tremors is higher for short-duration tremors. Increases of tidal sensitivity have been also observed after large-amplitude tremors occur. Correlations between these parameters can be qualitatively explained by a model, which is extended from models proposed by previous studies, in which the frictional heterogeneity on the plate interface is important.

Previous studies showed that the frictionally heterogeneous fault model have potential to explain both regular earthquakes and slow earthquakes. Therefore, slip behavior of the frictionally heterogeneous infinite linear fault governed by the rate and state friction law has been examined with numerical simulations to investigate how it changes with the frictional heterogeneity. Results show that slip behavior transits according to the spatial average of a-b value on the fault. When the spatially averaged a-b is positive, seismic slip is limited within a velocity-weakening zone on the fault. On the other hand, when the spatial average of a-b value is negative, the entire fault including velocity-strengthening zones slip seismically. At this transition where the spatial average of a-b is close to zero, slower deformation dominates during seismic events, which may correspond the slow earthquakes.

The seismicity of regular earthquakes, such as the maximum earthquake size or statistical parameter, has been compared among subduction zones in the field of comparative subductology. Quantifications of tremor activities made by the first half of this study enable this comparison of comparative subductology for slow earthquakes. As a result of comparisons, the constraint for the source model of slow earthquake has been obtained. The latter half of this thesis models the frictionally heterogeneous fault, which could qualitatively explain the observation of data analysis, revealing the slower deformation dominated by complex interactions between seismic slip and aseismic slip on the fault. Although there is still a long way to go, diverse slip behavior on the plate interface may be explained by the frictional heterogeneity on the fault, which should reflect tectonic environments. Construction of this model will provide us a new tool to search the relation between tectonic environment and earthquake genesis.

Contents

1. General Introduction

Since the Earth formation, the Earth gets cooler and cooler. The internal heat of the Earth is transmitted from the center of the Earth to the surface by the mantle convection due to the high Rayleigh number of the Earth's mantle (Holmes, 1931; Turcotte and Schubert, 2002). It is very unique that plate tectonics occurs on the Earth. In the theory of plate tectonics, every individual plate on the Earth moves in different directions, as confirmed by geodetic observations (e.g., Christodouridis et al., 1985). Divergence of plate motion is accommodated by upwelling of mantle, which forms a new oceanic plate. In contrast, convergence of plate motions is accommodated by plate subduction. An important point is that the Earth surface is so soft for some reason that plates can be subducted into the mantle. Otherwise, the internal heat is transported by conduction at the surface (stagnant-lid convection), as in Mars and Venus. Plate tectonics contributes to stabilize the climate by removing carbon from the surface (Walker et al., 1981). Hence, the Earth is habitable.

The human society has been suffered from severe damage by devastating earthquakes and resultant tsunamis for long time. We hope that there were no earthquakes on the Earth. However, seismic hazards are prices for the existence of plate tectonics. When an oceanic plate is subducted beneath a continental plate, a frictional force acts between two plates. Strain is accumulated in subduction zone while the plate interface is locked by frictional force (e.g., Savage, 1983), and a frictional force finally reaches a frictional strength of the plate interface. At the moment, slip velocity on a plate interface is accelerated, which we call an earthquake. An earthquake results transient and permanent deformation around the source area including radiations of seismic waves (e.g., Aki and Richards, 2002). With seismological and geodetic measurements of such deformation, we can analyze source process of earthquakes. For a long time, we know only "regular" earthquakes, which sometimes bring us disastrous damage, such as 1995 Kobe earthquake and 2011 Tohoku-oki earthquake. However, recent seismic and geodetic observations revealed more complex situation. A new

type of slip behavior of the fault, which we call “slow earthquake”, has been discovered in the beginning of 21st century (e.g., Dragert et al., 2001; Obara, 2002). Source areas of slow earthquakes adjoin to source areas of regular earthquakes in some subduction zones (Dragert et al., 2001; Obara, 2002). Whereas, source areas of slow earthquakes and regular earthquakes seem to overlap in other subduction zones (Ito et al., 2013). An earthquake science in the new era has to understand the physical mechanism of slip diversity on the fault.

A final goal of my study is to understand the physical mechanism of slip diversity. This thesis tries to constrain the physical mechanism of slow earthquake by analyzing seismic signals of slow earthquake. Results are qualitatively interpreted by extending one of pre-existed models explaining diversity of slip behavior. In this model, frictional heterogeneity on the fault is important to explain slip diversity on the fault. Then, slip behavior of the fault with the simplest frictional heterogeneity is also investigated with numerical simulations to explore the possibility that frictional heterogeneity is a key to reach a unified seismic source model of various slip behavior on the fault. In this chapter, first of all, observations and models of diverse slip behavior by previous studies are reviewed.

1.1. Diversity of Slip Behavior on the Fault

Japanese people have recognized regular earthquakes for more than a thousand years. Severe damage by strong ground shaking and related tsunamis are documented in many ancient texts, including Chronicles of Japan established in 720 (Ishibashi, 1999). However, ancient people didn’t understand what brings such disaster. Instead, they sometimes believed that an earthquake occurs when a catfish under the ground run wild. Modern research on regular earthquake has begun in Meiji era. In 1880, Yokohama earthquake occurred, which surprised many foreigners hired by the Meiji government, including John Milne. He established the first seismological society of Japan (SSJ) as the vice president to investigate earthquakes, and made great effort to design seismometers. In 1891, Nobi

earthquake, which is the largest inland earthquake ever in Japan, hits the central Japan. After Nobi earthquake, the Japanese government established Disaster Prevention Committee, and instead first SSJ was dissolved in 1892. In 1896, Meiji Sanriku earthquake has occurred. Although the ground shaking of this earthquake was not much strong, very high tsunami hit the Pacific coast of Tohoku region. Such strange earthquake is called tsunami earthquake (Kanamori, 1972). In 1923, Kanto earthquake hits Tokyo, which caused more than a hundred thousand deaths. After Kanto earthquake, Disaster Prevention Committee was dissolved and Earthquake Research Institution was established. Since then, many disastrous earthquakes hit Japan again and again. Disastrous earthquakes have been also occurred in various places around the world. Modern seismic and geodetic measurements have been conducted for those earthquakes. Geodetic measurements revealed transient deformation (Smith and Wyss, 1968), which is now called afterslip. The theory of seismology has been developed in 20th century analyzing those data. It was understood that earthquakes are caused by rapid slip on the fault, which can be expressed by the double-coupled moment in elastodynamics (Maruyama, 1963). In 1995, Kobe earthquake has occurred, which was the most disastrous earthquake in Japan since 1923 Kanto earthquake. After this earthquake, seismic and geodetic observations were drastically improved constructing Hi-net, F-net, Kik-net (Okada et al., 2004), and GEONET (Sagiya, 2004) all over Japan. These new observation networks enable us to see the new slip phenomena called slow earthquakes (Obara, 2002). After the 2011 Tohoku earthquake, which was the largest earthquake recorded in Japan, new ocean bottom network S-net is also being constructed. Now in 21st century, we need to understand the physical mechanism of diverse slip behavior on the fault. In this section, important characteristics of diverse slip behaviors are reviewed.

1.1.1. Regular earthquake

Regular earthquakes are characterized by rapid shear slip on the fault at about 1 m/s. Its rupture propagates at about shear wave velocity (e.g., Andrews, 1976). An individual regular earthquake can be characterized by

several parameters. To characterize the size of an earthquake, it is convenient to use slip, rupture area, or the duration of earthquake. However, there are two physical quantities representing the size of an earthquake. One is the seismic moment defined as the slip integrated over the fault multiplied by the rigidity (Aki, 1966). Because dynamic behaviors of an earthquake, such as slip velocity during an earthquake, are not included in its definition, the seismic moment measures the static nature of an earthquake. The other is the seismic radiation energy, which measures the dynamic nature of an earthquake (e.g., Rudnicki and Freund, 1981). It is defined as the energy radiated by an earthquake. It can be calculated by integrating the power spectrum of velocity seismogram calibrated for the seismic attenuation and the site amplification. Basic characteristics of the power spectrum are explained by the omega-square model of Brune (1970). In the model, the power spectrum of displacement seismogram is constant below the specific frequency, which is called a corner frequency. Above a corner frequency, the power spectrum falls by f^2, where f is frequency. A corner frequency is inversely proportional to the size of rupture area divided by the shear wave velocity.

An earthquake releases accumulated strain and decreases stress on the fault. A parameter called the stress drop characterizes the stress decreases on the fault. If the slip distributions on the fault can be resolved by seismic and geodetic observations, stress drop can be calculated in the elastodynamics (Ide and Takeo, 1997). If not, stress drop can be estimated assuming a circular crack model, such as Eshelby (1957), in which the length scale of circular crack is estimated from the corner frequency of the event.

Considering the energy budget of an earthquake, the strain energy, which is released by an earthquake, is converted to friction energy, radiation energy, and fracture energy (Kostrov, 1974; Dahlen, 1977). Friction energy is consumed by frictional sliding during an earthquake. However, it is very difficult to estimate its absolute value because the absolute stress cannot be estimated from seismic observations. To estimate the amount of friction energy, direct observations of the fault after an earthquake measuring temperature on and around the fault is required (Kano et al., 2006). Fracture

energy is consumed to break the cohesion at the fault tip during the seismic rupture propagation (Barenblatt, 1959). Because the summation of the seismic radiation energy and the fracture energy can be estimated from the history of stress and slip during an earthquake, the fracture energy can be also evaluated from the seismological observations (Ide and Takeo, 1997).

Although characteristics of events vary for earthquakes, some statistical natures exist among them. The first statistics is the power law statistics in the size-frequency distributions of earthquakes, so-called Gutenberg-Richter law (GR law; Gutenberg and Richter, 1944). The number of earthquakes N larger than the moment magnitude M, which is defined using the seismic moment, is represented by

$$\log_{10} N = a - bM \,. \quad (1.1)$$

The lower limit, to which GR law can be applied, is usually determined by the detectability of observation networks. It is confirmed that GR law can be applied down to micro-earthquakes (M-4) in the mine (Kwiatek et al., 2010). At large magnitude, it is suggested that the size-frequency distribution is tapered by Gamma distribution (Kagan, 1993). *b*-value is usually close to 1, though it seems to vary with stress state around earthquake source region (Mogi, 1962; Schorlemmer et al., 2005). It is relatively smaller for thrust-type events (higher stress), and larger for normal-type events (lower stress). It is also observed that *b*-value changes with the age of subducting plate (Nishikawa and Ide, 2014). Temporal decrease of *b*-value just before large earthquake is sometimes observed as well (Tanaka et al., 2002a). It may be related to the preparation process of large earthquakes.

Power law statistics can be observed in the conventional size representation of earthquakes as well. The seismic moment is proportional to the cube of the length or width of rupture area (Mai and Beroza, 2000). The seismic moment is also proportional to the cube of the duration (Houston, 2001). This power-law statistics is observed in the dynamic process of earthquake growth as well. At the initial part of earthquakes, the seismic moment increases with the cube of time from the rupture initiation regardless of the final size of events (Uchide and Ide, 2010). They observed complex slip behavior during small earthquakes, as observed in large

earthquakes. Fractal heterogeneity is observed in slip distributions of various earthquakes (Mai and Beroza, 2002). The fracture energy of earthquakes also seems to obey power law. The fracture energies estimated from the seismic observations (~1 MJ/m^2; Beroza and Spudich, 1988; Abercrombie and Rice, 2005) are much larger than those estimated in rock experiments (1-10 kJ/m^2; Scholz, 2002; Ohnaka, 2003).

In contrast, some parameters are scale-invariant. The scaled energy, which is a ratio of the radiation energy to the seismic moment, is almost constant for the wide range of the magnitude from -3 in the mine to 7 on a natural fault (Ide and Beroza, 2001), though there has been debates that the scaled energy weakly depends on the magnitude (e.g., Mayeda and Walter, 1996). It is also known that the stress drop of earthquakes is also constant for the wide range of the magnitude (Abercrombie and Rice, 2005; Allmann and Shearer, 2009). Rupture propagation velocity is usually about constant at about shear velocity, though sometimes super-shear ruptures are reported (Archuleta, 1984). These power-law statistics and scale-invariant parameters suggest that the earthquake generating process has self-similar nature.

When looking at earthquakes as a group, statistical nature is observed in the seismicity. That is summarized as the Epidemic-Type Aftershock Sequence (ETAS) model (Ogata, 1988). In this model, seismicity is considered as a point process governed by non-stationary Poisson process. The probability where an earthquake occurs is expressed as a summation of ambient triggering by the tectonic loading and aftershock-triggering by previous earthquakes. The occurrence rate of aftershocks is inversely proportional to the time from the mainshock, which is known as the Omori's law (Omori, 1894; Utsu, 1970). We observe power-law statistics here again. ETAS model fits the observed seismicity very well. However, the swarm-type activity cannot be explained by ETAS model with parameters estimated for mainshock-aftershock-type seismicity because earthquakes in swarm activities would be triggered by background process such as transient slip or fluid migrations, which is not considered in ETAS model (Ogata, 1992).

Although the earthquake generating process seems to be random in

the time domain, seismicity does not seem to be random in the space domain. An extreme example is repeating earthquakes (Nadeau and McEvilly, 1997). Repeating earthquakes are defined as earthquakes, which occur at the almost same place and show high waveform similarities (usually cross-correlation coefficient larger than 0.9). Repeating earthquakes are interpreted as seismic ruptures occurring at almost the same locked region, which we usually call asperity, surrounded by the ductile area. An interesting feature of repeating earthquakes is that they obey their unique scaling law between recurrence intervals and the seismic moment (Nadeau and Johnson, 1998). Moderate examples will be the slip distributions of M7 class earthquakes in Tohoku subduction zones. Several M7 class earthquakes have been recorded and analyzed off Tohoku and Hokkaido so far. Although each earthquake has its own unique slip distribution, the area where large slip occurred were roughly overlapped (Yamanaka and Kikuchi, 2004; Okada et al., 2005). Geodetic observations during an inter-seismic period describe the locked plate interface around such region (Suwa et al., 2006). These observations imply the existence of some spatial structure on the plate interface, which is related to the earthquake generating process.

1.1.2. Tsunami earthquake

Tsunami earthquakes occur at the shallow plate interface and generate great tsunamis, such as 1899 Meiji Sanriku earthquake. They are earthquakes, which have larger seismic moment than expected from the body-wave magnitude (Kanamori, 1972). That is, some part of deformation is so slow that it does not radiate large high-frequency seismic waves. The duration of tsunami earthquakes is longer than those of regular earthquakes with the same seismic moment, and it is a common feature of shallow regular earthquakes near the trench (Bilek and Lay, 2002). Longer duration of seismic events may be attributed to a frictional difference due to the unconsolidated sediment on the shallow plate interface (Marone and Scholz, 1988). Hence, tsunami earthquakes are considered to be similar to regular earthquakes.

1.1.3. Afterslip

Even after the regular earthquakes finish, surface deformation continues for a long time (Smith and Wyss, 1968). This deformation is usually proportional to logarithm of lapse time from the mainshock (Bucknam et al., 1978). Slip on the fault during regular earthquakes releases accumulated stress in the slip area. On the other hand, stress in surrounding aseismic area is invoked due to the seismic slip. Increased stress is accommodated by the transient slip, called afterslip, which generates long-lasting surface deformation. Its slip velocity is so low that it does not generate any seismic radiations and tsunamis. Instead, afterslip transmits stress to the surrounding area, and triggers aftershocks. Temporal expansions of aftershock area are sometimes observed (Mogi, 1968), which is interpreted as the reflection of temporal expansions of afterslip area (Kato, 2007).

1.1.4. Slow earthquake

Slow earthquakes are the group of slip behavior on the fault newly discovered in the begging of 21st century. Recent dense seismic and geodetic observations enable us to observe faint signals of slow earthquakes. Signals of slow earthquakes are differently named according to their frequency range. Geodetic signal, which lasts usually more than a week, is called slow slip event (SSE; Dragert et al., 2001). Seismic signal of 10-200 s frequency range observed by broadband seismometers is called very low frequency earthquakes (VLFEs; Ito et al., 2007). Seismic signal of 1-10 Hz frequency range is called non-volcanic tremors or tectonic tremors (Obara, 2002). Among tectonic tremors, which have ambiguous arrivals of P- and S- waves, short-period signals with clearer P-wave arrival are sometimes observed, which is called low frequency earthquakes (LFEs; Katsumata and Kanaya, 2003). Shelly et al. (2007a) showed that tectonic tremor is a swarm of LFEs. Although there seems to be frequency gaps between tectonic tremors and VLFs and between VLFs and SSEs, in which signals of slow earthquake have not been observed, these gaps corresponds to observational gaps (Ide, 2014). At the beginning of slow earthquake study, SSEs and tectonic tremors

have been identified at the deeper extension of locked zone in Nankai and Cascadia subduction zones (Rogers and Dragert, 2003; Obara et al., 2004). Afterwards, VLFEs have been identified in Nankai subduction zone, and recently in Cascadia subduction zone (Ito et al., 2007; Ghosh et al., 2015). Because all of these phenomena have low-angle thrust focal mechanism (Dragert et al., 2001; Ito et al., 2007; Ide et al., 2007a), and because tectonic tremors are located on a thin line above intra-slab regular earthquakes (Shelly et al., 2006), slow earthquakes are interpreted to represent shear slip on the plate interface. Every component of slow earthquakes are usually synchronized each other (recently exception is reported by Hutchison and Gosh, 2016) with relatively constant recurrence intervals. Hence, their activities are called episodic tremor and slip (ETS; Rogers and Dragert, 2003; Obara et al., 2004). Now, slow earthquakes have been identified not only in Nankai and Cascadia subduction zones, but also in various subduction zones and transform faults around Pacific, and even in inland faults (e.g., Schwartz and Rokosky, 2007; Beroza and Ide, 2011; Obara, 2011; Chao and Obara, 2016). Slow earthquakes have been identified on the shallower plate interface in subduction zones as well (e.g., Obara and Ito, 2005). Because slow earthquakes are usually located at the along-dip transition zones from locked zone to the stable slip zone on the fault, slow earthquakes are interpreted as brittle-ductile transitional phenomena. However, in some subduction zones, such Boso peninsula in Japan and Hikurangi subduction zone in New Zealand, swarm activities of regular earthquakes, instead of tectonic tremors, have been observed synchronizing with SSEs (Ozawa et al., 2003; Wallace et al., 2012). SSEs are also observed in the source area of 2011 Tohoku-oki earthquake before the mainshock (Ito et al., 2013) accompanying small regular earthquakes (Kato et al., 2012). In such subduction zones, the source area of regular earthquakes seems to be mixed or overlapped with that of slow earthquakes. Because similar swarm activities of regular earthquakes are observed in many subduction zones (Holtkamp and Brudzinski, 2011), SSEs may exist in wider tectonic environment than VLFs and tectonic tremors, though validation is difficult due to the limited observation network. Furthermore, some of SSEs, which are called long-term

SSEs with long recurrence intervals, are seismically silent, such as in Bungo Channel and Tokai in Nankai subduction zone, though they activate nearby tectonic tremors.

Slow earthquake can be characterized with the same parameters as regular earthquakes, such as the seismic moment, the seismic radiation energy, and the stress drop. The size-frequency distributions of slow earthquakes have not been clarified enough yet. The seismic moments of SSEs are reported to obey power law (i.e., GR law) with *b*-value of 1, as regular earthquakes, in Cascadia subduction zone (Wech et al., 2010). On the other hand, the size distributions of tectonic tremors or VLFEs are controversial. Watanabe et al. (2007) showed that distributions of displacement amplitude of tectonic tremors obey exponential law, not the power law. Aso et al (2013) estimated *b*-value for LFEs, and found that *b*-value is pretty high around 3, though magnitude distributions have cutoff around 0.5. They mentioned that power law is not appropriate to describe the size distributions of LFEs. In contrast, Bostock et al. (2015) insisted that the seismic moment distribution of LFEs can be described by the power law, but *b*-value is about 5, which is pretty higher than that for regular earthquakes. The moment magnitude of SSEs usually ranges from 5.5 to 7.5 (e.g., Schwartz and Rokosky, 2007). VLFs have magnitudes about 3-4 (Obara and Ito, 2005; Ito et al., 2007). Although the estimation of magnitudes of LFEs is difficult, it is estimated to be about 0-2 from the amplitude of LFEs (Aso et al., 2013; Bostock et al., 2015). Comparing those magnitudes with their duration, it has been revealed that slow earthquakes have a very different scaling relation from regular earthquakes (Ide et al., 2007b), though the revised scaling relation is proposed by Ide (2008) and Gomberg et al. (2016). As explained above, magnitudes of regular earthquakes are proportional to the cube of their duration (Houston, 2001). Meanwhile, magnitudes of slow earthquakes are linearly proportional to their duration, i.e., the moment rate of slow earthquakes are almost constant at 10^{12}-10^{13} Nm/s. Therefore, the duration of slow earthquake is much longer than that of regular earthquakes with the same magnitude. That is, the deformation by slow earthquakes is, as its name suggests, slower than regular earthquakes.

This means that slow earthquakes are not self-similar, which is the fundamental characteristic of regular earthquakes. On the other hand, the scaled energy and the stress drop are constant for slow earthquake as well. However, the scaled energy of slow earthquake is about 10^{-10} (Ide et al., 2008), which is much smaller than that of regular earthquakes at 10^{-5} (Ide and Beroza, 2001). The stress drop of slow earthquake is estimated about 10 kPa (Ide et al., 2007b), which is also much smaller than that of regular earthquakes at about 3 MPa (Abercrombie and Rice, 2005).

Fourier spectrum of displacement seismogram of slow earthquake falls inversely proportional to the frequency in high frequency (Ide et al., 2007b). This is different from that of regular earthquakes, which can be explained by the omega-square model. The constant moment rate function observed in the scaling relation (Ide et al., 2007b) can explain this f^1 spectrum. However, f^1 spectrum cannot continue to the infinite frequency, unless the seismic radiation energy becomes infinite. Zhang et al. (2011) stacked array data located at Cascadia subduction zone to improve signal to noise ratio, and observed that Fourier spectrum decays by f^2 as regular earthquakes at high frequency around 10-20 Hz. Combined with the observation of Shelly et al. (2007a) that tectonic tremors is a swarm of LFEs, slow earthquake can be considered as a swarm of very tiny seismic events with the lower stress drop.

Tectonic tremors in ETS sometimes show migrations both in along-strike and along-dip directions (Obara, 2002; Houston et al., 2011; Peng et al., 2015). Migration speed varies with the scale we look at, which can be characterized as the diffusive migration pattern (Ide, 2010a). Analysis combined seismic and geodetic data shows that migration of tectonic tremors manifests the migration of SSEs (Hirose and Obara, 2010). Considering the constant moment rate of slow earthquakes with this migration of slow earthquakes, the essential nature of slow earthquakes may be the propagation of slip pulse at slow slip velocity, which cannot accelerate to fast slip velocity for some reason, instead of self-similarity.

As it is for regular earthquakes, slow earthquakes also show spatially unique characteristics. Precise hypocentral locations of tectonic

tremors or LFEs have revealed that the spatial distribution of them is not random, but has some spatial structure. Such spatial structure of LFE hypocenters is preserved among different SSEs (Peng et al., 2015; Peng and Rubin, 2016), which suggests the similarity to repeating earthquakes. Several lineaments of tremor hypocenters have been identified in western Shikoku. Directions of those lineaments are consistent with current or past plate motion directions (Ide, 2010a). Therefore, spatial structure of tremor or LFE hypocenters should be related to some property on the plate interface. Furthermore, activities of slow earthquake are separated into segments. A preferable along-strike migration direction seems to exist in each segment (Obara, 2010). The time invariant segment boundary invokes its relation to some spatial characteristics of the plate interface.

Further difference between slow earthquakes and regular earthquakes is the sensitivity to small stress perturbations. Various stress perturbations exist on the fault, such as tidal stress and transient stress by the passing surface wave. Tidal triggering of regular earthquakes was the controversial topic in seismology. Although tidal triggering can be statistically verified in some specific tectonic setting or conditions, their correlation is generally statistically very weak for regular earthquakes (e.g., Tsuruoka, et al., 1995; Cochran et al., 2004). However, tectonic tremors are highly sensitive to tidal stress (Shelly et al., 2007b). Tectonic tremors are triggered by the passage of surface waves as well (Miyazawa and Mori, 2005). Because slow earthquakes lie adjacent to the locked zone on the plate interface, and because slow earthquakes are very sensitive to small stress changes, it is suggested that stress accumulation process in the locked zone may influence slow earthquake activities (e.g., Obara and Kato, 2016). For example, an activation of tectonic tremors has been reported in San Andreas Fault three weeks before M6 earthquake (Nadeau and Guilhem, 2009). If it is true, monitoring slow earthquake will be helpful for earthquake forecasting, though further physical understanding is definitely necessary.

1.2. Models for Diverse Slip on the Fault

As reviewed in the previous section, diverse modes exist in the shear slip behavior on the plate interface. Understanding the physical mechanism of this diversity is inevitable to understand the whole seismic cycle in subduction zones because these diverse slips occur side-by-side on the same plate interface interacting each other. Many previous studies have tried to model slip diversity. In this section, various models constructed by previous studies are reviewed.

1.2.1. Rate and state friction model

Many previous studies numerically simulated shear-slip behavior on the fault using rate and state friction (RSF) law. RSF law is empirically derived based on rock experiments (Dieterich, 1979), which defines the relation between stress and slip velocity on the fault as

$$\tau = \tau_0 + a\sigma \log\left(\frac{V}{V_*}\right) + b\sigma \log\left(\frac{\theta}{\theta_*}\right). \quad (1.2)$$

In Equation (1.2), σ is the normal stress on the fault. τ and V represent shear stress and slip velocity on the fault, respectively. τ_0 is ambient shear stress on the fault when the fault slips at the reference slip velocity V_*. The second term on the right-hand side of Equation (1.2) is called the direct effect, which increases stress with increasing slip velocity. The direct effect reflects rheological resistivity of the fault. θ in Equation (1.2) is called the state variable, which represents the strength of coupling on the fault (e.g., Nakatani, 2001). θ_* is a reference state variable when the fault steadily slips at the reference slip velocity V_*. The third term on the right-hand side of Equation (1.2) decreases stress on the fault with the weakening of the fault coupling (decreasing state variable). Temporal changes of the state variable are empirically derived in many ways. Popular formulations are the aging law (Dieterich, 1979)

$$\frac{d\theta}{dt} = 1 - \frac{V\theta}{D_c}, \quad (1.3)$$

and the slip law (Ruina, 1983)

$$\frac{d\theta}{dt} = -\frac{V\theta}{D_c}\log\left(\frac{V\theta}{D_c}\right), \quad (1.4)$$

where D_c is the characteristic slip distance. With those laws, the reference state variable θ_* can be expressed as

$$\theta_* = \frac{D_c}{V_*}. \quad (1.5)$$

RSF parameters a and b are dependent on the tectonic environment, such as rock types, temperature and pressure (e.g., Blanpied et al., 1991). In the single spring-block system, the fault shows velocity-strengthening (VS) behavior, which results in stable slip, when a-b value is positive. When a-b is negative, the fault shows velocity-weakening (VW) behavior in the steady state, which results in stick-slip behavior if the system stiffness is small enough.

RSF law can reproduce shear slip behavior on the fault at relatively low slip velocity around 10^{-6}-10^{-3} m/s. On the other hand, the strength of the fault decreases rapidly contrary to the prediction by RSF law at seismic slip velocity (Di Toro et al., 2004). This is called the dynamic weakening effect. Various mechanisms have been proposed to reduce frictional strength at seismic slip velocity, such as thermal pressurization (Sibson, 1973) and flash melting (Tsutsumi and Shimamoto, 1997).

Shear slip behavior of a strike-slip fault governed by RSF law is numerically simulated by Tse and Rice (1986). They considered depth-dependent a-b values on the fault based on a temperature profile along the fault. In rock experiments results, a-b values are negative at lower temperature (i.e., shallower fault), which cause stick-slip behavior. On the other hand, a-b values are positive at higher temperature (i.e., deeper fault). Therefore, in their numerical calculations simulating seismic cycles, regular earthquakes occur at the shallower fault, whereas afterslip occurs at the deeper fault following shallower regular earthquakes. Many studies have been done based on their study with various developments, such as inclusion of a realistic bending plate interface (e.g., Hori et al., 2004), interacting several seismic patches (e.g., Kato 2003, 2007), and considering various dynamic-weakening effects (e.g., Noda and Lapusta, 2013).

After the discovery of slow earthquake, RSF models are used to explain the diversity of slip behavior. When the size of VW zone (VWZ) is tuned such that it is close to the nucleation size (Rubin and Ampuero, 2005; Ampuero and Rubin, 2008), the fault shows aseismic stick-slip events, which is similar to SSE (Figure 1.1; e.g., Liu and Rice, 2005, 2007; Ariyoshi et al., 2009, 2012; Mitsui 2015). Because a-b value transits from a negative value to a positive value with increasing depth, the nucleation size of VWZ may increases at this transition, which could realize this tuning. However, Rubin (2008) pointed out that RSF-parameter range generating aseismic stick-slip is wide enough with the aging law, whereas it is too narrow with the slip law.

To reproduce the co-existence of various sizes of regular earthquakes on the same plate interface in the numerical simulation, cascade up model has been also proposed (Figure 1.1; Ide and Aochi, 2005; Hori and Miyazaki, 2010; Noda et al., 2013). In this model, various sizes of slip-weakening or VW patches are distributed on the fault with critical slip distance scaled by its size. Because larger seismic patches have longer critical distance, larger earthquakes occur less frequently, though it is not clarified in the model why the critical slip distance varies with the size of seismic patches. This model can explain the scaling of the initial moment growth as well (Ide and Aochi, 2005).

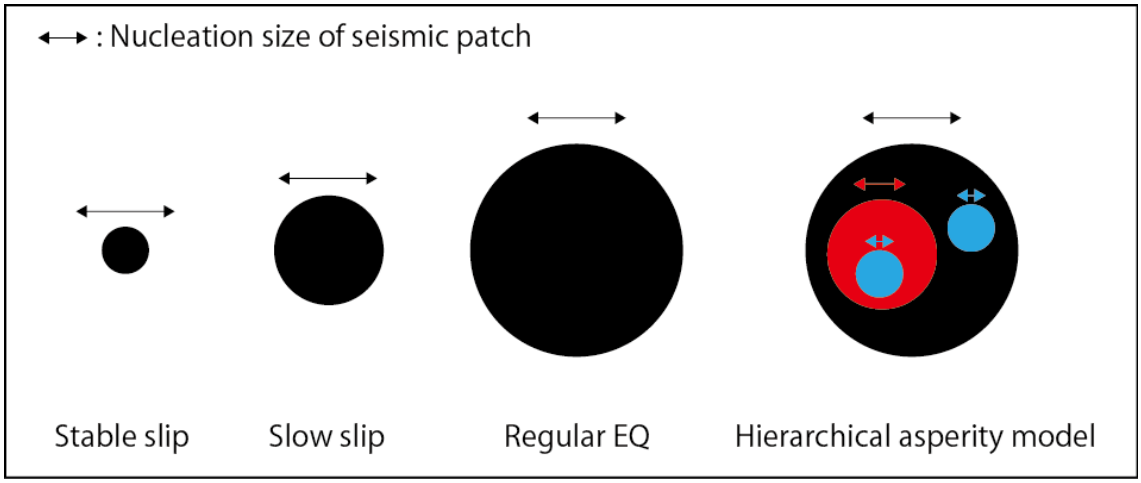

Figure 1.1: A schematic figure of RSF model. Circles are VWZ on the fault. Arrows represent the nucleation size of VWZ. In the hierarchical asperity model, colors of circles and arrows are corresponding.

1.2.2. Rate and state friction model with cut-off velocity

In the shear deformation experiments of halite, velocity-dependence of stress in the steady state (VW or VS behavior) has been changed with slip velocity (Shimamoto, 1986). In this experiment, VW behavior was observed at the lower slip velocity, whereas VS behavior was observed at the higher slip velocity. This behavior cannot be explained by the original RSF law. Shibazaki and Iio (2003) modeled such behavior by modifying RSF law with the cut-off velocity as

$$\tau = \tau_0 - a\sigma \log\left(\frac{V_1}{V}+1\right) + b\sigma \log\left(\frac{V_2\theta}{D_c}+1\right). \quad (1.6)$$

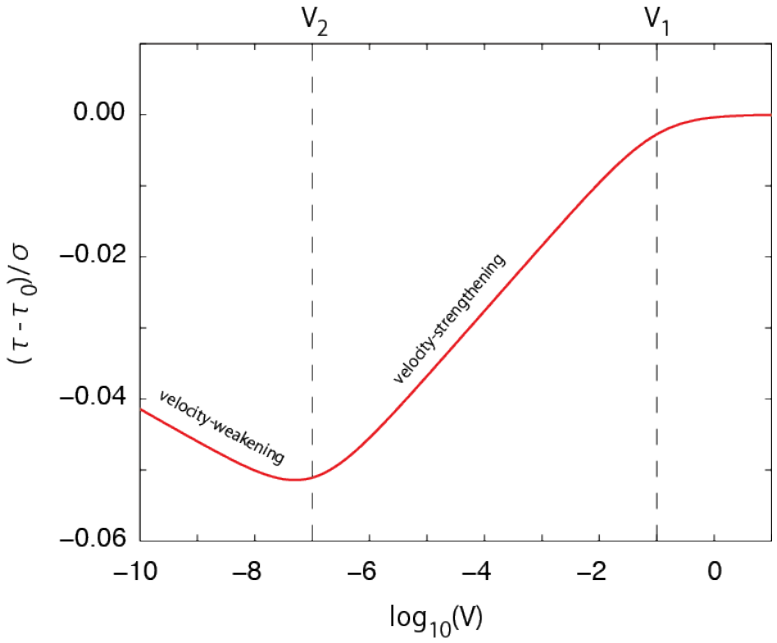

Figure 1.2: An example of velocity dependence of stress in the steady state of RSF law with cut-off velocity. Following parameters are used for the calculation; a=0.004, b=0.006, V_1=10^{-1} m/s, V_2=10^{-7} m/s.

Here, V_1 and V_2 are cut-off velocity for the direct effect and the fault weakening. When $V_2 << V_1$ and a-b < 0 is assumed, the fault shows VW behavior at $V < V_2$ in the steady state. At $V_2 < V < V_1$, the fault changes its behavior to VS. At $V_1 < V$, stress becomes constant regardless of slip velocity (Figure 1.2). Hence, using this frictional law, it is possible that the stick slip

initiated at low slip velocity is in reversal decelerated at higher slip velocity, resulting in aseismic stick-slip events (i.e., SSEs). Shibazaki and Shimamoto (2007) simulated seismic cycle in subduction zones including both shallower regular earthquake and deeper slow earthquakes assuming the depth dependence of cut-off velocity.

1.2.3. Dilatant hardening model

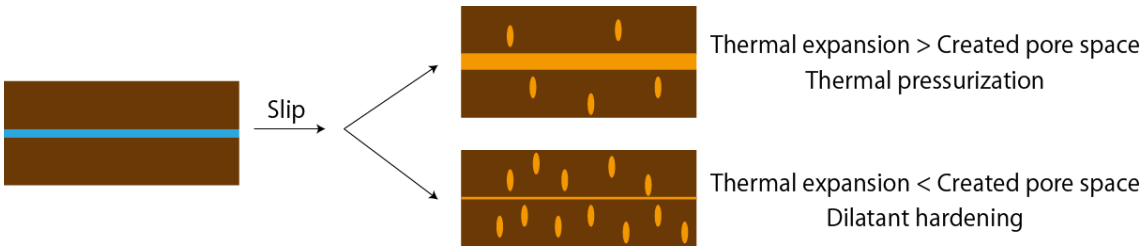

Figure 1.3: A schematic figure of the thermal pressurization and the dilatant hardening. The pore fluid (light blue) is heated by the slip. Heated pore fluid (orange) increases its volume. Slip also creates new pore space.

Some models decelerate slip velocity on the fault through a process called the dilatant hardening (e.g., Suzuki and Yamashita, 2009; Liu and Rubin, 2010; Segall et al., 2010; Yamashita and Suzuki, 2011). It is expected that pore fluid exists around the plate interface due to the dehydration of subducted minerals (Hacker et al., 2003). When the fault slips, frictional heating raise temperature of the pore fluid, which increases pore-fluid pressure on the fault. Higher pore-fluid pressure decreases the effective normal stress, which weakens the shear strength. As a result, seismic slip is enhanced. This process is called the thermal pressurization (Figure 1.3; Sibson, 1973). On the other hand, the pore space is also considered to increase by slip on the fault due to the dilatancy of rocks. When the pore space is increased, pore-fluid pressure decreases because the pore fluid escapes to the created pore space, which suppresses the slip on the fault. This process is called the dilatant hardening (Figure 1.3; Rice, 1975). When the thermal pressurization is dominant in the slip process, the fault shows seismic slip. In contrast, if the dilatant hardening is dominant, slip on the

fault and its rupture propagation are suppressed at slow velocity. Because the efficiency creating pore space with slip can be influenced by the tectonic environment, such as temperature and pressure, this model has also potential to explain the diversity in shear-slip behavior on the fault.

1.2.4. Frictionally heterogeneous fault model

A series of studies by Ando et al. (2010, 2012) and Nakata et al. (2011) have constructed slow earthquake model with the frictional heterogeneity on the fault. In their model, slip-weakening friction law with Newtonian rheology has been utilized instead of RSF law. Brittle patches, which generate seismic events, are embedded on the ductile background, on which stress diffuses to surroundings. When slow slip on the background reaches a brittle patch, a small seismic event occurs by breaking the brittle patch. Accumulated stress on the brittle patch is released, and it diffuses into surroundings, which accelerate background slow slip, though background cannot be accelerated up to seismic slip velocity due to the Newtonian viscosity. Accelerated background slow slip successively ruptures brittle patches, resulting in the boxcar shape of total moment rate function, which reproduces f^1 decay of displacement spectrum (Ide et al., 2007b). Newtonian viscosity reproduces diffusive migration pattern of tectonic tremors (Ide, 2010a) as well. Faster migrations of tectonic tremors in short time scale (rapid tremor reversals or RTRs; Houston et al., 2011) can be also reproduced as the rupture of brittle patches with higher frictional strength.

Nakata et al. (2011) has shown that this frictionally heterogeneous fault model is also useful to explain the diversity of slip behavior on the fault. They conducted numerical simulations of several frictionally heterogeneous faults with different density of brittle patches. As a result, some fault with low or medium density of brittle patches show slow-earthquake like slip behavior. In contrast, when the density of brittle patches is high, ductile background is also accelerated to seismic slip velocity. A total moment rate function is a triangular shape and its spectrum has f^2 decay, corresponding to regular earthquakes.

Skarbek et al. (2012) also explored the frictionally heterogeneous

fault model to explain the transition from regular earthquakes to slow earthquakes. In their model using RSF, VWZ and VS zone (VSZ) are divided into pieces smaller than the nucleation size of VWZ. They have investigated the shear slip behavior of the fault in such condition with various density and *a-b* value of VSZ. As a result, they have found that the entire fault including VSZ shows seismic slip behavior when *a-b* in VSZ is close to zero. On the other hand, when *a-b* value in VSZ is high, the fault shows aseismic stick-slip behavior (SSEs).

Dublanchet et al. (2013) also modeled the frictionally heterogeneous fault with RSF. In their model, VWZ, which generate regular earthquake, are distributed randomly on the infinite fault plane with cyclic boundary condition. Then, they have investigated shear-slip behavior of the fault with various proportions of VW zone on the fault and with various *a-b* values in VS zone. As a result, they have found that seismic events are restricted only within VWZ when *a-b* in VSZ is high, whereas the entire fault slips seismically when *a-b* value in VSZ is close to zero.

These studies suggest that the frictionally heterogeneous fault model can also be a candidate of the unified seismic source model explaining diverse seismic slip behavior (Figure 1.4).

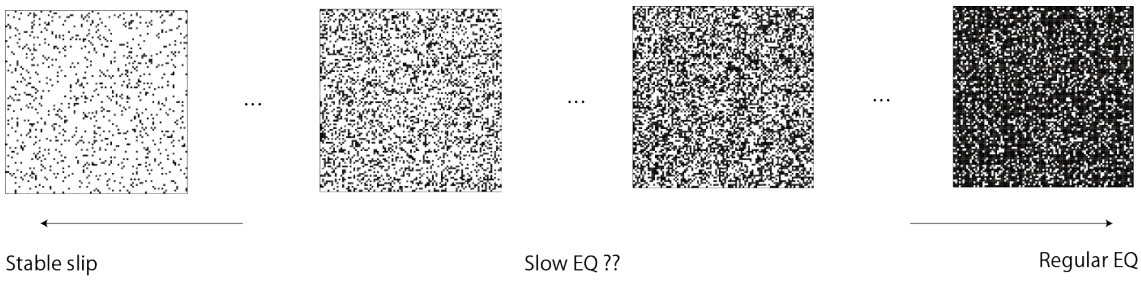

Figure 1.4: A schematic figure of the frictional heterogeneity model. Black color represents brittle patches. White color represents ductile region on the fault. Macroscopic shear slip behavior on the fault changes with the portion of brittle patches on the fault.

1.2.5. Mathematical model

Statistical properties of seismicity are sometimes modeled by a

mathematical model, in which the physical background is not necessarily clear. For regular earthquakes, ETAS model (Ogata, 1988) is well-known statistical model explaining the mainshock-aftershocks sequence. ETAS model regards seismicity of regular earthquakes as time-dependent Poisson process as

$$\lambda(t) = \mu + \sum_{t_i<t} \frac{K \exp\left[\beta\left(M_i - M_c\right)\right]}{\left(t - t_i + c\right)^p}. \quad (1.7)$$

Probability generating earthquakes λ at time t is the summation of background seismicity rate due to tectonic stress accumulation μ and triggering effect by previous earthquakes occurred at time t_i. Triggering effect is inversely proportional to the exponent p of the lapse time from the event with delay time c (Omori law; Omori, 1894; Utsu, 1970), and is exponential to the magnitude of the event M_i. K and β are constant model parameters. M_c is the complete magnitude of an earthquake catalog. Although the relation to the physical mechanism is unclear, ETAS model can characterize seismicity very well. Seismic swarms are characterized differently from regular seismicity as higher background seismicity rate with weak triggering effect. It implies that regular earthquakes in seismic swarms are triggered by other physical mechanisms than mainshock-aftershock triggering, such as fluid migrations or SSEs.

Brownian walk model is proposed for the seismicity of slow earthquake (Ide, 2008, 2010b). In this model, a parameter related to the length scale of rupture area is fluctuated by the random process called Orstein-Uhlenbeck process (Uhlenbeck and Ornstein, 1930). Though this model can explain various characteristics of slow earthquake, such as the scaling relation (Ide et al., 2007b), the displacement spectrum (Ide et al., 2007b), and exponential distributions of tremor amplitude (Watanabe et al., 2007), the relation to the physical mechanism on the fault is unclear.

Ben-Zion (2012) has constructed non-continuum fault model, in which a parameter related to the stress drop decreases with increasing the depth. At the shallower plate interface, the size-frequency distribution obeys power law with the characteristic earthquake, in which seismic slip occurs

on the entire fault. Because this model is in non-continuum limit, every discretized grid can slip seismically alone. GR law of resultant seismicity comes from this non-continuity of the model. The scaling relation between the duration and the seismic moment of the shallow seismicity obeys that of regular earthquakes. On the other hand, the characteristic earthquakes do not occur in the deeper fault where the stress drop is close to zero. Although the size-frequency distributions obey the power law as well, the seismic moment is proportional to the square of the duration when the seismic moment is small, and is linearly proportional to the duration when the seismic moment is large, as predicted by the Brownian walk model of Ide (2008, 2010b). However, how to relate this model to the continuum model is not still clear.

1.3. My Research Projects

Since I have started my research activity in 4th-year undergrad, my research goal has been to understand the physical mechanism of slip diversity on the fault. To reach this goal, I have done several research projects and published six papers as a first author and five papers as a co-author in international peer-reviewed journals. In this section, those papers excluded from this thesis are briefly reviewed.

1.3.1. Depth of tectonic tremors

The location of events is the basic and fundamental information for the analysis and the interpretations. However, it is difficult to estimate the precise locations, especially the depth, of tectonic tremors because of the invisible P-wave and the ambiguous S-wave. Therefore, there were controversies about their location in the early stage of slow-earthquake study (Kao et al., 2005). To overcome this problem, LFE signals among tectonic tremors are usually investigated because LFEs have relatively clearer P-wave and S-wave arrival. However, this method is not applicable where LFEs have not been identified. Therefore, a new method to estimate the depth of tectonic tremors has been constructed. This work was published

in Earth and Planetary Science (Yabe and Ide, 2013).

Measurements of arrival time differences between P-wave and S-wave are very useful to constrain the depth of events. Because the incident angle of seismic waves should be close to vertical due to the shallow low-velocity structure, P-wave should be mainly included in the vertical seismograms, though it is not visible due to its small signal and due to overlapping with S-waves of previous events. Whereas, S-wave should be included both in the vertical and horizontal seismograms. Therefore, the cross-correlation between vertical and horizontal seismograms will provide us information of S-P times. La Rocca et al. (2009) used seismic array data, and they stacked cross-correlation functions within the array. As a result, the peak corresponding to the S-P time is emphasized, which enabled them to locate tremors precisely. Their method has been modified to apply this method to the non-array data, because array data is not widely available. Instead of stacking within an array, cross-correlation functions are stacked for adjacent time windows at one station while tectonic tremors occur at similar hypocenter. S-P times are successfully measured with this new method, and tectonic tremors in east Kyushu Island are located around the plate interface estimated by Yagi and Kikuchi (2003).

1.3.2. Relation to thermal structure

Deep tectonic tremors have been usually observed in subduction zones where relatively young oceanic plate is subducted, such as Nankai, Cascadia, Mexico, and South Chile. In contrast, deep tectonic tremors have not been identified in Tohoku subduction zone, where the very old oceanic plate is being subducted (Muller et al., 2008). Because hotter subduction zones enhance the dehydrated reaction of subduting hydrated minerals at shallower plate interface (Hacker et al., 2003), and because the existence of high pressured pore fluid is expected from the sensitivity of slow earthquake to small stress perturbations (Miyazawa and Mori, 2005; Shelly et al., 2007b) and from the seismic velocity structure around the source area of deep tectonic tremors (Shelly et al., 2006), tectonic tremors are considered to be hosted at hotter subduction zones. However, deep tectonic tremors have been

identified in Hikuranki subduction zones in New Zeland, where the old oceanic plate is subducted (Taylor, 2006). Tectonic tremors in Hikurangi subduction zone show strong along-strike variation in the depth (Fry et al., 2011; Kim et al., 2011; Ide, 2012). The relation between the thermal structure and tremor depth has been tested, which was published in Earth and Planetary Science (Yabe et al., 2014a).

In the northeast part of Hikurangi subduction zone, SSEs and tectonic tremors occur at very shallow depth around 2-20 km (Wallace and Beavan, 2010; Kim et al., 2011; Wallace et al., 2016). On the other hand, SSEs and tectonic tremors occur at very deep depth around 30-70 km in the southwest part (Wallace and Beavan, 2010; Fry et al., 2011; Ide, 2012). Observed heat flow, which reflects the thermal structure under the ground, also shows the along-strike variation, high in northeast part and low in southwest part (Pollack et al. 1993; Townend 1997; Allis et al. 1998). The thermal structure of Hikurangi subduction zone is modeled with two-dimensional numerical simulations constructed by Yoshioka and Sanshadokoro (2002) and Torii and Yoshioka (2007). Frictional heating on the plate interface has been varied to fit the heat flow data on the surface. As a result, we reached the conclusion that it is possible that tremor depth changes according to the along-strike variation of thermal structure on the plate interface. However, it has been also recognized that uncertainty of thermal structure estimation is very large due to the limited number of heat flow observations.

1.3.3. Amplitude variations of tectonic tremors

Although the seismic radiation energy is an important parameter to characterize the seismic event, its estimation for slow earthquakes has been conducted in a few limited cases (Ide et al., 2008; Maeda and Obara, 2009). Because slow earthquakes show diverse activities among subduction zones and even within an individual subduction zone, uniform estimations of the seismic radiation energy are needed for various places. To estimate the seismic radiation energy, evaluations of the seismic attenuation is also important (Ide et al., 2003). In this project, the seismic attenuation has been

estimated using seismic signals of tectonic tremors. Using the estimated seismic attenuation, the seismic radiation energy is widely estimated for tectonic tremors in Nankai, Cascadia, Mexico, and South Chile subduction zones. Results were published in Bulletin of the Seismological Society of America (Yabe et al., 2014b) and in Journal of Geophysical Research (Yabe and Ide, 2014).

Some of subduction zones, such as Nankai and Cascadia, have a large locked zone on the plate interface. Almost no earthquakes occur during an inter-seismic period on the plate interface. Hence, in such subduction zones, it is difficult to estimate an attenuation of seismic waves with regular earthquakes on the plate interface. Instead, such subduction zones usually host deep tectonic tremors, which radiate small seismic signals from the deep plate interface. This study utilized seismic signals of tectonic tremors to estimate the seismic attenuation. The seismic attenuation is estimated as a function of hypocentral distance. Because the shallow structure around a seismic station also affects amplitude of seismograms, site effects are also estimated. The seismic radiation energy of tectonic tremors is estimated by calibrating observed energy with the estimated seismic attenuation and site effects. Amplitude of tectonic tremors is defined as the seismic radiation energy divided by the duration of tectonic tremors. Amplitude of tectonic tremors obeys exponential law, rather than the power law. Tremor activity usually initiates at the down dip edge of tremor zone, where amplitude of tremors is low. Small tremor activities during an inter-SSE period are limited within the small-amplitude area. When the large-amplitude area is activated after the initiation of tremor activity in the small-amplitude area, ETS starts long migration in the along-strike direction. During migrations of tectonic tremors, RTRs are observed with relatively larger-amplitude tremors. The large slip area of SSEs is also consistent with the high-amplitude area of tectonic tremors. These observations suggest that amplitude of tectonic tremors is related to the strength of local coupling on the fault. That is, lower-amplitude tremors represent weaker coupling, which can be activated frequently. Higher-amplitude tremors represent stronger coupling, which can endure higher stress with infrequent ruptures.

1.3.4. Universal existences of VLFEs

In Nankai subduction zone, where slow earthquakes have been discovered at the earliest stage of slow earthquake study, tectonic tremors and SSEs have been widely identified (Obara, 2002; Nishimura et al., 2013). On the other hand, VLFEs have been identified only in the limited part of Nankai subduction zone (Ito et al., 2007). If tectonic tremors, VLFEs, and SSEs are manifestations of the same slip on the plate interface observed in different frequency ranges, those phenomena should be co-located. Hence, the existence of VLFEs is explored by Ide and Yabe (2014), published in Geophysical Research Letter. A case study in Taiwan is also published in Geophysical Research Letter (Ide et al., 2015).

Assuming that VLFEs are synchronized with tectonic tremors, seismograms band-passed between 0.02-0.1 Hz are stacked aligned by the hypocentral time of tectonic tremors. As a result, clear signals of VLFEs become visible at every point where tectonic tremors occur (e.g., Takeo et al., 2010). Focal mechanisms are estimated using the stacked waveform of VLFEs. Estimated focal mechanisms are low-angle thrust, consistent with the subduction. More precisely, slip vectors are parallel to the direction of plate motion of subducting Philippine Sea plate (Miyazaki and Heki, 2001). The normal vectors of fault planes are consistent with the local plate models (Ide et al., 2010). The magnitudes of VLFEs are estimated to be about M2-3. The averaged moment rate, the seismic moment divided by the duration of VLFEs, is linearly proportional to the averaged radiation energy rate estimated by Yabe and Ide (2014). The scaled energy is 10^{-10}-10^{-9}, which is consistent with Ide et al. (2008), and much smaller than that of regular earthquakes (10^{-5}; Ide and Beroza, 2001).

1.3.5. Recurrence intervals of tectonic tremors

Idehara et al. (2014), published in Earth, Planets and Science, uniformly quantified the characteristic recurrence interval of tectonic tremors in various subduction zones. The recurrence interval of tremor activities is expected to reflect the stress accumulation process and the strength of the coupling. They showed that the recurrence intervals tend to

be shorter for deeper tectonic tremors, as already pointed out by Obara et al. (2010) and Wech and Creager (2011). Deeper tremor zone should have shorter recurrence intervals because stable slip occurs at the deepest subduction zone accumulating stress on the plate interface. They have also shown that recurrence intervals positively correlate with the duration of tectonic tremors.

1.3.6. Tidal modulation of seismicity

As shown by previous studies (Thomas et al., 2012; Beeler et al., 2013; Ide and Tanaka, 2014; Houston, 2015), and also shown in this thesis (Chapter 2), tectonic tremors are non-linearly sensitive to tide. If tidal sensitivity of tectonic tremors represents the modulation of slip velocity on the background plate interface, stress perturbations on the deep plate interface will influence the stress accumulation of locked zone on the shallower plate interface as well. Tanaka et al. (2015), published in Earth, Planets and Science, evaluate the effect of non-tidal stress perturbations due to the long-term variation of ocean height, and then temporal stress perturbations are compared with the seismicity. Ide et al. (2016), published in Nature Geoscience, investigated the relation between *b*-value of GR law and tidal stress. They showed that when the tidal stress enhances the slip on the plate interface, it is expected that the earthquakes are more likely to be larger, that is *b*-value is smaller.

1.4. Composition of This Thesis

In my research project so far, spatial heterogeneities of various parameters characterizing slow earthquake activities have been investigated, including duration, amplitude and recurrence intervals of tectonic tremors and the seismic moment of VLFEs. In the first part of this thesis, another parameter has been examined. That is tidal sensitivity of tectonic tremors. Because the scaled energy rate is constant for slow earthquake, occurrences of tectonic tremors are expected to represent a slow slip on the background plate interface. Therefore, tidal sensitivity of tectonic tremors reflects the

relation between slip or slip velocity and tidal stress (i.e., friction law). The correlations between those parameters will also constrain source process of slow earthquake. Based on the result of the analysis, a qualitative model for slow earthquake has been constructed, following the model of Ando et al. (2010, 2012) and Nakata et al. (2011).

In the proposed model, frictional heterogeneities on the fault play an important role to make tremor activities diverse. Some previous studies (Nakata et al., 2011; Skarbek et al., 2012) show that a class of frictionally heterogeneous fault model may explain the transition from regular earthquakes to slow earthquakes as well. To explore such possibilities further, numerical simulations of seismic rupture on the fault with frictional heterogeneities have been conducted in the latter half of this thesis. To understand the basic physics of seismic rupture on frictionally heterogeneous fault, the simplest situation is considered; a linear fault in 2D elastic medium. RSF law is used as a friction law based on results of tidal-sensitivity analysis. It has been found that slip behavior of heterogeneous fault changes with the proportion of VWZ or spatially averaged a-b value on the fault. The result of this numerical simulation implies that frictionally heterogeneous fault model has potential to explain the diversity of seismic phenomena.

This thesis is organized as follows. In Chapter 2, tidal sensitivity of tectonic tremors has been investigated, which is published in Journal of Geophysical Research (Yabe et al., 2015). In Chapter 3, numerical simulations of seismic ruptures on an infinite frictionally heterogeneous fault in the simplest situation have been conducted, which is published in Journal of Geophysical Research (Yabe and Ide, 2017). In Chapter 4, some examples of numerical simulations of shear-slip behavior on a finite planar fault with frictional heterogeneities have been presented, which is not published yet. In Chapter 5, the importance of constructing frictionally heterogeneous fault model has been discussed in terms of understanding diverse seismicity, followed by conclusions in Chapter 6.

2. Tidal sensitivity Analysis

This chapter is modified from Yabe et al. (2015), published in Journal of Geophysical Research.

2.1. Introduction

Tidal sensitivity of regular earthquakes has been a long debate in the field of seismology since 19th century. An early work was done by Schuster (1897), who showed that there are no statistical correlations between seismicity and the Earth tide. Since then, many studies reported no correlations between the Earth tide and regular earthquakes, whereas other studies reported significant correlations between them. For example, Heaton (1975) argued that tidal sensitivity of regular earthquakes located at shallower than 30 km depth with oblique-slip or dip-slip focal mechanism is statistically significant. Tsuruoka et al. (1995) also reported significant tidal sensitivity for normal-fault earthquakes. Tanaka et al. (2002b) and Cochran et al. (2004) found tidal correlations for reverse-fault earthquake as well. On the other hand, Vidale et al. (1998) concluded that tidal sensitivity is statistically insignificant for earthquakes on San Andreas Fault. Discussions on tidal triggering of regular earthquakes seem to reach a consensus that it cannot be observed globally, though weak sensitivity could be observed for a selected group of seismicity (for example, focal mechanism). Stress perturbations due to tidal stress are only about 1 kPa, which is much smaller than the stress drop of regular earthquakes (~3 MPa; Abercrombie and Rice, 2005). Hence, tidal stress is generally considered to be too small to trigger regular earthquakes, which is why regular earthquakes show only very weak tidal sensitivity. However, a series of studies by Tanaka et al. (2002a, 2006) and Tanaka (2010, 2012) provided interesting observations about temporal variations of tidal sensitivity of regular earthquakes. Those studies showed that tidal sensitivity increases before large earthquakes. It could be interpreted that even small tidal stress might influence regular earthquakes if the stress state on the plate interface is built up close to failure of large earthquakes.

Tidal sensitivity of slow earthquakes has been investigated soon after its discovery in the beginning of 21st century. Surprisingly, slow earthquakes are quite sensitive to tidal stress. It is first recognized by the 12.4 hr periodicity of tremor catalog (e.g., Shelly et al., 2007b; Rubinstein et al., 2008). Although tidal stress has various periodicities in its temporal variation, its dominant component has 12.4 hr periodicity, which is called M2 tide. The power spectrum of tremor catalog has a peak corresponding to M2 tide, as shown in Figure 2.1. In Figure 2.1, the power spectrum of tremor catalog detected by Yabe and Ide (2014) with the envelope correlation method is plotted. Tectonic tremors at 33.3-33.5°N and 132.7-132.9°E between April 2004 and March 2009 are considered. The tremor catalog is regarded as a sequence of delta function $\delta(t-t_i)$, where t is time and t_i is the timing of i-th tremor. The Fourier spectrum amplitude at frequency f is calculated as

$$P(f) = \frac{1}{N}\left|\sum_i \exp(2\pi i f t_i)\right|. \quad (2.1)$$

The largest amplitude in Figure 2.1 is located at the period of ~0.518 day (~12.4 hr), corresponding to the period of M2 tide. The second largest peak is located around the period of just 1 day. It might be due to an artificial effect of the human activity. Minor peaks are located at the period of S2, K1, and O1 tides, though its significance is not clear.

Focusing on the spectrum amplitude at M2 tidal period, spatial variations of tidal sensitivity of tectonic tremors can be evaluated (Ide, 2010a, 2012). In Figure 2.2, spatial distributions of spectrum amplitude at M2 tidal period of tremor catalog by Yabe and Ide (2014) is shown in Shikoku region. Spectrum amplitude at M2 tidal period is calculated every 0.1° grids with a bin size of 0.2°. Within each bin, 100 events are randomly selected and spectrum amplitude at M2 tidal period (Equation (2.1)) is calculated for 100 times. A mean value of 100 calculations is plotted at each grid.

Now it is interpreted that the tidal stress can trigger slow earthquake because the stress drop of slow earthquake is much smaller (~10 kPa; Ide et al., 2007b) than that of regular earthquakes due to near lithostatic pore-fluid pressure (e.g., Shelly et al., 2006; Audet et al., 2009). In

addition to tidal sensitivity of tectonic tremors, slip velocity of SSEs is modulated by tidal stress as well (Hawthorne and Rubin, 2010). We also recognized that the source of stress perturbations is not only the Earth tide. For example, triggering of tectonic tremors due to passing surface wave from distant earthquakes is reported (e.g., Miyazawa and Mori, 2005; Rubinstein et al., 2007). SSEs also seem to be triggered by small stress perturbations due to passing typhoons in Taiwan (Liu et al., 2009).

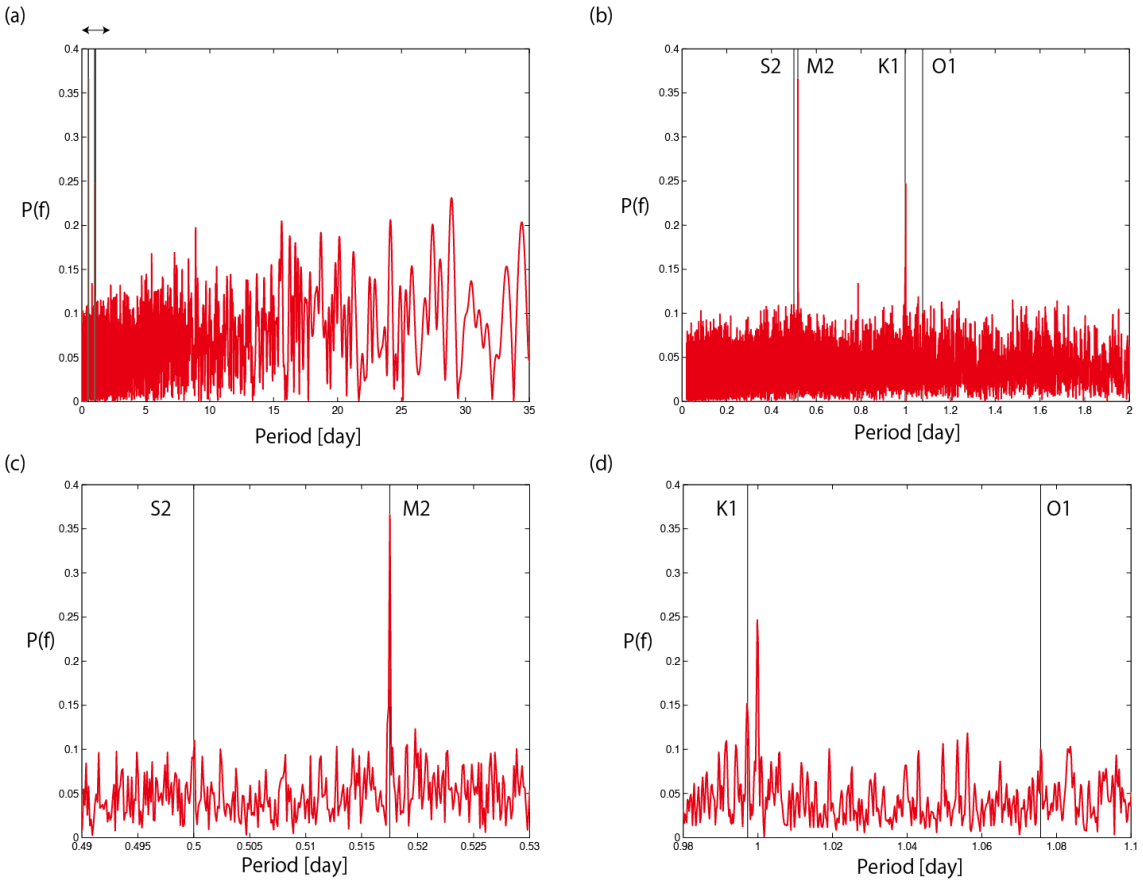

Figure 2.1: The power spectrum of tremor catalog (Equation (2.1)) constructed by Yabe and Ide (2014) at 33.3-33.5°N and 132.7-132.9°E between April 2004 and March 2009.

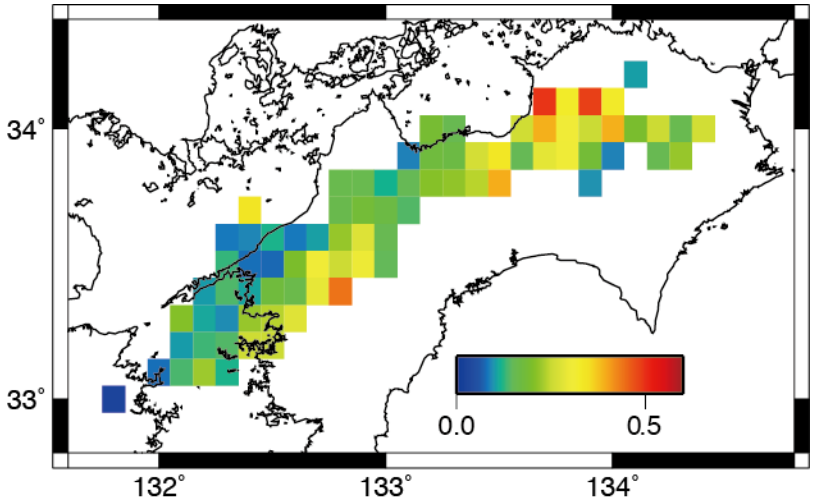

Figure 2.2: Spatial variations of spectrum amplitude at M2 tidal period (12.4 hr) in Shikoku region.

Because tidal sensitivity of tremors represents slip responses of the plate interface to stress perturbations, tidal sensitivity should be related to frictional properties on the fault. Hence, spatial variations of tidal sensitivity, such as Figure 2.2, would reflect spatial variations of frictional properties on the deep plate interface. However, quantitative evaluations of frictional properties are difficult based on the periodicity of tremor catalog. Instead, quantitative calculations of tidal stress enable us to estimate frictional properties on the plate interface. Nakata et al. (2008) explained the phase delay of tremor activities to tidal stress by RSF law (Dieterich, 1979), and estimated frictional parameters of RSF law. Thomas et al. (2009) estimated an effective frictional coefficient with the assumption that maximum tidal sensitivity should be realized, and showed that an effective frictional coefficient is very small (<0.1). Recent studies (Thomas et al., 2012; Beeler et al., 2013; Ide and Tanaka, 2014; Houston, 2015) found an exponential relation between tremor rate and tidal stress. Assuming that tremor rate is proportional to the background slip rate, this exponential relation means slip velocity is proportional to exponential of stress. Thomas et al. (2012) and Beeler et al. (2013) investigated tectonic tremors in San Andreas Fault, and found an exponential relation between tremor rate and tidal shear stress. Beeler et al. (2013) examined dislocation creep, dislocation glide, and RSF

law to explain the relation, and interpreted this exponential relation as the direct effect of RSF. Ide and Tanaka (2014) investigated an isolated tremor cluster in Nankai subduction zone, which is very sensitive to tide, and found an exponential relation between tremor rate and tide level recorded at nearby tide gauge. They interpreted this relation as the RSF-type rate-strengthening friction law. Houston (2015) investigated tremors in large ETS episodes in Cascadia subduction zone, and found that tremors in the early and intermediate stage of ETS do not show tidal sensitivity, whereas tremor rate in the later stage of ETS is an exponential function of the calculated tidal stress. She interpreted that this relation as Weibull-type friction law, and that temporal change of tidal sensitivity is due to the slip weakening of plate interface by SSE.

This study investigates the tidal sensitivity of tectonic tremors in Nankai, Cascadia, and Mexican subduction zones. We particularly focus on the spatial variations of tidal sensitivity because previous studies were spatially limited or averaged. The estimation of spatial variations of tidal sensitivity enables comparison with the spatial variations of tremor duration and amplitude, which were estimated by Yabe and Ide (2014). The spatial variations of the two latter properties should also reflect the heterogeneity on the plate interface. Hence, comparison of these characteristics will be helpful to constrain the source physics of slow earthquakes. In Section 2.2, methodology is first presented, including tidal stress calculations, the categorization of tremors into "initiation", "front", and "later" groups, and the tidal sensitivity estimation using the maximum likelihood method. In Section 2.3, spatial distributions of the estimated tidal sensitivity are shown, and they are compared with spatial variations of duration and amplitude. Finally, we discuss how a frictional property can be estimated from tidal sensitivity of tremors, and present a qualitative physical model of slow earthquakes in Section 2.4, followed by conclusions in Section 2.5.

2.2. Analysis Method

2.2.1. Tidal stress calculation

In the tidal stress calculation, both body tide and ocean tide are estimated (e.g., Tsuruoka et al., 1995). First of all, we calculate Green's function for body tide and ocean tide. Then, tidal stress by body tide and ocean tide are calculated respectively, by multiplying driving force (gravitational potential change for body tide and ocean height change for ocean tide) with the calculated Green's function.

We calculate the Green's function for a spherical earth for the sake of tidal stress calculation. Here, we assumed that physical properties of the Earth change only in the radial direction, and used PREM structure (Dziewonski and Anderson, 1981). To obtain Green's function, we solve the following equation of motion (Takeuchi and Saito, 1972)

$$\begin{aligned}
&\left(\vec{\nabla}\cdot\tau\right)_r - \nabla_r\left(\rho g u\right) - \rho\nabla_r\Phi + g\left(\vec{\nabla}\cdot\rho\vec{s}\right) - \frac{1}{r}\left(\tau_{\theta\theta}+\tau_{\phi\phi}\right) = \omega^2\rho u \\
&\left(\vec{\nabla}\cdot\tau\right)_\theta - \nabla_\theta\left(\rho g u\right) - \rho\nabla_\theta\Phi + \frac{1}{r}\left(\tau_{r\theta} - \frac{\cos\theta}{\sin\theta}\tau_{\phi\phi}\right) = \omega^2\rho v \\
&\left(\vec{\nabla}\cdot\tau\right)_\phi - \nabla_\phi\left(\rho g u\right) - \rho\nabla_\phi\Phi + \frac{1}{r}\left(\tau_{r\phi} + \frac{\cos\theta}{\sin\theta}\tau_{\theta\phi}\right) = \omega^2\rho w
\end{aligned} \qquad (2.2)$$

where τ is stress tensor, ρ is density before reformation, g is initial gravity, Φ is gravity potential change, $\vec{s} = (u, v, w)$ is displacement vector, and ω is frequency of tidal loading. The gravity potential change is related to density by,

$$\nabla^2\Phi = 4\pi G\vec{\nabla}\cdot\rho\vec{s} \qquad (2.3)$$

where G is gravitational constant. We also need constitutive equation between traction and displacement, assuming complete elasticity and isotropy,

$$\tau_{rr} = \lambda\varepsilon + 2\mu\frac{\partial u}{\partial r}$$

$$\tau_{\theta\theta} = \lambda\varepsilon + 2\mu\left(\frac{1}{r}\frac{\partial v}{\partial\theta} + \frac{u}{r}\right)$$

$$\tau_{\phi\phi} = \lambda\varepsilon + \frac{2\mu}{r\sin\theta}\left(\frac{\partial w}{\partial \phi} + u\sin\theta + v\cos\theta\right) \tag{2.4}$$

$$\tau_{r\theta} = \mu\left\{\frac{\partial v}{\partial r} + \frac{1}{r}\left(\frac{\partial u}{\partial \theta} - v\right)\right\}$$

$$\tau_{r\phi} = \mu\left\{\frac{\partial w}{\partial r} + \frac{1}{r\sin\theta}\left(\frac{\partial u}{\partial \phi} - w\sin\theta\right)\right\}$$

$$\tau_{\theta\phi} = \mu\left\{\frac{1}{r}\frac{\partial w}{\partial \theta} + \frac{1}{r\sin\theta}\left(\frac{\partial v}{\partial \phi} - w\cos\theta\right)\right\}$$

$$\varepsilon = \frac{\partial u}{\partial r} + \frac{1}{r}\frac{\partial v}{\partial \theta} + \frac{u}{r} + \frac{1}{r\sin\theta}\left(\frac{\partial w}{\partial \phi} + u\sin\theta + v\cos\theta\right)$$

To solve Equations (2.2)-(2.4), we expand it using Legendre polynomial like Equation (2.5).

$$u = \sum_{n=0}^{\infty}\sum_{m=-n}^{n} U_n(r)Y_{nm}(\theta,\phi)$$

$$v = \sum_{n=0}^{\infty}\sum_{m=-n}^{n} V_n(r)\frac{\partial Y_{nm}(\theta,\phi)}{\partial \theta}$$

$$w = \sum_{n=0}^{\infty}\sum_{m=-n}^{n} V_n(r)\frac{\partial Y_{nm}(\theta,\phi)}{\sin\theta\,\partial \phi} \tag{2.5}$$

$$\tau_{rr} = \sum_{n=0}^{\infty}\sum_{m=-n}^{n} T_n^{rr}(r)Y_{nm}(\theta,\phi)$$

$$\tau_{r\theta} = \sum_{n=0}^{\infty}\sum_{m=-n}^{n} T_n^{r\theta}(r)\frac{\partial Y_{nm}(\theta,\phi)}{\partial \theta}$$

$$\tau_{r\phi} = \sum_{n=0}^{\infty}\sum_{m=-n}^{n} T_n^{r\theta}(r)\frac{\partial Y_{nm}(\theta,\phi)}{\sin\theta\,\partial \phi}$$

$\tau_{\theta\theta}$, $\tau_{\theta\phi}$ and $\tau_{\phi\phi}$ can be constructed using u, v, τ_{rr} and $\tau_{r\theta}$ if they are given.

Gravity potential is also expanded by Legendre polynomial as follows.

$$\Phi = \sum_{n=0}^{\infty}\Psi_n(r)P_n(\cos\theta) \tag{2.6}$$

We also introduce new parameter Q_n defined below.

$$Q_n = \frac{\partial \Psi_n}{\partial r} - 4\pi G\rho U_n + \frac{n+1}{r}\Psi_n \tag{2.7}$$

Then Equations (2.2)-(2.4) to be solved are re-written as a first order system of differential equations with six variables as follows (Takeuchi and Saito, 1972).

$$\frac{\partial U_n}{\partial r} = \frac{1}{\lambda + 2\mu}\left[T_n^{rr} - \frac{\lambda}{r}\{2U_n - n(n+1)V_n\}\right]$$

$$\frac{\partial V_n}{\partial r} = \frac{T_n^{r\theta}}{\mu} + \frac{V_n - U_n}{r}$$

$$\frac{\partial T_n^{rr}}{\partial r} = \frac{2}{r}\left(\lambda\frac{\partial U_n}{\partial r} - T_n^{rr}\right) + \frac{1}{r}\left(\frac{2\lambda + 2\mu}{r} - \rho g\right)\{2U_n - n(n+1)V_n\} + \frac{n(n+1)}{r}T_n^{r\theta} + \rho\left(Q_n - \frac{n+1}{r}\Psi_n - \frac{2g}{r}U_n\right)$$

$$\frac{\partial T_n^{r\theta}}{\partial r} = -\frac{\lambda}{r}\frac{\partial U_n}{\partial r} - \frac{\lambda + 2\mu}{r^2}\{2U_n - n(n+1)V_n\} + \frac{2\mu}{r^2}(U_n - V_n) - \frac{3}{r}T_n^{r\theta} - \frac{\rho}{r}(\Psi_n - gU_n) \qquad (2.8)$$

$$\frac{\partial \Psi_n}{\partial r} = Q_n + 4\pi G\rho U_n - \frac{n+1}{r}\Psi_n$$

$$\frac{\partial Q_n}{\partial r} = \frac{n-1}{r}(Q_n + 4\pi G\rho U_n) + \frac{4\pi G\rho}{r}\{2U_n - n(n+1)V_n\}$$

The problem is solved with two kinds of boundary condition according to body tide and ocean tide. For body tide, the boundary condition is Equation (2.9), and that for ocean tide is Equation (2.10) (Tsuruoka et al., 1995).

$$\begin{aligned} &U_n(0) = 0 \\ &V_n(0) = 0 \\ &T_n^{rr}(a) = 0 \\ &T_n^{r\theta}(a) = 0 \\ &\Psi_n(0) = 0 \\ &Q_n(a) = \frac{2n+1}{a} \end{aligned} \qquad (2.9)$$

$$\begin{aligned} &U_n(0) = 0 \\ &V_n(0) = 0 \\ &T_n^{rr}(a) = -\frac{(2n+1)g}{4\pi G a} \\ &T_n^{r\theta}(a) = 0 \\ &\Psi_n(0) = 0 \\ &Q_n(a) = \frac{2n+1}{a} \end{aligned} \qquad (2.10)$$

Here, a is the radius of the Earth. These differential equations are solved

with the code of Okubo and Tsuji (2001) with Runge-Kutta method, which consider attenuation effect as well.

Tidal stresses due to body tides are generated by the deformation of the solid Earth produced by the gravitational potential change due to the relative motions of the Moon, Sun, and Earth. The gravitational potential can be expanded in the Legendre polynomials, and only the second and third terms are important in the deformation of the Earth because the distance between the Earth and the Moon or the Sun is sufficiently greater than the radius of the Earth (e.g. Tsuruoka et al., 1995). Body tides can be calculated as follows using Green's function calculated in the previous section.

$$
\begin{aligned}
\tau_{rr}(r,\theta,\phi,t) &= \sum_{n=2}^{3} \Psi_n^{body}(r,\theta,\phi,t) \times T_n^{rr}(r) \\
\tau_{r\theta}(r,\theta,\phi,t) &= \sum_{n=2}^{3} \frac{\partial \Psi_n^{body}(r,\theta,\phi,t)}{\partial \theta} \times T_n^{r\theta}(r) \\
\tau_{r\phi}(r,\theta,\phi,t) &= \sum_{n=2}^{3} \frac{\partial \Psi_n^{body}(r,\theta,\phi,t)}{\sin\theta \partial \phi} \times T_n^{r\theta}(r)
\end{aligned}
\qquad (2.11)
$$

$$
\begin{aligned}
\tau_{\theta\theta}(r,\theta,\phi,t) = \sum_{n=2}^{3} & \Psi_n^{body}(r,\theta,\phi,t) \times \left(\frac{\lambda}{\lambda+2\mu} T_n^{rr}(r) + \frac{2\mu(3\lambda+2\mu)}{\lambda+2\mu} \frac{U_n}{r} \right) + \frac{\partial \Psi_n^{body}(r,\theta,\phi,t)}{\partial \theta} \times \frac{2\lambda\mu}{\lambda+2\mu} \frac{\cos\theta}{\sin\theta} \frac{V_n(r)}{r} \\
& + \frac{\partial^2 \Psi_n^{body}(r,\theta,\phi,t)}{\partial \theta^2} \times \frac{4\mu(\lambda+\mu)}{\lambda+2\mu} \frac{V_n(r)}{r} + \frac{\partial^2 \Psi_n^{body}(r,\theta,\phi,t)}{\sin^2\theta \partial \phi^2} \times \frac{2\lambda\mu}{\lambda+2\mu} \frac{V_n(r)}{r} \\
\tau_{\phi\phi}(r,\theta,\phi,t) = \sum_{n=2}^{3} & \Psi_n^{body}(r,\theta,\phi,t) \times \left(\frac{\lambda}{\lambda+2\mu} T_n^{rr}(r) + \frac{2\mu(3\lambda+2\mu)}{\lambda+2\mu} \frac{U_n}{r} \right) + \frac{\partial \Psi_n^{body}(r,\theta,\phi,t)}{\partial \theta} \times \frac{4\mu(\lambda+\mu)}{\lambda+2\mu} \frac{\cos\theta}{\sin\theta} \frac{V_n(r)}{r} \\
& + \frac{\partial^2 \Psi_n^{body}(r,\theta,\phi,t)}{\partial \theta^2} \times \frac{2\lambda\mu}{\lambda+2\mu} \frac{V_n(r)}{r} + \frac{\partial^2 \Psi_n^{body}(r,\theta,\phi,t)}{\sin^2\theta \partial \phi^2} \times \frac{4\mu(\lambda+\mu)}{\lambda+2\mu} \frac{V_n(r)}{r} \\
\tau_{\theta\phi}(r,\theta,\phi,t) = \sum_{n=2}^{3} & \frac{\partial^2 \Psi_n^{body}(r,\theta,\phi,t)}{\sin\theta \partial\theta \partial\phi} \times 2\mu \frac{V_n(r)}{r} - \frac{\partial \Psi_n^{body}(r,\theta,\phi,t)}{\sin\theta \partial\phi} \times 2\mu \frac{\cos\theta}{\sin\theta} \frac{V_n(r)}{r}
\end{aligned}
$$

In each mode of the polynomial, the temporal change of the gravitational potential $\Psi_n^{body}(r,\theta,\phi,t)$ can be expressed as the summation of various tidal constituents, whose frequency can be represented by the combination of six fundamental frequencies, whose coefficient is called Doodson's number. In our calculation, tidal potential listed in Tamura (1987) is used. Calculated green function for body tide ($U_n(r)$, $V_n(r)$, $T_n^{rr}(r)$ and $T_n^{r\theta}(r)$ in Equation 2.8 or 2.11) is shown in Figure 2.3.

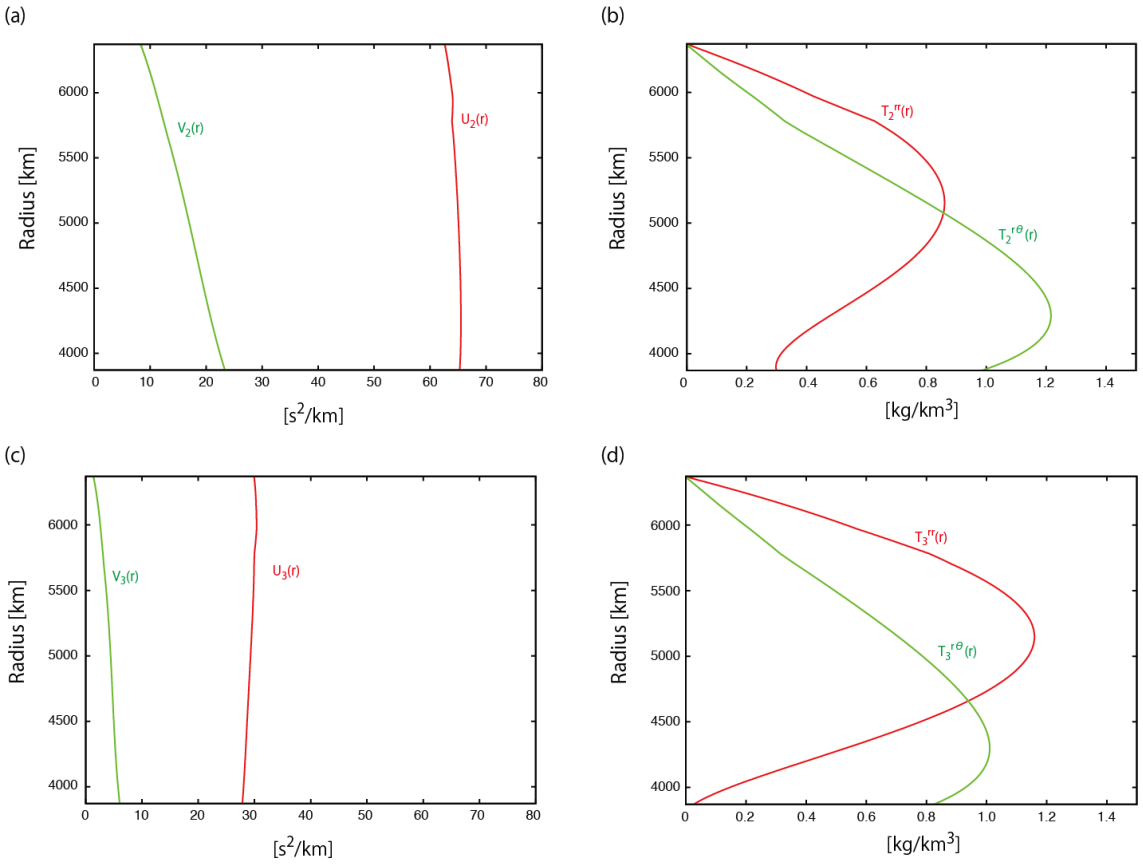

Figure 2.3: Depth distribution of calculated Green's functions for body tide. (a) Green's functions of radial ($U_n(r)$; red) and tangential displacement ($V_n(r)$; green) for n=2. (b) Green's function of $T_n^{rr}(r)$ (red) and $T_n^{r\theta}(r)$ (green) for n=2. (c) Same as (a), except for n=3. (d) Same as (b), except for n=3.

Tidal stresses due to ocean tides are generated by the mass loading of ocean water on the Earth's surface. The gravitational potential change, which causes the body tides, also triggers the movement of ocean water, which then produces the stress change in the solid Earth. The Temporal change of sea surface height is predicted from oceanography. SPOTL (Agnew, 2012) calculates such time series using a given ocean model. We used ocean models listed in Table 1 as an input for SPOTL. We used major ten tidal constituents (K1, K2, M2, N2, O1, P1, Q1, S2, mf, mm), eight of which are short period tides and the remainder long period tides. By multiplying the sea surface height change with the Green's function for point mass loading at

the surface and integral over the surface, we obtain the tidal stress due to ocean tide, as in Equation (2.12).

$$\tau_{ij}(r,\theta,\phi,t) = \int H(\theta',\phi',t)\rho(\theta',\phi')R_{ijkl}(\theta,\phi,\theta',\phi')\tau'_{kl}(r,\theta,\phi,\theta',\phi')d\theta' d\phi' \quad (2.12)$$

where $H(\theta',\phi',t)$ and $\rho(\theta',\phi')$ are the ocean height change and the density of ocean water, $R_{ijkl}(\theta,\phi,\theta',\phi')$ is a rotation tensor to change coordinates, and τ'_{kl} is Green's function for point loading on the surface,

$$u' = \frac{ag}{m_e}\sum_{n=2}^{\infty} U_n(r)P_n(\cos\vartheta)$$

$$v' = \frac{ag}{m_e}\sum_{n=2}^{\infty} V_n(r)\frac{\partial P_n(\cos\vartheta)}{\partial\vartheta}$$

$$\tau'_{rr} = \frac{ag}{m_e}\sum_{n=2}^{\infty} T_n^{rr}(r)P_n(\cos\vartheta)$$

$$\tau'_{r\theta} = \frac{ag}{m_e}\sum_{n=2}^{\infty} T_n^{r\theta}(r)\frac{\partial P_n(\cos\vartheta)}{\partial\vartheta} \quad (2.13)$$

$$\tau'_{\theta\theta} = \frac{ag}{m_e}\sum_{n=2}^{\infty}\frac{\lambda}{\lambda+2\mu}T_n^{rr}(r)P_n(\cos\vartheta) + \frac{2\mu(3\lambda+2\mu)}{\lambda+2\mu}\frac{U_n(r)}{r}P_n(\cos\vartheta) - \frac{2\mu}{r}\frac{\cos\vartheta}{\sin\vartheta}V_n(r)\frac{\partial P_n(\cos\vartheta)}{\partial\vartheta} - \frac{4\mu(\lambda+\mu)}{\lambda+2\mu}\frac{n(n+1)}{r}V_n(r)P_n(\cos\vartheta)$$

$$\tau'_{\phi\phi} = \frac{ag}{m_e}\sum_{n=2}^{\infty}\frac{\lambda}{\lambda+2\mu}T_n^{rr}(r)P_n(\cos\vartheta) + \frac{2\mu(3\lambda+2\mu)}{\lambda+2\mu}\frac{U_n(r)}{r}P_n(\cos\vartheta) + \frac{2\mu}{r}\frac{\cos\vartheta}{\sin\vartheta}V_n(r)\frac{\partial P_n(\cos\vartheta)}{\partial\vartheta} - \frac{2\lambda\mu}{\lambda+2\mu}\frac{n(n+1)}{r}V_n(r)P_n(\cos\vartheta)$$

where $\vartheta(\theta,\phi,\theta',\phi')$ is an angular distance between (θ,ϕ) and (θ',ϕ'). To calculate infinite summations in Equation (2.13) accurately, we divide the infinite summation into two parts as in Okubo (1988). An example for τ'_{rr} in the case of $r < a$ is shown below.

$$\begin{aligned}\tau'_{rr} &= \sum_{n=2}^{\infty} T_n^{rr}(r)P_n(\cos\vartheta)\\ &= \sum_{n=2}^{\infty} N_n n^2\left(\frac{r}{a}\right)^n P_n(\cos\vartheta)\\ &= N_\infty\sum_{n=2}^{\infty} n^2\left(\frac{r}{a}\right)^n P_n(\cos\vartheta) + \sum_{n=2}^{\infty}(N_n - N_\infty)n^2\left(\frac{r}{a}\right)^n P_n(\cos\vartheta)\end{aligned} \quad (2.14)$$

In the numerical calculation, we calculate N_n up to n=45,000, and N_∞ is

replaced by $N_{45,000}$. Generating function is substituted in $\sum_{n=2}^{\infty} n^2 \left(\frac{r}{a}\right)^n P_n(\cos\vartheta)$.

The second term in Equation (2.14) is summed up to n=45,000. Calculated Green's function for ocean tide (Equation (2.13)) is shown in Figure 2.4 and 2.5.

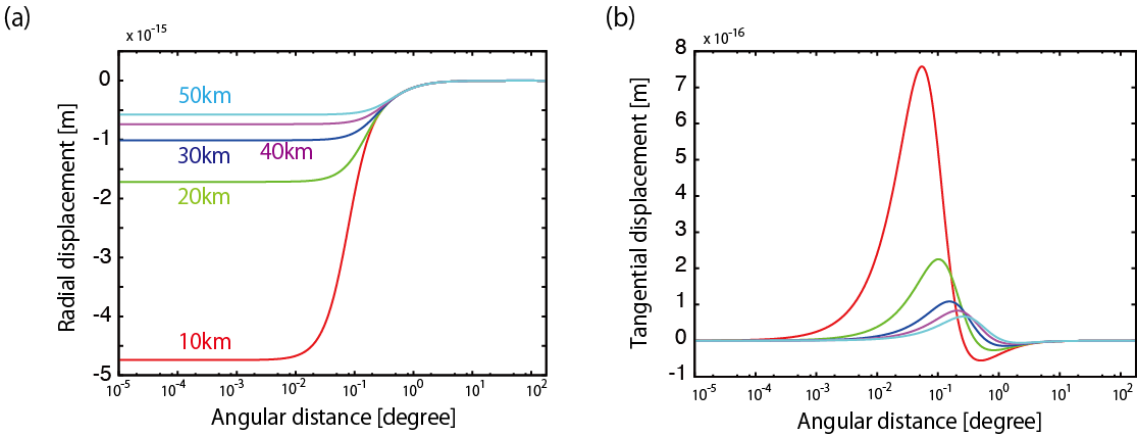

Figure 2.4: Calculated Green's function of displacement for ocean tide. (a) Radial displacement at 10km (red), 20km (green), 30km (blue), 40km (magenta), and 50km (light blue) depth by 1kg load at the surface is plotted. (b) Same as (a), except for tangential displacement.

For the integration of Equation (2.12), we used finer mesh (~0.5km x ~0.5km) around the origin, where tidal stress is calculated, and coarser mesh (~20km x ~20km) if further than 100 km from the origin. Ocean height change is calculated using the SPOTL program (Agnew, 2012) with ocean models in Table 2.1 for ocean tide. Land-sea distribution is distinguished with 1/64° grid in SPOTL program. We integrate ocean loads over 500 km from the origin.

Because slow earthquakes occur on the plate interface (e.g., Dragert et al., 2001; Ide et al., 2007a; Ito et al., 2007; Shelly et al., 2007a), we calculate the tidal stress tensor on the inferred plate interface. We used the plate model by Baba et al. (2002), Nakajima and Hasegawa (2007), and Hirose et al. (2008a) for Nankai subduction zone, McCrory et al. (2012) for

Cascadia, and Pardo and Suarez (1995) for Mexican subduction zone. We interpolate these models into 0.01° grids and calculate strike and dip of the fault on each grid. We calculate tidal stress tensor at every 0.1° grid points. To convert the stress tensor to traction (normal stress, slip-parallel shear stress, and slip-orthogonal shear stress) on the plate interface, we need the strike, dip and rake of the slip vector on the plate interface. We calculate strike and dip from the interpolated plate models. Rake is calculated so as that the horizontal components of a slip vector on the plate interface are consistent with the motion vector of the subducting oceanic plate at that location. Relative plate motion is calculated using DeMets et al. (2010).

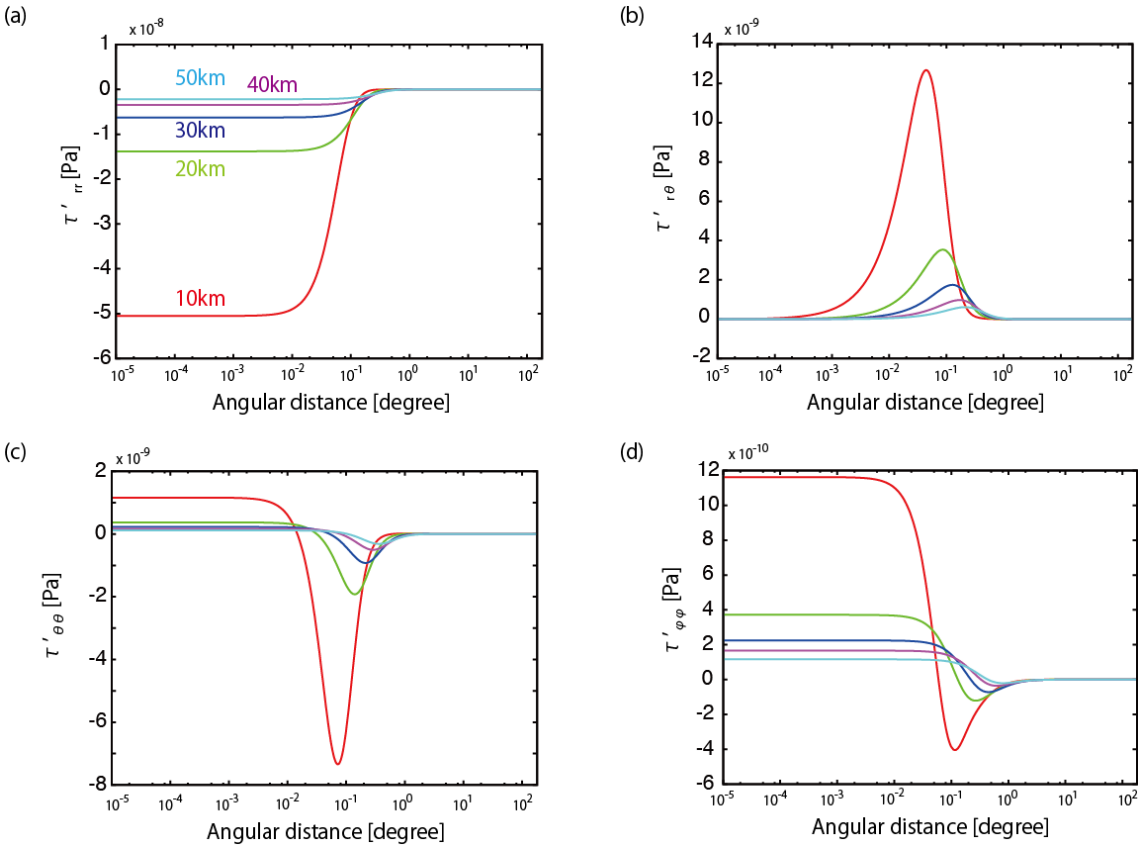

Figure 2.5: Calculated Green's function of stress for ocean tide. (a) Same as Figure 2.4a, except for τ'_{rr}. (b) Same as Figure 2.4a, except for $\tau'_{r\theta}$. (c) Same as Figure 2.4a, except for $\tau'_{\theta\theta}$. (d) Same as Figure 2.4a, except for $\tau'_{\phi\phi}$.

Table 2.1: List of ocean model used as an input for SPOTL.

Region	Short-period constituents	Long-period constituents
Nankai	Guo et al. (2010) Matsumoto et al. (2000)	Matsumoto et al. (2000)
Cascadia	Egbert and Erofeeva (2002) Savcenko and Bosch (2012)	Savcenko and Bosch (2012)
Mexico	Savcenko and Bosch (2012)	Savcenko and Bosch (2012)

To validate calculated tidal stress, tidal stress calculations in this study are compared with the tidal stress calculated with the method of Tanaka et al. (2002b) in Figure 2.6. In Figure 2.6, comparison is conducted at two different places. One is at Iwate prefecture (39.03°N, 140.88°E, 8km depth), where body tide is dominant (Figure 2.6a, 2.6b). The other is in Shikoku (33.92°N, 133.72°E, 30km depth), where ocean tide also plays an important role (Figure 2.6c, 2.6d). Results in both places are consistent with each other both for shear stress and normal stress.

In Figure 2.7, spatial distributions of RMS amplitudes of tidal shear stress and normal stress calculated for 10 years from April 2004 are shown for Nankai and Cascadia subduction zones. Because both subduction zones have an inland sea, where tidal sea level change is much larger than the outer Pacific Ocean, tidal stress distribution is highly heterogeneous. In Nankai SZ, the bending plate geometry (Figure 2.8) also contributes to the complication of tidal stress distribution. The amplitude of normal stress is usually larger than shear stress beneath the sea, but comparable beneath land. In general, tidal shear stress and tidal normal stress are correlated at offshore regions and anti-correlated at onshore regions (Figure 2.7c and 2.7f). Around the coastline, the relation between them is complex.

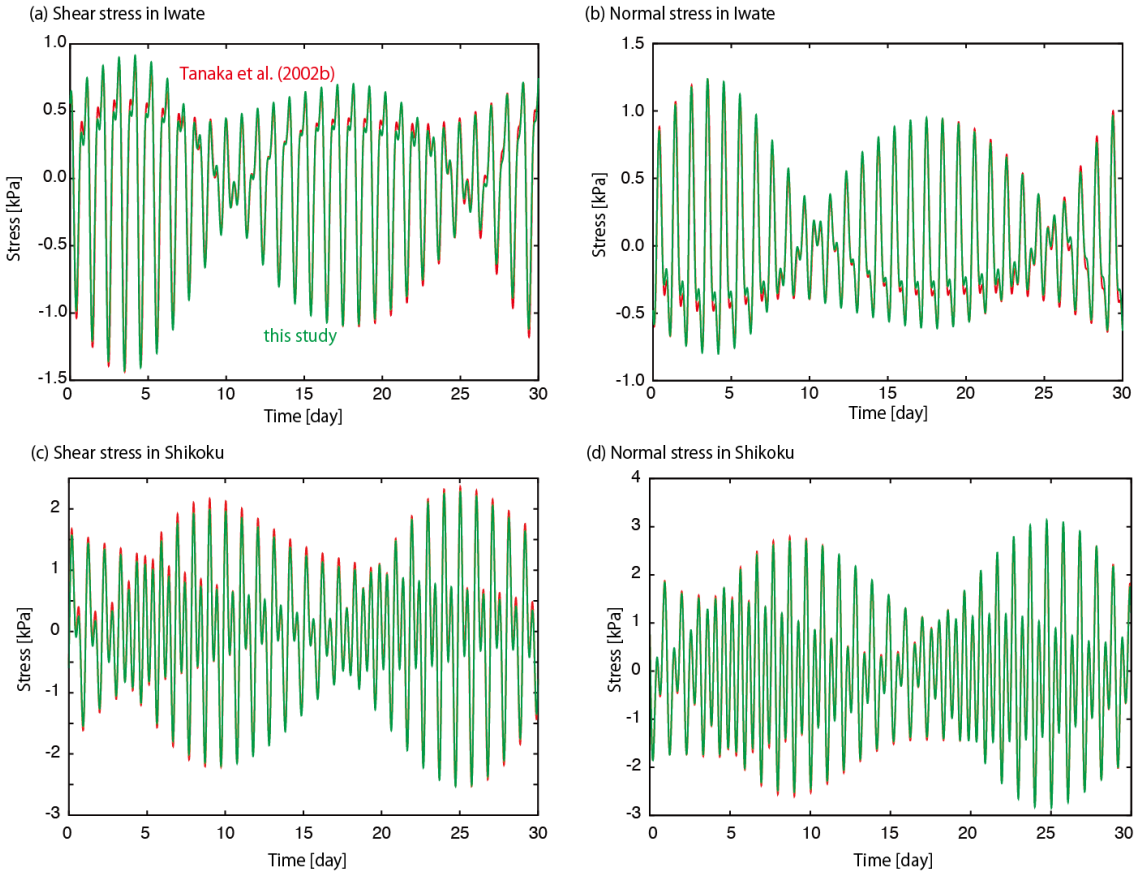

Figure 2.6: Comparison of calculated tidal stress between this study (green) and the method of Tanaka et al. (2002b) (red). (a) Tidal shear stress in Iwate (39.03ºN, 140.88ºE, 8km depth, Strike: 209º, Dip: 39º, Rake: 101º) from the begging of June 2008 (JST). (b) Same as (a), except for tidal normal stress. (c) Same as (a), except for Shikoku region (33.92ºN, 133.72ºE, 30km depth, Strike: 250º, Dip: 10º, Rake: 100º) from the begging of May 2005 (JST). (d) Same as (c), except for tidal normal stress.

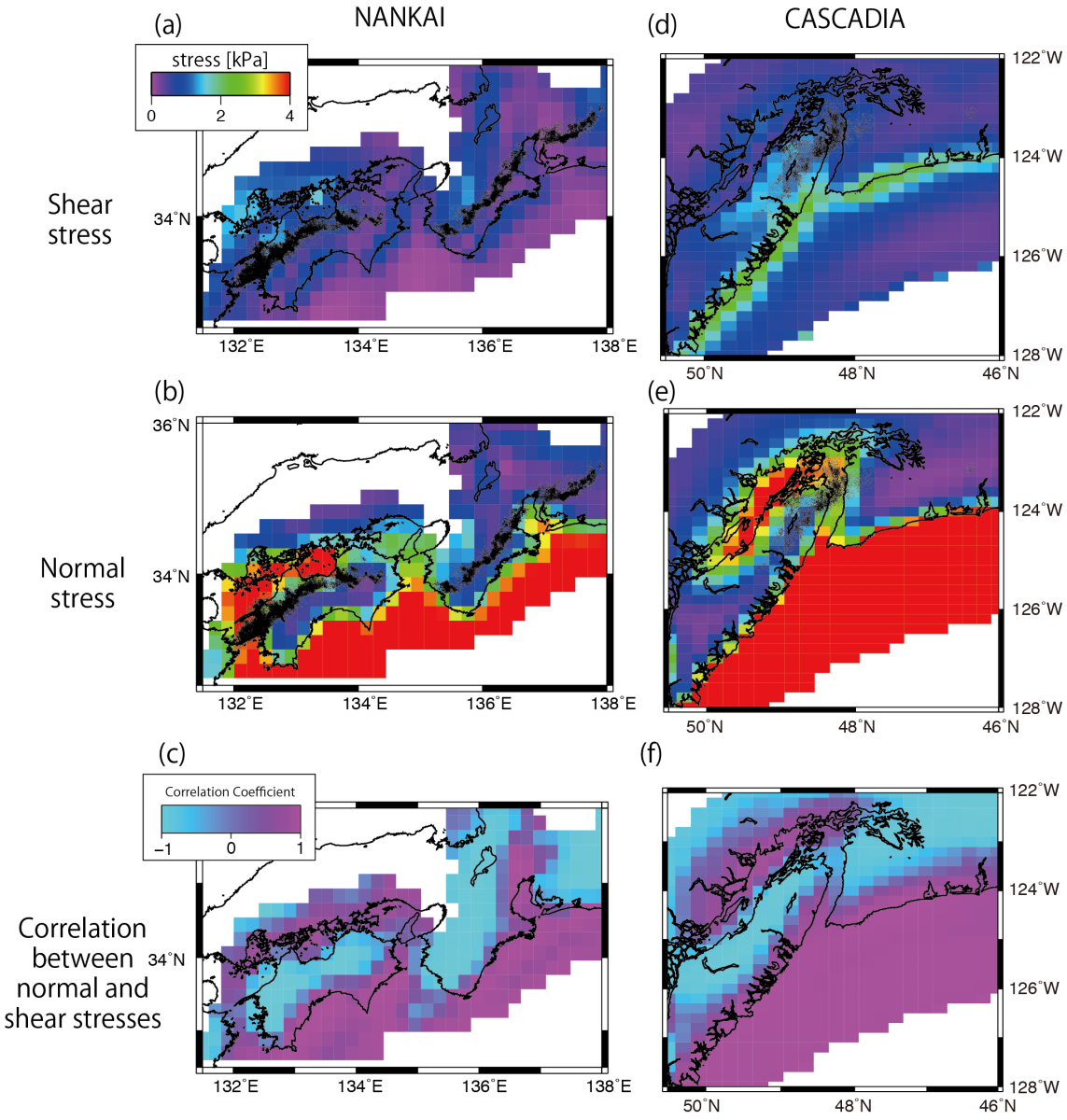

Figure 2.7: Map view of calculated tidal stress in Nankai and Cascadia subduction zones. (a) Shear stress distribution in Nankai subduction zone. The color represents the RMS amplitude of tidal shear stress on the plate interface. The color scale is common for (a), (b), (d), and (e). The distributions of detected tremor events used for analysis are shown by black dots. (b) Same as (a), but for tidal normal stress. (c) The correlation coefficient between tidal normal stress and tidal shear stress is shown. They are correlated in offshore regions, while they are anti-correlated in onshore regions. (d) Same as (a), but for Cascadia subduction zone. (e) Same as (b), but for Cascadia subduction zone. (f) Same as (c), but for Cascadia subduction znoes.

2.2.2. Tremor clustering

In this study, tremor catalogs constructed by Yabe and Ide (2014) with the envelope correlation method are utilized in Nankai and Cascadia subduction zones. The duration of tremors ranges from 10 s to 300 s. The period of catalog is from April 2004 to March 2009 in Nankai subduction zone and from January 2005 to December 2009 in Cascadia subduction zone. Houston (2015) analyzed tremors in large ETSs in Cascadia subduction zone, and found that tidal sensitivity appears in tremors in the later stage of ETSs. Hence, this study also categorizes tremors in large tremor activities into "initiation", "front", and "later" tremors.

First, tremors in the catalogs are grouped into clusters by connecting tremor pairs within 2 days and 20 km. These values are adopted based on the typical duration and length of minor tremor activities. We only look at large clusters within which more than 200 events are contained, and call them ETSs in this study. There were 107 and 13 such ETSs in Nankai and Cascadia subduction zone, respectively. In Figure 2.8, all tremors in the catalogs and selected tremors in ETSs defined above are shown.

Then, tremors in ETSs are divided into three categories. Here, we define the along-strike coordinate as the curvilinear coordinate along 30 km depth of the slab model (Figure 2.8). In each along-strike bin of 10 km width, we measure the number of events per day every 0.1 days. We define the "front" stage of ETS as 24 hours starting when tremor rate first exceeds 20 events per day in the bin. This rate is determined empirically so as that tremors increasing their amplitude after the initiation of ETS are categorized into front tremors. Tremors within this 1-day period are categorized as "front" tremors. "Initiation" tremors are defined as tremors occurring before the front stage, and "later" tremors occur after the front stage. The "initiation" and "front" stages in this study are analogous to the "initial" stage in Houston (2015). An example of categorization of tremors in the Shikoku region is shown in Figure 2.9.

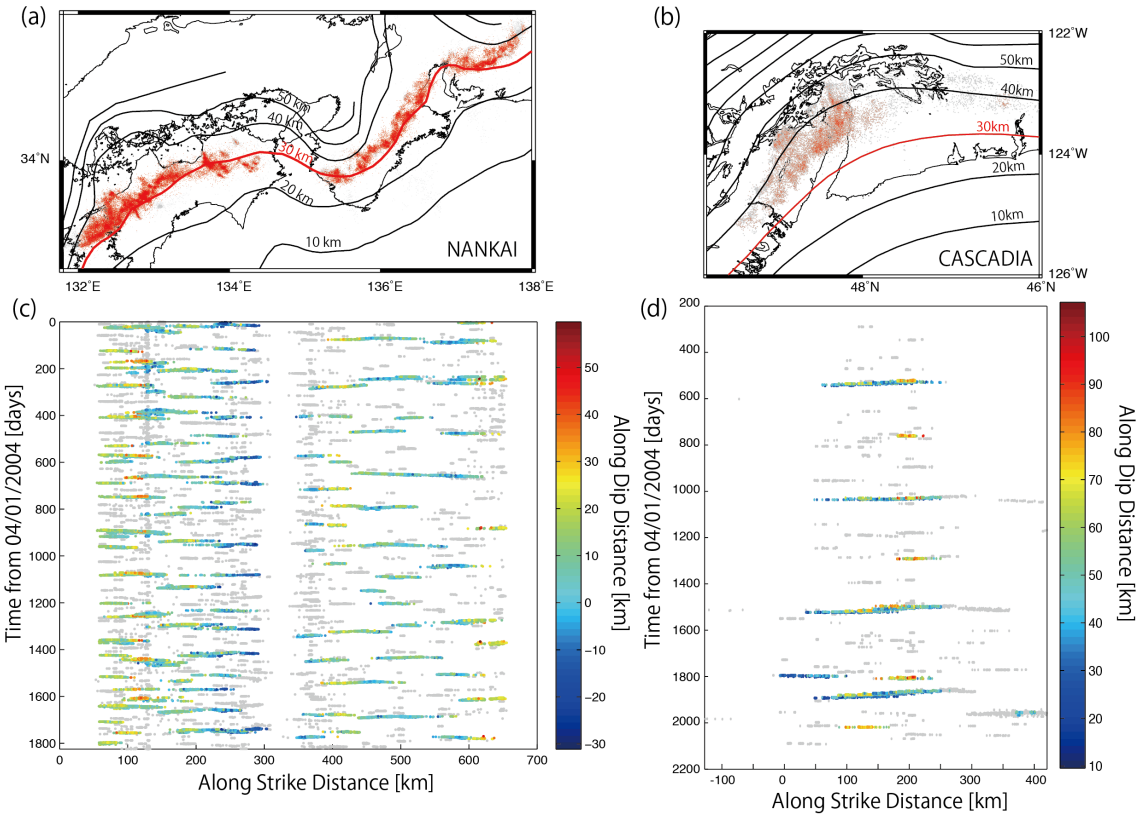

Figure 2.8: Map and time plot of detected tremor events in Nankai and Cascadia subduction zones. (a) Tremor distributions in Nankai subduction zone detected by Yabe and Ide (2014) is shown in map view. Gray dots are all tremors in the catalog, and red dots are tremors used in the analysis. Plate model by Baba et al. (2002), Nakajima and Hasegawa (2007), and Hirose et al. (2008a) are also shown. (b) Same as (a) for Cascadia subduction zone. Plate model is by McCrory et al. (2012). (c) Time plot of tremors in Nankai subduction zone. The horizontal axis is along-strike distance, which is calculated using curvilinear coordinate along 30 km depth of plate model (red line in (a)). Gray dots are all tremors in the catalog, and colored dots are tremors used in the analysis, which are color-coded by along-dip distance, which is also measured from 30 km depth contour. (d) Same as (c) for Cascadia subduction zone.

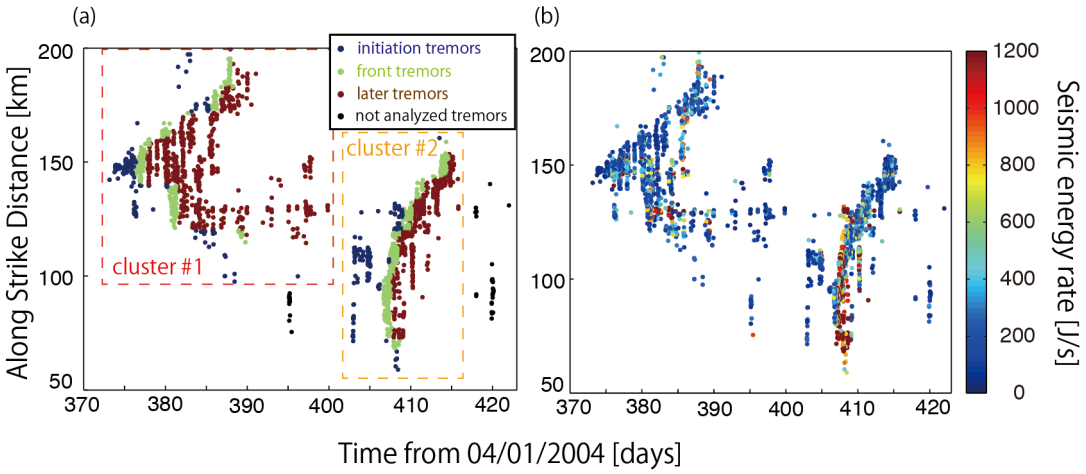

Figure 2.9: An example of tremor categorization in Shikoku region. A portion of time plot of tremors (Figure 2.8a) in Shikoku region is shown. (a) Colors of dots represent the type of tremors (blue: "initiation", green: "front", and red: "later"). (b) The same time plot as (a), but colors of dots represent seismic energy rate (amplitude) estimated by Yabe and Ide (2014).

2.2.3. Tidal sensitivity estimation

We investigate the spatial distributions of tidal sensitivity of tremor, for every 0.1° grid point in latitude and longitude. Tremors with epicenters within 20 km from each grid point are considered. We compare tremor activity only with tidal shear stress because previous studies suggest that friction coefficient is very small in the tremor region and insensitive to normal stress (e.g., Thomas et al., 2009; Thomas et al., 2012; Houston, 2015). We also assume here that the relation between tremor rate and tidal shear stress is exponential as

$$R(\tau) = R_0 \exp(\alpha\tau) \qquad (2.15)$$

because such a relation is suggested by observational studies (Thomas et al., 2012; Beeler et al., 2013; Ide and Tanaka, 2014; Houston, 2015) and theoretical analysis of simple spring-block system with RSF (Ader et al., 2012). In Equation (2.15), R is tremor rate, R_0 is a reference tremor rate when tidal shear stress is zero, τ is tidal shear stress, and the parameter α represents tidal sensitivity. We estimate this parameter α using maximum likelihood method.

The Maximum likelihood method for this problem is formulated as

follows. Tremor rate is proportional to the probability of tremor occurrence per unit time, obeying exponential law as,

$$P(t) \propto R(\tau(t)) \propto \exp(\alpha\tau(t)) . \qquad (2.16)$$

The probability of tremor occurrence at tidal stress τ can be expressed as,

$$P(\tau) = QT(\tau)\exp(\alpha\tau) , \qquad (2.17)$$

where $T(\tau)$ is time distribution density function, and Q is normalized factor, which is expressed as,

$$Q^{-1} = \int_{\tau_{\min}}^{\tau_{\max}} T(\tau)\exp(\alpha\tau)d\tau . \qquad (2.18)$$

τ_{min} and τ_{max} in Equation (2.18) is the minimum and maximum of tidal shear stress at the location. In the observed data, N tremors occurred when tidal stress is τ_1, …, τ_N, respectively. Such probability can be expressed as follows,

$$\log\left\{L(\alpha|\tau_1,...,\tau_N)\right\} = \sum_{i=1}^{N}\log(T(\tau_i)) + \alpha\sum_{i=1}^{N}\tau_i - N\log\left\{\int_{\tau_{\min}}^{\tau_{\max}} T(\tau)\exp(\alpha\tau)d\tau\right\} \qquad (2.19)$$

Likelihood L of Equation (2.19) becomes its maximum when the parameter α satisfy

$$\frac{\int_{\tau_{\min}}^{\tau_{\max}} \tau T(\tau)\exp(\alpha\tau)d\tau}{\int_{\tau_{\min}}^{\tau_{\max}} T(\tau)\exp(\alpha\tau)d\tau} = \frac{\sum_{i=1}^{N}\tau_i}{N} \qquad (2.20)$$

We solve Equation (2.20) numerically to estimate the parameter α. After estimating α, R_0 in Equation (2.15) can be calculated as NQ/T_0, where T_0 is total period of tremor activity.

The uncertainty in the estimated parameter α can be assessed from Equation (2.19). When the likelihood at its maximum, $\partial\log(L)/\partial\alpha$ is zero, but $\partial^2\log(L)/\partial\alpha^2$ is not. Because $\Delta\log(L) = 2$ corresponds to the 95% confidence interval for a Gaussian distribution, the uncertainty in the estimated parameter α can be expressed as follows.

$$\Delta\alpha = 2\left|\frac{\partial^2\log(L)}{\partial\alpha^2}\right|^{-1/2} \qquad (2.21)$$

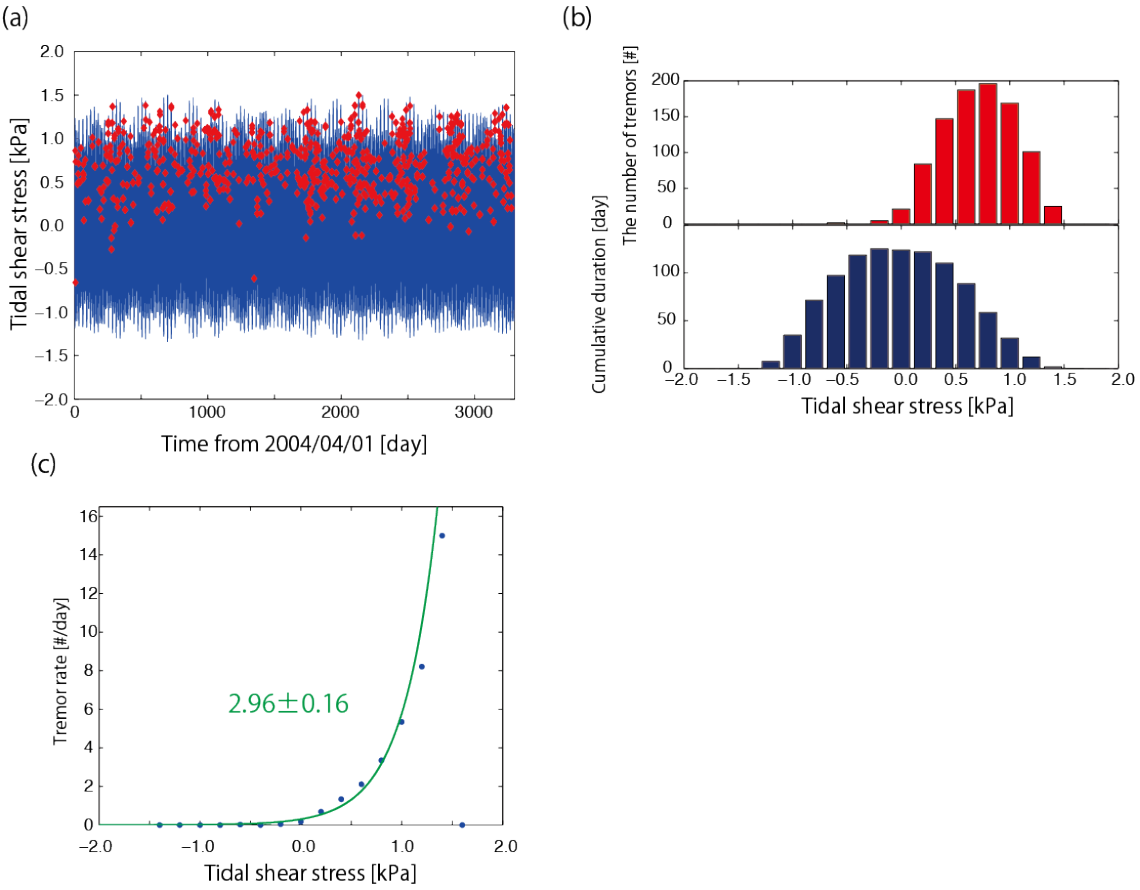

Figure 2.10: Example of tidal sensitivity analysis in Okayama tremor cluster. (a) Time history of tidal shear stress (blue) at 34.6ºN, 134.2ºE and the timing of tremors (red). (b) Histogram of the number of tremors (top) and the cumulative duration (bottom) at each tidal stress level. (c) Tremor rate at each tidal stress (blue) and estimated exponential curve (green).

In Figure 2.10, example of analysis procedure is shown. As an example, we conduct analysis for tremor cluster in Okayama prefecture, which has high tidal sensitivity as demonstrated by Ide and Tanaka (2014). For this analysis, clustering of tremor catalog has not been done because of the small number of tremors in the catalog. First of all, tremor activity is compared with time history of tidal shear stress, and tidal shear stress at the timing of tremor occurrence is calculated (Figure 2.10a). Second, time histories of tidal shear stress and tremors are divided into bins of tidal shear stress making histogram of Figure 2.10b. These histograms are used for the calculation of integrations in Equation (2.20). By solving Equation (2.20)

numerically, tidal sensitivity α is estimated. Estimated relation of Equation (2.15) is compared with data, which is obtained by dividing red histogram by blue histogram in Figure 2.10b (Figure 2.10c). Exponential relation of Equation (2.15) can fit data well. In Okayama tremor cluster, tidal sensitivity shows very high value around 3 kPa^{-1}. Exponential relation of Equation (2.15) can be confirmed in other tremor region in Nankai and Cascadia regions, though tidal sensitivity is lower than that of Okayama tremor cluster (Figure 2.11).

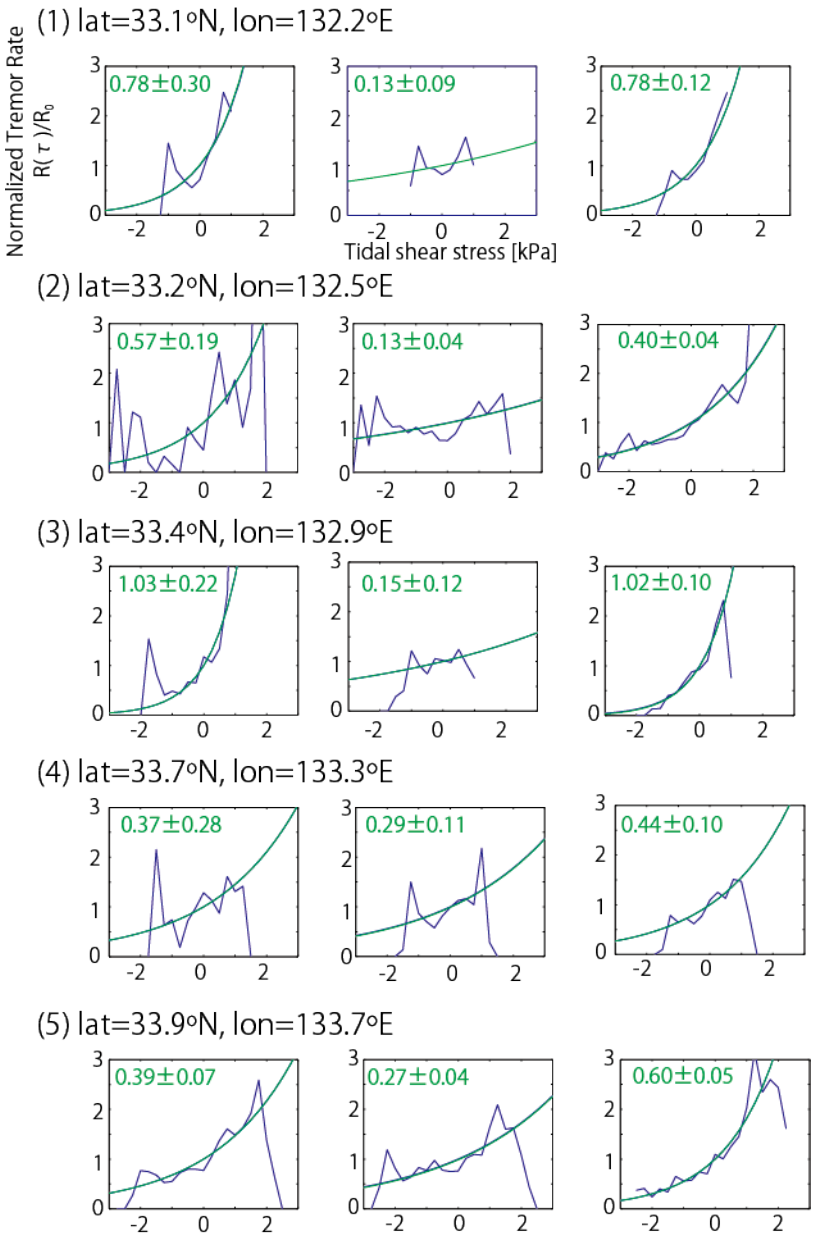

Figure 2.11: Observed and estimated tidal sensitivity of tremor rate to tidal shear stress. For several locations in Nankai and Cascadia subduction zones where the number of later tremors in a grid exceeds 1000, observed tremor rate at each tidal shear stress level is plotted with a blue line. Estimated fit of Equation (2.15) is shown with a green curve. Estimated tidal sensitivity (α value) and its uncertainty are given in each panel. Left, middle, and right panels shows the result of initiation, front, and later tremors, respectively.

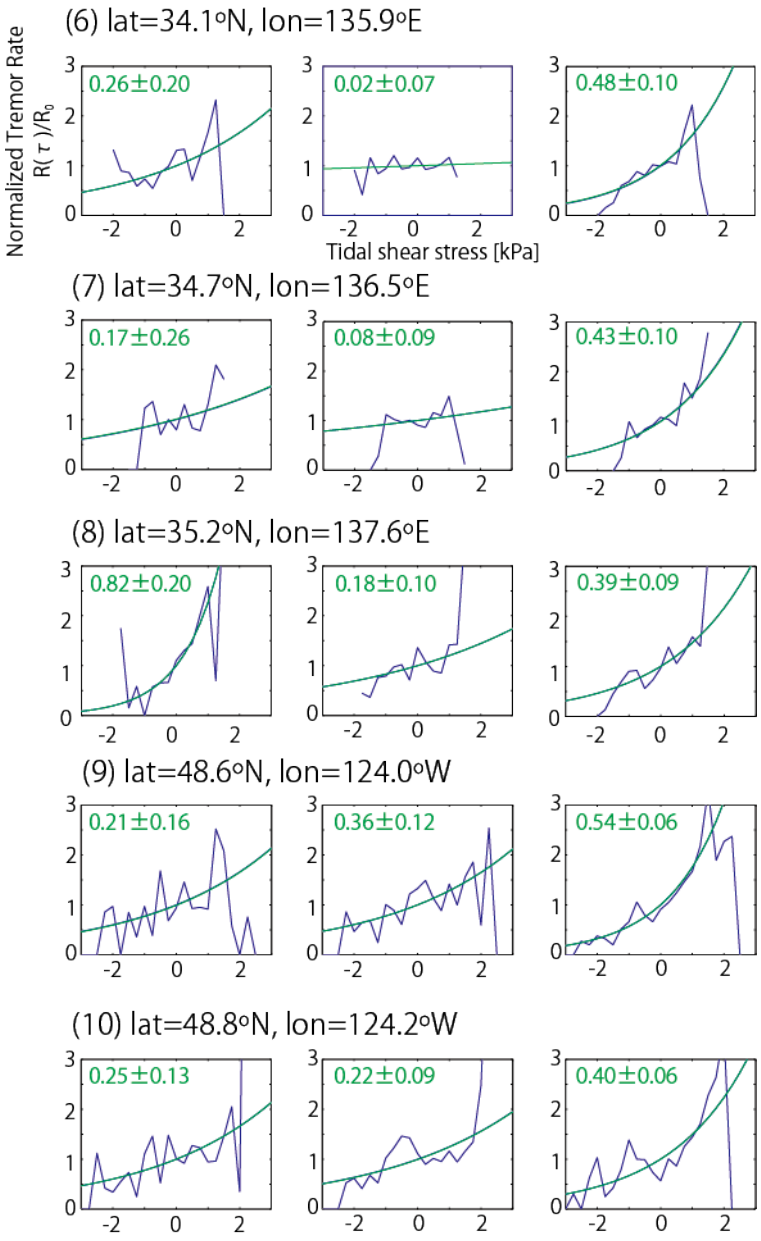

Figure 2.11(continued)

2.3. Estimated Tidal Sensitivity

In Figure 2.12 and 2.13, spatial distribution of tidal sensitivity is shown for Nankai and Cascadia subduction zones, respectively, for initiation, front and later tremors. These are selected reliable estimations with small uncertainty ($\Delta\alpha < 0.3$ kPa^{-1}). We can identify some regions of high sensitivity, such as in western Shikoku, where Shelly et al. (2007b) found strong sensitivity, and in eastern Shikoku. Sensitivity is relatively low in Kii region

of Nankai subduction zone. These features are consistent with the spatial variation of tidal sensitivity in Figure 13 of Ide (2012), who investigated tidal sensitivity of tremors using a frequency-based method, without categorizing initiation, front, and later tremors. In Cascadia subduction zone, sensitivity is generally lower than Nankai subduction zone. However, there are some regions with locally high sensitivity, such as around 48.5°N, 124°W and around 47.8°N, 123.2°W. The former is consistent with the result of Ide (2012). In Figure 1 of Houston (2015), both regions are observed as high-consistency regions where large portion of tremors occur when tidal stress is positive (i.e., tidal sensitive regions). The latter area is also roughly consistent with the initiation area of ETSs (Houston, 2015). Royer et al. (2015) also investigate tidal sensitivity of many families of LFEs detected in Cascadia subduction zone. They describe LFE families around 48.5°N, 124°W as tidal sensitive ones, which is consistent with our result. However, tidal sensitivity of LFE families is not so high around 47.8°N, 123.2°W. Rather, in their study, LFE families around 48.0°N, 123.2°W show high sensitivity, where our result shows relatively higher sensitivity.

Tremor activities in Mexican subduction zone have been also investigated. Tremor activities are documented in three parts of Mexican subduction zone; Jalisco-Colima (Ide, 2012), Guerrero (Payero et al., 2008), and Oaxaca (Brudzinski et al., 2010). In this study, tremor catalog constructed by Yabe and Ide (2014) is utilized in Jalisco-Colima region from January 2006 to June 2007. In Guerrero region, tremor catalog by Idehara et al. (2014) is utilized from January 2005 to June 2007, which used similar envelope correlation method for hypocenter locations as Yabe and Ide (2014) based on Ide (2010a, 2012). Tremor activities in Oaxaca regions could not be investigated because seismograms are not opened to public. In Figure 2.14, tremor activities in Mexican subduction zones and spatial distribution of its tidal sensitivity are shown. Categorization of three stages in tremor activity has not been done in Mexican subduction zone due to the small number of tremor detections.

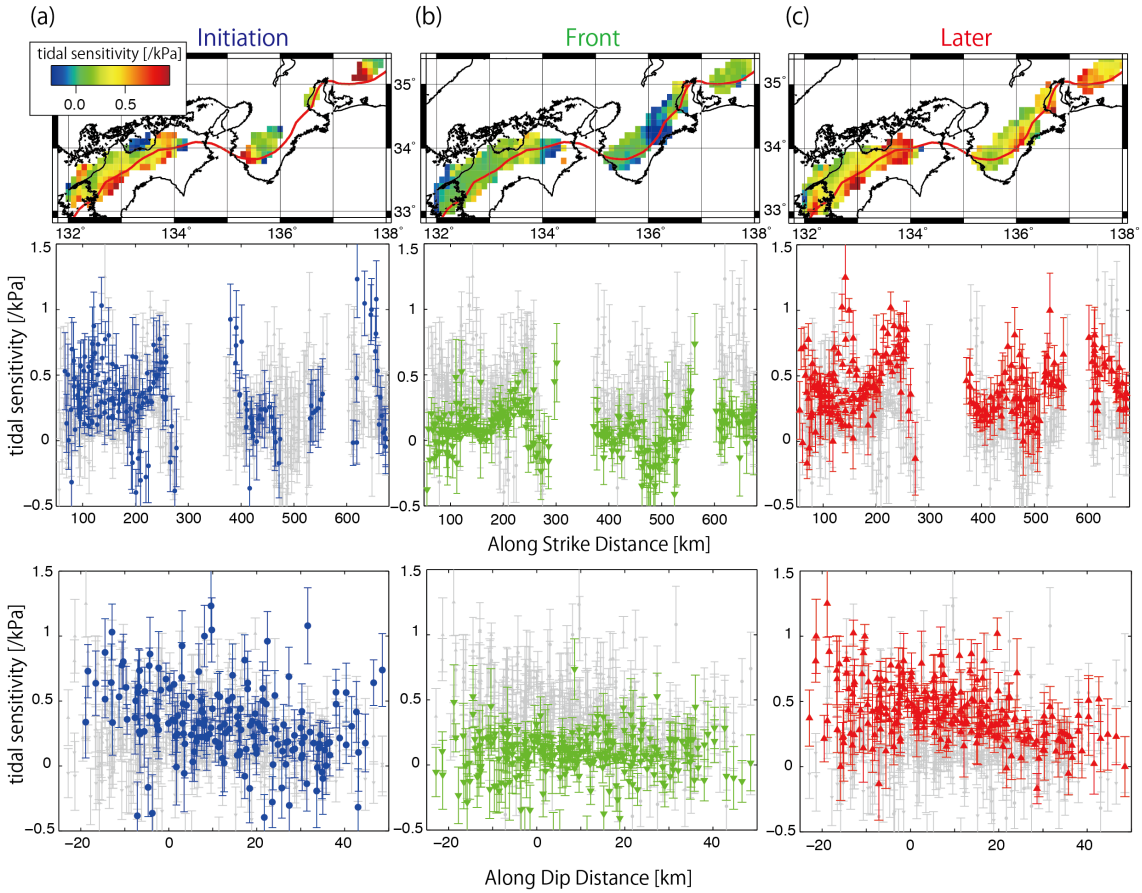

Figure 2.12: Spatial distribution of tidal sensitivity in the Nankai subduction zone. (a) Upper panel shows tidal sensitivity of initiation tremors in map view. Only estimations with uncertainty $\Delta\alpha < 0.3$ kPa^{-1} are shown. The color shows tidal sensitivity. Red line represents 30 km depth contour of plate model, which is reference line for along-dip distance. Middle panel shows tidal sensitivity of each grid point versus along-strike distance (km) at the grid point. Blue symbols represent tidal sensitivity of initiation tremors at each grid point, while gray symbols show results for all three types of tremor. In the lower panel tidal sensitivity of each grid point is plotted against along-dip distance in the same manner as middle panel. (b) Same as (a), but for front tremors. (c) Same as (a), but for initiation tremors.

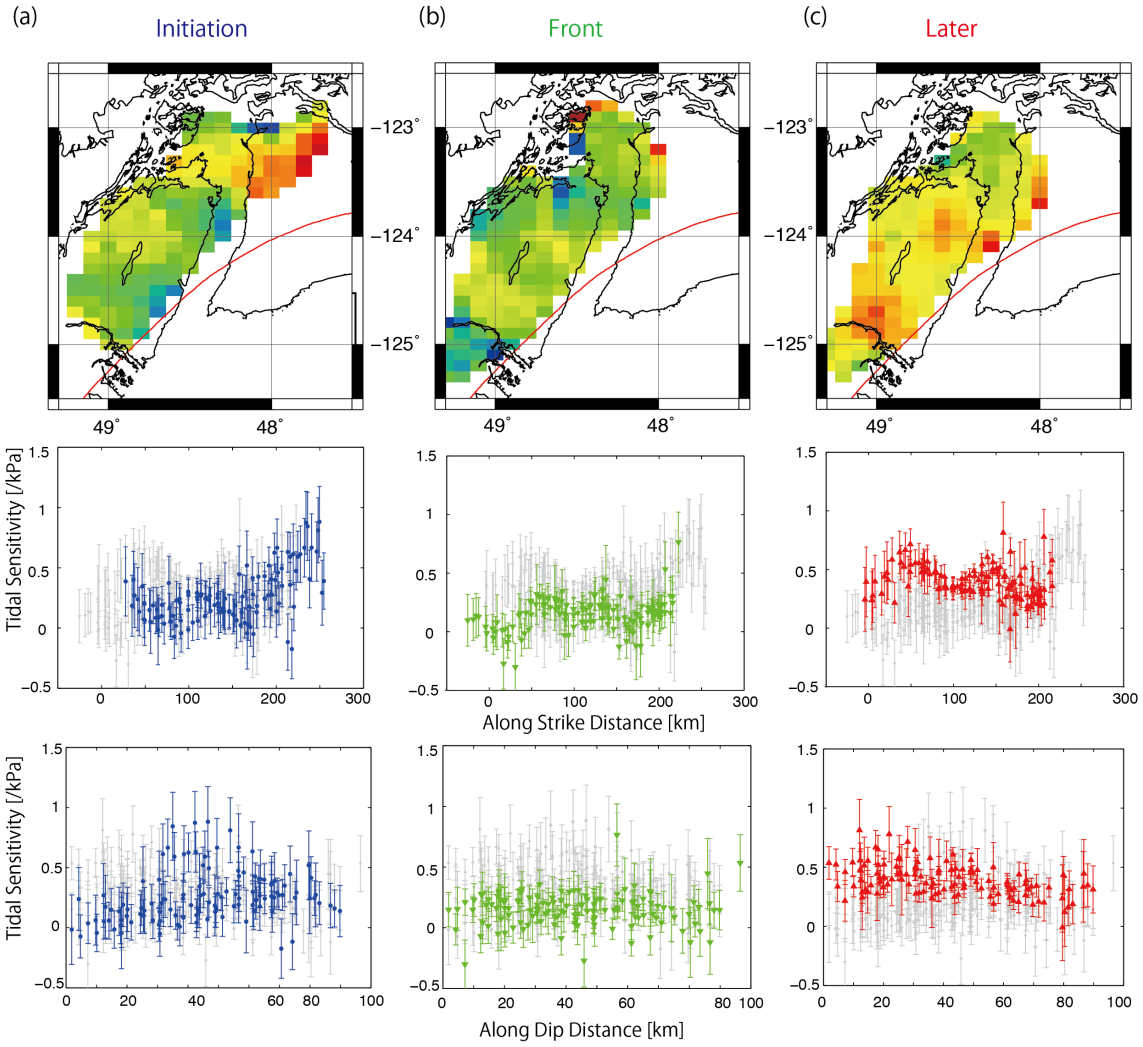

Figure 2.13: Spatial distribution of tidal sensitivity in the Cascadia subduction zone. (a) Upper panel shows tidal sensitivity of initiation tremors in map view (North in left). Only estimations with uncertainty $\Delta\alpha < 0.3$ kPa^{-1} are shown. The color shows tidal sensitivity. Red line represents 30 km depth contour of plate model, which is reference line for along-dip distance. Middle panel shows tidal sensitivity of each grid point versus along-strike distance (km) at the grid point. Blue symbols represent tidal sensitivity of initiation tremors at each grid point, while gray symbols show results for all three types of tremor. In the lower panel tidal sensitivity of each grid point is plotted against along-dip distance in the same manner as middle panel. (b) Same as (a), but for front tremors. (c) Same as (a), but for initiation tremors.

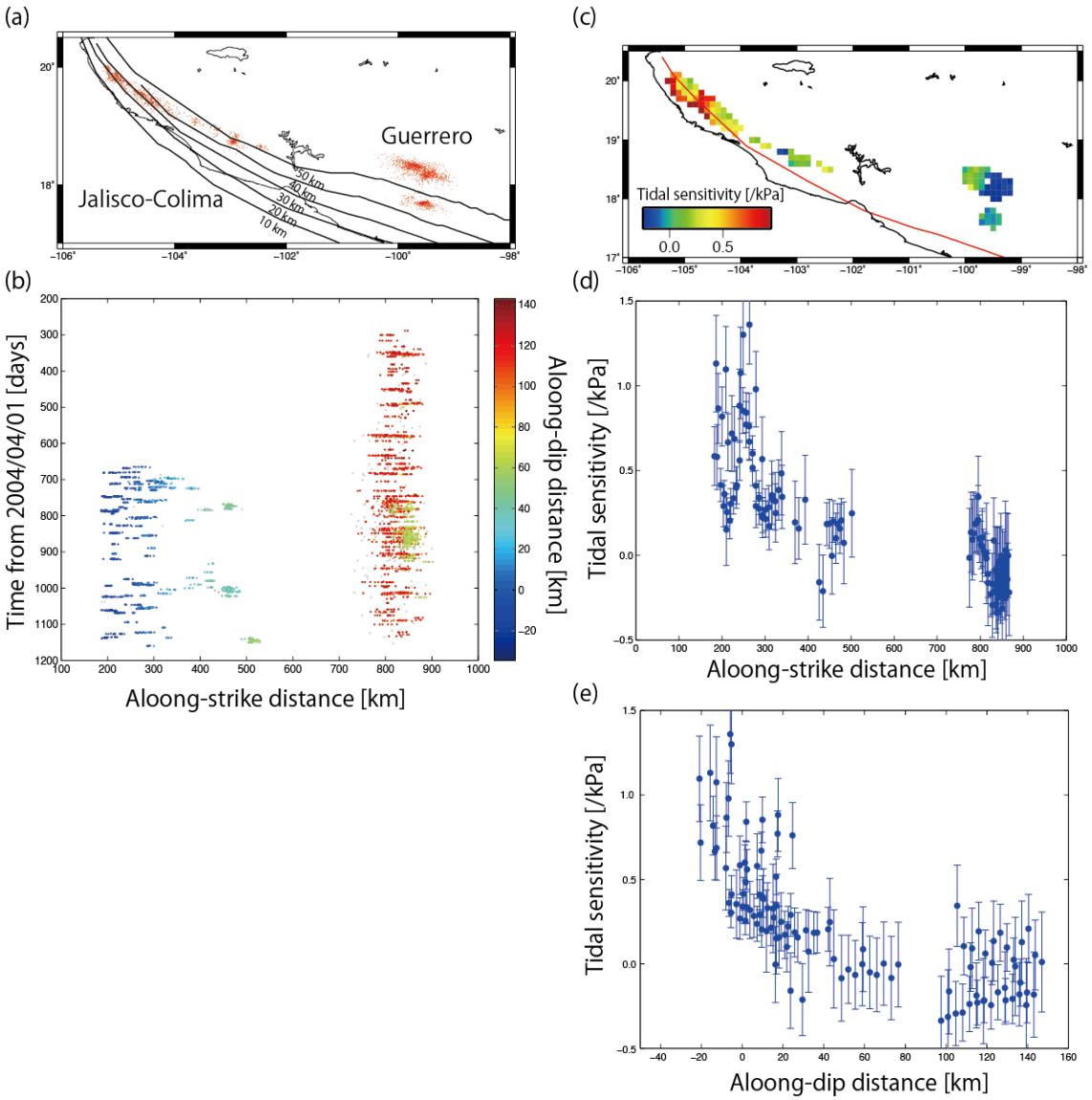

Figure 2.14: Tremor activity and its tidal sensitivity in Mexican subduction zone. (a) Spatial distribution of detected tremors. Black lines represent depth contours of subducting plate interface estimated by Pardo and Suarez (1995). (b) Time plot of tremor activity as Figure 2.8c. (c) Spatial distribution of tidal sensitivity of tremor acitivities as Figure 2.12a. (d) Variation of tidal sensitivity in the along-strike direction. (e) Variation of tidal sensitivity in the along-dip direction.

Generally, front tremors are less sensitive to tidal stress, which is consistent with the observation by Houston (2015). Figure 2.15 compares tidal sensitivities for initiation and later tremors. In Nankai subduction zone,

initiation tremors also show tidal sensitivity comparable to later tremors. In Cascadia subduction zone, initiation tremors in most regions do not show tidal sensitivity, whereas later tremors show higher sensitivity. Average sensitivities for each stage and each subduction zone are shown in Table 2.2.

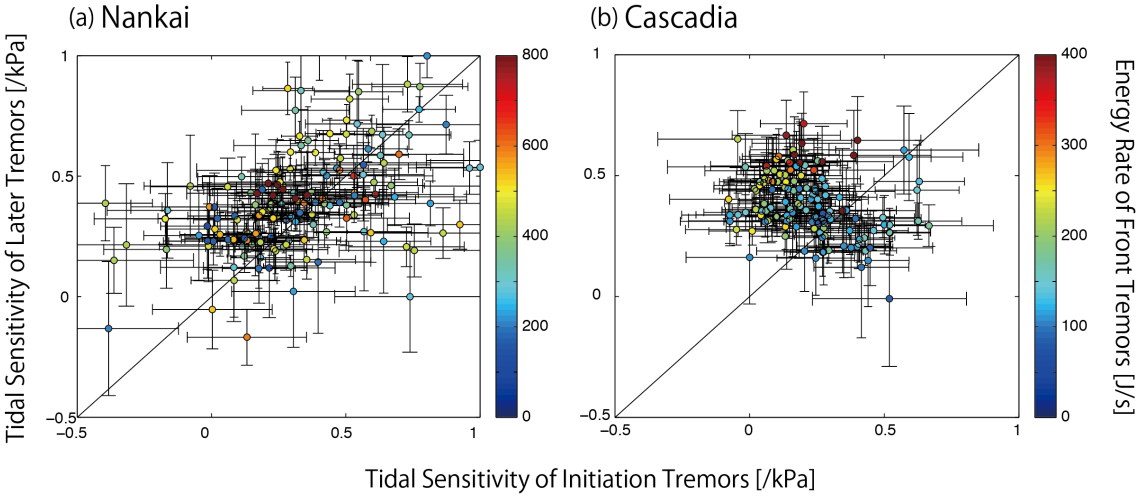

Figure 2.15: Comparison of tidal sensitivity between initiation and later tremors. (a) Tidal sensitivity of initiation tremors (horizontal axis) at each grid point is compared with that of later tremors (vertical axis). The color of symbols represents the amplitude of front tremors at the grid point, which are measured as the median value of seismic energy rate of tremors in the grid estimated by Yabe and Ide (2014). (b) Same as (a), but for Cascadia subduction zone.

Table 2.2: Average sensitivity a (kPa^{-1}) in Equation (2.15) during each stage for each subduction zone

Stage	Definition	Nankai	Cascadia
Initiation tremors	Before front period	0.33	0.25
Front tremors	First one day exceeding 20 tremors per day	0.08	0.16
Later tremors	After front period	0.41	0.38

In addition to the along-strike variation, we observe along-dip variation (Figures 2.12 and 2.13). In Nankai subduction zone, initiation and later tremors show higher sensitivity in shallower region, whereas deeper tremors are less sensitive. In Cascadia subduction zone, only later tremors show higher sensitivity in shallower region. Front tremors are insensitive for all depths in both subduction zones. When we apply linear regression analysis to confirm theses trends considering the estimation uncertainty of tidal sensitivity, we obtain slopes of -6 ± 3 Pa^{-1} km^{-1} (3 sigma), -5 ± 2 Pa^{-1} km^{-1}, and -3 ± 2 Pa^{-1} km^{-1} for initiation tremors in Nankai subduction zone, later tremors in Nankai subduction zone, and later tremors in Cascadia subduction zone, respectively, with the assumption that standard variation for fitting data is on the same order of uncertainty in the tidal sensitivity estimation (0.2 kPa^{-1}). Along-dip dependence of tidal sensitivity can be observed in the results of Mexican subduction zone as well. In contrast, Thomas et al. (2012) found that tidal sensitivity is higher in deeper LFEs, and lower in shallower LFEs in San Andreas Fault.

Figure 2.16 compares estimated tidal sensitivity with the duration of tremor signals estimated by Yabe and Ide (2014), which is defined as the half-value width of tremor envelope (Ide, 2010a, 2012). Typical duration for each grid point is defined as the median value of durations of tremors used for the tidal sensitivity analysis. Comparing duration of tremors in Nankai subduction zone with that in Cascadia subduction zone, Nankai subduction zone generally have shorter duration. Initiation and later tremors with shorter durations, which are concentrated in Nankai subduction zone, tend to have higher sensitivity, and it decreases with duration. Meanwhile, tremors with longer duration in Cascadia subduction zone tend to show lower sensitivity without dependency to duration of tremors. As a whole, there seems to exist tendency that shorter tremors tend to show higher sensitivity, and vice versa. This tendency was also suggested by Ide (2010a, 2012). Along-dip dependency of duration can be confirmed here as well by the color scale of Figure 2.16 (also see Figure 2.18a). Duration dependence of tidal sensitivity can be confirmed in Mexican subduction zone as well (Figure 2.17).

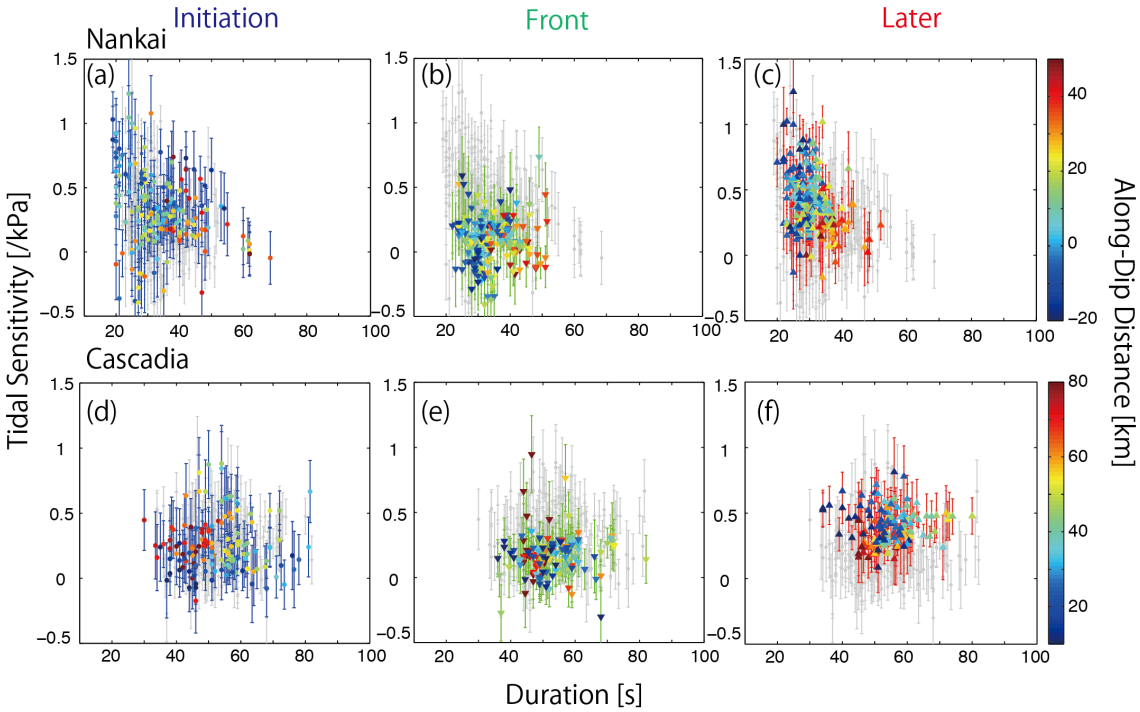

Figure 2.16: Dependence of tidal sensitivity on tremor duration in Nankai and Cascadia subduction zones. Tidal sensitivity at each grid point from Figure 2.12 and 2.13 is shown versus duration of tremors, which was defined as the median value of durations of tremors in the grid estimated by Yabe and Ide (2014). The color of dots represents along-dip distance of the grid point. (a) For initiation tremors in Nankai subduction zone. (b) For front tremors in Nankai subduction zone. (c) For later tremors in Nankai subduction zone. (d) For initiation tremors in Cascadia subduction zone. (e) For front tremors in Cascadia subduction zone. (f) For front tremors in Cascadia subduction zone.

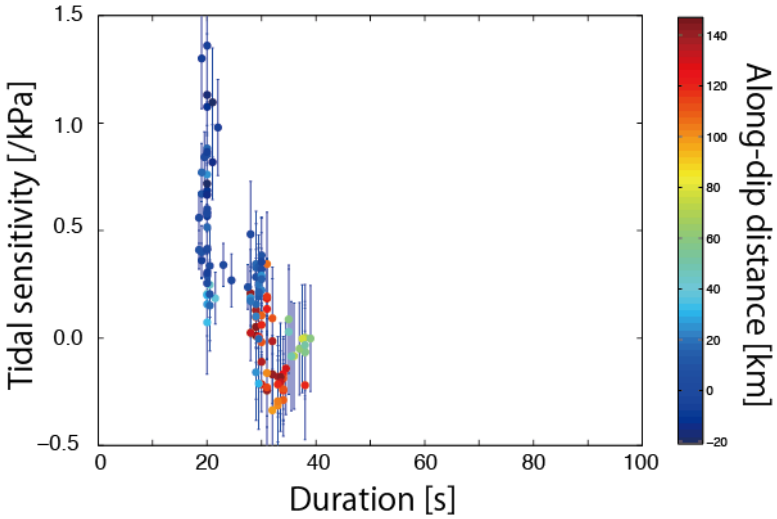

Figure 2.17: Same as Figure 2.16, except for Mexican subduction zone.

Yabe and Ide (2014) estimated the amplitude of tremors at each grid point as the median value of seismic energy rates of tremors. Amplitudes of tremors vary spatially, and shallower tremors tend to be larger (Figure 2.18b; Figure 7 of Yabe and Ide, 2014). As Yabe and Ide (2014) pointed out, and can be seen in Figure 2.9, the initiation stage of ETSs begins with small-amplitude tremors, followed by a large-amplitude tremor burst with high tremor rate in the front stage. The amplitude of tremors in the front stage seems to influence the tidal sensitivity of the later stage. Figure 2.19 compares the energy rate of front tremors with the tidal sensitivity of later tremors and along-dip distance at all grid points. On the deeper part of ETS zone, only small-amplitude tremors occur in the front stage followed by less tidal-sensitive tremors in the later stage. Meanwhile, on the shallower part, various amplitude tremors occur in the front stage followed by higher tidal sensitive tremors in the later stage (also see Figure 2.18b for along-dip dependency of tremor amplitude). Especially in Cascadia subduction zone, tidal sensitivity tends to increase from initiation stage to later stage in the region where energetic tremors occur in front stage of ETS (Figure 2.15).

Tidal sensitivity does not show significant dependence on the variation of tidal shear stress measured with RMS amplitude, although a weak negative correlation might exist (Figure 2.20). The uncertainty in the estimation is large when the stress variation is small. Although some

correlations exist among the variability of tidal stress, duration, and amplitude of tremors (Figure 2.21), it is not obvious to derive general relationships for three stages of tremor in two subduction zones.

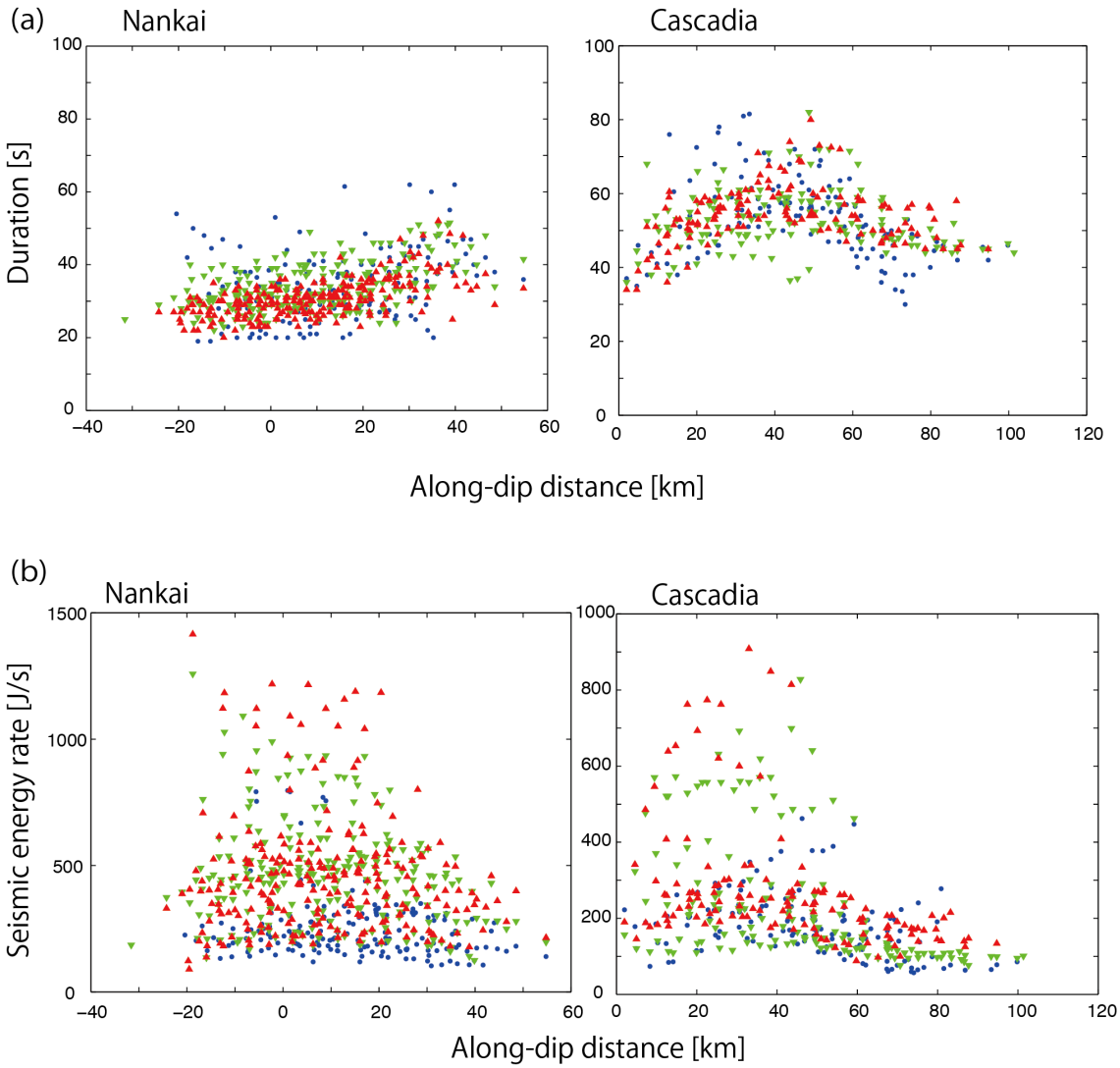

Figure 2.18. Dependence of tremor durations and amplitudes on along-dip distance. (a) Duration of tremors is shown against along-dip distance. Blue, green and red symbols represent initiation, front, and later tremors respectively. The left panel is for Nankai subduction zone, and the right panel is for Cascadia subduction zone. (b) Same as (a), but for amplitude of tremors, which is estimated as seismic energy rate of tremors by Yabe and Ide (2014).

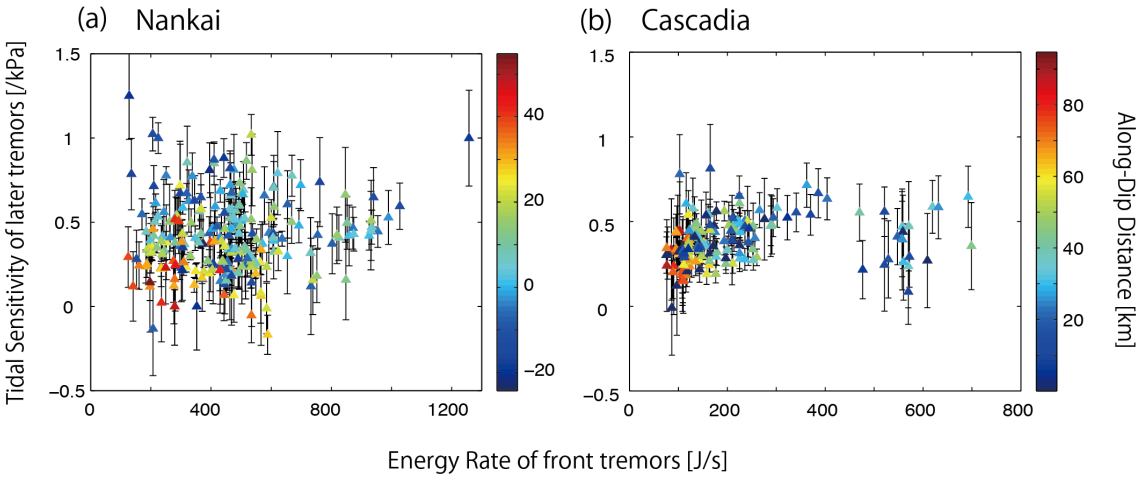

Figure 2.19: Tremor amplitude dependency of tidal sensitivity in Nankai and Cascadia subduction zones. Tidal sensitivity of later tremors at each grid point from Figure 2.12 and 2.13 is shown versus amplitude of front tremors at the grid point, which was defined as the median value of seismic energy rate of tremors in the grid estimated by Yabe and Ide (2014). The color of dots represents along-dip distance at the grid point. (a) For Nankai subduction zone. (b) For Cascadia subduction zone.

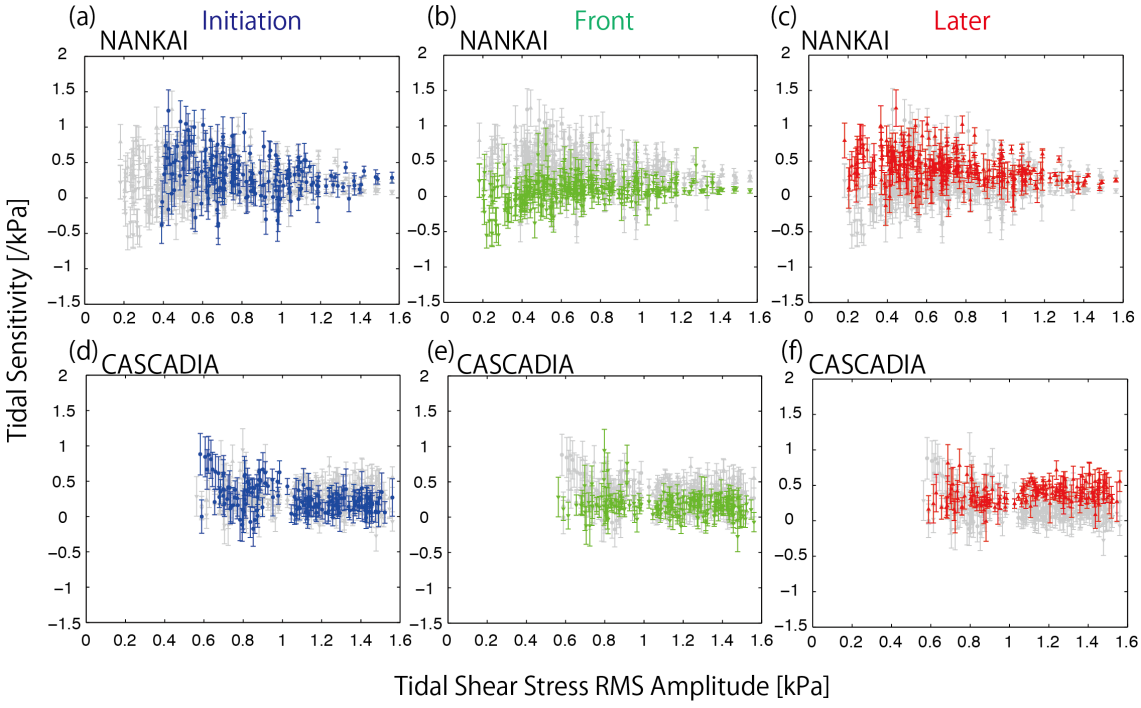

Figure 2.20: Dependence of tidal sensitivity to amplitude of tide stress in Nankai and Cascadia subduction zones. Tidal sensitivity from Figure 2.12

and 2.13 is shown along tidal-stress amplitude (Figure 2.7). (a) For initiation tremors in Nankai subduction zone. (b) For front tremors in Nankai subduction zone. (c) For later tremors in Nankai subduction zone. (d) For initiation tremors in Cascadia subduction zone. (e) For front tremors in Cascadia subduction zone. (f) For later tremors in Cascadia subduction zone.

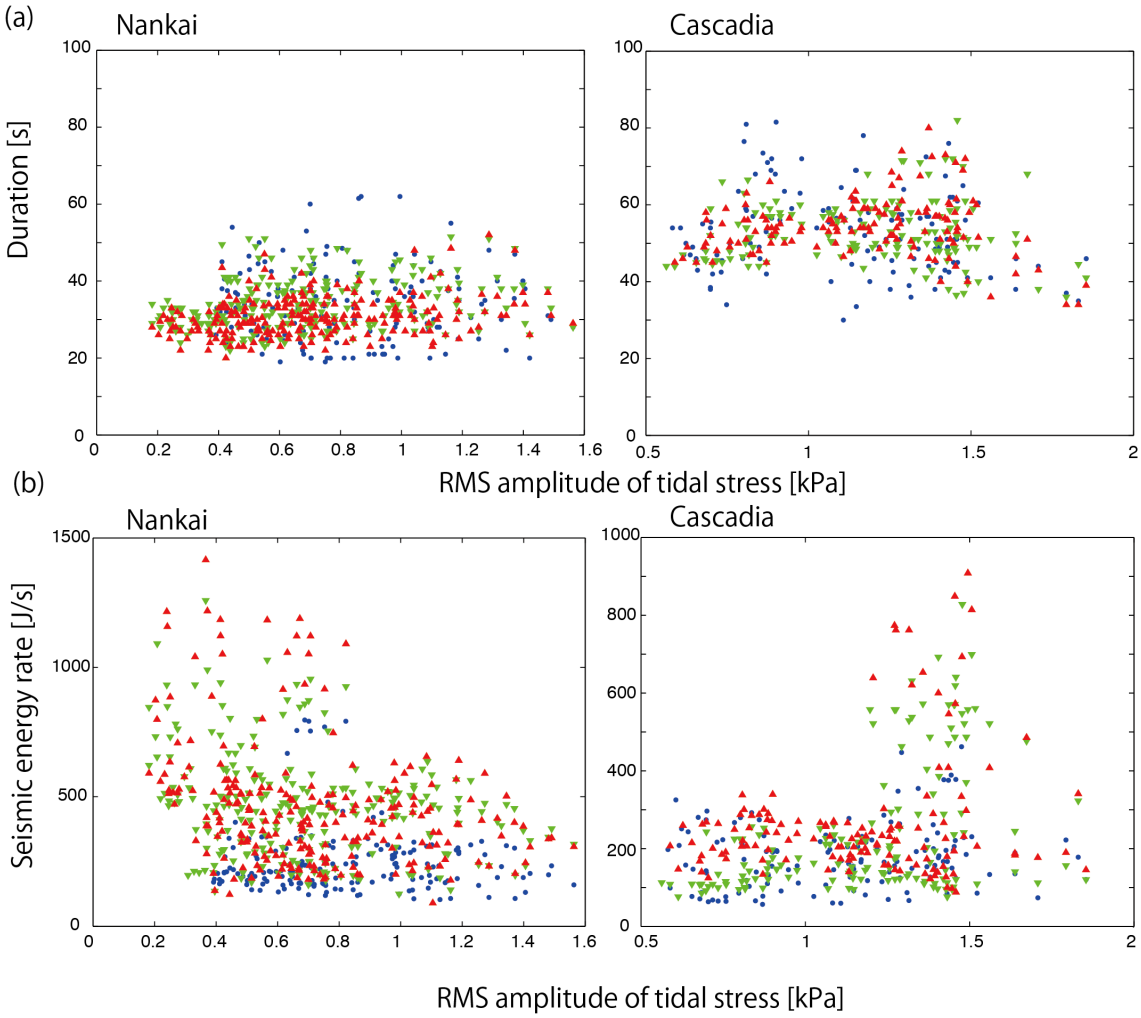

Figure 2.21: Dependence of tremor durations and amplitudes on RMS amplitude of tidal shear stress. Same as Figure 2.18, but for RMS amplitude of tidal shear stress.

2.4. Discussion

2.4.1. Reliability of tidal sensitivity estimation

In tremor analysis, some criteria have been used (such as criteria for tremor clustering of 2 days and 20 km). Ideally, these clustering and

categorizing of tremor activities should be done using the technique of seismic statistics (for example, ETAS model for ordinary earthquakes; Ogata, 1988), which is not done by this study. Hence the uncertainty of the estimation might be larger than values estimated in the maximum likelihood method. However, we observe common features in spatial distribution of tidal sensitivity with previous studies with frequency-based method (Shelly et al., 2007b; Ide, 2012). A negative correlation between tidal sensitivity and duration of tremor is also observed by Ide (2012). These coincidences suggest that the uncertainty in our estimation is not so large that results presented here would be changed by the uncertainty.

In this analysis, we only compare tidal shear stress with tremor activities because frictional coefficient in slow earthquake region seems to be very small (e.g., Thomas et al., 2009; Thomas et al., 2012; Houston, 2015). Wide area shows positive correlation between tidal shear stress and tremor activities, which suggests that our assumption is basically valid. However, in some cases, we had better to consider coulomb stress rather than shear stress only. For example, wide negative-correlation patch exists in front tremors of Kii region. In this region, tidal shear stress roughly anti-correlates with tidal normal stress (Figure 2.7c). Therefore, negative correlation with tidal shear stress might suggest positive correlation with tidal normal stress in this region, although we need further analysis to make it clear.

2.4.2. Estimated frictional parameter

Tidal effect on the fault is investigated in some previous studies (Ader et al., 2012; Beeler et al., 2013; Hawthorne and Rubin, 2013). Ader et al. (2012) especially focused on time-period dependency of slip velocity response of a spring slider following RSF to harmonic stress perturbations. They found that induced velocity changes depend exponentially on the stress perturbation if the period falls within two specific ranges related to the characteristic timescale for the evolution of the state variable, T_θ. $T_\theta = 2\pi D_c / V_{ss}$ where V_{ss} is the steady-state velocity and D_c is the characteristic slip distance for friction to evolve between two steady states. If

the time period of perturbation is longer than this time scale, state variable can change and quasi-steady state is realized. Meanwhile if the time period of perturbation is shorter than characteristic time scale, state variable does not change, and only direct effect works. In the context of this Ader et al. model, because we observe exponential behavior quantified by the sensitivity α in our Equation (2.15), one of two situations must pertain: either the dominant period of oscillation must lie in a specific period range much larger than T_e in which case $V/V_{ss} = \exp\left[\Delta\tau/(a-b)\sigma\right]$, or it must be less than T_e in which case $V/V_{ss} = \exp\left[\Delta\tau/a\sigma\right]$. Thus, assuming the exponential relation in our observation represents RSF, in the first case our observations of α can constrain $(a\text{-}b)\sigma$, and in the second, $a\sigma$.

Appropriate values of V_{ss} are not well known for ETSs in the slow-slip region and likely decrease as slip accumulates at a point during ETS. In the later stage of an ETS, V_{ss} is probably still well above its long-term inter-ETS value. We considered a range of values for V_{ss} from 10^{-8} to 10^{-7} m/s based on estimates in Rubin (2011). Nor are appropriate values of D_c known for the slow slip environs, or even for natural crustal faults. We considered D_c ranging from 2 to 500 μm (Dieterich, 1978; Marone, 1998). These values yield T_e ranging from 0.015 to 3.6 days. The dominant tidal period of 12.4 hr falls within that range, so with this model it is not clear whether our results for α can be interpreted as $\alpha^{-1} \sim (a\text{-}b)\sigma$ or $\alpha^{-1} \sim a\sigma$. If we assume that a or $a\text{-}b$ is of order 0.01, effective normal stress σ would be of order 0.3 MPa, which suggests the presence of near-lithostatic fluid pressure.

Note that the frictional parameter inferred in this study represents only a macroscopic property of friction. A small region with negative $a-b$ is required to accelerate slip and radiate seismic signals. The accelerated slip must be decelerated by surrounding VS region so as not to grow further into a large earthquake. Thus, as a whole, the frictional property estimated in this study suggests velocity strengthening.

2.4.3. Implications for physics of slow earthquakes

Key features observed in the previous section are: (i) the tremor region macroscopically has an exponential-type VS friction law, (ii) shorter-duration tremors tend to have higher tidal sensitivity, (iii) ETS starts with small amplitude tremors (initiation tremors) followed by large amplitude tremors (front / later tremors). Large-amplitude front tremors are insensitive to tides, whereas tremors in the later stage of ETS have higher tidal sensitivity, and (iv) tidal sensitivity, duration, and amplitude of tremors are dependent on down-dip position. These observations can be interpreted with the frictionally heterogeneous fault model of Ando et al. (2010, 2012) and Nakata et al. (2011), in terms of cluster size and density or local strength of VWZ, which characterize the frictional heterogeneity on the plate interface, as explained below.

In the frictionally heterogeneous fault model, microscopic VWZ are embedded in the VS background (Figure 5 of Ando et al., 2012, Figure 2.22a). Tremors and slow slips occur as a result of successive breakage of VWZ interacting with the surrounding VS background. This heterogeneous frictional distribution is statistically characterized by two quantities: cluster size and density or local strength of VWZ. Because VWZ cannot interact directly beyond the size of cluster, due to their separation by VS background region, slip expands slowly compared to seismic slip, and quasi-constant moment rate (Ide et al., 2007b), which is a fundamental characteristic of slow earthquakes, is reproduced. The density or local strength of VWZ within the cluster controls the macroscopic strength of the cluster. The variation in the cluster size and density or local strength of VWZ results in various characteristics of tremors. For example, larger cluster size and higher density or local strength will result in longer duration and larger amplitude tremors (Nakata et al., 2011), respectively. The higher density or local strength region, which can bear higher stress accumulation, can also reproduce local speed up of tremor migrations of RTR (Houston et al., 2011).

The first key feature of our observations, the general prevalence of VS, is consistent with the assumption of background in frictionally heterogeneous fault model. However, Ando et al. (2012) suggested

Newtonian-viscosity type of friction law to reproduce diffusive migration of tremors, while we obtain an exponential friction law. Further studies will be necessary to understand this apparent contradiction. Although we assume exponential function as friction law (RSF), and it fits data well (Figure 2.5), some other function of Arrhenius-type creep law might be able to explain the data as well. Beeler et al. (2013) examined tree types of creep law, dislocation creep, dislocation glide, and RSF, to explain the relation between tidal stress and LFE rate in San Andreas Fault. They found that only RSF could explain the data with plausible physical quantities.

The second key feature, a negative correlation between duration and tidal sensitivity, could be explained as follows. When cluster size is large, slip in a cluster lasts for long duration by successive breakage of VWZ. During the inter-SSE period, these regions within cluster size collectively behave as a large locked area, which is less sensitive to stress change. The opposite is true for short duration tremors. Hence, long duration tremors are less sensitive to tides, and high tidal sensitivity is expected only for short tremors.

Ide et al. (2015) investigated tidal sensitivity of tremors in Taiwan using the same method as this study without any categorization of tremors, and they found that tidal sensitivity is about 2 kPa^{-1} in Taiwan tremors, which is much higher than that estimated in this study for Nankai and Cascadia subduction zone. Tremors in Taiwan have median duration of about 18 s. We can also analyze tremors in Okayama prefecture in Nankai SZ, which were investigated by Ide and Tanaka (2014). Applying the same analysis to their tremor catalog without any categorization of tremors, we found that tidal sensitivity is 3 kPa^{-1} for them. Tremors in Okayama prefecture have median duration of 23 s. These two tremor activities with high tidal sensitivity have short duration, which is also consistent with the second key feature.

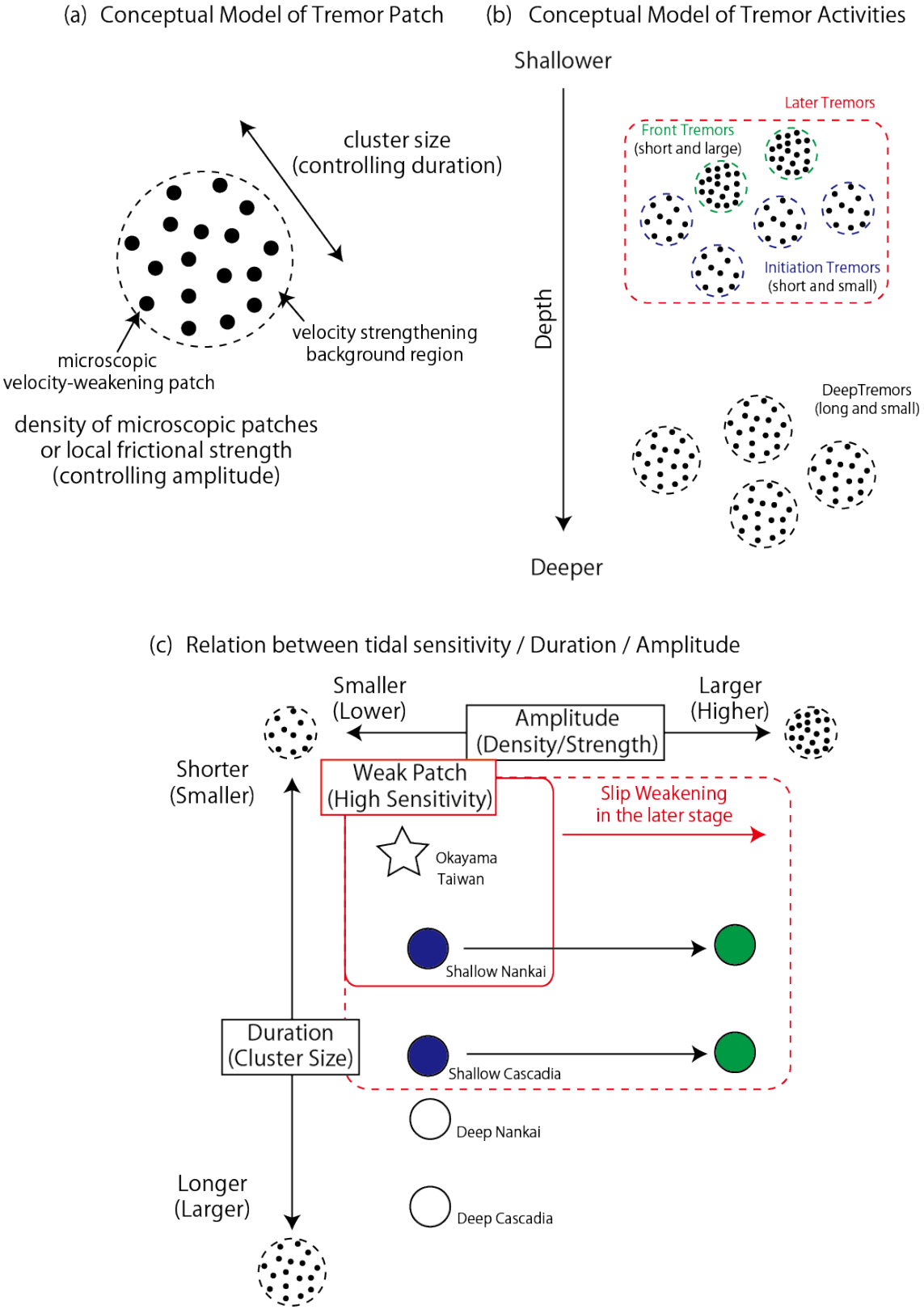

Figure 2.22: Schematic figure of plate interface in transition zone. (a) Conceptual model of tremor patch suggested by Ando et al. (2010, 2012) and

Nakata et al. (2011). Each small dot represents microscopic VW patch, which is embedded inVS background region. Size of the cluster (tremor patch) controls duration of tremors. Density or local strength of microscopic VWZ in the cluster controls amplitude of tremors (Nakata et al., 2011). (b) Distribution of tremor patches on the plate interface. In shallower part of transition zone, duration of tremors is short (i.e., cluster size of tremor patch is small). Both small-amplitude "initiation" tremors (lower density) and large-amplitude "front" tremors occur. In the later stage of ETS, both tremors occur as later tremors. In the deeper part, only long-duration and less energetic tremors occur. (c) Schematic relation between tidal sensitivity, duration, and amplitude of tremors.

The third key feature, variation among three stages, has been explained by Yabe and Ide (2014) as follows (Figure 2.22b and 2.22c). Since the density or local strength of VWZ controls macroscopic strength of the cluster, an ETS always starts from a relatively weak region with lower density or local strength. Thus initial tremors may be less energetic. Usually a high strength region works as a barrier against the slip in background region, but it sometimes breaks as well after sufficient tectonic stress accumulation. Once broken, a large energetic slip occurs in this region, probably changing physical conditions around the plate interface. Hence, tidal sensitivity is low during the front stage when strong tremor patch mainly breaks. Dilatant hardening may also reduce tidal sensitivity in front stage of ETS, then fluid pressure will diffusively recover in the later stage (e.g., Segall et al., 2010; Liu, 2013). Alternatively, large stress perturbations due to fast slip in the front stage overwhelm tidal stresses making them unimportant (Houston, 2015). It is also possible that the large slip velocity in the SSE front causes a decrease in the characteristic time scale T_a of Ader et al. (2012), over which stress perturbation is compensated by elastic deformation, to less than the tidal period, resulting in lower tidal sensitivity (Ampuero, 2015, personal communication). Large slip also weakens the plate interface and decreases the strength of VWZ, which enhances tidal sensitivity in the later stage of ETSs, which is consistent with the

interpretation of Houston (2015). Healing is presumed to occur after the ETS ends. This study provides further evidence that duration and amplitude of tremors are related to the strength of plate interface (i.e., tidal sensitivity).

In the later stage of ETS, RTRs are triggered as secondary fronts by tidal stress (Houston et al., 2011; Thomas et al., 2013; Royer et al., 2015). Peng et al. (2015) observe rapid tremor migrations near main front as well. These rapid tremor migrations will be explained as follows in our model. While slow slip propagates in the along strike direction, the first front passes many tremor patches, which have diverse strength (i.e., diverse amplitude and duration). Weaker patches are broken easily, which outline the propagating front. Meanwhile, stronger patches are less likely to be broken, although it will be broken after some stress accumulation. Once it breaks, it releases relatively higher stress, which accelerate slip, resulting in rapid tremor migrations. If it happens just after slip pulse reaches the region, it is regarded as the main front. Whereas, it happens after the main front has passed, it is regarded as RTRs. The amplitude of tremors in the main front and RTRs is relatively larger (Thomas et al., 2013; Yabe and Ide, 2014), which is consistent with this model.

In addition to tidal sensitivity, duration, and amplitude of tremors, the recurrence intervals of ETSs are also dependent on along-dip position (Obara et al., 2011; Wech and Creager, 2011). This fourth key feature suggests that cluster size and density or local strength of VWZ characterizing the frictional heterogeneity on the plate interface is governed by physical quantities, such as temperature, normal pressure, or fluid amount, etc.

Summarizing these observations and interpretations, our schematic model is provided in Figure 2.22. The frictional heterogeneity on the plate interface is characterized by the cluster size and density or local strength of VWZ (Figure 2.22a). On the shallower plate interface, the cluster size is shorter (resulting in short duration), but the density or local strength is more likely to be higher (resulting in large tremor amplitude) (Figure 2.22b). Large ETSs occur periodically here. They begin with short-duration and small-amplitude tremors (initiation tremors) followed by short-duration and

large-amplitude tremors (front tremors), which cause larger slip weakening and energetic tremors, resulting in increase of tidal sensitivity in the later stage of ETSs (Figure 2.22c). Deeper on the plate interface, cluster size is longer (long duration), but the density or local strength is lower (small tremor amplitude) (Figure 2.22b). Tremors occur more often, but tidal sensitivity is low here because it has higher strength due to large cluster size (Figure 2.22c).

Relatively short duration of tremors (Figure 2.16) and high sensitivity in initiation tremors in Nankai subduction zone (Figure 2.12 and 2.13) suggest that the plate interface in Nankai subduction zone is generally weaker than in Cascadia subduction zone. If this is the case, the time scale required for healing might be shorter in Nankai subduction zone and the strength of plate interface could recover its original state more easily, resulting in only a small increase of tidal sensitivity during slip in Nankai subduction zone.

2.5. Conclusion

Tectonic tremors in subduction zones are sensitive to tidal stress. This study investigates the tidal sensitivity of tremors in large tremor activities (ETSs) in Nankai, Cascadia, and Mexican subduction zones. Tremors are categorized into three types (tremors in the “initiation”, “front”, and “later” stage of ETSs). This study focuses on the spatial variation of tidal sensitivity of these three types of tremors to compare with the spatial variation of duration and amplitude of tremors. These characteristics are considered to reflect the heterogeneity on the plate interface. Hence, comparisons between these quantities give insights about the frictional property on the plate interface and the physics of slow earthquakes.

As previous studies suggested, an exponential relation between tremor rate and tidal stress is found. We measure the coefficient in the exponent with the maximum likelihood method, and define it as tidal sensitivity. Assuming that tremor rate is proportional to slip velocity of surrounding region and that this exponential relation represents a rate and state friction law, the $a\sigma$ or $(a-b)\sigma$ value of the law would be related to the

tidal sensitivity, considering the period of tidal stressing. Although we interpret the observed exponential relationship as RSF, it can also be interpreted as resulting from a Weibull-type fracture law as suggested by Houston (2015). Tidal sensitivity of tremors is spatially heterogeneous in both the Nankai and Cascadia SZs. Tremors in the initiation stage of ETS have tidal sensitivity in Nankai (about 0.3 kPa^{-1} in average, 1 kPa^{-1} at highest, corresponding to 3.3 kPa and 1 kPa for $a\sigma$ or $(a-b)\ \sigma$ value, respectively), but not in Cascadia (about 4 kPa in average). Front tremors have low sensitivity in both subduction zones. In the later stage of ETS, tidal sensitivity is as high as initiation tremors in Nankai subduction zone, whereas sensitivity increases over the course of ETS slip in Cascadia subduction zone (to about 2.5 kPa in average). Tidal sensitivity depends on down-dip position. Tremor has higher tidal sensitivity in the shallower ETS zone where short-duration and large-amplitude tremors tend to occur. Meanwhile, tidal sensitivity is lower at deeper depths, where longer-duration and lower-amplitude tremors occur.

Our observations show that deep plate interface generally follows an exponential-type VS friction law. The increase of tidal sensitivity when large-amplitude tremor occurs suggests that plate interface is slip-weakened by SSEs because the energy rate of tremors is proportional to the moment rate of slip in the region.

Based on the frictionally heterogeneous fault model, we consider that the frictional heterogeneity on the plate interface is characterized by the cluster size and density or local strength of VWZ. In this context, larger cluster size results in longer duration and lower tidal sensitivity, which is consistent with observed duration dependency of tidal sensitivity. Higher density or local strength represents higher strength of a cluster, resulting in larger slip in the front stage of ETS and higher tidal sensitivity in the later stage of ETS, which is consistent with observed tremor-amplitude dependency. Along-dip dependency of tremor characteristics suggest that cluster size and density or local strength characterizing frictional heterogeneity on the plate interface are controlled by physical quantities affected by depth, such as temperature, normal stress, or fluid amount.

3. 2D Numerical Model

This chapter is modified from Yabe and Ide (2017), published in Journal of Geophysical Research.

3.1. Introduction

In the previous chapter, it is suggested that observed correlations among duration, amplitude, and tidal sensitivity of tectonic tremors can be qualitatively interpreted with the frictionally heterogeneous fault model. Hence, in this chapter, slip behavior of the frictionally heterogeneous fault is addressed. A key aspect of this model is the heterogeneity in the frictional parameters of the fault surface, which must be related to the structure on the actual fault. In most theoretical studies, faults are treated as smooth planes, whereas geological field observations show that fault systems are complex, comprising kinks, jogs, steps, and branches (e.g., Tchalenko and Berberian, 1975). The topography of apparently smooth exhumed fault surfaces has a fractal nature over length scales from millimeters up to hundreds of kilometers (e.g., Candela et al., 2012). Field studies also observed that deformation style of mélange in subduction zone depends on the fault material, which has heterogeneous distribution (Fagereng and Sibson, 2010). Various heterogeneities on the plate interface may cause the frictional heterogeneity on the fault in various spatial scales. Many numerical simulations have considered the macroscopic heterogeneity of faults (e.g., Rice, 1993; Liu and Rice, 2007), because macroscopic heterogeneity can be resolved from seismicity. However, microscopic heterogeneity should also be considered because it also affects the rupture dynamics. Because some previous studies already constructed a seismic source model for slow earthquakes with frictional heterogeneity (Ando et al., 2010, 2012; Nakata et al., 2011; Skarbek et al., 2012), a brief review of them is provided in this section.

In a series of studies by Ando et al. (2010, 2012) and Nakata et al. (2011), slow earthquakes are considered as aggregations of small brittle patches embedded in the ductile fault surface. Because these patches are separated from each other by the ductile background, rupture propagations cannot accelerate to seismic speeds, resulting in slow propagation of slip. They used slip weakening friction law and Newtonian rheology as a friction law, and they calculated the rupture of small brittle patches triggered by the propagating acceleration of background slip rate. As a result, the

moment-rate function of the rupture could be temporally about constant, which is characteristic of slow earthquakes (Ide et al., 2007b). Furthermore, Nakata et al. (2011) has shown that frictionally heterogeneous fault model can explain not only slow earthquakes, but also regular earthquakes. When brittle patches are sufficiently dense and the barrier effect of the ductile background is weak, ruptures of small brittle patches are connected, and a cluster of small brittle patches will rupture as one large seismic patch in the frictionally heterogeneous model. This rupture behavior results in a triangular moment-rate function (i.e., an ordinary earthquake). The occurrence of small-scale frictional heterogeneity in the source areas of slow earthquakes has been supported by Zhang et al. (2011), who showed that at high frequencies of around 10–20 Hz the spectrum of tectonic tremors falls off f^2 as seen for ordinary earthquakes, implying that tremor signals are swarms of very small earthquakes with unusually low corner frequency. However, as described in the previous chapter, the result of tidal sensitivity analysis of tremor activities implies the existence of RSF law (Dieterich, 1979) on the plate interface, which is different from the assumption of those studies. Furthermore, the stress accumulation process is not considered in those studies. Hence, it is needed to evaluate how the transition of slip behavior occurs on frictionally heterogeneous fault governed by RSF law.

Skarbek et al. (2012) considered seismic cycle of frictionally heterogeneous fault governed by RSF law. Because their focus is deep slow earthquake, they set a no-slip boundary condition at the shallower edge, and a stable-slip boundary condition at the bottom edge of linear fault. In their model, the spatial scale of frictional heterogeneity is smaller than the nucleation size of VWZ on the fault, which is determined by the assumed frictional property. Hence, each VWZ on the fault cannot accelerate alone. As a result, the heterogeneous fault shows aseismic stick slip (i.e., SSE) when the portion of VWZ on the fault is low or a-b on VSZ is large. Whereas, when the portion of VWZ on the fault is large or a-b on VSZ is small, the entire model space slips seismically (i.e., regular earthquake). This model can explain the transition of slip mode from regular earthquake to slow earthquake with depth. However, this model cannot explain the co-existence of SSE and tectonic tremor because tectonic tremor represents local accelerations of slip in SSE (Thomas et al., 2016). To model such co-existence of aseismic and seismic slip on the fault, the spatial scale of the frictional heterogeneity should be larger than the nucleation size of VWZ on the fault.

Dublanchet et al. (2013) considered such frictional heterogeneity on the fault. They randomly distribute small VW patch, which can nucleate to seismic event alone, on an infinite planar fault. Then, they investigated the slip behavior of the fault with cyclic boundary condition by changing the portion of VWZ and *a*-*b* of VSZ. As a result, they observed that seismic slip is restricted within VWZ when the portion of VWZ is low or *a*-*b* of VSZ is high, whereas the entire fault experience seismic slip when the portion of VWZ is high or *a*-*b* of VSZ is low. However, the relation between their observations and the mechanism of slow earthquake is not clear. Although interesting slip behavior related to slow earthquake is expected around the transition between two modes of slip behavior, they did not go into details.

In the present study, it therefore has been investigated how shear-slip behavior varies according to the frictional heterogeneity on the fault governed by RSF law (Dieterich, 1979). To facilitate an understanding of the physics of the problem, our focus here is restricted to a 2D model with the simplest type of heterogeneity; that is, an infinite heterogeneous linear fault where VWZs and VSZs are cyclically distributed with a uniform characteristic slip distance. It has been tried to understand why the transition occurs and what kind of slip behavior appears around the boundary. In the following sections, it has been described how the shear-slip behavior of a heterogeneous fault changes as a function of the heterogeneity and stiffness of the system. The model setting is described in Section 3.2. In Section 3.3, the shear-slip behavior transition has been investigated as a function of the proportion of the fault that is VW when an external stress accumulation does not exist. An analytic explanation has been provided for the physical mechanism controlling the transition. Then, the shear-slip behavior transition has been investigated when an external stress accumulation exists. Parameter studies have been conducted to explore how the transition changes with stiffness. In addition to these simple simulations, slightly more complex and realistic examples have been provided (i.e., faults with a fractal heterogeneity in the distribution of the frictional parameters), followed by a discussion of the results in Section 3.4 and conclusions in Section 3.5.

3.2. Method

To understand how the slip behavior of heterogeneous faults changes with the degree of frictional heterogeneity, the present paper focuses on a very simple model, consisting of an infinite linear fault in a 2D anti-plane elastic space with spatially periodic bimodal distributions of RSF parameters (Figure 3.1). The fault is discretized into many sub-faults to calculate the slip evolution using a boundary integral equation method. Stress on the i-th sub-fault τ_i is expressed as

$$\tau_i = \tau_0 + k_0 \left(V_{pl} t - \frac{\sum_j u_j}{N} \right) + \sum_j K_{ij} u_j - \frac{\mu}{2\beta} V_i \,, \quad (3.1)$$

where τ_0 is an ambient stress when the fault slips at the plate velocity V_{pl}, which does not affect the slip behavior of the fault in this system. The second term in Equation (3.1) represents an external stress accumulation due to constant motion at velocity V_{pl} at a distance $W/2$ from the fault plane (Figure 3.1) (e.g., Ziv and Rubin, 2003; Dublanchet et al., 2013). k_0 is the external loading stiffness, t is time, u_j is the slip distance of the j-th sub-fault, and N is the total number of sub-faults used in the calculation. The third term corresponds to stress caused by elastic deformation due to fault displacement.

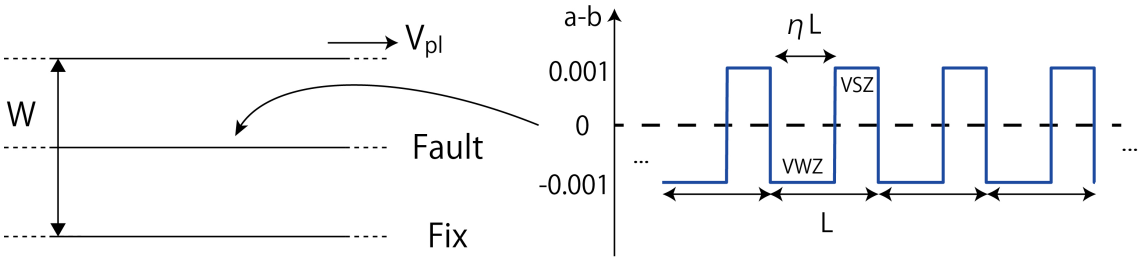

Figure 3.1: Model space and distribution of frictional parameters on the fault. (Left) An infinite fault is embedded in an anti-plane 2D elastic medium with width W. The elastic medium is sheared at the plate velocity V_{pl}. (Right) The frictional parameters of the RSF law have a cyclic bimodal distribution characterized by the length scale L. The η parameter characterizes the density of VWZ on the fault.

The static kernel K_{ij} in an infinite elastic medium with a cyclic boundary condition originally derived by Ampuero (2002) expresses the stress on the i-th

sub-fault induced by unit slip on the *j*-th sub-fault. The stress rate induced by a static deformation in a 2D infinite model space is represented by

$$\Delta\dot{\tau}\left(x_0\right)=\frac{\mu}{2\pi}\int_{-\infty}^{\infty}\frac{V\left(x\right)}{\left(x-x_0\right)^2}dx\,. \quad (3.2)$$

Because we assume a cyclic boundary condition with recurrence distance *L*, Equation (3.2) can be rewritten as

$$\begin{aligned}\Delta\dot{\tau}\left(x_0\right)&=\frac{\mu}{2\pi}\sum_{k=-\infty}^{\infty}\int_{0}^{L}\frac{V\left(x\right)}{\left(x+kL-x_0\right)^2}dx\\&=\frac{\mu}{2\pi L^2}\int_{0}^{L}\sum_{k=-\infty}^{\infty}\frac{V\left(x\right)}{\left(\frac{x-x_0}{L}+k\right)^2}dx\,.\end{aligned} \quad (3.3)$$

Using the identity

$$\sum_{k=-\infty}^{\infty}\frac{1}{\left(z+k\right)^2}=\frac{\pi^2}{\sin^2\left(\pi z\right)}, \quad (3.4)$$

Equation (3.3) becomes

$$\Delta\dot{\tau}\left(x_0\right)=\frac{\pi\mu}{2L^2}\int_{0}^{L}\frac{V\left(x\right)}{\sin^2\left(\frac{x-x_0}{L}\pi\right)}dx\,. \quad (3.5)$$

Now, the fault of length *L* is discretized into *N* sub-faults to obtain

$$\Delta\dot{\tau}_i=\frac{\pi\mu}{2L^2}\sum_{j=1}^{N}\int_{(j-1/2)\Delta x}^{(j+1/2)\Delta x}\frac{V_j}{\sin^2\left(\frac{x-x_i}{L}\pi\right)}dx\,. \quad (3.6)$$

The static kernel K_{ij} is defined as $\Delta\dot{\tau}_i=\sum_{j=1}^{N}K_{ij}V_j$.

For $i \neq j$, Equation (3.6) is integrated to

$$\Delta\dot{\tau}_i=\frac{\mu}{2L}\sum_{j=1}^{N}\left[-\frac{V_j}{\tan y}\right]_{\frac{j-i-1/2}{N}\pi}^{\frac{j-i+1/2}{N}\pi}, \quad (3.7)$$

where $y = \pi(x-x_i)/L$, resulting in,

$$K_{ij}=\frac{\mu}{2L}\frac{\sin\left(\frac{\pi}{N}\right)}{\sin\left(\frac{\left|i-j\right|-0.5}{N}\pi\right)\sin\left(\frac{\left|i-j\right|+0.5}{N}\pi\right)}\,. \quad (3.8)$$

For $i = j$, the static kernel is

$$K_{ii} = -\sum_{j \neq i} K_{ij} = -\frac{\mu}{2L} \frac{\sin\left(\frac{\pi}{N}\right)}{\sin^2\left(\frac{\pi}{2N}\right)}. \qquad (3.9)$$

Hence, Equation (3.8) is also valid for $i = j$.

Because we use a static kernel in an infinite medium, stiffness $k_0 = 0$ is the only physically correct value in this situation. However, the error introduced by using a static kernel in an infinite medium rather than an elastic medium of width W is acceptably small when the recurrence distance of frictional parameters L is much smaller than W (Rice and Ruina, 1983). In our numerical calculations, we test stiffness values of k_0 = 10^5, 10^6, and 10^7 Pa/m, corresponding to W = 300, 30, and 3 km, respectively, using μ = 30 GPa. Geodetic measurements of slow slip events have implied that the actual stiffness in deep subduction zone is at 5 x 10^5 Pa/m (Maury et al., 2014). The recurrence distance of frictional parameters L is 60 m in our calculations. The last term in Equation (3.1) is a radiation-damping term (Rice, 1993) that mimics the energy loss by radiating seismic waves to the surrounding elastic material. V_i is the slip velocity on the i-th sub-fault, μ is rigidity, and β is the shear wave velocity.

The RSF law on the i-th sub-fault is expressed as

$$\tau_i = \tau_0 + a_i\sigma \log\left(\frac{V_i}{V_{pl}}\right) + b_i\sigma \log\left(\frac{\theta_i}{\theta_{pl}}\right), \qquad (3.10)$$

where a_i and b_i are the frictional parameters of the RSF law on the i-th sub-fault. In a fault with homogeneous frictional property, when $a - b < 0$, the fault shows VW behavior in the steady state, resulting in stick-slip behavior when the system stiffness is sufficiently small, whereas if $a - b > 0$, then VS behavior results and the fault undergoes stable slip. We distribute a and b bimodally on the fault with a cyclic spatial distribution (Figure 3.1). The parameter η defines the proportion of the fault length that is assigned to be VW; herein this value is referred to as the density. In Equation (3.10), σ is the effective normal stress, and θ_i and θ_{pl} are state variables on the i-th sub-fault and its reference value when the fault slips at the plate velocity, respectively. The state variable is related to the frictional strength of the fault (e.g., Nakatani, 2001). Its temporal evolution can be expressed empirically in a number of ways. Popular forms

are the aging law (Dieterich, 1979) and the slip law (Ruina, 1983); other forms have been proposed recently (e.g., Nagata et al., 2012). The present study discusses mainly the results obtained using the aging law

$$\frac{d\theta_i}{dt} = 1 - \frac{V_i \theta_i}{D_c}, \quad (3.11)$$

where D_c is the characteristic slip distance, because an analytical discussion is possible for this law. Following Rubin and Ampuero (2005), we refer to the second term of the right-hand side of Equation (3.11) as the "weakening effect". For completeness, we also show the results of numerical simulations calculated using the slip law,

$$\frac{d\theta_i}{dt} = -\frac{V_i \theta_i}{D_c} \ln\left(\frac{V_i \theta_i}{D_c}\right). \quad (3.12)$$

From Equations (3.11) and (3.12), θ_{pl} is written as $\theta_{pl} = D_c / V_{pl}$. For simplicity, we assume a uniform value of D_c and effective normal stress σ on the fault. The time derivatives of Equations (3.1) and (3.10) yield

$$\left(\frac{a_i \sigma}{V_i} + \frac{\mu}{2\beta}\right)\frac{dV_i}{dt} = k_0 \left(V_{pl} - \frac{\sum_j V_j}{N}\right) + \sum_j K_{ij} V_j - \frac{b_i \sigma}{\theta_i}\frac{d\theta_i}{dt}. \quad (3.13)$$

Using Equations (3.11) and (3.13), or (3.12) and (3.13), we can calculate the temporal evolution of slip velocity and the state variables for each sub-fault. Because we use cyclic boundary conditions, the convolution in Equation (3.13) can be calculated using a fast Fourier transform to accelerate the evaluation of the expression. We use the Runge–Kutta–Fehlberg method (Fehlberg, 1969) with an adaptive time increment for the numerical calculation. Grid discretization of the fault should be smaller than L_b to perform the calculation in the continuum limit (Rubin and Ampuero, 2005), where

$$L_b = \frac{\mu D_c}{b\sigma}. \quad (3.14)$$

Therefore, we divided the fault into sub-faults, each with length equal to $L_b/8$, where L_b is calculated with the maximum b value on the fault. The basic parameter values used in this study are listed in Table 3.1. Similar values are chosen for a and b as Dublanchet et al. (2013).

From Equation (3.13), when the slip velocity is higher than $V_{dyn} = 2\beta a\sigma / \mu$

(Rubin and Ampuero, 2005), the radiation-damping term (i.e., the second term on the left-hand side) is more important than the direct effect of RSF (i.e., the first term on the left-hand side). Hence, we use this velocity as a threshold for "seismic" slip; for the parameters listed in Table 3.1, this seismic slip velocity is 6×10^{-3} m/s.

Parameter	Value
a	0.001 (VW) / 0.002 (VS)
b	0.002 (VW) / 0.001 (VS)
D_c	10 μm
Normal stress σ	30 MPa
Rigidity μ	30 GPa
Shear wave velocity β	3 km/s
Plate velocity V_{pl}	10^{-9} m/s
L_b	5 m
Sub-fault size Δx	0.625 m
Recurrence size L	60 m

Table 3.1. The reference parameter set used for the numerical simulations presented in this study.

3.3. Results

We performed numerical calculations for various values of η, k_0, a, b, and L, using the aging law and the slip law. The initial conditions for the simulations are uniformly set as $(V_i, \tau_i) = (0.5V_{pl}, \tau_0)$ for all sub-faults. The initial condition of the state variable is set so that Equation (3.10) is satisfied. Because we did not introduce any randomness in the heterogeneity of the distribution of frictional parameters or in that of the initial conditions, the fault-slip ultimately evolves to stable slip at a uniform velocity,

or to a limit cycle of stick-slip behavior after transient behavior, except for when the system enters the "entire-stick" regime, as discussed in the next section.

3.3.1. Without an external stress accumulation ($k_0 = 0$)

First, we show results for the situation where no external stress accumulation exists (i.e., $k_0 = 0$ in Equation (3.13)). We investigate the shear-slip behavior of a heterogeneous fault by varying η in increments of 0.05 between 0 and 1, inclusive. The other model-parameter values used are as listed in Table 3.1, which we refer to as the reference parameter set using the aging law. At this boundary condition, constant ambient stress τ_0 (the value does not change slip behavior; e.g., Equation (3.13)) is applied to the fault, which enables the fault to be deformed. We observed four types of shear-slip behavior (Figure 3.2a–d) in these simulations. When η is small (i.e., $0 \leq \eta \leq 0.2$), the fault creeps at a spatially uniform slip velocity (Figure 3.2a), which we term the "stable-slip" regime. The VWZ begins to show stick-slip behavior at $\eta = 0.25$, although the VWZ cannot accelerate to seismic slip velocity in this case (Figure 3.2b); we term this the "non-seismic stick-slip" regime. At larger values of η (i.e., $0.3 \leq \eta \leq 0.45$), the VWZ shows stick-slip behavior reaching seismic slip velocity, and the VSZ shows delayed acceleration to intermediate slip velocities, that is, afterslip behavior (Figure 3.2c). We call this slip behavior the "partial-seismic" regime. However, at $\eta \geq 0.5$, the entire fault continuously decelerates (Figure 3.2d). In this regime, seismic events never occur and the entire fault sticks. We term this regime the "entire-stick" regime.

When the external stress loading does not exist (k_0=0), stress is kept at ambient stress τ_0 at an infinite boundary condition. Hence, energy is inputted into the system by the ambient stress. In the case where the fault slips stably, the same amount of energy is consumed as frictional energy (radiation energy can be neglected). When the fault shows stick-slip behavior in VWZ, less amount of energy is consumed as frictional energy than inputted energy by the ambient stress in VWZ. Saved energy is used for radiation energy and acceleration of VSZ.

Next, we vary some parameters from their reference values to investigate how shear-slip behavior changes with the assumed modeling parameters. We observe three or four of the four regimes discussed above during this parameter study, although the boundaries between the regimes in some cases shift from their reference-parameter-set

locations. These results are summarized in Figure 3.2e.

Figure 3.2 (next page): Shear-slip behavior under zero-stiffness (i.e., $k_0 = 0$) conditions. (a) Time evolution of slip velocity for the case of $\eta = 0.1$ calculated with the reference parameter set (Table 3.1) and aging law. Slip velocity averaged over the entire fault is shown by the green line; slip velocities at the center of the velocity-weakening zone (VWZ) and velocity-strengthening zone (VSZ) are shown by the red and blue lines, respectively. This figure represents a typical example of the stable-slip regime. (b) As for (a), except with $\eta = 0.25$. Because the peak velocity of the VWZ does not reach seismic slip velocity (i.e., 6×10^{-3} m/s; see main text for definition), this figure represents a typical example of the non-seismic stick-slip regime. The right-hand panel of this figure shows a close-up view of the seismic event indicated by the dashed line in the left-hand panel. (c) As for (b), except with $\eta = 0.40$. Because the peak velocity of the VWZ reaches seismic slip velocities, whereas the peak velocity of the VSZ does not reach seismic slip velocities (i.e., afterslip), this figure represents a typical example of the partial-seismic regime. (d) As for (a), except with $\eta = 0.65$. This figure represents a typical example of the entire-stick regime because slip velocity is continually decelerating, and seismic events never occur. (e) Table summarizing the results of the parameter study. The far-left column describes how the modeling parameters differ from the reference parameter set (see Table 1); arrows show where each regime shown in (a)–(d) exists.

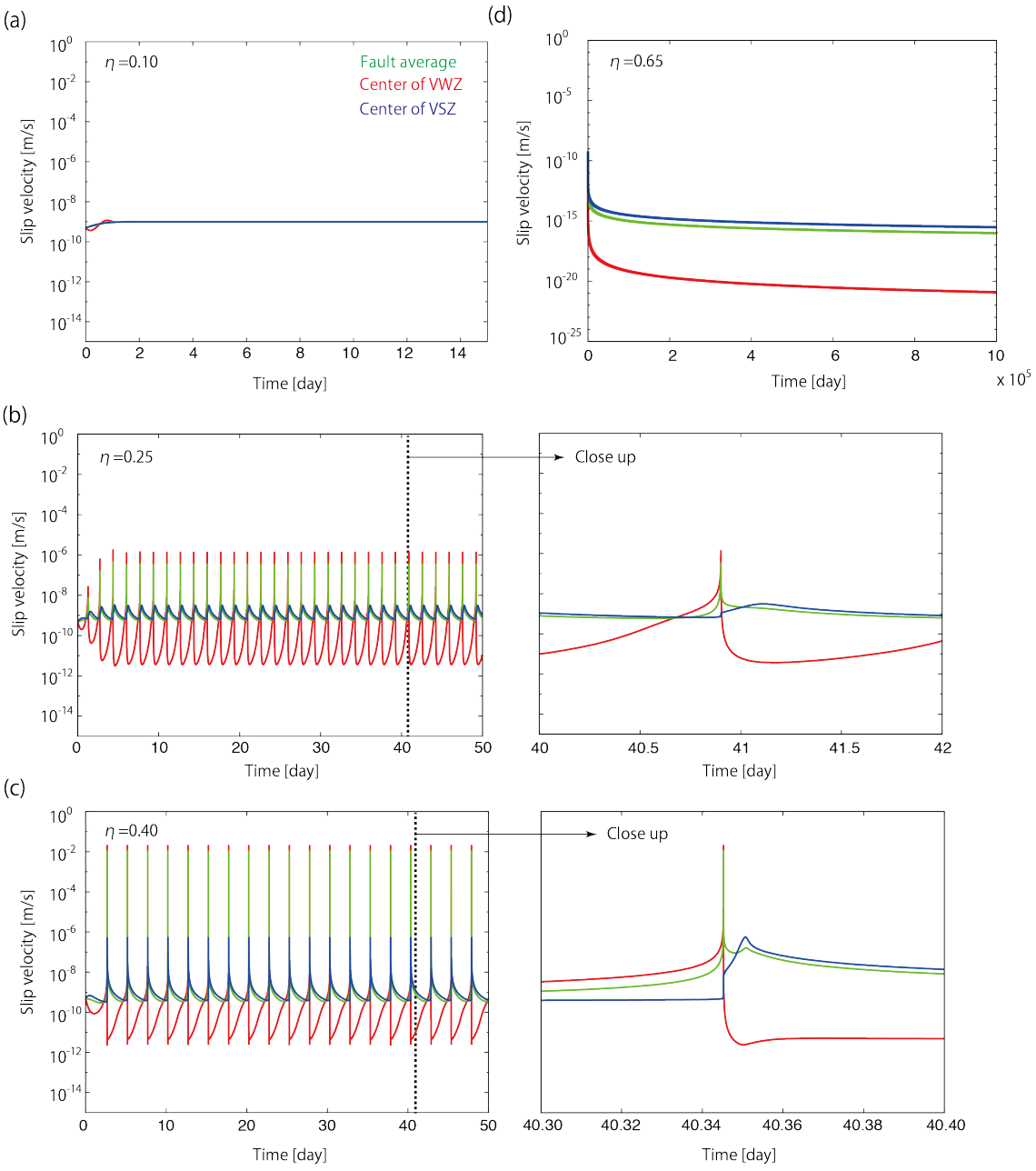
(a)
η =0.10
Fault average
Center of VWZ
Center of VSZ
Slip velocity [m/s]
Time [day]
(d)
η =0.65
Slip velocity [m/s]
Time [day]
x 10^5
(b)
η =0.25
Close up
Slip velocity [m/s]
Time [day]
Time [day]
(c)
η =0.40
Close up
Slip velocity [m/s]
Time [day]
Time [day]

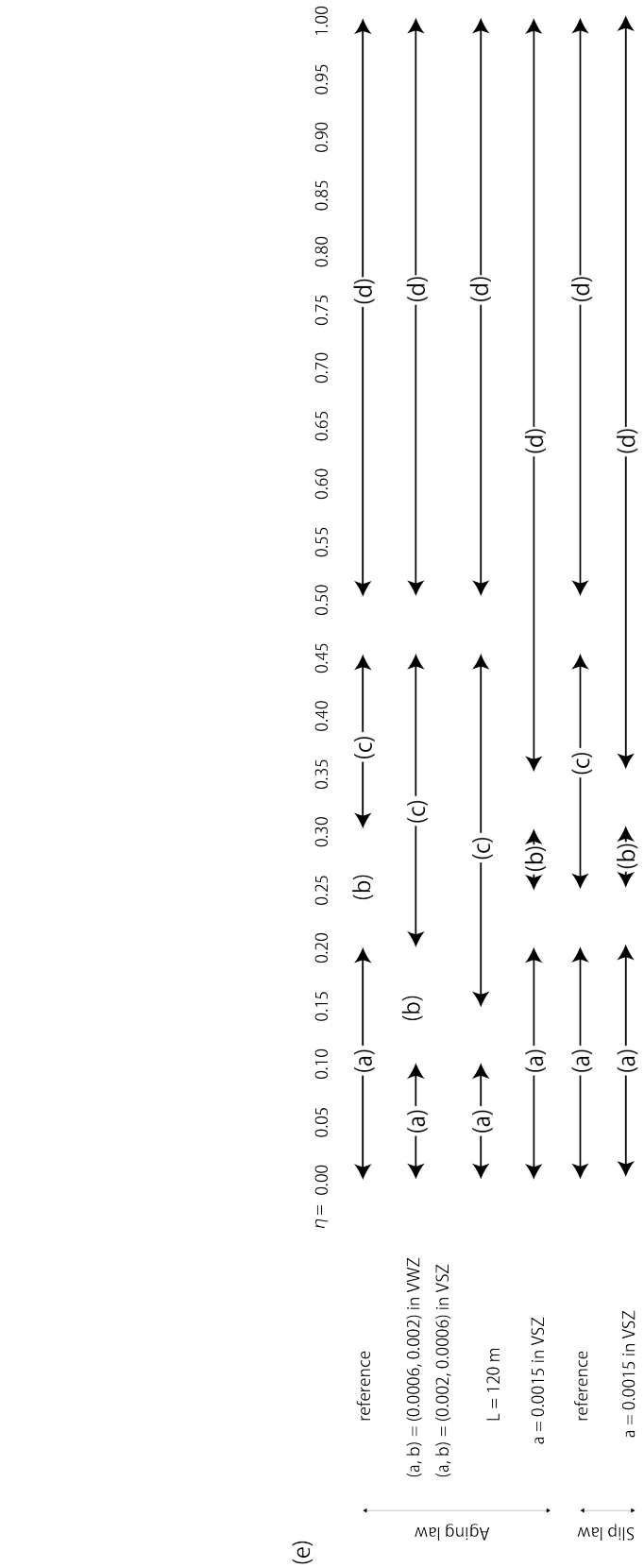

Figure 3.2 (continued)

When we use (a, b) = (0.0006, 0.002) in the VWZ and (a, b) = (0.002, 0.0006) in the VSZ instead of the reference-parameter-set values, that is, when a/b is changed from 0.5 to 0.3, we observe all four regimes. The non-seismic stick-slip regime occurs at η = 0.15 in this case, and the stable-slip regime and the partial-seismic regime are respectively observed below and above this η value. The entire-stick regime is entered when $\eta \geq 0.5$; the same threshold is seen with the reference parameter set. When L = 120 m is used rather than the reference-parameter-set value (L = 60 m), non-seismic stick-slip behavior is not observed. For $0 \leq \eta \leq 0.1$, the stable-slip regime is observed. Above $\eta = 0.15$, the partial-seismic regime is observed. The entire-stick regime again appears when $\eta \geq 0.50$. When only the value of a in the VSZ is changed to 0.0015 from the reference-parameter-set value of 0.002, the partial-seismic regime is not observed. The stable-slip regime is observed when $\eta \leq 0.20$, as also seen for simulations using the reference parameter set. The onset of the entire-stick regime shifts to $\eta = 0.35$ in this case; non-seismic stick-slip behavior is observed between those two regimes.

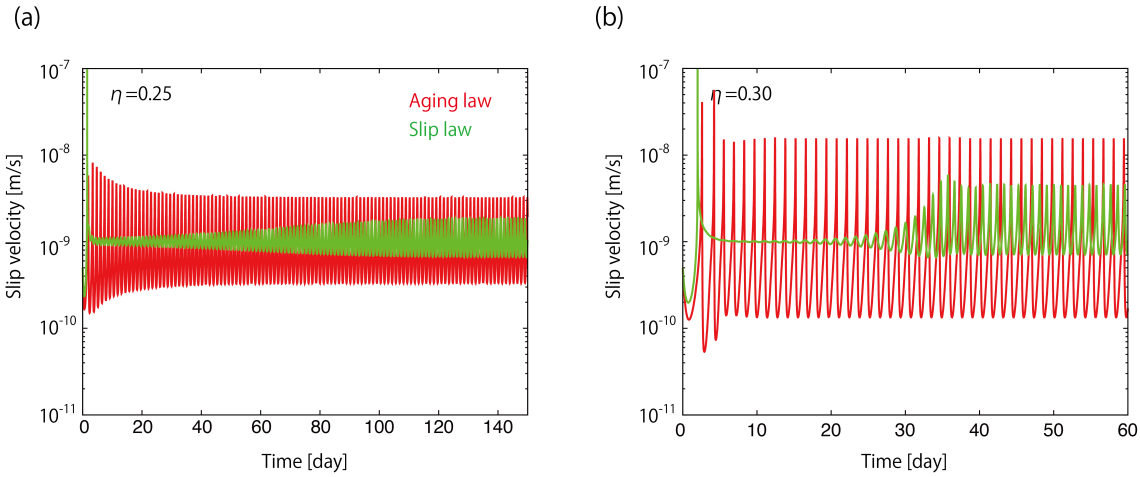

Figure 3.3: Comparison of slip velocity between the aging law and the slip law in the non-seismic stick regime. (a) A red and green line show slip velocity at the center of VWZ for the aging law and the slip law, in the case of η = 0.25 and a = 0.0015 in VSZ. (b) Same as (a), but for η = 0.30.

In addition to the aging law, we also investigate simulations using the slip law as the state-variable evolution law. When the slip law is used with the reference parameter set, we observe very similar results to those obtained with the aging law, except that non-seismic stick-slip behavior is not observed. Using the slip law while

changing the value of a in the VSZ to 0.0015, we observe the same behavior as seen with the aging law. However, the maximum slip velocity of the VWZ in the non-seismic stick-slip regime is several times higher with the aging law than with the slip law (Figure 3.3).

The transitions between these four regimes can be understood from an analytical viewpoint. The boundary between the stable-slip regime and the stick-slip regime of the VWZ (i.e., the partial-seismic regime) is determined by the nucleation size of the VWZ. When the size of VWZ is smaller than its nucleation size, the entire fault including VWZ stably slips. Its slip velocity is at plate velocity V_{pl} because we set the initial stress condition at $\tau = \tau_0$. When the size of VWZ exceeds its nucleation size, stick-slip behavior is initiated. The nucleation of the frictionally homogeneous VW fault is controlled by the quantities $a - b$ and a/b (Rubin and Ampuero, 2005; Ampuero and Rubin, 2008). Rubin and Ampuero (2005) noted that in the case of the aging law, the weakening effect (the second term on the right-hand side of Equation (3.11)) is much larger than unity until the fault reaches instability when $a/b < 0.3781$. In this case, the nucleation size in the VWZ is $L_{cr} \sim 2.7L_b$, though the minimum nucleation size can be smaller than this value (Figure 8 of Rubin and Ampuero, (2005)). For a/b larger than about 0.5, the weakening effect approaches a constant value of ~1, and the nucleation size in the VWZ is given as

$$L_{cr} = \frac{2}{\pi}\left(\frac{b}{b-a}\right)^2 L_b \,. \quad (3.15)$$

In the case of the slip law, Ampuero and Rubin (2008) noted that the nucleation size is smaller than that of the aging law and continues to shrink with increasing slip velocity when the weakening effect is much larger than unity, until the fault reaches stability. When the weakening effect is close to 1 during nucleation, the nucleation zone propagates as a pulse. Rubin (2008) and Mitsui and Hirahara (2011) reported that in the case of the aging law, stick slip reaches seismic slip velocity when the patch size is much larger than its nucleation size, but does not reach seismic slip velocity when the patch size is close to its nucleation size. However, in the case of the slip law, stick slip almost always achieves seismic slip velocity when the patch size is larger than its nucleation size.

For the simulation runs using the reference parameter set with the aging law, $a/b = 0.5$ and the weakening effect at the center of the nucleation zone is about 10

(Figure 3.4), similar to figure 1d of Rubin and Ampuero (2005). In this case, L_{cr} = 12.7 m, corresponding to $\eta_{cr} \approx 0.21$. From Figure 3.2e, we see that the stable-slip regime ends at η = 0.2 (i.e., a VWZ size of 12 m), and stick slip appears in the VWZ above this value, although the non-seismic stick-slip regime exists when η = 0.25 (i.e., a VWZ size of 15 m). When a/b is changed to a value of 0.3, the weakening effect at the center of the nucleation zone is about 200 during nucleation period, that is, much larger than unity (Figure 3.4b), in which case typical nucleation size is $L_{cr} \sim 2.7L_b$ (13.5 m), corresponding to $\eta_{cr} \approx 0.23$, though minimum nucleation size is smaller than that value (Rubin and Ampuero, 2005). From Figure 3.2e, the non-seismic stick-slip regime is observed at η = 0.15 (i.e., a VWZ size of 9 m), and the partial seismic regime is initiated from η = 0.2 (i.e., a VWZ size of 12 m).

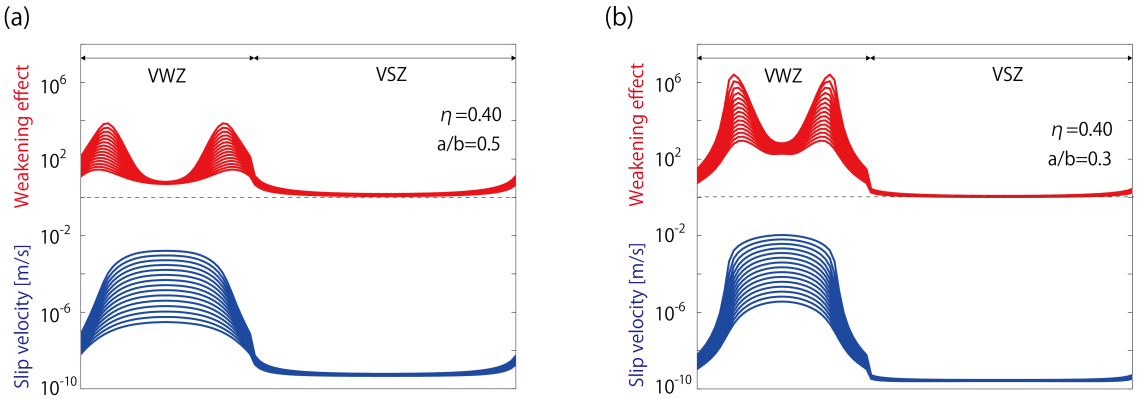

Figure 3.4: Snapshots of slip velocity and the weakening effect during nucleation in VWZ. (a) Snapshots of slip velocity (blue) and weakening effect (red; see the text for the definition) for the partial seismic regime (η = 0.40) during the nucleation of seismic events, calculated with a reference parameter set (Table 3.1). (b) Same as (a), but for the case calculated with a/b = 0.3.

When L is doubled from the reference-parameter-set value, the value of L_{cr} is unchanged at L_{cr} = 12.7 m, corresponding to $\eta_{cr} \approx 0.11$. In our numerical simulations, the stable-slip regime is observed up to η = 0.10 (i.e., a VWZ size of 12 m) and the partial-seismic regime is observed above η = 0.15 (i.e., a VWZ size of 18 m). In this case, the non-seismic stick-slip regime falls between η = 0.10 and 0.15, and, as is apparent from Figure 3.2e, is not encountered because of the 0.05 increment in η used in our parameter study.

When a in the VSZ is changed to 0.0015, L_{cr} again does not change ($\eta_{cr} \approx 0.21$). The non-seismic stick-slip regime starts at $\eta = 0.25$ (i.e., a VWZ size of 15 m), which is consistent with the results obtained with the reference parameter set. In this case, the transition to the entire-stick regime shifts to lower η–values, and the non-seismic stick-slip regime extends up to η = 0.30 (i.e., a VWZ size of 18 m). The boundary of the entire-stick regime is discussed further below.

When the slip law is used with the reference parameter set, although the nucleation size of the VWZ changes with slip velocity (Ampuero and Rubin, 2008), the boundary between the stable-slip regime and the partial-seismic regime is the same as for the aging-law case, and the non-seismic stick-slip regime is not observed, as reported by Rubin (2008) and Mitsui and Hirahara (2011). When a in the VSZ is changed to 0.0015 with the slip law, the same results are obtained as for the aging law. Because the boundary of the entire-stick regime is closer to the nucleation size in this case, the non-seismic stick-slip regime occurs even with the slip law.

Next, we consider the boundary between the partial-seismic regime and the entire-stick regime. An analytical solution for this boundary can be obtained for the aging-law case as follows. Neglecting the radiation-damping term in Equation (3.13), the acceleration of the fault during the inter-seismic period is

$$a_i \sigma \frac{\dot{V}_i}{V_i} \cong \sum_j K_{ij} V_j - b_i \sigma \frac{\dot{\theta}_i}{\theta_i} . \qquad (3.16)$$

In this system, elastic deformation due to faster creep in the VSZ than in the VWZ accelerates the VWZ, while an increase of the state variable decelerates the fault. During inter-seismic periods, the state variable in the VWZ evolves linearly with time because weakening effect in Equation (3.11) is much smaller than 1 (Rubin and Ampuero, 2005). Hence, we can assume,

$$\frac{\dot{\theta}_i}{\theta_i} = \frac{1}{t + t_c} , \qquad (3.17)$$

where t_c is a constant. Considering the functional form of the slip velocity

$$V_i = \frac{A_i}{t + t_c} , \qquad (3.18)$$

where A_i is the slip-velocity shape function, the time dependency of Equation (3.16) can be removed by substituting Equations (3.17) and (3.18) into Equation (3.16) to obtain

$$\sum_j K_{ij} A_j = \left(-a_i + b_i\right)\sigma \qquad (3.19)$$

for i taking values from 1 to N. Taking the average of Equation (3.19) with respect to i yield

$$\frac{1}{N}\sum_{i,j} K_{ij} A_j = \frac{1}{N}\sum_i \left(-a_i + b_i\right)\sigma \qquad (3.20)$$

.

Because the left-hand side of Equation (3.20) is zero, as $\sum_j K_{ij} = 0$, a solution for the shape function A_i exists only when $\frac{1}{N}\sum_i a_i - b_i = 0$. Hence, we can obtain the synthetic shape function A_i when the spatial average of $a - b$ ($\frac{1}{N}\sum_i a_i - b_i = \eta\left(a-b\right)_{VWZ} + \left(1-\eta\right)\left(a-b\right)_{VSZ}$) is zero, through a zero-mean constraint on A_i, because the spatial average of A_i is not constrained by Equation (3.16).

Above analytic derivations are validated by the comparison with numerical results. In Figure 3.5a, the time evolution of weakening effect at the center of VWZ and VSZ are plotted. They are temporally constant at values smaller than 1. Hence, state variable increases linearly with time (Figure 3.5b), which ensures the assumption of Equation (3.17). In Figure 3.5c, the time evolution of slip velocity at the center of VWZ and VSZ are shown, which validate that slip velocity falls as t^{-1} when $t>>t_c$ (Equation (3.18)). A synthetic shape function A_i, calculated by inverting Equation (3.19) with a zero-mean constraint on A_i, is compared with the numerical simulation results in Figure 3.5d. In Figure 3.5d, the synthetic shape function A_i is shown by the red line. Snapshots of slip velocity on the fault multiplied by time from the beginning of the calculation and shifted to a zero mean are shown by lines whose color changes from blue to green with time for a simulation with η = 0.5 using the reference parameter set, that is, the spatial average of $a - b$ is zero. Initially, the shape function from the numerical calculation is uniform as a result of the initial condition assumed in the numerical model. The function shape then evolves after the calculation starts and converges to match the synthetic shape function.

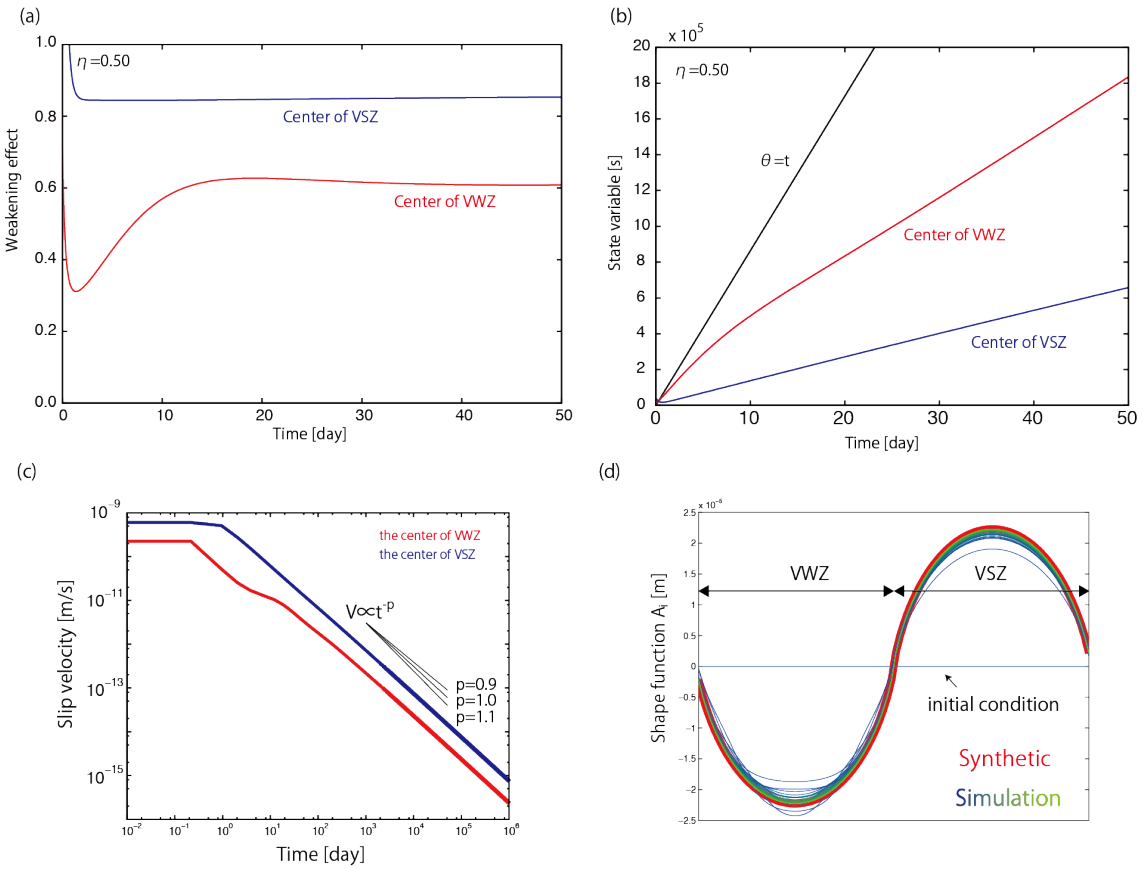

Figure 3.5: Results of numerical simulations at the critical density (η = 0.50) with a reference parameter set (Table 3.1) and the aging law. (a) Time history of weakening effect at the center of VWZ (red) and VSZ (blue). (b) Time history of state variables at the center of VWZ (red) and VSZ (blue). (c) Time history of slip velocity at the center of VWZ (red) and VSZ (blue). Three black lines represents the falloff of slip velocity with time as $V \propto t^{-0.9}$, $V \propto t^{-1.0}$, and $V \propto t^{-1.1}$. (d) A comparison of synthetic shape function with that of numerical simulations. The horizontal axis represents horizontal position along the fault, with the locations of the VWZ and VSZ shown by the black arrows. The synthetic shape function of the slip velocity, defined by Equation (3.18), is shown by the red line; other lines denote snapshots of simulated slip velocity, which are obtained by multiplying by time from the beginning of the numerical calculation and subtracting the average value. Snapshots are plotted for every $10^{0.25}$ times the change in slip velocity averaged over the fault. The change in line color from blue to green indicates increasing time after the start of the simulation run.

The analytical derivation of slip-velocity shape function shows the existence of solutions for slip velocity and state variables that are inversely and positively proportional to time at the critical density of VWZ such that the spatial average of $a-b$ is zero. Using aging law, state variable cannot increase faster than linearly with time. At the critical density, the deceleration speed of slip velocity is inversely proportional to time, which balances with the increasing speed of state variable, resulting in the constant weakening effect at a value smaller than 1 (Figure 3.5a). Because the weakening of the fault (decrease of state variable) never occurs in this case, the nucleation of seismic events never appear. When the spatial average of $a-b$ is not zero, the above solutions cannot exist. If the spatial average of $a-b$ is positive, creep on the wider VSZ causes stress to accumulate on the VWZ more rapidly than for the critical case. As a result, slip velocity decelerates as $V \propto t^{-p}$, where p<1. Hence, weakening effect, which is proportional to the multiplication of slip velocity and state variable, will increase with time, and at last exceeds one (Figure 3.6a), resulting in the initiation of nucleation of seismic events (Figure 3.2c). In contrast, if the spatial average of $a-b$ is negative, creep in the narrower VSZ causes stress to accumulate on the VWZ more slowly than in the critical case. As a result, slip velocity decelerates as $V \propto t^{-p}$, where p>1. In this case, weakening effect keeps decreasing with time (Figure 3.6b). Hence, weakening of the fault and resultant seismic rupture never occurs (Figure 3.2d).

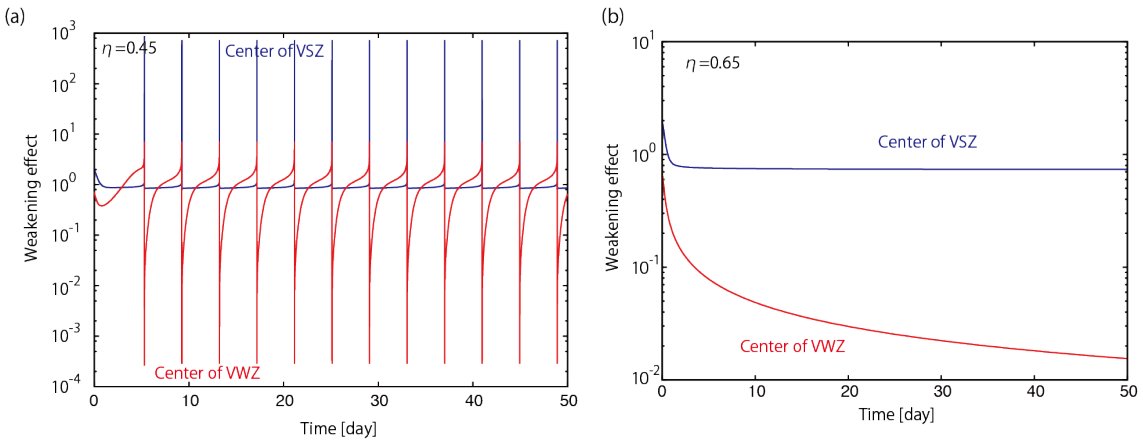

Figure 3.6: Time evolution of weakening effect in (a) partial seismic regime and (b) entire stick regime. Red and blue lines represent the center of VWZ and VSZ, respectively.

We note here that this derivation does not depend on the dimensions of the model. We neglect the radiation-damping term and use $\sum_j K_{ij} = 0$ only because of the infinite fault length assumed for this derivation. Therefore, we obtain a general analytical prediction that it is critical for the spatial average of $a - b$ over the fault to be zero for an infinite fault without an external stress loading to exhibit slip-behavior transition.

The above expressions can explain the location of the boundary between the partial-seismic regime and the entire-stick regime in the numerical simulation results shown in Figure 3.2e. Although the discussion above is valid only for the aging-law case, the results for the slip law are also consistent with these results for the aging law. The complex form of Equation (3.12) precludes the derivation of analytical expressions for the slip law.

In summary, the shear-slip behavior of a heterogeneous fault without an external stress loading is controlled by two boundaries. The location of the first boundary is determined by the nucleation size of the VWZ. Below the density of the first boundary, stable-slip behavior is observed, whereas seismic slip and afterslip are respectively observed in the VWZ and VSZ above the density of this first boundary. Around the density of the first boundary, non-seismic stick-slip is observed in some cases. The second boundary is located at the density where the spatial average of $a - b$ on the fault becomes zero. Above the density of the second boundary, the entire fault (including the VSZ) sticks, and seismic rupture never occurs.

3.3.2. With an external stress accumulation ($k_0 > 0$)

In this section, we investigate the shear-slip behavior of a heterogeneous fault with a bimodal distribution of frictional parameters when k_0 is positive, by changing η in increments of 0.05 in the range 0 to 1, inclusive. When an external stress accumulation exists, stick-slip events will always occur unless the size of the VWZ is smaller than its nucleation size. We observed five types of slip behavior in these numerical experiments: (i) the stable-slip regime; (ii) the non-seismic stick-slip regime; (iii) the partial-seismic regime where stick-slip events and afterslip occur in the VWZ and VSZ, respectively; (iv) transitional behavior between the partial-seismic regime and the entire-seismic regime; and (v) the entire-seismic regime where seismic slip occurs in

both the VWZ and the VSZ.

To characterize the slip behavior of the fault, we calculated the radiation energy consumed by the radiation-damping term of Equation (3.1)

$$E_R^i = \Delta x \int \frac{\mu}{2\beta} V_i \, du_i \,, \qquad (3.21)$$

where E^i_R is the radiation energy on the *i*-th sub-fault and Δx is the length of grid discretization. This value is related to the characteristic deformation rate given by

$$\bar{V}_i = \frac{\int V_i \, du_i}{\int du_i} \,, \qquad (3.22)$$

as

$$\bar{V}_i = \frac{2\beta E_R^i}{\Delta x \mu \int du_i} \approx \frac{2\beta}{\Delta x \mu V_{pl}} \frac{E_R^i}{T} \,, \quad (3.23)$$

where T is the duration of long-term calculation. At each time step, we average the calculated radiation energy over the VWZ and VSZ as

$$E_R^{VWZ} = \frac{\sum_{i \in VWZ} E_R^i}{L\eta} \,, \qquad (3.24)$$

and

$$E_R^{VSZ} = \frac{\sum_{i \in VSZ} E_R^i}{L(1-\eta)} \,. \qquad (3.25)$$

Then we estimate the long-term average radiation-energy rate $\overline{\dot{E}_R^j}$ (j=VWZ or VSZ; Figure 3.7). The long-term average radiation-energy rate is proportional to the characteristic deformation rate averaged in VWZ or VSZ as

$$\bar{V}^j \equiv \frac{\sum_{i \in j} \bar{V}_i}{N^j} = \frac{2\beta}{\mu \int du_i} \frac{\sum_{i \in j} E_R^i}{\Delta x N^j} \approx \frac{2\beta}{\mu V_{pl}} \bar{\dot{E}}_R^j \,, \qquad (3.26)$$

where N^j is the number of grids in VWZ or VSZ. Consequently, the long-term average radiation-energy rate can be a measure of the rapidity of deformation. By fitting a linear function to the temporal evolution of the calculated energy averaged over the VWZ and VSZ, the long-term spatially averaged energy rate for both the VWZ and VSZ can be evaluated as a slope of cumulative frictional energy (Figure 3.7). To avoid artifacts

arising from transient slip episodes at the beginning of the calculation, the linear fit is applied to the second half of the modeled time period.

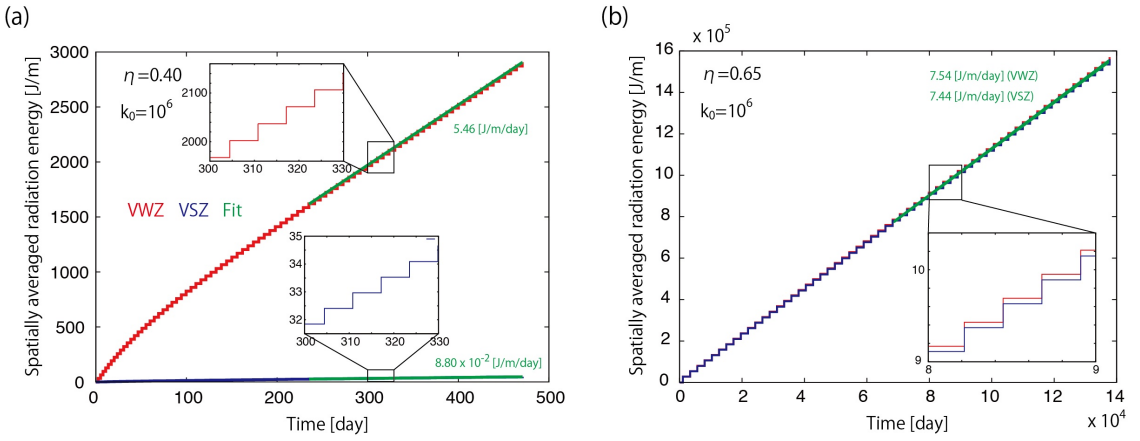

Figure 3.7: Time evolution of calculated radiation energy. (a) Radiation energy, calculated for η = 0.4 and k_0 = 10^6 using the reference parameter set and aging law, plotted against time. The radiation energies averaged over the VWZ and VSZ are shown by the red and blue lines, respectively. The green lines denote the least-squares fit to the radiation energy in the second half of the calculation period; the slopes of these regression lines give the long-term average radiation-energy rate. Green values are estimated radiation energy rate. (b) As for (a), except with η = 0.65.

Figure 3.8 shows estimated long-term radiation-energy rates in the VWZ and VSZ for k_0 = 10^6 Pa/m, computed using the reference parameter set and the aging law for different densities of VWZ (i.e., η values) for the heterogeneous fault. The recurrence intervals of seismic events are also plotted in Figure 3.8. We define the start time of each seismic cycle as the moment when the slip velocity of any sub-fault exceeds the plate velocity; the recurrence interval is then the measured time interval between two such occurrences.

When η is low (i.e., $0 \leq \eta \leq 0.2$), radiation-energy rates in the VWZ and VSZ are identical and quite low; this behavior represents the stable-slip regime (i). At η = 0.25, the radiation-energy rate is increasing, but is still very low, representing the behavior of the non-seismic stick-slip regime (ii). The location of this regime is consistent with the results seen in the k_0 = 0 case, because this boundary is controlled by the nucleation size of the VWZ. For $0.3 \leq \eta \leq 0.45$, the radiation-energy rate in the

VWZ is 2–3 orders of magnitude higher than that seen in the VSZ, representing partial seismic-slip behavior (iii), whereby seismic events occur in the VWZ and afterslip occurs in the VSZ. Example time histories of slip velocities for simulations in these regimes are shown in Figure 3.9. Snapshots of slip velocity in the partial-seismic regime are also shown in Figure 3.10.

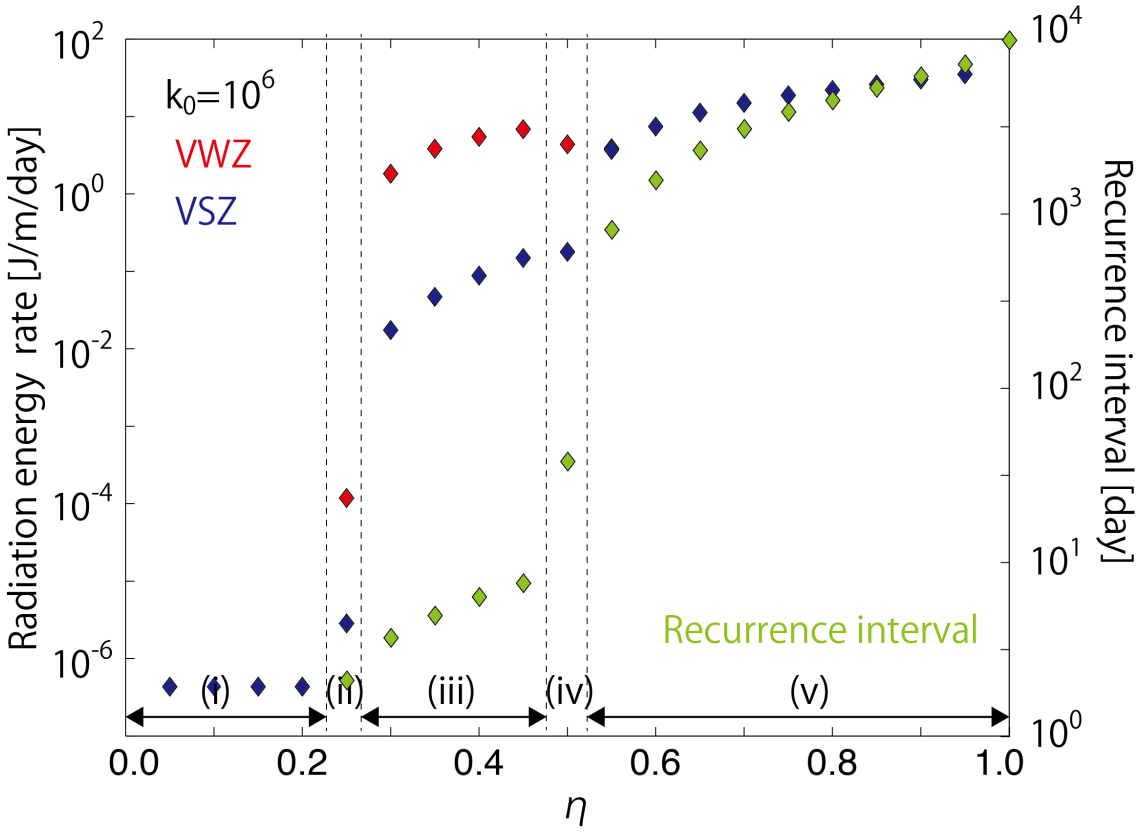

Figure 3.8: Radiation-energy rate and recurrence interval plotted against the density of velocity-weakening zone on the fault η. The radiation-energy rates in the VWZ and VSZ (left axis), calculated for $k_0 = 10^6$ using the reference parameter set and aging law, are shown by the red and blue symbols, respectively. Green symbols represent recurrence intervals of seismic events (right axis). The boundaries between, and extents of, the slip regimes are respectively indicated by the dashed lines and arrows: (i) the stable-slip regime; (ii) the non-seismic stick-slip regime; (iii) the partial-seismic regime; (iv) the transitional-slip regime; and (v) the entire-seismic regime.

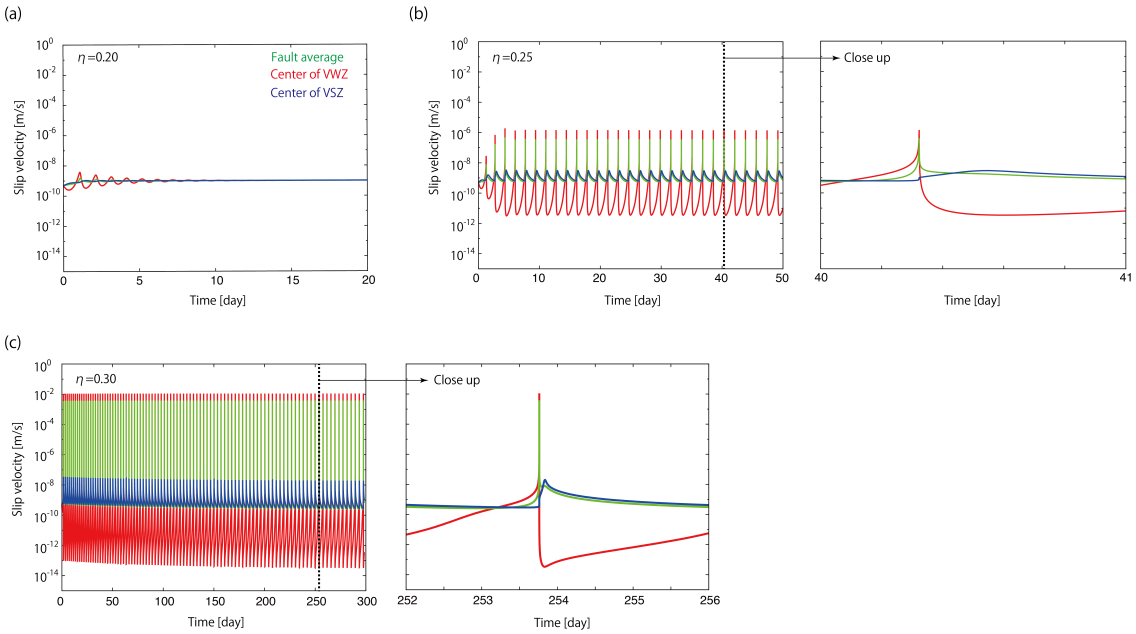

Figure 3.9: Examples of shear-slip behavior with $k_0 = 10^6$. (a) Time evolution of slip velocity for the case $\eta = 0.20$ calculated using the reference parameter set (Table 1) and aging law. Slip velocity averaged over the entire fault is shown by the green line. Slip velocities at the center of the velocity-weakening zone (VWZ) and velocity-strengthening zone (VSZ) are shown by the red and blue lines, respectively. This figure represents a typical example of the stable-slip regime. (b) As for (a), but with $\eta = 0.25$. This figure represents a typical example of the non-seismic stick-slip regime. The right-hand panel of this figure shows a close-up of view of the seismic event indicated by the dashed line in the left-hand panel. (c) As for (b), except with $\eta = 0.3$. This figure represents a typical example of the partial-seismic regime. The right-hand panel of the figure shows a close-up view of the seismic event indicated by the dashed line in the left-hand panel.

Radiation energy emitted in the VSZ is comparable to that in the VWZ when $\eta \geq 0.55$, that is, the VSZ also slips at seismic velocities during seismic events (Figure 3.11). We refer to this the "entire-seismic regime" (v). In this regime, seismic rupture initiates in the VWZ and propagates into the VSZ. The VSZ is then accelerated to seismic velocities soon after rupture of the VWZ, and the entire fault slips seismically.

At $\eta = 0.50$, where the transition occurs from the partial-seismic regime to the entire-stick regime in the $k_0 = 0$ case, the fault shows very complex behavior (Figure 3.12), in which seismic slip in the VWZ and aseismic slip in the VSZ strongly interact.

Seismic rupture initiates in the VWZ and propagates into the VSZ. Slip in the VSZ accelerates, but it does not slip seismically with the VWZ as seen in the entire-seismic regime. Accelerated slip of the VSZ propagates into the VWZ, and so the VWZ is reaccelerated soon after the first rupture. Rupture propagates back and forth between the VWZ and VSZ several times.

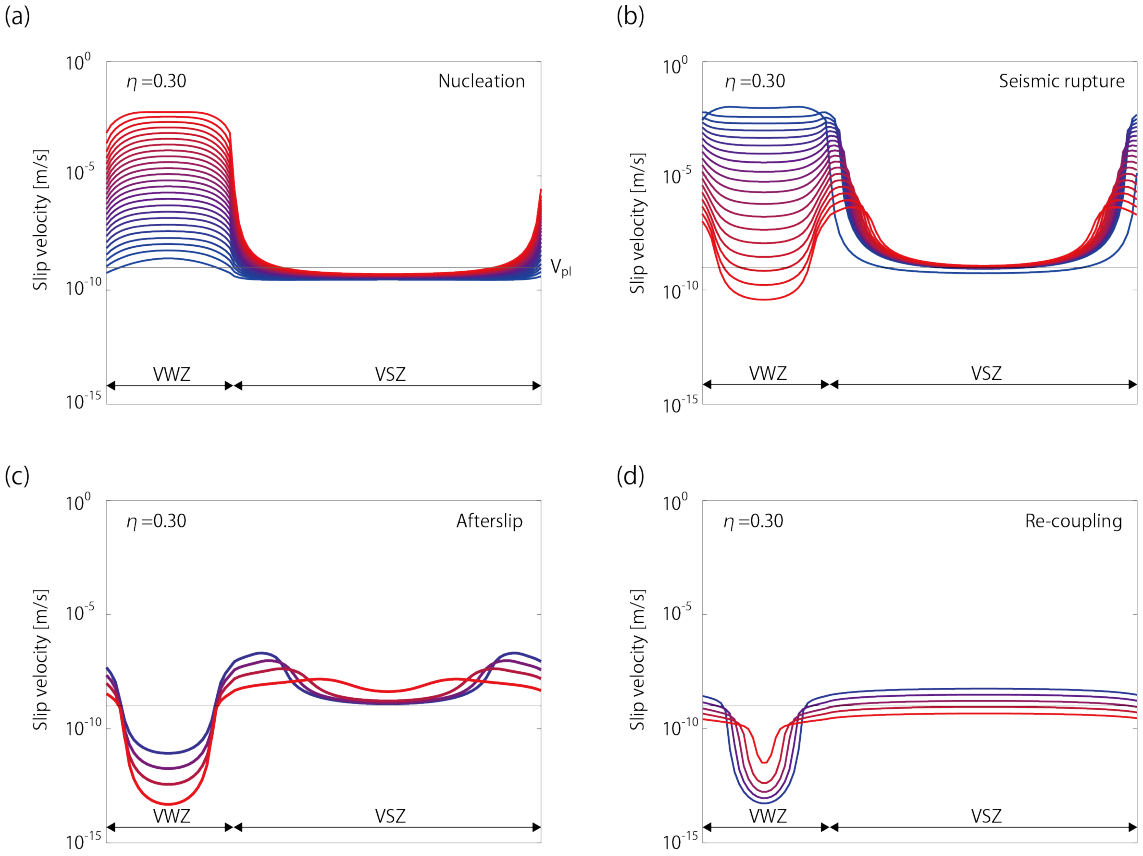

Figure 3.10: Snapshots of slip velocity in the case of the partial seismic regime ($\eta = 0.30$), calculated with a reference parameter set (Table 1) and with the aging law. The locations of VWZ and VSZ are shown by black arrows. (a) Nucleation of seismic events in VWZ. (b) Rupture propagation into VSZ. (c) Afterslip in VSZ. (d) Re-coupling of the fault. Snapshots are plotted for every $10^{0.25}$ times the change in slip velocity averaged over the fault. The change in line color from blue to red indicates increasing time in each panel.

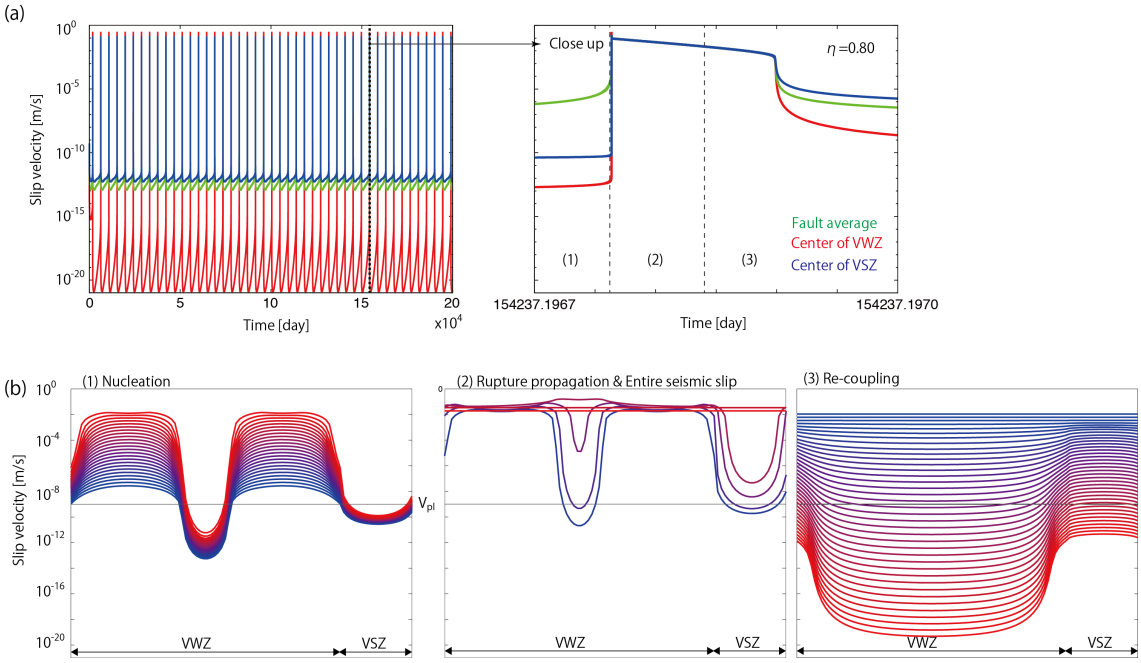

Figure 3.11: An example of shear-slip behavior with $k_0 = 10^6$ in the entire-seismic regime. (a) Time evolution of slip velocity in the case $\eta = 0.8$, calculated using the reference parameter set (Table 3.1) and aging law. Colors and lines have the same meanings as for Figure 3.9a. Because the peak velocities in both the VWZ and VSZ reach seismic slip velocity (i.e., 6×10^{-3} m/s; see main text for definition), this figure represents a typical example of the entire-seismic regime. The right-hand panel of this figure shows a close-up view of the seismic event indicated by the dashed line in the left-hand panel. Periods denoted by (1), (2), and (3) are corresponding to durations of snapshots in (b). (b) Snapshots of slip velocity during the seismic events presented in (a). The locations of the VWZ and VSZ are shown by the black arrows; the black horizontal line denotes the plate velocity. The left-hand panel shows the nucleation of seismic events in the VWZ. The middle panel shows the rupture propagation into the VSZ and seismic slip on the entire fault. The right-hand panel shows the re-coupling of the fault. Snapshots are plotted for every $10^{0.25}$ times the change in slip velocity averaged over the fault. The change in line color from blue to red indicates increasing time in each panel.

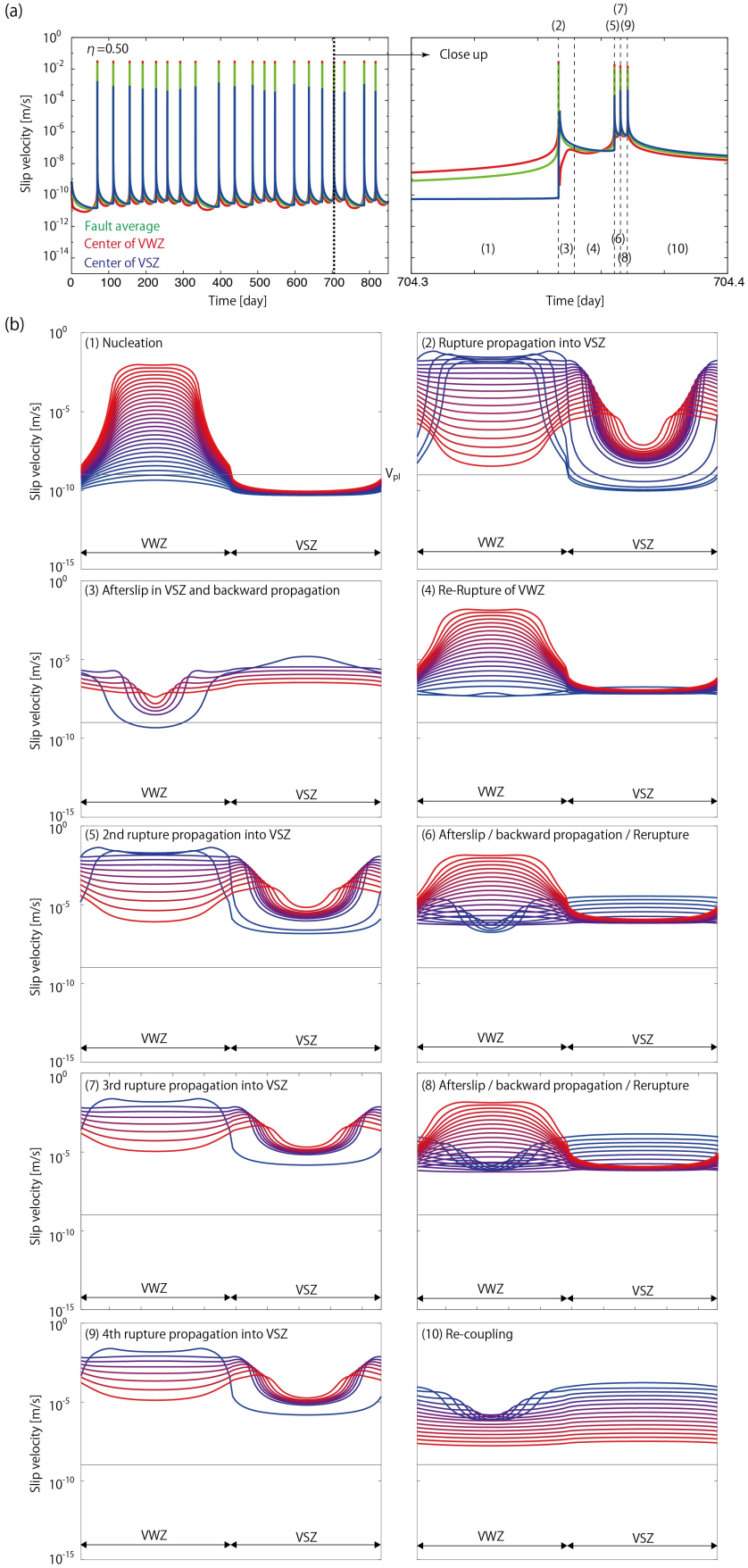
(a)
η=0.50
Close up
Slip velocity [m/s]
Time [day]
Fault average
Center of VWZ
Center of VSZ
(1)
(2)
(3)
(4)
(5)
(6)
(7)
(8)
(9)
(10)
704.3
704.4
(b)
(1) Nucleation
(2) Rupture propagation into VSZ
(3) Afterslip in VSZ and backward propagation
(4) Re-Rupture of VWZ
(5) 2nd rupture propagation into VSZ
(6) Afterslip / backward propagation / Rerupture
(7) 3rd rupture propagation into VSZ
(8) Afterslip / backward propagation / Rerupture
(9) 4th rupture propagation into VSZ
(10) Re-coupling
VWZ
VSZ
Slip velocity [m/s]

Figure 3.12 (previous page): Example of shear-slip behavior with $k_0 = 10^6$ in the transitional-slip regime. (a) Time evolution of slip velocity for the case $\eta = 0.5$, calculated using the reference parameter set (Table 3.1) and aging law. Colors and lines have the same meanings as for Figure 3.9a. The right-hand panel of this figure shows a close-up view of the seismic event indicated by the dashed line in the left-hand panel. Because seismic slip is induced several times during one event by the strong and complex interaction between slip in the VWZ and VSZ, this figure represents a typical example of the transitional-slip regime that separates the partial- and entire-seismic regimes. Periods denoted by (1)-(10) are corresponding to durations of snapshots in (b). (b) Snapshots of slip velocity during the seismic events seen in (a). Colors and lines have the same meanings as for Fig. 3.11b.

To investigate the details of the slip-behavior transition from the partial-seismic regime to the entire-seismic regime, we conducted numerical simulations using a finer grid discretization $\Delta x = L_b / 32$ around the critical density, changing η in increments of 0.0026 for $0.49 \leq \eta \leq 0.51$. In addition, to investigate the dependency of slip behavior on stiffness, we tested three values of stiffness: $k_0 = 10^5$, 10^6, and 10^7 (corresponding to W = 300, 30, and 3 km). In Figure 3.13, the radiation-energy rate and recurrence intervals are plotted against η for these stiffness values.

In the partial-seismic regime, recurrence intervals have similar values regardless of the value of k_0. Recurrence intervals of seismic events are determined by the balance between stress accumulation and fault strengthening (increase of state variable) in VWZ. As discussed in previous section, the stress accumulation in the VWZ is controlled mainly by creep in the VSZ in the partial seismic regime. Although the external stress loading term also accumulate stress on VWZ, its effect is small compared with stress by elastic deformation because characteristic stiffness of this system defined by $\mu / L \approx 5 \times 10^8$ is much larger than k_0 used in this study. Hence, recurrence intervals in the partial seismic regime have similar values regardless of k_0. In contrast, in the entire-seismic regime, recurrence intervals are strongly dependent on stiffness k_0, because external stress loading is the main cause of stress accumulation on the VWZ in this regime. Around the critical density (η=0.5), the recurrence intervals increase markedly, corresponding to the phase transition from the partial-seismic regime

to the entire-seismic regime, though the phase transition is less sharp for larger stiffness values. The radiation-energy rate of the VWZ significantly decreases at the critical density whereas that of the VSZ increases, until they eventually converge. Because the long-term average radiation-energy rate is proportional to the characteristic deformation rate, moderate values of the long-term average energy rate in both VWZ and VSZ around the critical density means that slower deformation relatively dominates around the critical density. However, this transition is also less sharp at larger stiffness values. Larger stiffness k_0 results in larger stress drop with slip. Therefore, complex interactions between seismic slip in VWZ and aseismic slip in VSZ are stabilized by increasing stiffness (Figure 3.14).

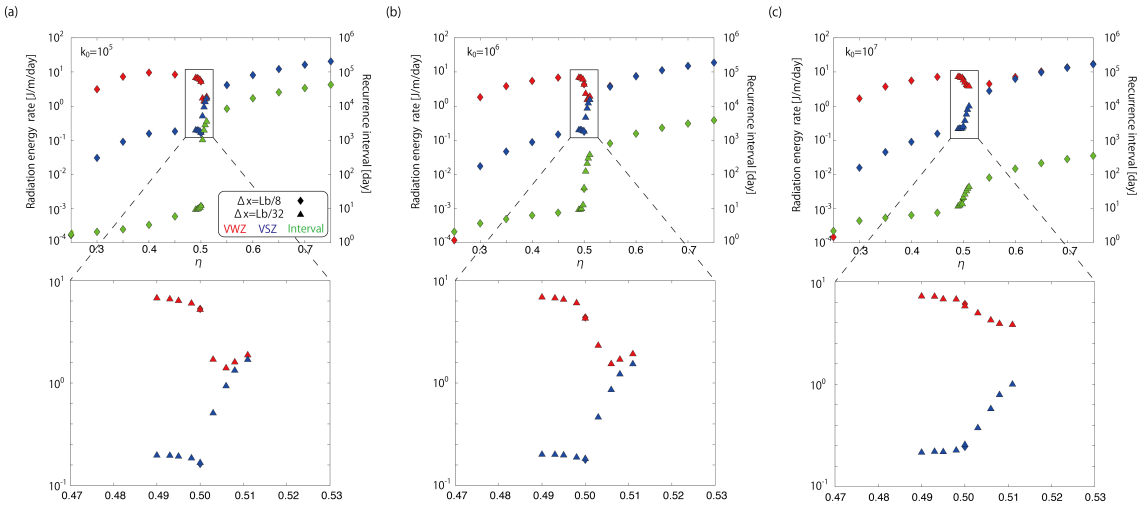

Figure 3.13: Comparisons of radiation-energy rate and recurrence intervals for different stiffness values, plotted against the density of velocity-weakening zone on the fault η. (a) Results for $k_0 = 10^5$ calculated using the reference parameter set (Table 3.1) and aging law. Results for $\Delta x = L_b/8$ and $\Delta x = L_b/32$ are indicated by the diamonds and triangles, respectively. Radiation-energy rates averaged over the VWZ and VSZ are shown by the red and blue symbols, respectively, with values given on the left axis; green symbols show recurrence intervals of seismic events, and correspond to the right axis. The bottom panel shows a close-up view of the rectangular region outlined in the top figure. (b) As for (a), except with $k_0 = 10^6$. (c) As for (a), except with $k_0 = 10^7$.

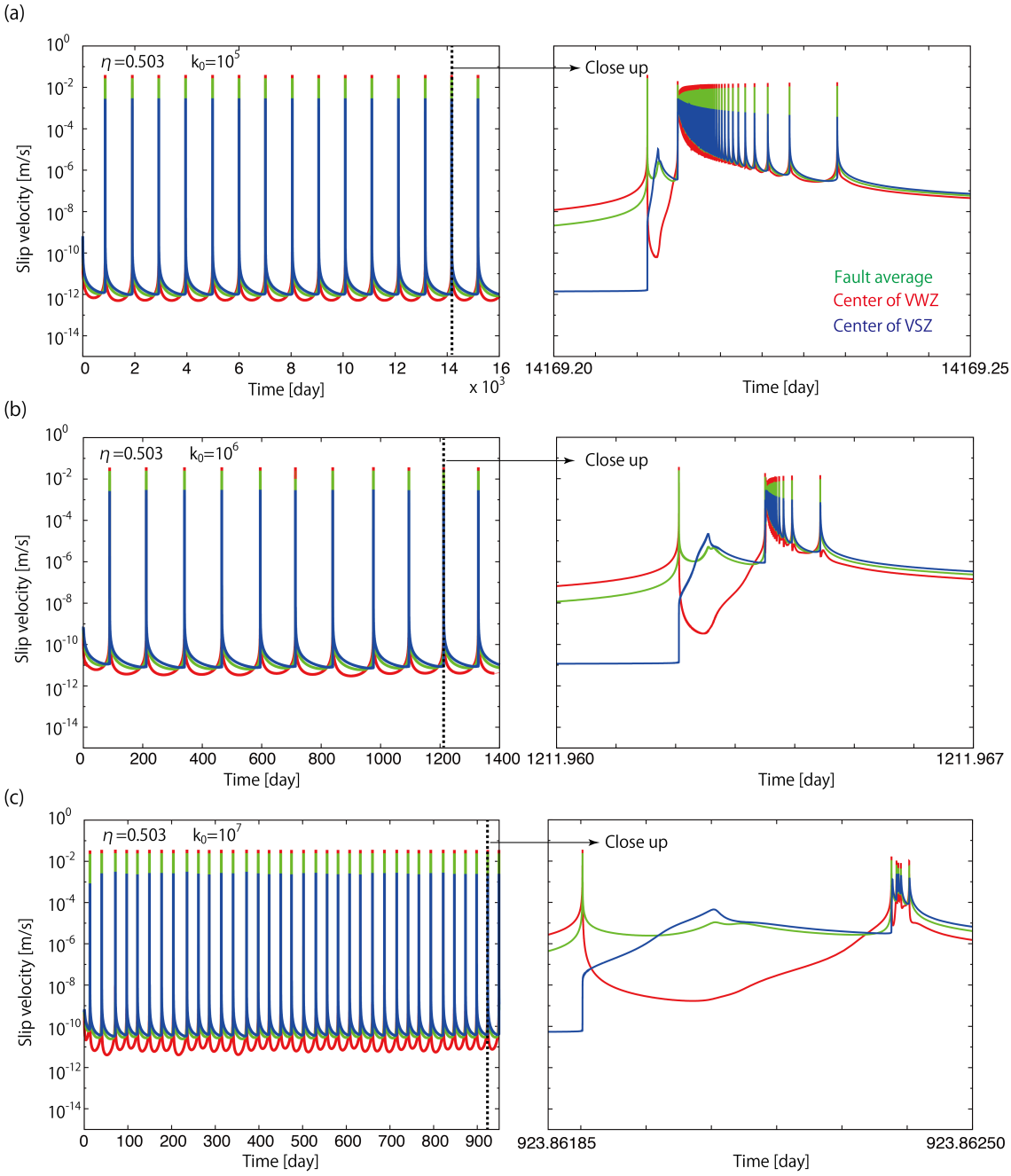

Figure 3.14: Time evolutions of slip velocity for different stiffness in the transitional slip regime. (a) A red and blue line show time evolutions of slip velocity at the center of VWZ and VSZ, respectively, calculated with the length of sub-faults $\Delta x=L_b/32$, $k_0=10^5$, and $\eta = 0.503$ using a reference parameter set (Table 3.1) and the aging law. A green line shows the time evolution of slip velocity averaged over the fault. The left figure is a close up of one seismic event denoted by a black line in the left figure. (b) Same as (a), but for $k_0=10^6$. (c) Same as (a), but for $k_0=10^7$.

Figure 3.15a shows the radiation-energy rate and recurrence intervals of seismic events as a function of η when the a value of the VSZ is changed to 0.0015 from the reference value of 0.002, calculated using the aging law. Numerical simulations with $\Delta x = L_b / 8$ show that the stable-slip regime occurs up to η = 0.20, as for the case of k_0 = 0. The non-seismic stick-slip regime occurs at $0.25 \leq \eta \leq 0.3$. Above η = 0.35, where the entire-stick slip regime exists in the k_0 = 0 case, the entire-seismic regime appears. In this case, the critical density is predicted from the analytical solution with k_0=0 to be at η = 1/3. Numerical simulations with $\Delta x = L_b / 32$, in which η is varied from 0.323 to 0.344, show that large releases of radiation energy commence at η = 0.333. Complex transitional slip behavior is observed around the critical density (Figure 3.16).

When the slip law is used with the reference parameter set instead of the aging law, the non-seismic stick-slip regime is not encountered and hence only four types of shear-slip behavior are observed (Figure 3.15b). The existence of transitional-slip behavior is also confirmed for the slip law via simulation runs around the critical density (Figure 3.17). Hence, transitional shear-slip behavior, in which slip in the VWZ and VSZ interact strongly and slower deformation dominates, is widely observed under the condition that the spatially averaged value of $a - b$ is near zero, regardless of the chosen evolution law of the state variable.

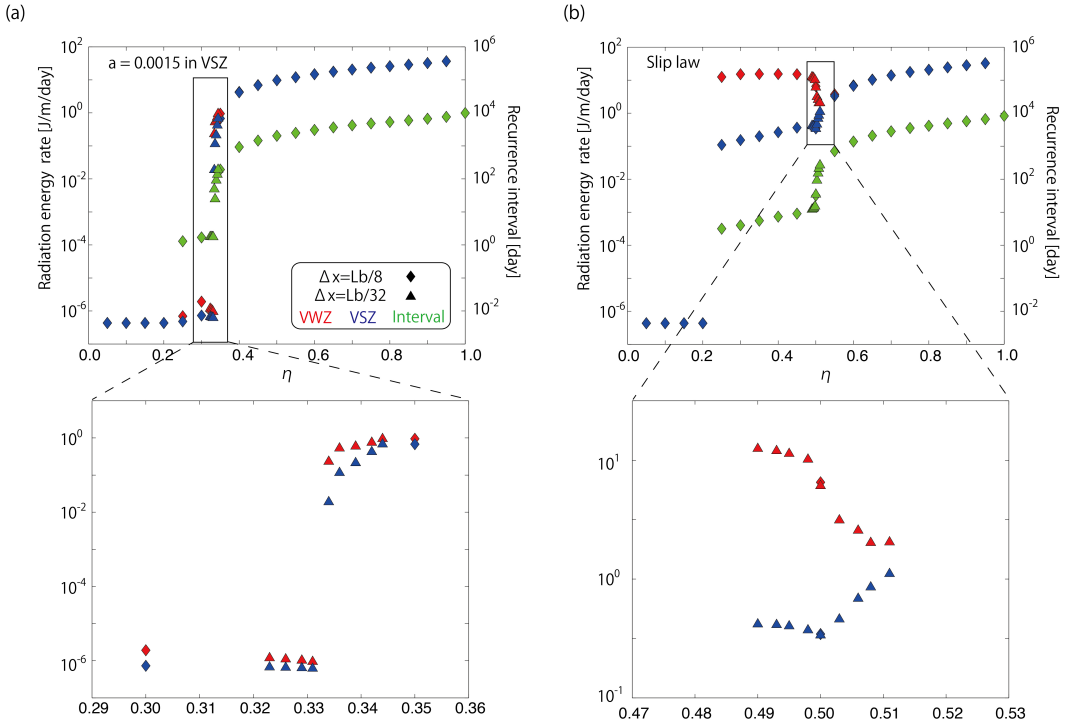

Figure 3.15: Radiation-energy rate and recurrence interval plotted against the density of velocity-weakening zone on the fault η. (a) As for Figure 3.13b, except for the case when a in the VSZ is changed to 0.0015 from the reference-parameter-set value of 0.002 (Table 3.1). (b) As for Figure 3.13b, except for the case when the slip law is used instead of the aging law.

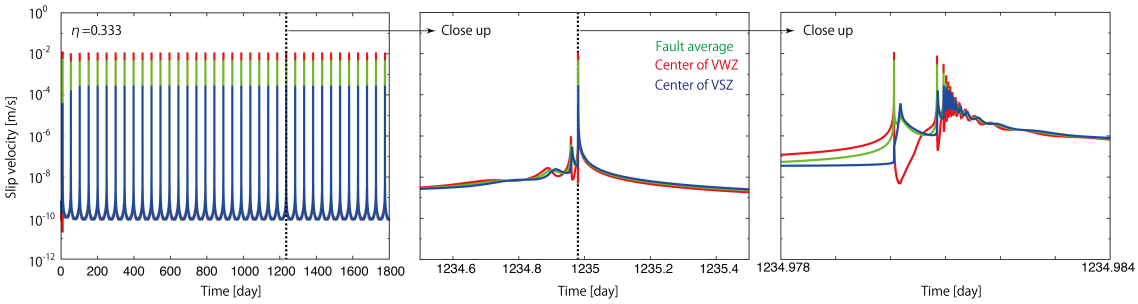

Figure 3.16: Time evolutions of slip velocity in the transitional slip regime for the case where a value in VSZ is changed to 0.0015 from 0.002 in a reference parameter set (Table 3.1) with the aging law. A red and blue line show time evolutions of slip velocity at the center of VWZ and VSZ, respectively, calculated with the length of sub-faults $\Delta x=L_b/32$, $k_0=10^6$, and $\eta = 0.503$. A green line shows the time evolution of slip velocity averaged over the fault. The right and middle panels are a close up of one seismic event denoted by a black dash line in the middle and left figure, respectively.

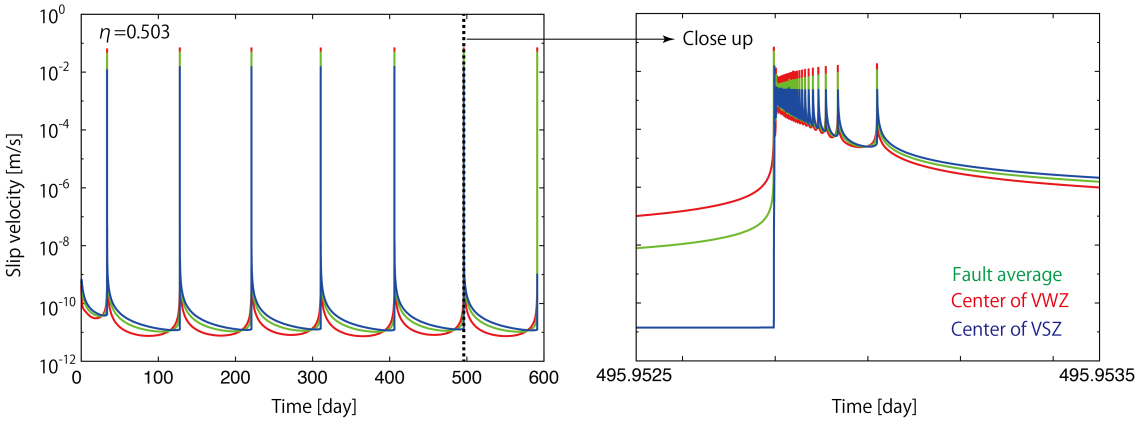

Figure 3.17: Time evolutions of slip velocity in the transitional slip regime for the case where the slip law is used instead of the aging law. A red and blue line show time evolutions of slip velocity at the center of VWZ and VSZ, respectively, calculated with the length of sub-faults $\Delta x=L_b/32$, $k_0=10^6$, and $\eta = 0.503$. A green line shows the time evolution of slip velocity averaged over the fault. The right figure is a close up of one seismic event denoted by a black line in the left figure.

3.3.3. Cantor-set distributions

In this section, we present some examples of slip behavior observed on faults with more complex heterogeneity. Here, we consider an infinite fault with cyclic Cantor-set distributions of frictional parameters (Figure 3.18). This type of frictional heterogeneity is constructed as follows. First, a basic unit of the frictional-parameter distribution is prepared, in which the VSZ is flanked by VWZs each of 20 grids (12.5 m length). The length of the central VSZ is set as a fraction 1-γ of the total length L_0. Higher-rank heterogeneities are constructed by sandwiching a VSZ between two lower-rank heterogeneities. The length of the central VSZ is also set as a fraction 1-γ of the new heterogeneity. The recurrence distance L_n of the frictional parameters becomes longer with increasing rank (see Table 3.2), as $L_n = \left(\frac{2}{\gamma}\right)^n L_0$, where n is the rank. Total length of VWZ within a recurrence unit also increases with increasing the rank as $L_n^{VWZ} = 2^n \gamma L_0$. Hence, the portion of the VWZ on the fault changes with increasing rank as $\eta = \gamma^{n+1}$. Therefore, the Cantor-set distribution of frictional parameters is characterized by two parameters: γ and the rank. To investigate the dependence of the slip behavior of a hierarchical heterogeneous fault on these parameters, we ran simulations using γ = 0.80, 0.85, and 0.90 for models using the aging law and the slip

law while varying rank from zero to three. The frictional parameters were set at (a, b) = (0.0006, 0.002) in the VWZ and (0.0007, 0.0006) in the VSZ so that all model runs show behavior in the entire-seismic regime. The length of each VWZ (i.e., 12.5 m) is enough long to initiate seismic event (Section 3.3.1, 3.3.2). The stiffness is set at k_0 = 10^6. The other parameter values used for the simulations are taken from the reference parameter set (Table 3.1). For comparison, we also calculate bimodal distributions of frictional parameters with the same density and recurrence distance as the Cantor-set distributions (Table 3.2).

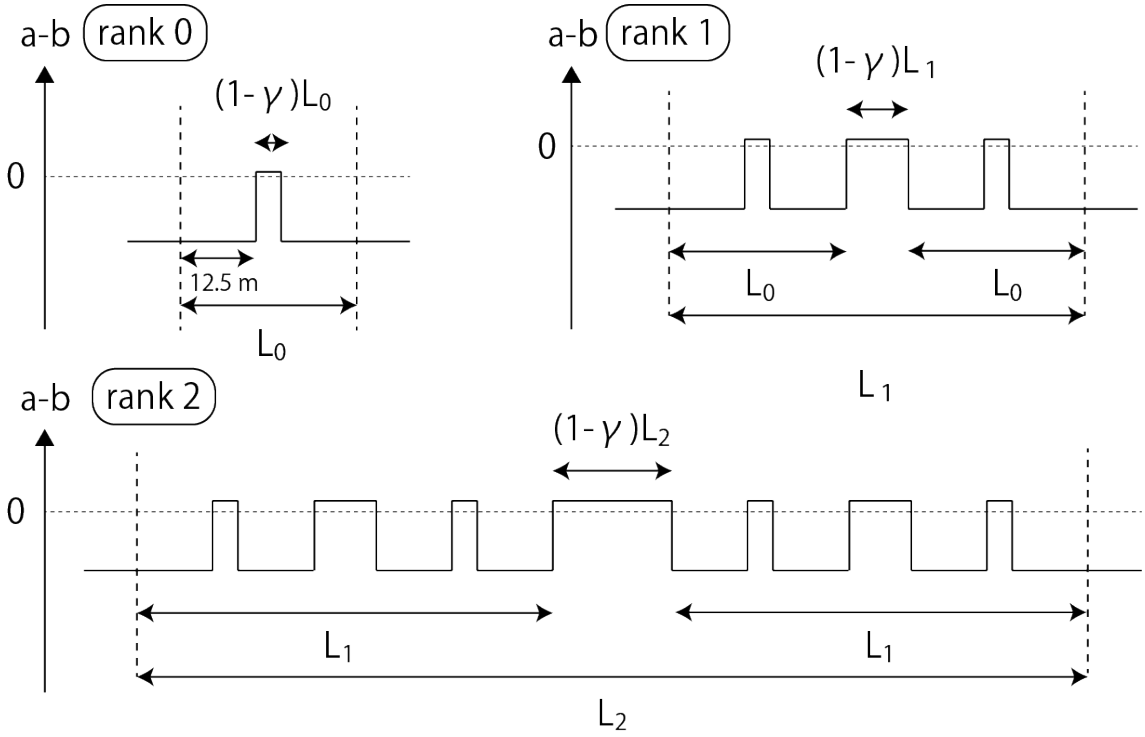

Figure 3.18: Cantor-set distributions of frictional parameters. In the rank 0 distribution, bimodal frictional-parameter distribution recurs with distance L_0. In the rank 1 distribution, two rank 0 distributions are separated by VSZ with the length of (1-γ) L_1. Frictional parameter distribution recurs with distance L_1. Higher-rank distributions are constructed with the same procedure.

γ / rank	0	1	2	3
0.90	44 (27.5 m) η=0.91	98 (61.25 m) η=0.82	218 (136.25 m) η=0.73	484 (302.5 m) η=0.66
0.85	47 (29.375 m) η=0.85	111 (69.375 m) η=0.72	261 (163.125 m) η=0.61	614 (383.75 m) η=0.52
0.80	50 (31.25 m) η=0.80	125 (78.125 m) η=0.64	313 (195.625 m) η=0.51	783 (489.375 m) η=0.41

Table 3.2: The number of grids for the recurrence (corresponding distances) and the density of VWZ of frictional parameters for various Cantor-set distributions.

In this section, we focus on the macroscopic parameters describing slip behavior on the fault, such as stress drop $\Delta\tau$, slip, slip-weakening distance S_w, and recurrence interval, which are defined as follows (Figure 3.19). Macroscopic stress drop is defined as the difference between the maximum and minimum spatially averaged stress on the fault during a seismic event. A seismic event is defined as the period for which the spatially averaged slip velocity of the fault exceeds the seismic slip velocity $V = 2\beta a\sigma / \mu$ (see Section 3.2). Here, we use 3.6×10^{-3} m/s for the seismic slip velocity with a = 0.0006. The macroscopic slip is defined as the spatially averaged slip distance during seismic events. The macroscopic slip-weakening distance is defined as the amount of slip that is needed for the spatially averaged stress on the fault to drop by 95% of the macroscopic stress drop. Recurrence intervals are defined in the same way as in the previous section.

Figure 3.20a shows the recurrence interval of seismic events plotted against rank of the Cantor-set distribution for simulations using the aging law. An example of the resulting slip behavior is shown in Figure 3.21. The recurrence interval is shorter when the fault has higher-rank distributions of frictional parameters. This behavior is observed because the fault can endure less stress accumulation with increasing rank because of the lower density of the VWZ for higher-rank distributions. Comparing the

Cantor-set distributions and bimodal distributions with the same density and recurrence distance, faults with Cantor-set distributions have longer recurrence intervals. For the Cantor-set distributions, the VSZ is divided into smaller pieces than for the bimodal distributions, resulting in less efficient strain accumulation at the edge of the VWZ.

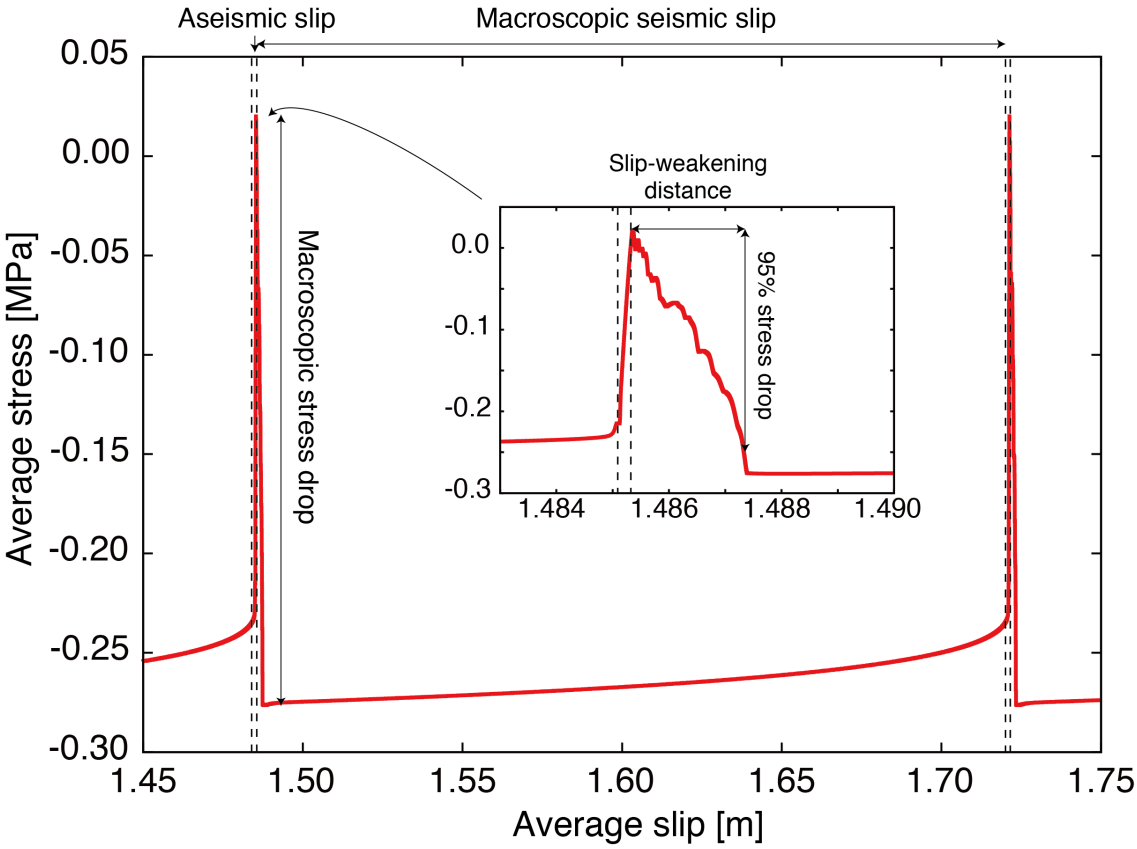

Figure 3.19: A definition of macroscopic stress drop, slip, and slip weakening for slip behavior of fractal distributions. Stress averaged over the fault is plotted against the slip averaged over the fault in the case of rank 3 of Cantor-set distribution with $\gamma = 0.80$. Seismic events are defined as period when the spatial average of slip velocity exceeds a threshold where radiation-damping term becomes dominant (see the text for details). Macroscopic stress drop is defined as the difference between maximum and minimum stress averaged over the fault during seismic events. Macroscopic slip of seismic events is defined as slip averaged over the fault during seismic events. Macroscopic slip-weakening distance is defined as the macroscopic slip required for the macroscopic stress to drop 95% of its stress drop.

Because all seismic events in these simulations rupture the entire fault, the stress drop and slip distance are determined by the seismic-event recurrence intervals regardless of the frictional-parameter distribution (Figure 3.20b and 3.20c). The macroscopic slip-weakening distance increases with increasing the hierarchy of frictional parameter distributions (Figure 3.20d). We also calculate $\Delta\tau S_w/2.0$ as an approximation of fracture energy (Figure 3.20e). This value increases with increasing portion of VSZ on the fault (i.e., increasing the rank of hierarchy).

Figure 3.22 shows corresponding results obtained for simulations using the slip law. An example of the resulting slip behavior is shown in Figure 3.23. A common feature of the aging law and slip law simulation results is that recurrence intervals decrease with rank (Figure 3.22a), and the macroscopic stress drop and slip are determined by the recurrence interval (Figure 3.22b and 3.22c). The macroscopic slip-weakening distance also increases with rank (Figure 3.22d). Approximated fracture energy also increases with the portion of VSZ on the fault (Figure 3.22e). Hence, the change in slip-weakening distance and approximated fracture energy with frictional-parameter distribution is common to all simulations, regardless of which state-variable evolution law is chosen.

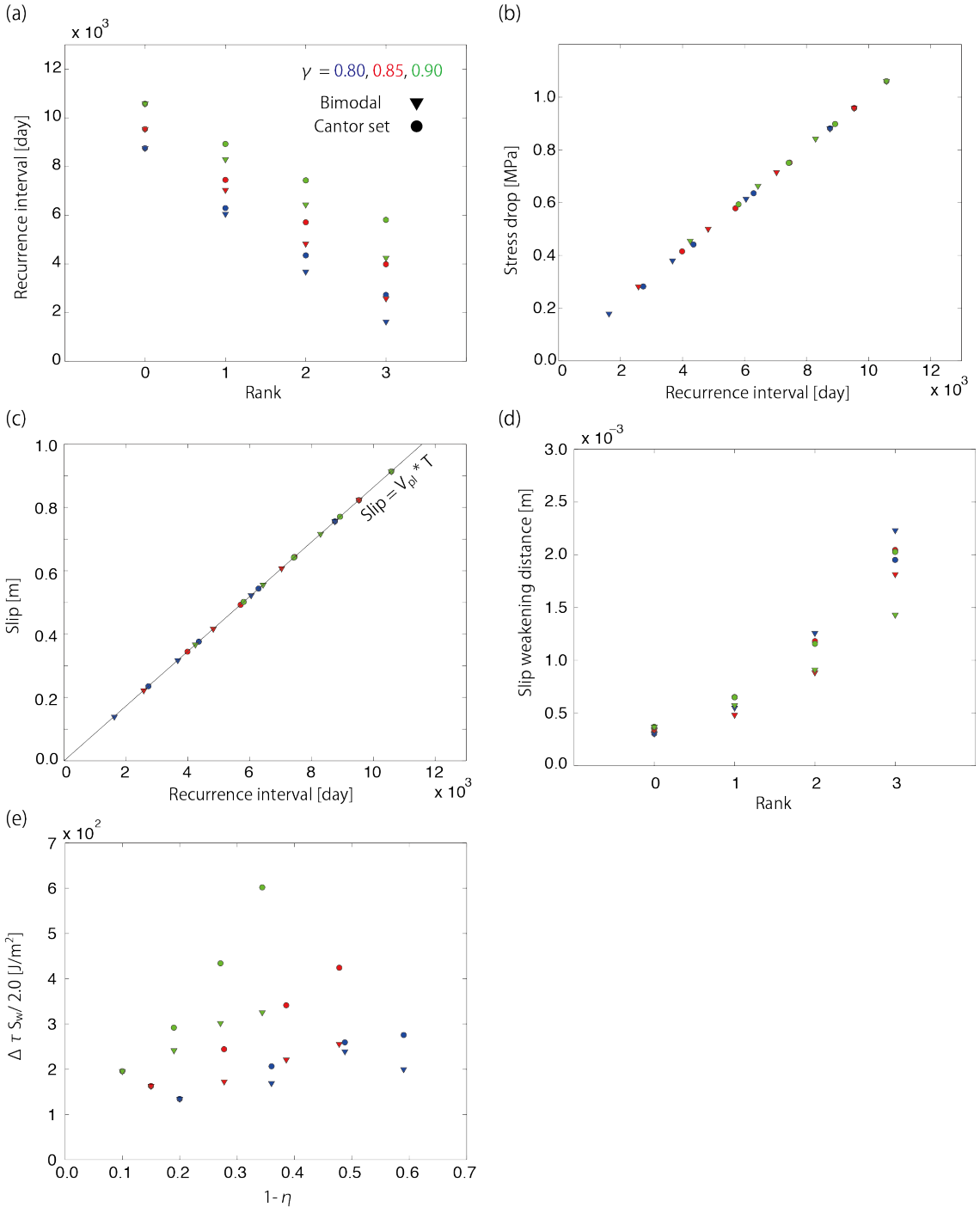
(a)
x 10^3
Recurrence interval [day]
Rank
γ = 0.80, 0.85, 0.90
Bimodal
Cantor set
(b)
Stress drop [MPa]
Recurrence interval [day]
x 10^3
(c)
Slip [m]
Slip = V_pl * T
Recurrence interval [day]
x 10^3
(d)
x 10^-3
Slip weakening distance [m]
Rank
(e)
x 10^2
Δ τ S_w / 2.0 [J/m^2]
1- η

Figure 3.20 (previous page): Comparison of slip behavior for heterogeneous faults obeying the aging law. (a) Recurrence intervals of seismic events plotted against rank of heterogeneity (see Figure 3.18). Results for γ = 0.80, 0.85, and 0.90 are shown by the blue, red, and green symbols, respectively. Circles denote results obtained for Cantor-set distributions, whereas inverse triangles represent results for the equivalent bimodal distributions (i.e., having the same density of velocity-weakening zone and recurrence distance of frictional-parameter distributions as the Cantor-set distributions). (b) Macroscopic stress drops plotted against recurrence intervals of seismic events. Symbols are the same as for (a). (c) As for (b), except that macroscopic slip is plotted against recurrence interval. (d) As for (a), except for macroscopic slip-weakening distance. (e) Approximated fracture energy, calculated as a multiplication of macroscopic stress drop and slip weakening distance divided by 2.0, is plotted against 1-η, which is the portion of VSZ on the fault. The portion of VSZ on the fault increases with increasing the rank of hierarchy.

Figure 3.21 (next page): An example of slip behavior of rank 3 Cantor-set distributions (γ = 0.80) with the aging law. (a) Time evolutions of slip velocity on the fault. A green line shows the slip velocity averaged over the fault, while a red and blue line show the slip velocity at the center of the largest VWZ and VSZ on the fault, respectively, which are located by stars in (b). The right figure is a close up of one seismic event denoted by a black line in the left figure. (b) Snapshots of slip velocity on the fault. Snapshots are plotted for every $10^{0.25}$ times the change in slip velocity averaged over the fault. The change in line color from blue to red indicates increasing time in each panel.

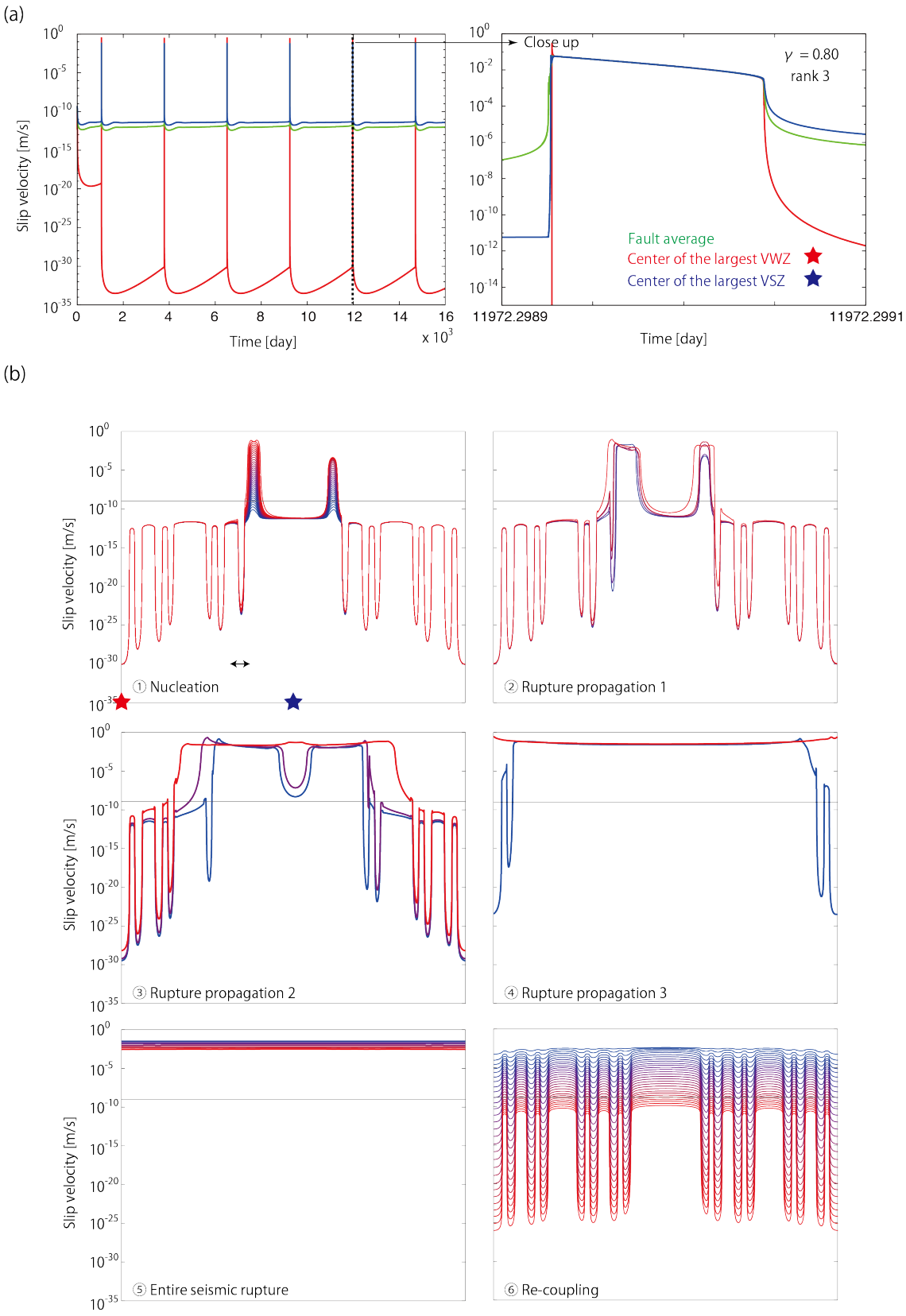
(a)
Slip velocity [m/s]
Time [day]
x 10^3
Close up
γ = 0.80
rank 3
Fault average
Center of the largest VWZ
Center of the largest VSZ
11972.2989
11972.2991
Time [day]
(b)
① Nucleation
② Rupture propagation 1
③ Rupture propagation 2
④ Rupture propagation 3
⑤ Entire seismic rupture
⑥ Re-coupling

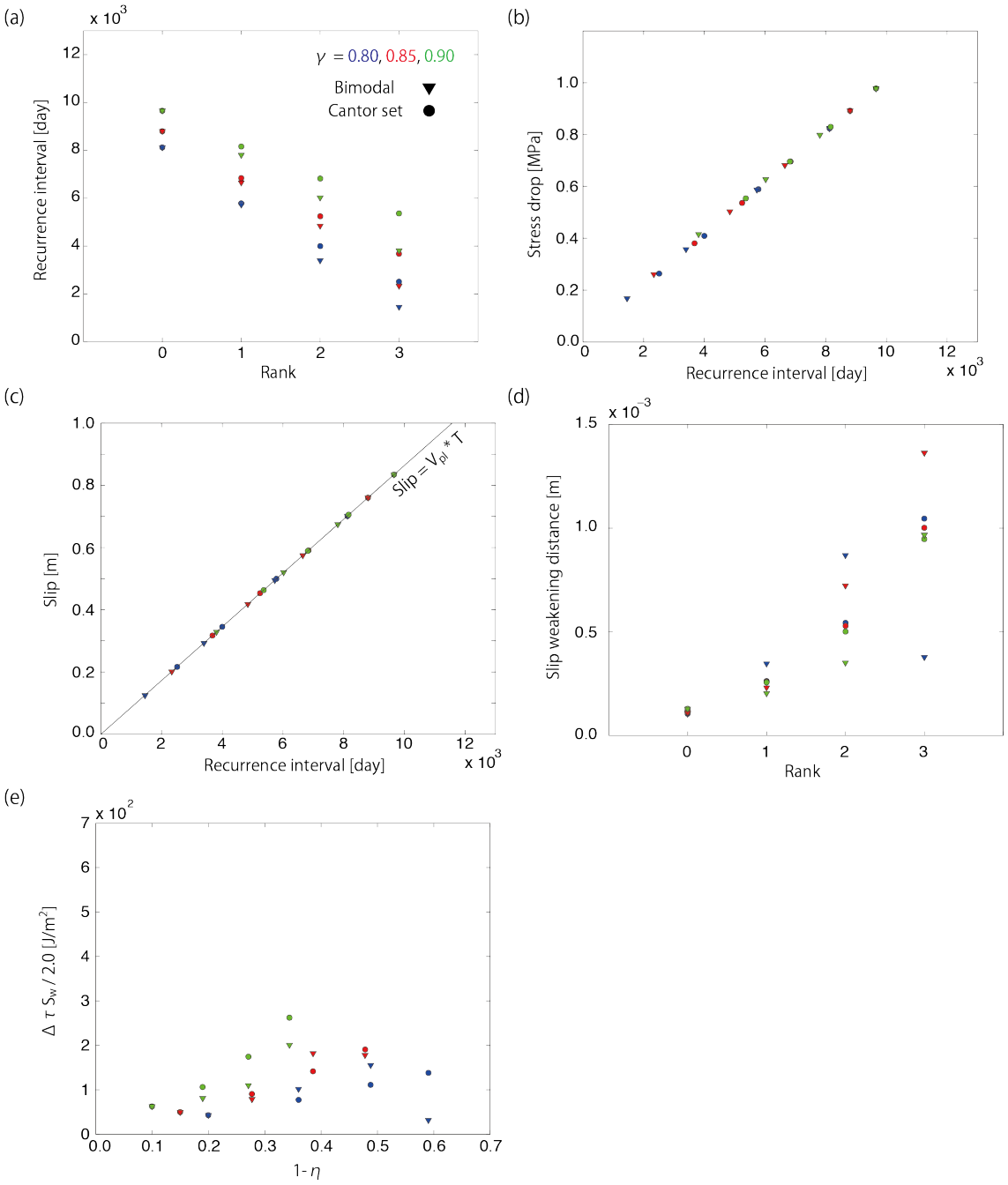

Figure 3.22: Comparison of slip behavior for heterogeneous faults obeying the slip law. Symbols and colors have the same meaning as the corresponding parts of Figure 3.20.

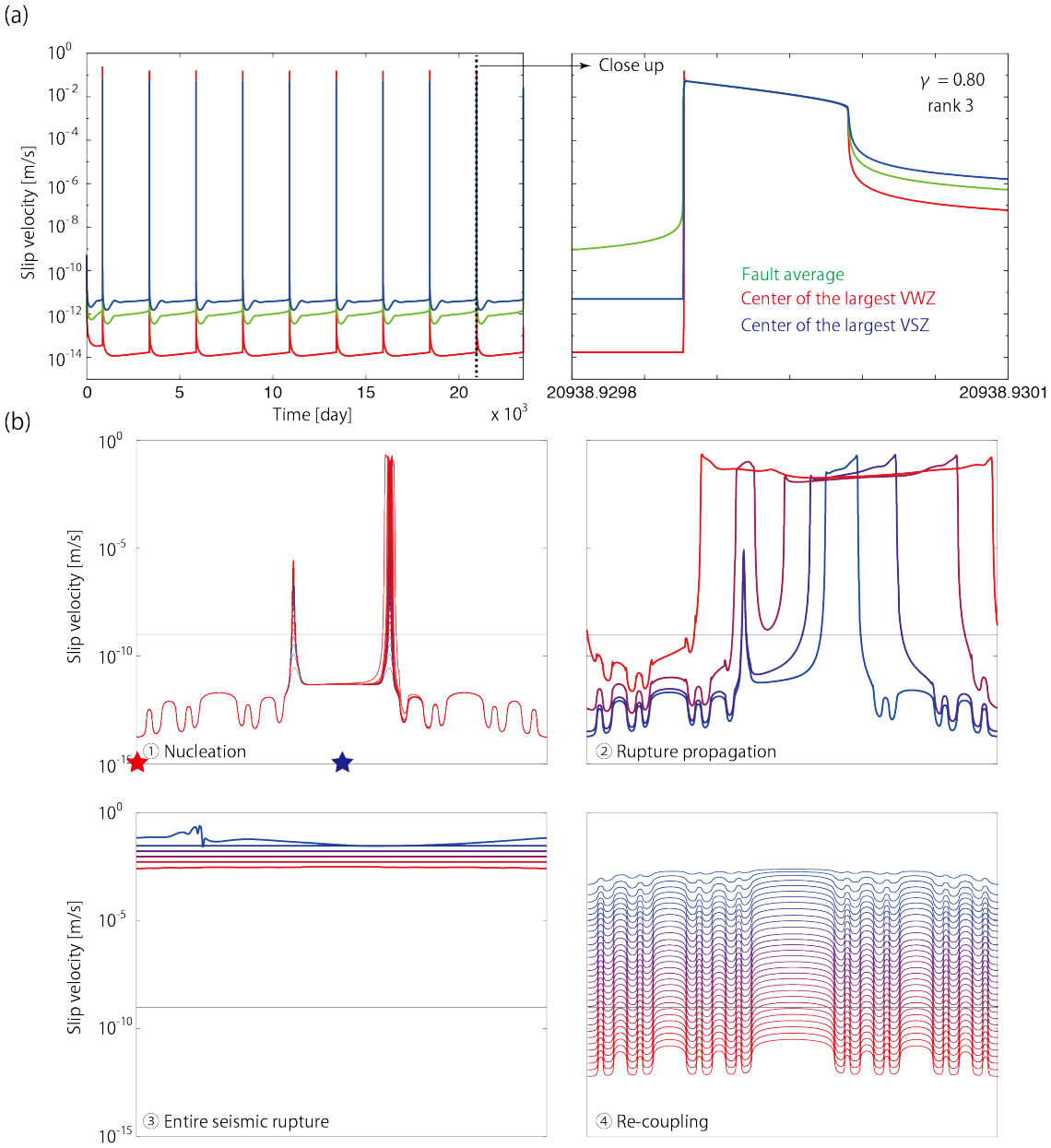

Figure 3.23: An example of slip behavior of rank 3 Cantor-set distributions ($\gamma = 0.80$) with the slip law. (a) Time evolutions of slip velocity on the fault. A green line shows the slip velocity averaged over the fault, while a red and blue line show the slip velocity at the center of the largest VWZ and VSZ on the fault, respectively, which are located by stars in (b). The right figure is a close up of one seismic event denoted by a black line in the left figure. (b) Snapshots of slip velocity on the fault. Snapshots are plotted for every $10^{0.25}$ times the change in slip velocity averaged over the fault. The change in line color from blue to red indicates increasing time in each panel.

3.4. Discussion

We have shown that when an external stress loading exists, a fault model with a simple bimodal distribution of frictional parameters obeying RSF law displays five types of slip behavior that may be related to the different types of earthquakes. Nakata et al. (2011) reported that the connectivity of ruptures on small, brittle fault patches determines whether the rupture of a heterogeneous fault becomes an ordinary earthquake or a slow earthquake. In the entire-seismic regime of our study, the VSZ around the VWZ is also accelerated to seismic slip velocity during the seismic rupture of the VWZ. Seismic ruptures on separate VWZs are therefore connected by seismic rupture of the VSZ. In contrast, in the transitional-slip regime, seismic ruptures of the VWZs are separated by fast aseismic slip in the VSZ as a result of strong and complex interactions between slip in the VWZ and the VSZ. Therefore, the transitional-slip regime and the entire-seismic regime correspond to slow earthquakes and ordinary earthquakes, respectively, in the sense of their rupture connectivity.

Experimental studies have shown that the frictional property $a - b$ depends on pressure and temperature (e.g., Blanpied et al., 1991), and so the frictional behavior of subducting rock is expected to change with depth. At shallower parts of the plate interface where temperature is low, $a - b$ is negative; such area corresponds to the seismogenic zone where ordinary earthquakes occur. In contrast, $a - b$ is positive at deeper parts of the plate interface where temperature is high, and is associated with stable slip. Geological studies also reveal that the geometry of the fault surface changes with the accumulation of slip (Sagy et al., 2007). Various along-dip heterogeneities in the fault zone could raise frictional heterogeneity (including the spatial average of a-b and the portion of VWZ on the fault) varying with depth. At the shallower plate interface, the spatial average of a-b is negative, and the portion of VWZ on the fault is high. Our results show that entire seismic regime occurs in such condition, which may be attributed to regular earthquakes. At the deeper plate interface, in contrast, the spatial average of a-b is positive and the portion of VWZ on the fault is low. Our results show that the partial seismic regime or stable slip regime appears in this condition. Transitional slip regime will be appeared between these two conditions.

From the classical viewpoint of numerical simulation studies, the depth dependence of $a - b$ corresponds to the occurrence of different types of shear slip on the plate boundary (e.g., Liu and Rice, 2007). At shallower parts of the plate interface,

$a-b$ is negative; these areas correspond to the seismogenic zone where ordinary earthquakes occur. In contrast, $a-b$ is positive at deeper parts of the plate interface, and is associated with stable slip. Slow earthquakes occur in the brittle–ductile transition zone where $a-b$ changes from negative to positive values. Transitional slip behavior in our study may correspond to slow earthquakes in that it occurs at similar condition where the spatial average of *a*-*b* is close to zero. Our results also show that transitional-slip behavior becomes more ambiguous for larger stiffness values. Hence, if transitional-slip behavior corresponds to a slow earthquake, the difference in stiffness or difference in the width of the shear zone may explain the observed variability between subduction zones in terms of their capacity for sustaining slow earthquakes.

However, results in this study are of the simplest situation of frictional heterogeneity with an infinite fault. Slip-behavior transitions of a finite heterogeneous fault, where stress is accumulated by the creep of surrounding fault, should be investigated in the future work (some examples are presented in the next chapter). Furthermore, various characteristics of slow earthquakes remained to be quantitatively reproduced with our model. For example, Ando et al. (2012) reported that the diffusive migration pattern of tremor activity (Ide, 2010a) can be reproduced with a slip-weakening law and a Newtonian rheology, whereas RSF law fails to reproduce these diffusive migration patterns. However, frictional law estimated from tidal sensitivity of tectonic tremors support the existence of RSF law on the deep plate interface. Recently, many studies (Thomas et al., 2012; Beeler et al., 2013; Ide and Tanaka, 2014; Houston, 2015; Ide et al., 2015; Yabe et al., 2015) quantitatively compared tremor seismicity with tidal stress, revealing that tremor rate (the number of tremors per unit time) is exponential to tidal stress. Assuming that tremor rate is proportional to background slip velocity, the observed exponential relation means that slip velocity is exponential to stress, which implies that VS RSF law exists on the plate boundaries in areas where slow earthquakes occur (Ader et al., 2012). Beyond this problem, large differences in the stress drop between ordinary earthquakes (~1–10 MPa; Abercrombie and Rice, 2005) and slow earthquakes (~10 kPa; Ide et al., 2007b) are also not considered in our model. We note that effective normal stress used in our numerical calculations is 30 MPa, which may be too large for slow earthquake. We may need to consider other factors, such as the existence of high-pressure pore fluid.

Frictional heterogeneities should also exist in the strike direction. For

example, irregular topography such as seamounts or horst–graben structures are in some cases observed on the surface of oceanic plates, although their spatial distribution is not uniform. Subduction of these irregular geometries is known to influence seismicity (e.g., Tanioka et al., 1997; Mochizuki et al., 2008). It has also been suggested that the heterogeneous distribution of trench sediments controls the potential for giant earthquakes in subduction zones (e.g., Heuret et al., 2012). Various along-strike heterogeneities of fault structure could be approximated as the frictional heterogeneity on the planar fault in numerical simulations. Such large-scale heterogeneity in frictional properties along strike in subduction zones may result in the segmentation of seismicity (e.g., Lay and Kanamori, 1981; Obara, 2010).

Our model also may have potential to explain the scale dependency of frictional parameter. For example, the fracture energy of a fault (i.e., the energy required to initiate frictionally unstable slip) estimated from laboratory experiments is 1–10 kJ/m^2 (Scholz, 2002; Ohnaka, 2003), which is much smaller than the ~1 MJ/m^2 that is estimated from seismological observations (Beroza and Spudich, 1988; Abercrombie and Rice, 2005). Fracture energy is estimated to scale with event size (Ohnaka, 2003); that is, it is more difficult for larger earthquakes to occur. The hierarchical structure of fracture energy proposed by Ide and Aochi (2005, 2014), Hori and Miyazaki (2010), and Noda et al. (2013) is essential to explain the characteristic, but also random, nature of earthquakes over a wide range of scales. Ide and Aochi (2005) assumed that the slip-weakening distance is proportional to the size of a seismic patch, and that the patch size distribution obeys a power law. Such models can reproduce complex rupture events with Gutenberg–Richter size–frequency statistics, average sub-shear rupture-propagation velocity with regional super-shear acceleration, and apparent initial nucleation phases. However, the cause of the scale dependence of fracture energy is not obvious. For example, Andrews (2005) demonstrated that energy consumption by off-fault damage will result in a scale dependence of fracture energy. The development of off-fault damage and the resultant increase in fracture energy have also been demonstrated by the crack models of Ando and Yamashita (2007). Microscopic frictional heterogeneity introduced in this study may provide another explanation for the scale dependence of frictional parameters. In Section 3.3.3, we tested how macroscopic parameters (macroscopic stress drop, slip, and slip-weakening distance) change with the frictional heterogeneity in the entire seismic regime. In our

simple situation with an infinite fault, macroscopic slip decreases with increasing rank (increasing characteristics spatial scale L_n) (Figure 3.20abc, 3.22abc). This contradicts with natural case, in which slip of earthquake increases with its size. This is because we use an infinite fault with cyclic boundary condition in our calculation, which is not the case in the actual earthquake. However, our results show that macroscopic slip weakening distance or approximated fracture energy increases with increasing characteristic size (Figure 3.20de, 3.22de). Because energy is consumed to accelerate VSZ up to seismic slip velocity, areal density increase of VSZ on the fault with the size of earthquake could explain the increase of fracture energy of regular earthquakes with its size (Figure 3.20e, 3.22e). These results imply that some hierarchical structures embedded in seismic regions may explain the observed scale dependence of frictional parameters. Furthermore, our results show that spatial structure of frictional heterogeneity also affects slip behavior even when the spatial average of a-b and recurrence distance is the same. To explore this possibility, further investigation with more realistic situation (a frictionally heterogeneous finite planar fault) will be necessary.

In this study, we used quasi-dynamic rupture simulation, which does not consider the inertial effect of propagating seismic waves. Therefore, these calculations are, strictly speaking, not accurate, especially when the slip velocity is so high that the radiation-damping term on the left-hand side of Equation (3.13) is dominant. Moreover, the RSF law itself is not accurate at high slip speeds. Experimental results show that the friction coefficient decreases at seismic slip-speeds, a phenomenon known as dynamic weakening, which is not considered in RSF (e.g., Di Toro et al., 2004). At seismic speeds, various processes such as thermal pressurization (e.g., Sibson, 1973) and flash melting (e.g., Tsutsumi and Shimamoto, 1997) should be considered in numerical simulations to reproduce dynamic weakening. Hence, fully dynamic calculations using RSF alone are not necessarily correct (e.g., Thomas et al., 2014). If inertial and dynamic weakening effects were considered in our simulation, the window where the transitional-slip regime can exist would become narrower, as the energy budget at the rupture tip would change. However, these modeling limitations do not affect our conclusion that transition from the partial-seismic regime to the entire-seismic regime occurs when the spatially averaged value of $a-b$ is zero, because this transition is governed by the stress balance during the inter-seismic period, as discussed in Sections

3.3.1 and 3.3.2.

Dublanchet et al. (2013) investigated the slip behavior of an infinite heterogeneous planar fault using the RSF law. They distributed VW patches randomly on a VS infinite fault with cyclic boundary condition, and observed that a heterogeneous fault shows partially or entirely seismic slip behavior depending on the density of VWZs on the fault. Their observations are therefore consistent with the partial- and entire-seismic regimes seen in our study. Dublanchet et al. (2013) estimate the approximate position of the boundary between these two regimes by considering the stress required to accelerate the VSZ to seismic slip velocity as

$$\left(a-b\right)_{VS}^{cri}=\frac{\Delta\tau}{\sigma\ln\left(V_{seis}/V_{pl}\right)}\frac{\eta}{1-\eta}\equiv\alpha\frac{\eta}{1-\eta}, \qquad (3.27)$$

where $\Delta\tau$ is the stress drop in the VWZ and V_{seis} is the seismic slip velocity (see equation 16 of Dublanchet et al. (2013)). Dublanchet et al. (2013) also showed that Equation (3.27) is consistent with their numerical calculations for $\Delta\tau$ = 6 MPa, σ = 100 MPa, V_{seis} = 0.01 m/s, and V_{pl} = 10^{-9} m/s. Using these values, the coefficient α in Equation (3.27) is approximately 0.0037. In the context of our study, the boundary between the partial-seismic regime and the entire-seismic regime exists when the spatially averaged value of $a-b$ is zero. Hence, this boundary can be written as

$$\left(a-b\right)_{VS}^{cri}=(b-a)_{VW}\frac{\eta}{1-\eta}, \qquad (3.28)$$

where Dublanchet et al. (2013) use $b-a$ = 0.004 in the VWZ. Therefore, the boundary that they estimate is consistent with that obtained using our analytical expression and that of Skarbek et al. (2012). In addition, we discovered very complex transitional-slip behavior around this boundary, which was not discussed by Dublanchet et al. (2013).

Skarbek et al. (2012) also considered the heterogeneous distribution of RSF parameters to explain ordinary earthquakes and slow earthquakes. However, the heterogeneity that they used is different to that investigated here. In their finite-fault model, the recurrence distance of the frictional parameters is shorter than or comparable to L_b. Hence, it is difficult for just a VWZ to be accelerated to seismic slip velocities. This is why they do not observe our transitional slip regime in which seismic slip in VWZ and aseismic slip in VSZ are complexly interacted. Seismic slip observed in Skarbek et al. (2012) will correspond to our entire seismic regime. Slow slip observed

by them does not correspond to any five regimes in our study. In their slow slip, both VWZ and VSZ are accelerated to similar aseismic slip velocity (Supplemental animation S2 of Skarbek et al. (2012)), which is different from our non-seismic stick slip regime. If the heterogeneity of the frictional parameters on the fault arises partly from irregularity in the fault geometry, there should be strong heterogeneity in the normal stress. Therefore, we consider that it is possible for the nucleation size to be much smaller than the recurrence distance. The fact that we observe tectonic tremors in the slow-earthquake region also shows that slip velocity can locally accelerate to seismic velocities even in the slow-earthquake region (Thomas et al., 2016). Slow slip of Skarbek et al. (2012) cannot explain such colocation of tectonic tremors and SSEs. A linear stability analysis of spring-slider system made by Skarbek et al. (2012) also predicts that slip behavior will change when when the spatial average of a-b is zero in the case of k_0=0 (e.g., equation 5 of Skarbek et al. (2012)).

Using a heterogeneous distribution of the strength-change parameter, Ben-Zion (2012) successfully modeled two phases of slip behavior on a fault, which obey scaling laws for ordinary earthquakes and slow earthquakes (Ide et al., 2007b), although their model is in the non-continuum limit. When the strength-change parameter is large enough, the rupture of the fault is crack-like, and the slip distribution is smooth. The frequency–size distribution becomes a power law at small scales in the case of a large characteristic earthquake. The seismic moment of the event is scaled by the cube of event duration. When the strength-change parameter is close to zero, the rupture of the fault is divided into many patches, and the slip distribution becomes fractal. The frequency–size distribution becomes a tapered Gutenberg–Richter law, and the seismic moment of an event is scaled by the square of event duration for smaller-sized events but is scaled linearly by event duration for larger-sized events. Our model and the model by Dublanchet et al. (2013) is a continuum-limit counterpart of the model by Ben-Zion (2012), because these studies consider the heterogeneity of frictional parameter and the connectivity of small ruptures in their model. Detailed exploration of how results changes between continuum calculation and non-continuum calculation and how the statistics of frictional heterogeneity affects the statistics of seismicity and source parameters is left for future studies.

3.5. Conclusion

The spatial distribution of frictional properties should be heterogeneous on a fault. On a frictionally heterogeneous fault where both VWZs and VSZs are distributed, VSZs essentially operate as barriers preventing the propagation of seismic ruptures that nucleate at VWZs. However, the ability of a VSZ to stop seismic ruptures depends on the distribution of heterogeneity. Inspired by Nakata et al. (2011), who showed that a heterogeneous fault can be a unified source model for slow earthquakes and ordinary earthquakes, this study investigated the slip behavior of heterogeneous faults in detail.

We conducted a parameter study exploring the dependence of slip behavior on the proportion of fault length that is VW and on the stiffness of the plate loading, using an infinite linear fault in a 2D anti-plane elastic space with a spatially periodic bimodal distribution of RSF parameters. When an external stress accumulation does not exist, the fault model displays four types of slip behavior: (i) stable slip; (ii) non-seismic stick-slip; (iii) seismic slip at VWZs and afterslip at VSZs (herein referred to as the partial-seismic regime); and (iv) the entire-stick regime, where the entire fault keeps decelerating and seismic events never occur. The boundary between the stable-slip regime and the partial-seismic regime is determined by the nucleation size of the VWZ. Around the boundary between these regimes, non-seismic stick-slip behavior is observed in some cases, depending on the frictional parameters and evolution law of the state variable. The boundary between the partial-seismic regime and the entire-stick regime is located at the VWZ density where the spatial average of $a - b$ on the fault becomes zero. When an external stress loading exists, the fault model displays five types of slip behavior: (i) stable slip; (ii) non-seismic stick-slip; (iii) the partial-seismic regime; (iv) transitional slip, where slip in the VWZ and VSZ strongly interact; and (v) entire-stick slip, where the entire fault including the VSZ slips seismically. The location of the boundary between the partial-seismic regime and the entire-seismic regime corresponds to that of the boundary of the entire-stick regime for the $k_0 = 0$ case, although we observed a transitional regime in a narrow window around this boundary for simulations using the aging law and the slip law, in which slower deformation dominates in the shear-slip behavior. The sharpness of this transition is affected by the stiffness of the external stress loading, with larger stiffness values making the transition more diffuse. The transitional regime and the entire-seismic regime may correspond to slow-earthquake and ordinary-earthquake behavior, respectively, in terms of the

connectivity of seismic rupture in VWZs.

When the frictional parameters have a cyclic Cantor-set distribution on the fault, the macroscopic approximated fracture energy, estimated from the spatially averaged stress and slip, increases with increasing the characteristic spatial scale of the frictional-parameter distributions. Because the statistics of heterogeneity will change with tectonic environment, for example with depth along a subduction interface, a heterogeneous fault model may explain the scale dependency of frictional parameter as well as the diversity of seismic phenomena observed in subduction zones.

4. 3D Numerical Model

This chapter has not been published in any peer-reviewed journals.

4.1. Introduction

In the previous chapter, the shear-slip behavior of an infinite linear fault has been investigated with spatially periodic frictional-parameter distributions. It is physically simple, and is useful to understand the physical mechanism of slip diversity. However, the assumptions of an infinite linear fault and a cyclic boundary condition are unlikely to occur in the natural fault. A finite planar fault needs to be considered for the sake of a quantitative comparison between numerical simulations and the actual seismicity.

Dublanchet et al. (2013) has investigated shear-slip behavior of an infinite planar fault with spatially periodic frictional heterogeneities. They have observed the partial seismic regime and the entire seismic regime, according to the frictional heterogeneity, though they have not discussed its relation to slow earthquake. Based on the result in the previous chapter, it could be expected that the transitional regime between the partial seismic regime and the entire seismic regime corresponds to the behavior of slow earthquake.

Kato (2007) has investigated interactions of many seismic patches on the fault. However, their main aim is to investigate an influence of a mainshock to surrounding smaller seismic patches (i.e., aftershocks). For this purpose, a large seismic patch is located at the center of the model space, and many other small seismic patches are distributed around it. The main purpose of this study is to investigate how a cluster of similar seismic patches behaves as a whole. Hence, the same seismic patches are distributed on the fault in this study. Some studies (e.g., Kato, 2004; Kaneko et al., 2010) investigated interactions of two seismic patches. However, this study focuses on interactions among many seismic patches.

In this chapter, some examples of shear-slip behavior on a finite planar fault with the frictional heterogeneity have been presented, though

the detailed analysis and quantitative reproductions of diverse seismic phenomena are left for future studies. It is confirmed that a finite planar fault also changes its slip behavior from the partial seismic regime to the entire seismic regime according to the frictional heterogeneity. Complex slip behavior is also observed between two modes of slip behavior.

In the next section, the method of numerical simulations is explained. Because the basic method is common to the previous chapter, a modified part is mainly explained. In Section 4.3, results of numerical simulations have been provided. In the discussion section (Section 4.4), it has been discussed how the model should be developed in future studies to explain diverse seismic phenomena quantitatively.

4.2. Method

As is in the previous chapter, we again use quasi-dynamic simulation with RSF law (Dieterich, 1979). We consider a planar fault with the size of 300 m x 300 m (Figure 4.1). We set the boundary condition that surrounding fault slips stably at the plate velocity V_{pl}. A fault is discretized into 1m x 1m sub-faults, each of which has a VW or VS frictional parameter, to calculate the time evolution of fault slip using a boundary integral equation method. The frictional-parameter distribution is shown in Figure 4.1. Within the 300 m x 300 m model space, a cluster of VW patches has 150 m x 150 m size. This region is divided into 25 sub-squares with 30 m x 30 m size. Each sub-square has a VW patch with 20 m x 20 m size internally. The location of a VW patch is randomly perturbed around the center of each sub-square. The same frictional-parameter distribution shown in Figure 4.1 is used for all calculations in this chapter. Parameters used in calculations are listed in Table 4.1. $L_b \equiv \mu D_c / b\sigma$ in VWZ is 6 m with parameters in Table 4.1. Grid discretization of 1 m is smaller enough than L_b.

Stress on the i-th sub-fault τ_i is expressed as

$$\tau_i = \tau_0 + \sum_j K_{ij}\left(u_j - V_{pl}t\right) - \frac{\mu}{2\beta}V_i, \qquad (4.1)$$

where τ_0 is an ambient stress on the fault, K_{ij} is the static kernel of elastic

deformation, u_j is slip distance at j-th subfault, t is time, μ is rigidity, β is shear wave speed, and V_i is slip velocity at i-th subfault. The static kernel K_{ij} (Kato, 2003) is expressed as

$$K_{ij}=\frac{\mu}{4\pi}\left\{\begin{array}{l}2(1-\alpha)\left[\frac{\sqrt{(\Delta x+0.5)^2+(\Delta y-0.5)^2}}{(\Delta x+0.5)(\Delta y-0.5)}-\frac{\sqrt{(\Delta x+0.5)^2+(\Delta y+0.5)^2}}{(\Delta x+0.5)(\Delta y+0.5)}+\frac{\sqrt{(\Delta x-0.5)^2+(\Delta y+0.5)^2}}{(\Delta x-0.5)(\Delta y+0.5)}-\frac{\sqrt{(\Delta x-0.5)^2+(\Delta y-0.5)^2}}{(\Delta x-0.5)(\Delta y-0.5)}\right]\\ -\frac{1-2\alpha}{\Delta x+0.5}\left[\frac{\sqrt{(\Delta x+0.5)^2+(\Delta y-0.5)^2}}{\Delta y-0.5}+\frac{\Delta y-0.5}{\sqrt{(\Delta x+0.5)^2+(\Delta y-0.5)^2}}-\frac{\sqrt{(\Delta x+0.5)^2+(\Delta y+0.5)^2}}{\Delta y+0.5}-\frac{\Delta y+0.5}{\sqrt{(\Delta x+0.5)^2+(\Delta y+0.5)^2}}\right]\\ -\frac{1-2\alpha}{\Delta x-0.5}\left[\frac{\sqrt{(\Delta x-0.5)^2+(\Delta y+0.5)^2}}{\Delta y+0.5}+\frac{\Delta y+0.5}{\sqrt{(\Delta x-0.5)^2+(\Delta y+0.5)^2}}-\frac{\sqrt{(\Delta x-0.5)^2+(\Delta y-0.5)^2}}{\Delta y-0.5}-\frac{\Delta y-0.5}{\sqrt{(\Delta x-0.5)^2+(\Delta y-0.5)^2}}\right]\end{array}\right\},$$

(4.2.)

where, $\alpha=\lambda+\mu\big/\lambda+2\mu$ (λ is another Lame's constant). Δx and Δy is distance between the center of i-th and j-th subfaults in the direction of the plate movement, and the direction perpendicular to the plate movement. We assume $\lambda=\mu$ in this study.

The RSF law on the i-th fault is expressed as

$$\tau_i=\tau_0+a_i\sigma\log\left(\frac{V_i}{V_{pl}}\right)+b_i\sigma\log\left(\frac{\theta_i}{\theta_{pl}}\right),\quad (4.3)$$

where a_i and b_i are RSF parameters on i-th sub-fault (Dieterich, 1979). θ_{pl} in Equation (4.3) is the state variable when the fault slips at plate velocity in the steady state. The aging law (Dieterich, 1979) is tested in this chapter,

$$\frac{d\theta_i}{dt}=1-\frac{V_i\theta_i}{D_c},\quad (4.4)$$

where D_c is the characteristic slip distance of RSF law. From Equation (4.4), $\theta_{pl}=D_c\big/V_{pl}$ is derived. The time derivative of Equations (4.1) and (4.3) yields

$$\left(\frac{a_i\sigma}{V_i}+\frac{\mu}{2\beta}\right)\frac{dV_i}{dt}=\sum_i K_{ij}\left(V_j-V_{pl}\right)-\frac{b_i\sigma}{\theta_i}\frac{d\theta_i}{dt}.\quad (4.5)$$

Using Equations (4.4) and (4.5), time evolutions of slip velocity and the state variable in every sub-fault can be calculated with the Runge–Kutta–Fehlberg method (Fehlberg, 1969) with an adaptive time increment. From Equation (4.5), the absolute value of τ_0 does not affect slip behavior. A convolution in Equation (4.5) is evaluated using a two-dimensional fast Fourier transform. Because a

wide VSZ is distributed around a cluster of VWZs (Figure 4.1), an artifact due to the use of a fast Fourier transform is small enough.

Parameter	Value
VSZ outside cluster	a=0.005, b=0.001
VWZ	a=0.001, b=0.005
VSZ inside cluster	a=variable, b=0.003
D_c	10 μm
Normal stress σ	10 MPa
Rigidity μ	30 GPa
Shear wave velocity β	3 km/s
Plate velocity V_{pl}	10^{-9} m/s
L_b	6 m
Sub-fault size	1 m

Table 4.1. A list of parameters used in this chapter.

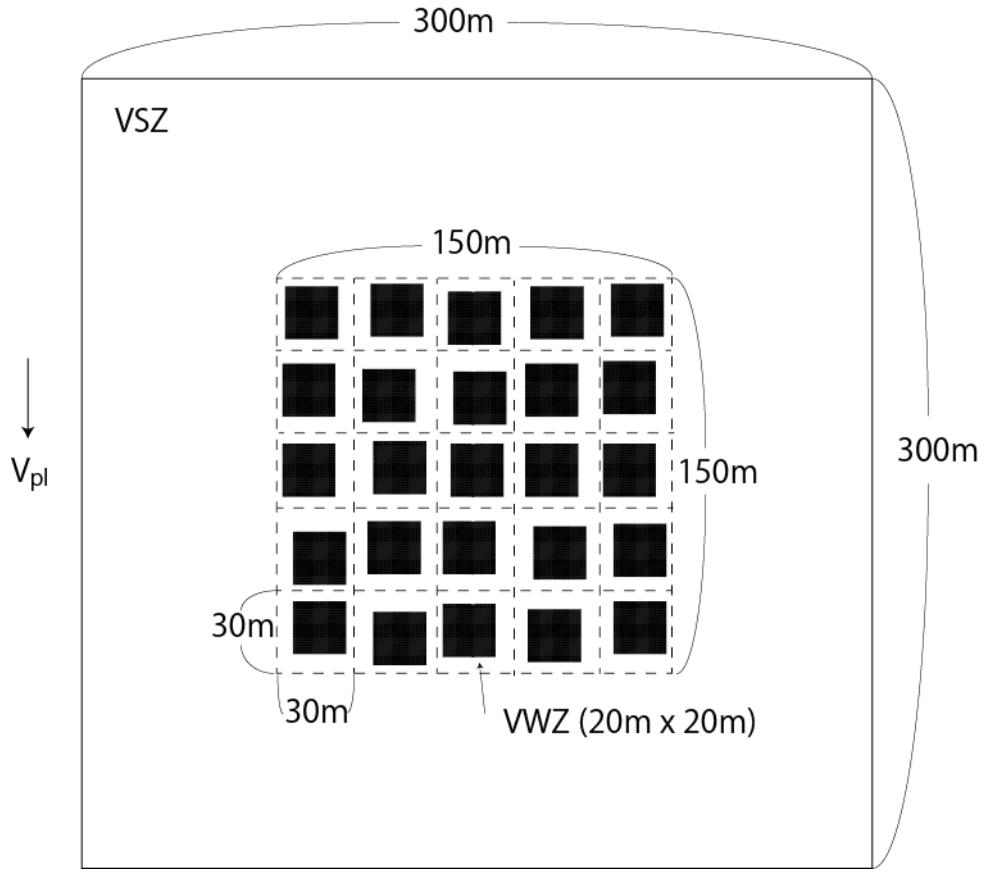

Figure 4.1. The frictional-parameter distribution used in this chapter. Black squares represent VW patches, which have 20 m x 20 m size each. Background white area is VSZ.

4.3. Results

4.3.1. Partial seismic regime

When *a-b* value of background VSZ is large, the fault shows partial seismic regime, as is expected from the result of previous chapter. In Figure 4.2, a time evolution of slip velocity averaged in a cluster is shown when *a-b* of a background VSZ is 0.003. Snapshots of slip velocity in a cluster are shown in Figure 4.3. In this regime, VWZ patches in a cluster are separately ruptured at similar timings. Rupture is started at the rim of a cluster because of the steady slip of surrounding VSZ (Figure 4.3b, 4.3c). Although afterslip occurs around ruptured VWZs, co-seismic rupture cannot propagate in background VSZ because the barrier effect of background VSZ is high due to high a-b value. Hence, VW patches ruptures one by one. Every VW patch

ruptures only once in one event. At the end of rupture of a cluster, the central background part of a cluster is accelerated to about 10^{-8}-10^{-7} m/s by afterslip triggered by several VWZ patches (Figure 4.3h, 4.3i).

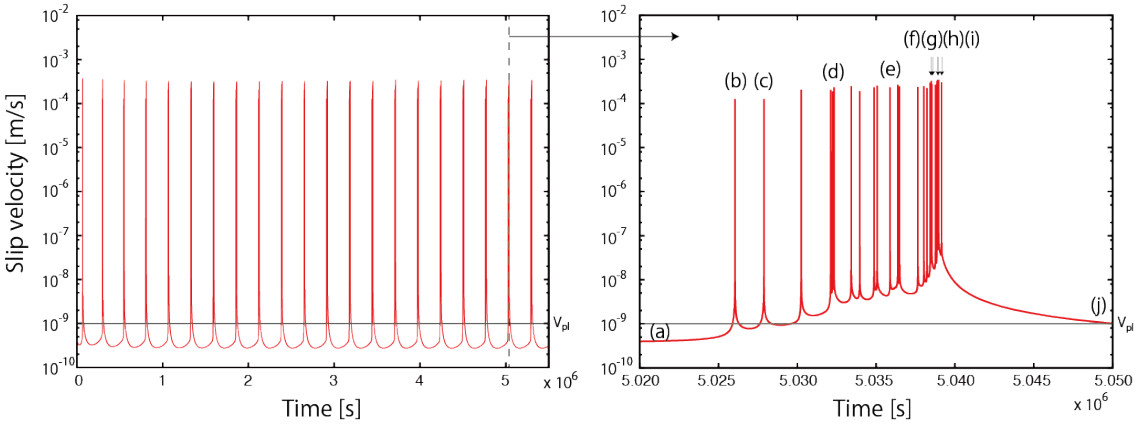

Figure 4.2: Time evolution of slip velocity averaged within a cluster. The left panel shows the entire time evolution, and the right panel shows the close up figure at stick-slip events. (a)-(j) in the right panel correspond to snapshots shown in Figure 4.3.

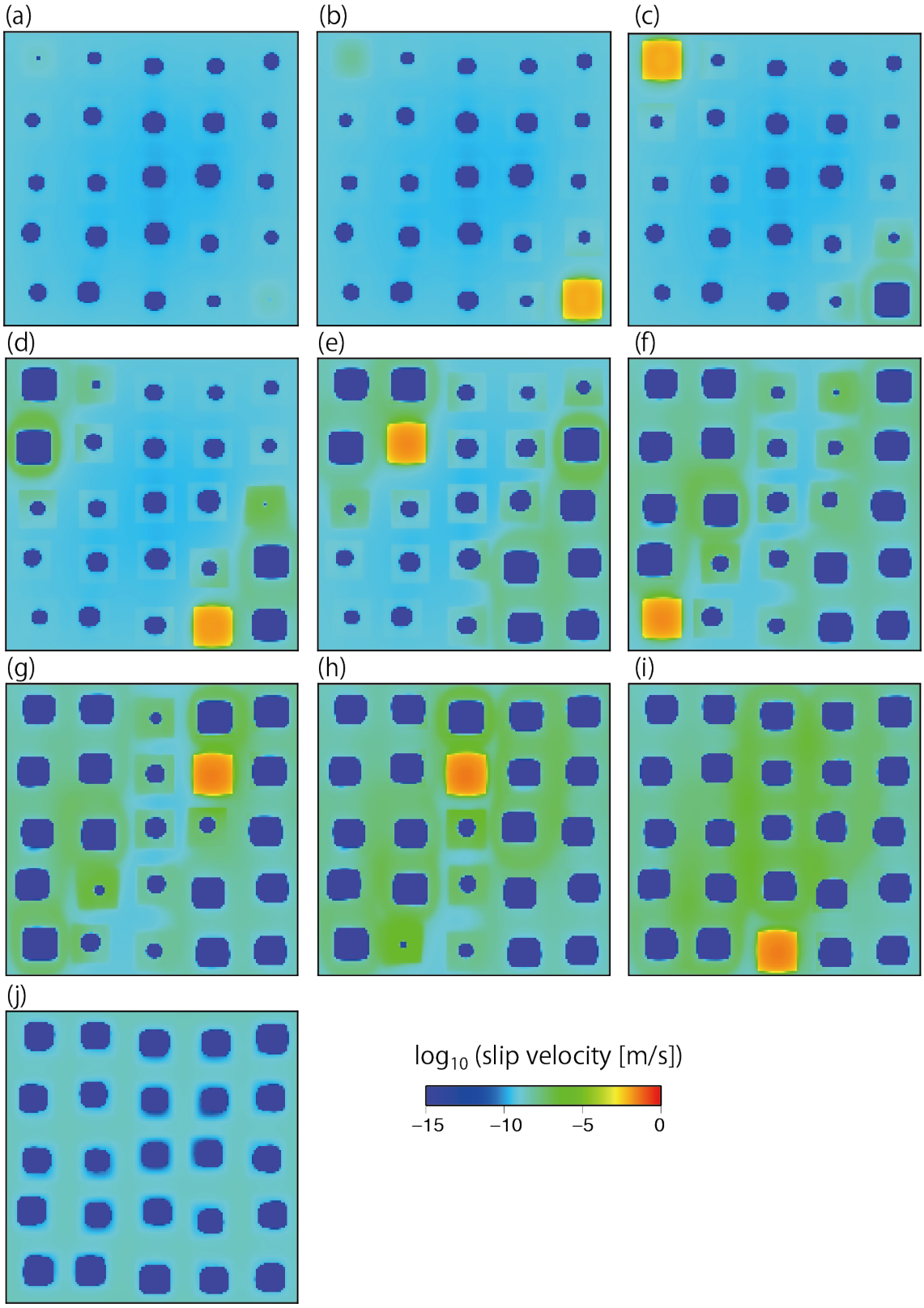

Figure 4.3: Snapshots of slip velocity in a cluster. The time of these snapshots are indicated in the right panel of Figure 4.2.

4.3.2. Entire seismic regime

When *a*-*b* value of background VSZ is close to zero, a cluster shows the entire seismic regime. In Figure 4.4, a time evolution of slip velocity averaged in a cluster is shown when *a*-*b* of a background VSZ is 10^{-6}. Snapshots of slip velocity in a cluster are shown in Figure 4.5. In this regime, two sizes of stick-slip events occur in the calculation. One is the rupture of each VW patch in a cluster (for example, Figure 4.5b). The other is the entire rupture of a cluster including a background VSZ (Figure 4.5p). After the entire rupture occurs, a cluster sticks for a while (Figure 4.5a), and almost no aftershocks occur. Then, small stick-slip events, which are ruptures of individual VW patches, are initiated from the rim of a cluster (Figure 4.5b-h). A series of small ruptures weakens the coupling of a cluster. At last, the entire rupture of a cluster occurs (Figure 4.5i-p).

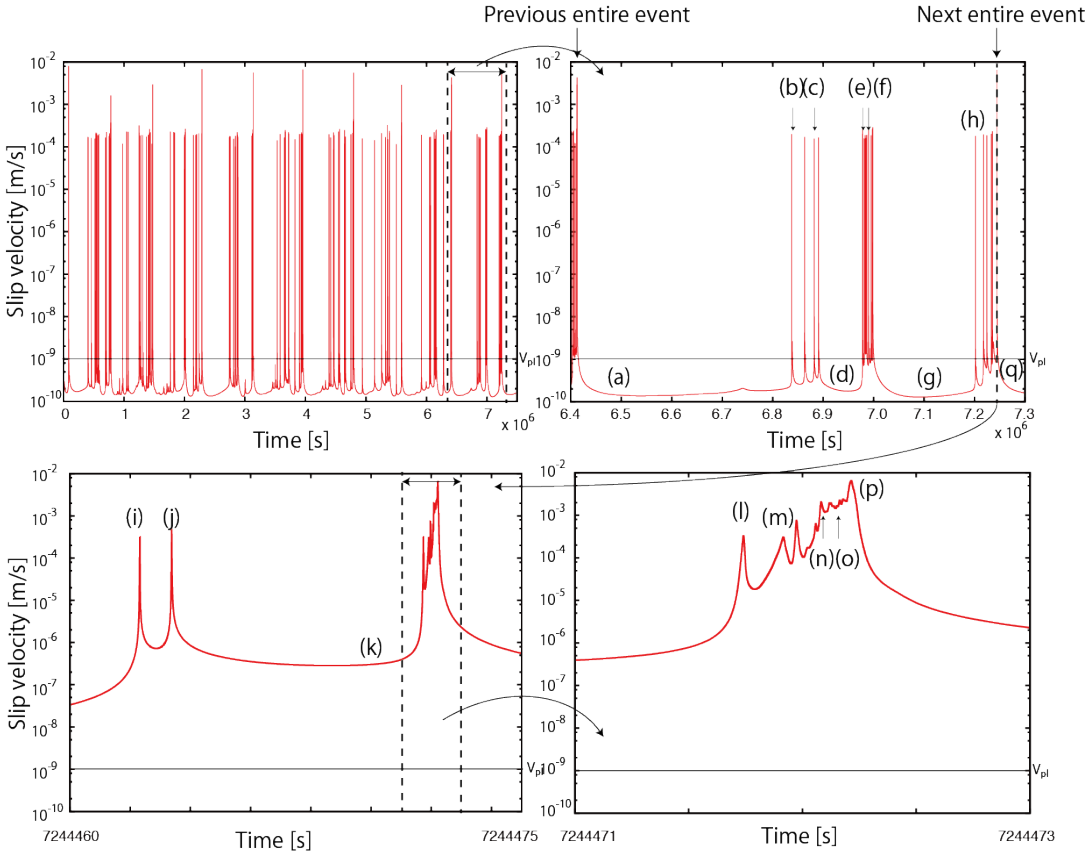

Figure 4.4: Time evolution of slip velocity averaged within a cluster. (a)-(q) in the figure correspond to snapshots shown in Figure 4.5.

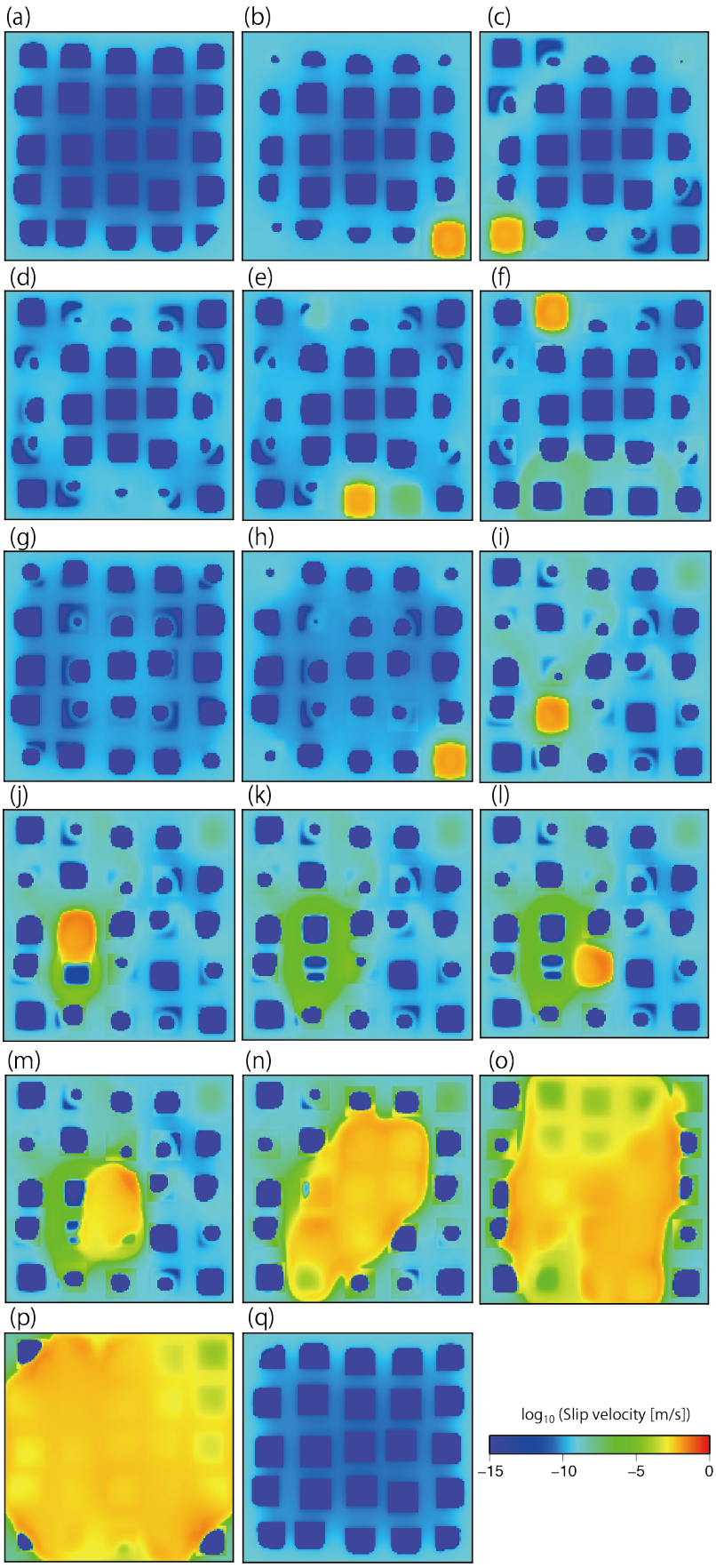
(a)
(b)
(c)
(d)
(e)
(f)
(g)
(h)
(i)
(j)
(k)
(l)
(m)
(n)
(o)
(p)
(q)
log10 (Slip velocity [m/s])
−15
−10
−5
0

Figure 4.5 (previous page): Snapshots of slip velocity in a cluster. The time of these snapshots are indicated in the right panel of Figure 4.4.

4.3.3. Transitional slip behavior

When a-b value of a background VSZ is moderate, a cluster shows transitional slip behavior. In Figure 4.6, a time evolution of slip velocity averaged in a cluster is shown when a-b of a background VSZ is 0.0003. Snapshots of slip velocity in a cluster are shown in Figure 4.7. In this regime, periodicity of seismicity observed in the partial seismic regime and the entire seismic regime is less obvious. In an example shown in Figure 4.6, co-seismic ruptures of VW patches are interacted each other through a moderate acceleration of background VSZ. Several seismic ruptures of individual VW patches accelerate slip velocity of a background VSZ up to 10^{-7}-10^{-6} m/s (Figure 4.7d-g). Accelerated background slip trigger next ruptures of VW patches, and they accelerate a background VSZ again. Such complex interaction between seismic and aseismic slips on the fault keeps background slip velocity at about constant for about 100 s. This behavior is similar the transitional slip regime in the previous chapter. Another example is shown in Figure 4.8. Snapshots of slip velocity in a cluster are shown in Figure 4.9. In this event, several (but not all) VW patches ruptures seismically at the same time (Figure 4.9g-i). Although no aftershocks occur after the largest seismic event in the entire seismic regime (Figure 4.5a), aftershocks occur after larger earthquakes in the transitional regime (Figure 4.9j, 4.9l, 4.9m).

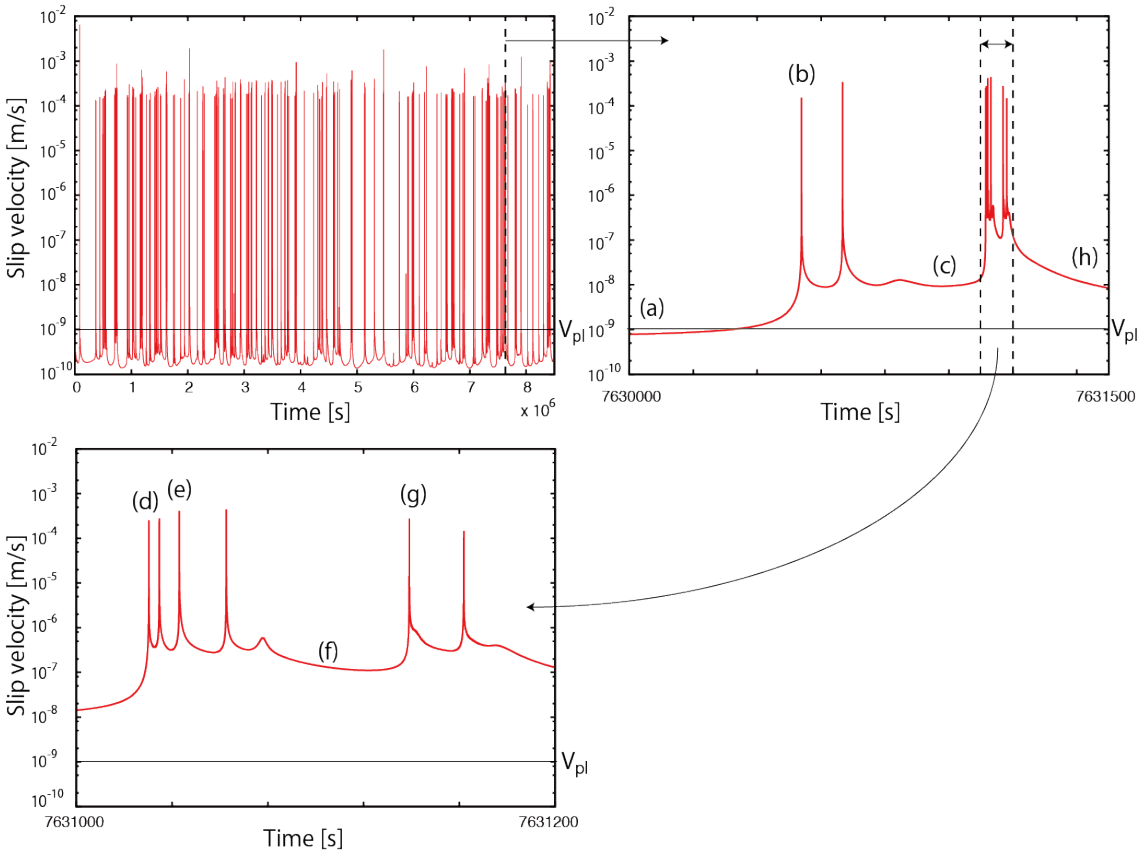

Figure 4.6: Time evolution of slip velocity averaged within a cluster. (a)-(h) in the figure correspond to snapshots shown in Figure 4.7.

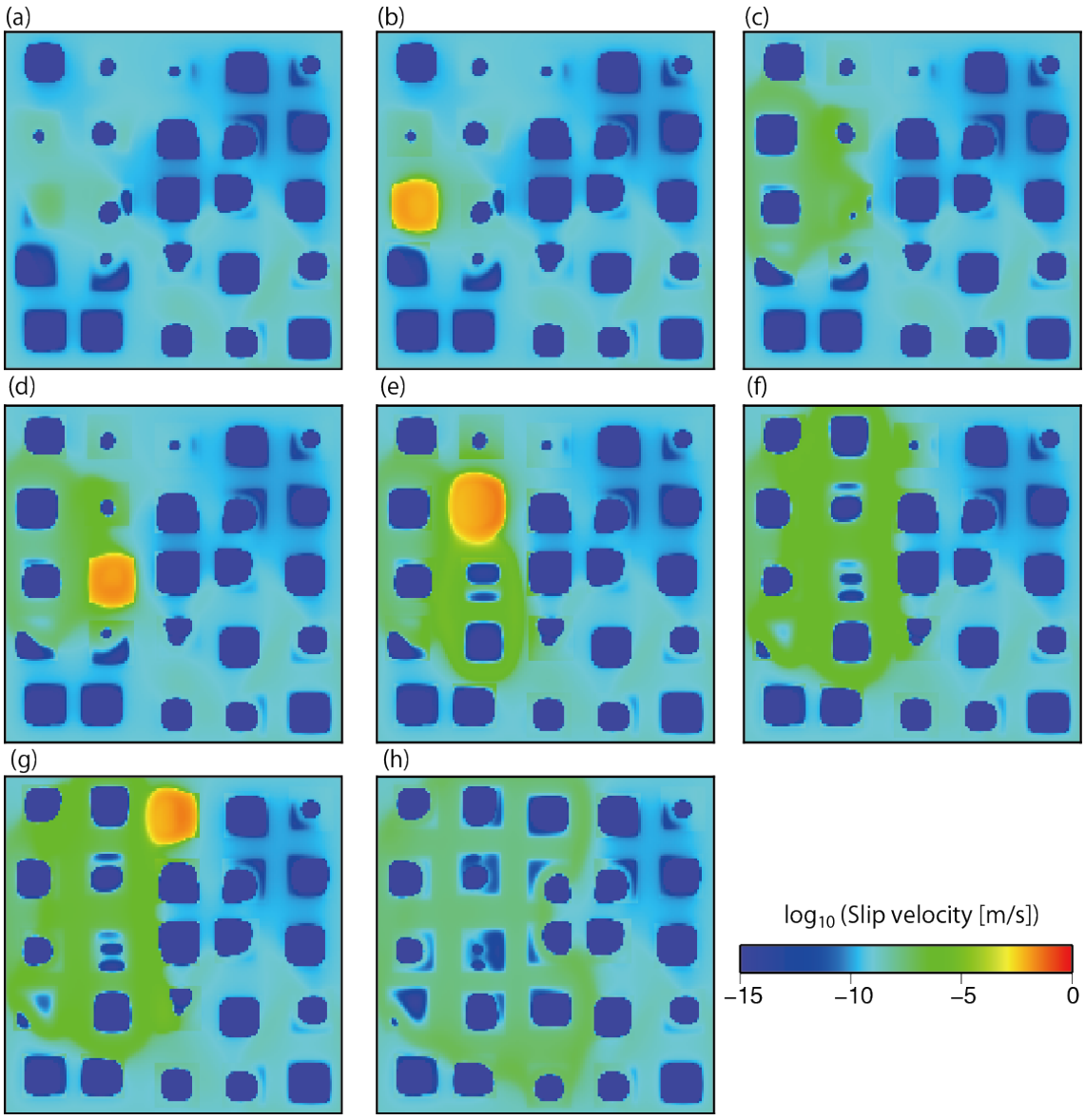

Figure 4.7: Snapshots of slip velocity in a cluster. The time of these snapshots are indicated in the right panel of Figure 4.6.

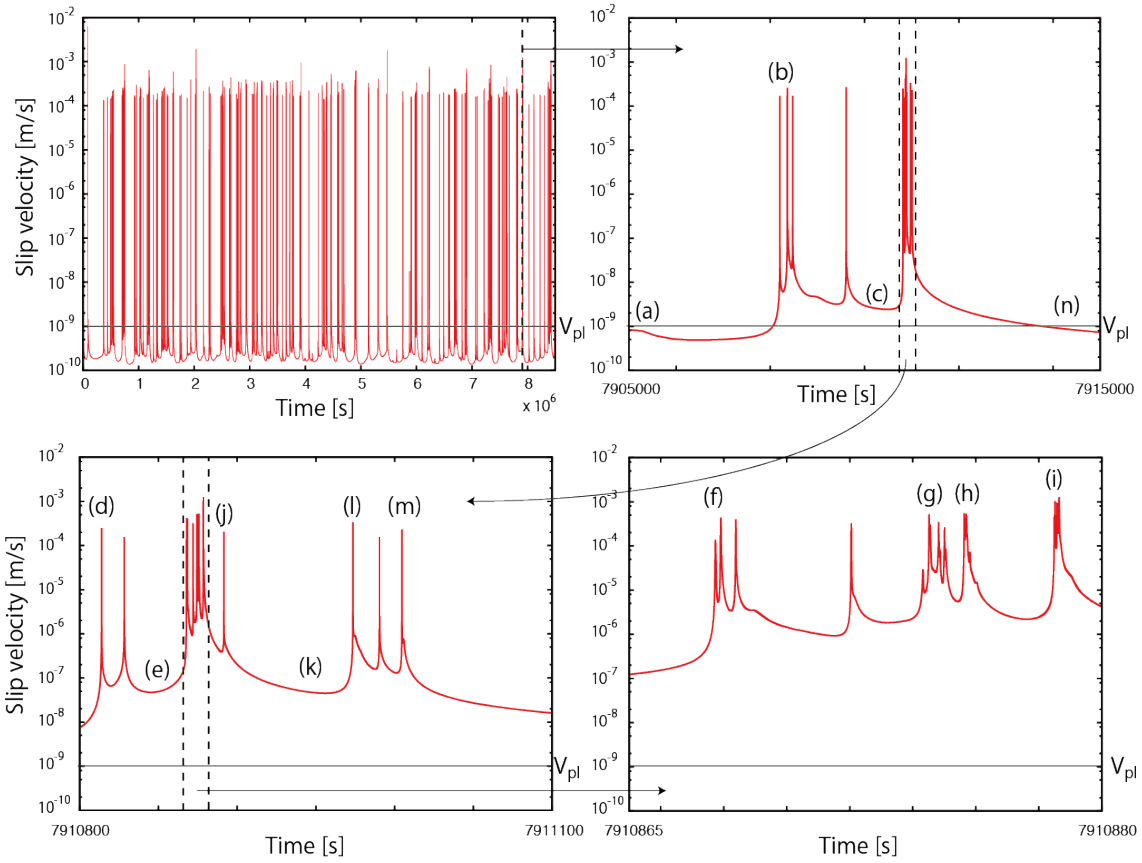

Figure 4.8: Time evolution of slip velocity averaged within a cluster. (a)-(n) in the figure correspond to snapshots shown in Figure 4.9.

Figure 4.9 (next page): Snapshots of slip velocity in a cluster. The time of these snapshots are indicated in the right panel of Figure 4.8.

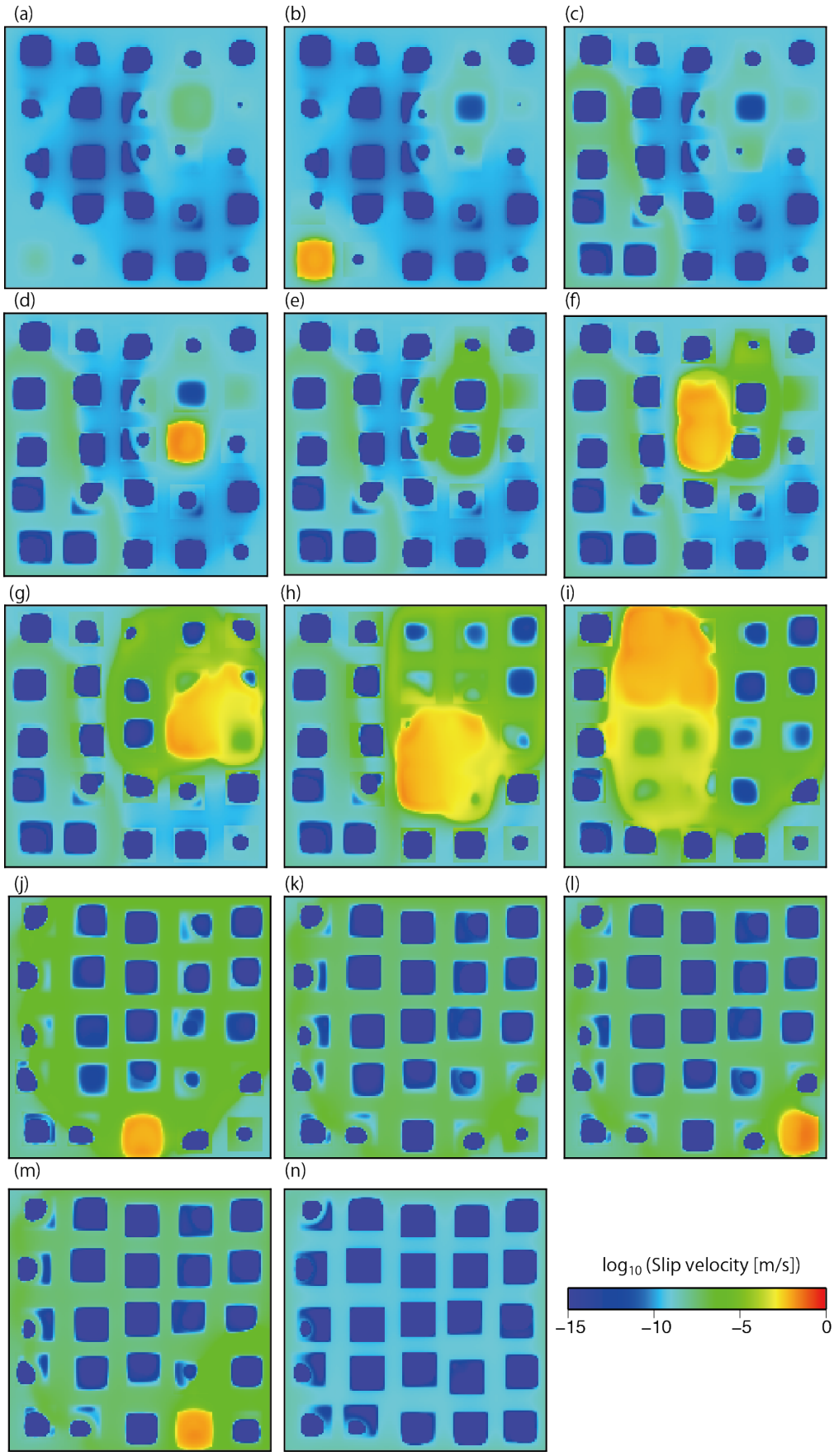
(a)
(b)
(c)
(d)
(e)
(f)
(g)
(h)
(i)
(j)
(k)
(l)
(m)
(n)
log10 (Slip velocity [m/s])
−15
−10
−5
0

4.4. Discussion

It has been confirmed that slip diversity can be observed even with a finite planar fault, in a way it has been discussed in a previous chapter. When a-b value of a background VSZ is large, every VW patch seismically ruptures individually (i.e., the partial seismic regime). Whereas a-b value of a background VSZ is close to zero, the entire cluster ruptures seismically at the same time without occurrences of aftershocks, though it accompanies foreshocks. This behavior can be regarded as the entire seismic regime. In the transition from the partial seismic regime to the entire seismic regime with moderate a-b value of a background VSZ, complex slip behavior is observed, which is not observed in the partial seismic or the entire seismic regime, such as a long-lasting aseismic acceleration of VS background accompanying successive ruptures of individual VW patches and a simultaneous rupture of several (not all) VW patches with surrounding VSZ.

Then, what to be done in a next step is to develop a model, which can quantitatively reproduce the statistics of regular earthquakes and slow earthquakes (for example, the scaling relation between the seismic moment and duration). A future plan to develop the frictionally heterogeneous fault model is discussed in this section.

A big issue is how the transitional slip regime described in the previous section can be related to slow earthquake. The principle feature of slow earthquake is that the seismic moment rate is temporally about constant. Although a VS background is accelerated to 10^{-6}-10^{-7} m/s for a while, which is appropriate to reproduce SSEs (Rubin, 2011), overlapping seismic rupture in VW patches have too large seismic moment rate to represent tremors. How this problem can be solved? Let us consider following frictionally heterogeneous cluster on a fault. A VS background is accelerated to aseismic slip velocity V_a during the transitional slip behavior. When a VW patch ruptures, slip velocity in the patch is locally accelerate to seismic slip velocity V_s. An area of a cluster is L^2, and the portion of a VW patch in a cluster is η. The seismic moment of a cluster is written as,

$$\dot{M} = \mu V_s \eta L^2 + \mu V_a (1-\eta) L^2 . \quad (5.1)$$

If $\eta \sim V_a / V_s$, the moment rate could be kept at about constant value. That is, the size of VW patches should be much smaller than the size of a cluster of VW patches (Figure 4.8). However, the calculation cost will be a problem for numerical simulations of such sumulations. As explained in the previous chapter, the grid discretization should be much smaller than the nucleation size of VW patch. Hence, very large number of grids will be necessary to represent the fault like Figure 4.10. Some technical improvements of calculation algorithm will be required to solve this problem.

Simulating diffusive migration pattern of tremors (Ide, 2010a) is also problematic. Ando et al. (2012) has argued that it cannot be explained with RSF law. It has to be tackled in a future study as well.

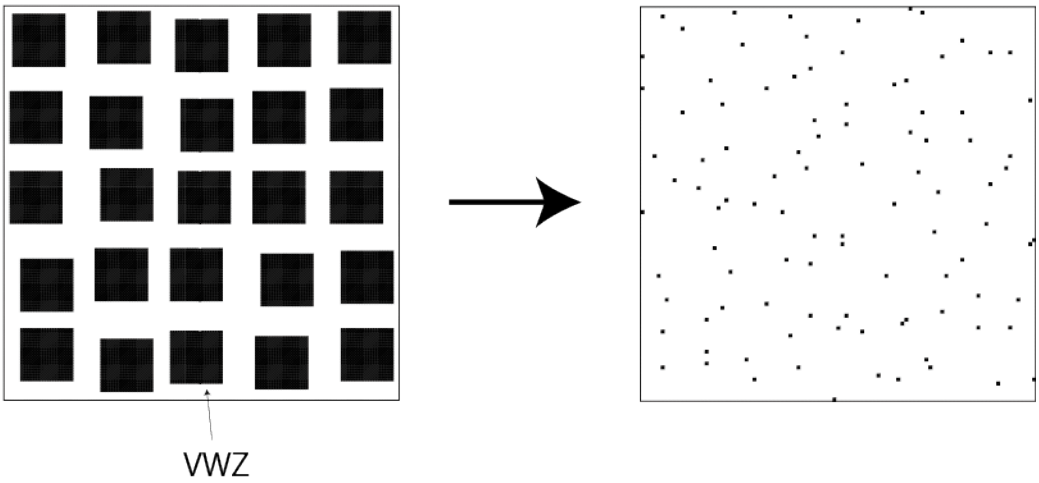

Figure 4.10: A schematic figure of the frictional heterogeneity, which has a potential to reproduce slow earthquake. Black and white areas represent VWZ and VSZ, respectively.

Another big issue should be how to reproduce the constant stress drop and the scale dependency of fracture energy in regular earthquakes. As implied in the previous chapter, the hierarchical distribution of frictional parameters could be a key to solve this problem (Figure 4.11). In such distributions, larger earthquake contains larger portion of VSZ within its rupture area. Because VSZs consume energy to be accelerated, fracture

energy could be scaled by the size of earthquakes. Although higher stress drop can occur locally as well, it will be averaged out, and the average stress drop becomes lower (e.g., Wang and Bilek, 2014). The calculation cost will be a problem for numerical simulations here again.

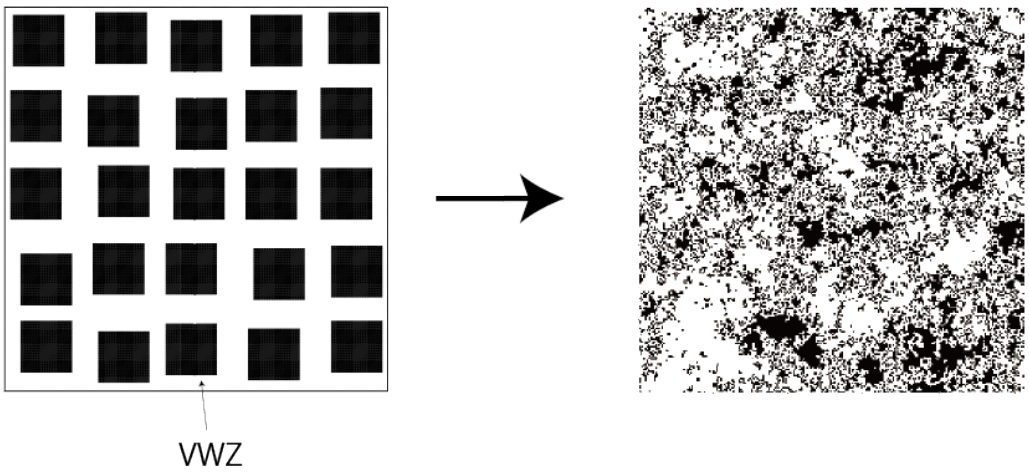

Figure 4.11: A schematic figure of the hierarchical frictional heterogeneity, which has a potential to reproduce scaling of regular earthquakes, as is Figure 4.10. The right panel is made with a method of Klimes (2002) with a fractal dimension of 1.8.

Summarizing the proposed model, the fault is composed of a heterogeneous distribution of RSF parameters, which has the fractal nature. The nucleation size of VWZ is tiny, and the rupture connectivity of VW patches determines the slip behavior. When connected ruptures of VW patches can accelerate VSZ up to seismic slip velocity, the fault shows slip behavior of regular earthquakes. Because the frictional parameter distribution has fractal nature, regular earthquakes will have self-similarity. Afterslip will occur when the seismic rupture of a regular earthquake reaches a wide VSZ on the fault. Transmitted stress by afterslip will trigger aftershocks. When each VW patch ruptures independently without interactions with other VW patches, the fault will show quasi-steady slip because a seismic rupture of an individual tiny VW patch is difficult to observed from the ground surface. At the transitional regime between

regular earthquakes and the quasi-steady slip, the slip behavior of slow earthquakes will be observed. In this regime, seismic ruptures of tiny VW patches are loosely connected, which accelerate a VS background to some extent. A moderate acceleration of a background VSZ is observed as SSE, and local accelerations of slip due to VW patches are observed as tectonic tremors. Such heterogeneities and values of frictional parameter should vary in both along-dip and along-strike direction due to the variation of temperature, pressure (e.g., Blampied et al., 1991; Sawai et al., 2016), irregularity of fault geometry (e.g., Sagy et al., 2007; Candela et al., 2012), material on the fault (e.g., Heuret et al., 2012), etc. Variations of the frictional heterogeneity will result diverse types of subduction zones as discussed in the comparative subductology, such as Chilean-type and Mariana-type subduction zone (Figure 4.12).

In the process constructing this model, it should be first confirmed that this model could explain various statistical feature of regular earthquakes and slow earthquakes. The sensitivity of this model to stress perturbations, such as tidal stress, should be investigated as well to reveal whether observations in Chapter 2 could be explained with this model. When this model is recognized as a candidate of the unified seismic source model, the prediction of this model have to be explored to prove that this model is better than other models. For example, this model could connect statistical parameters of frictional-parameter distributions with statistical parameters of the seismicity. If the frictional heterogeneity is partly attributed to the irregularity of the fault geometry, statistical parameters of fault geometry (such as a fractal dimension) should be related to the seismicity. In the rock experiment, the fault geometry could be directly observed. Seismicity in the experiment could be compared with the prediction of this model. Anyway, there is a long way to go.

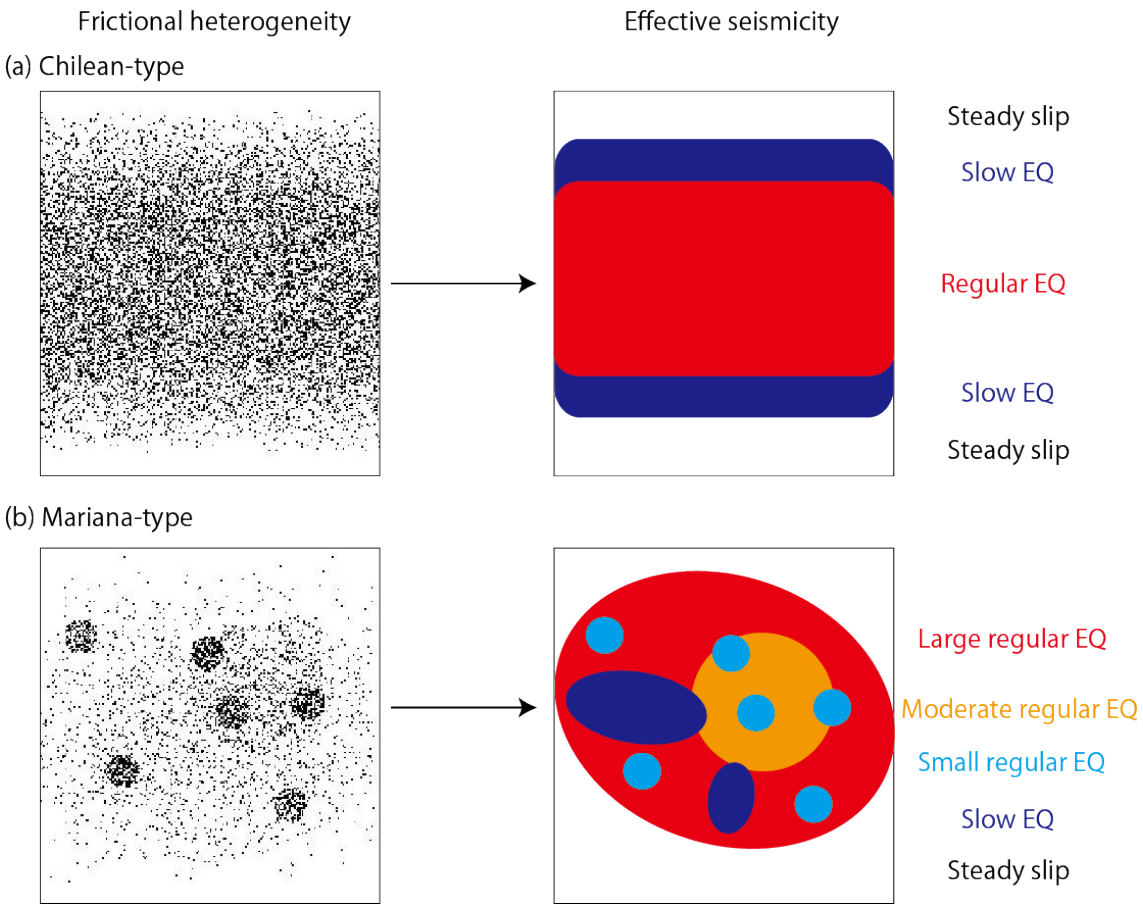

Figure 4.12: A schematic figure of the frictional heterogeneity and seismicity in (a) Chilean-type subduction zones and (b) Mariana-type subduction zone. In the left panel showing the frictional heterogeneity, black dots represents VWZs. A white background represents VSZ.

5. General Discussion

5.1. Significance of This Thesis

A big goal of this research project is to understand the physical mechanism of slip diversity on the plate interface. In Chapter 2 (Yabe et al., 2015), tremor activities in several subduction zones have been quantified in terms of tidal sensitivity. In Yabe and Ide (2014), tremor activities have been quantified in terms of duration and amplitude. Quantifications of tremor activities enable us to compare tremor activities in different places quantitatively. As a result of this comparison, correlations among those values are observed. These correlations are the constraint condition, which should be reproduced by any slow-earthquake source models, many of which are already proposed by previous studies as reviewed in Chapter 1. Among several models, it is suggested in Chapter 2 that observed correlations could be qualitatively explained by the frictionally heterogeneous fault model.

Based on the interpretation in Chapter 2, transitions of slip behavior on the frictionally heterogeneous fault have been investigated in the simplest situation in Chapter 3 (Yabe and Ide, 2017). The simplest situation enables us to derive an analytic solution of the boundary, which will enhance the understanding of slip-behavior transitions of the heterogeneous fault. As a result, we observe the complex slip behavior with slow characteristic deformation rate around the boundary of two slip modes, which may correspond to slow earthquake. This model should be developed further to quantitatively reproduce features of regular earthquakes and slow earthquakes, as the way shown in Chapter 4. Even if the source mechanism of slow earthquake is not related to the frictional heterogeneity, an understanding of slip behavior on a frictionally heterogeneous fault is important because the existence of frictional heterogeneity on the actual fault has been confirmed by geologic field survey (Fagereng and Sibson, 2010).

Seismicity on the plate interface should be affected by many geological conditions, such as temperature, pressure, pore fluid, and materials around the fault. The relation between them has been investigated

for long time. Such a study field has been called “comparative subductlogy”, which has begun in the 1970’s as reviewed in the next section. When the frictionally heterogeneous fault model is successfully developed, this model will provide us a new tool to compare diverse seismicity, which includes not only regular seismicity but also slow earthquakes, with the geological condition, because this model characterize diverse seismicity with a unified index of the frictional heterogeneity. Such comparisons will become a new “comparative subductology”. Furthermore, understanding the fundamental source physics of earthquakes will help us to consider the possibility of earthquake forecasting.

5.2. Comparative Subductology

5.2.1. Classics

After the concept of “plate tectonics” was established in the 1970’s, various phenomena have been interpreted in its context. For example, normal-fault earthquakes at mid-ocean ridges occur due to the tensional stress regime where plates are splitting. Thrust-fault earthquakes around the Pacific occur due to plate subductions. Dipping seismicity has been recognized as Wadati-Benioff zones since the 1920’s (Wadati, 1935). This seismicity reflects subducting oceanic plates. Furthermore, it has been realized that there are differences in the seismicity among subduction zones. Diversity of seismicity in subduction zones has been characterized in terms of the maximum earthquake size by Ruff and Kanamori (1980). They have reported that the maximum earthquake size in each subduction zone is correlated with the age and convergence rate of subducting plate. In a subduction zone where the young oceanic plate is subducted with fast convergence rate, giant earthquakes occur on the plate interface. An extreme example of this type of subduction zone is Chilean subduction zone, where the largest recorded earthquake (M9.5) occurred in 1960 (Kanamori, 1977). On the other hand, in a subduction zone where the old oceanic plate is subducted with slow convergence rate, no great earthquakes had been reported. An extreme example is Mariana subduction zone. Uyeda and Kanamori (1979) insisted that these two subduction zones are end members

of subduction zones in terms of stress field as well (Figure 5.1). In Chilean-type subduction zone, an oceanic plate is subducted with the shallow dip, which causes compressional stress regime. Whereas in Mariana-type subduction zone, an oceanic plate is subducted with the steep dip. Furthermore, the back-arc spreading is ongoing in Mariana-type subduction zones. These features represent the extensional stress regime in Mariana-type subduction zone. Based on these comparisons, tectonic environments in subduction zones are attributed to the diversity of the maximum size of regular earthquake in the classic comparative subductology.

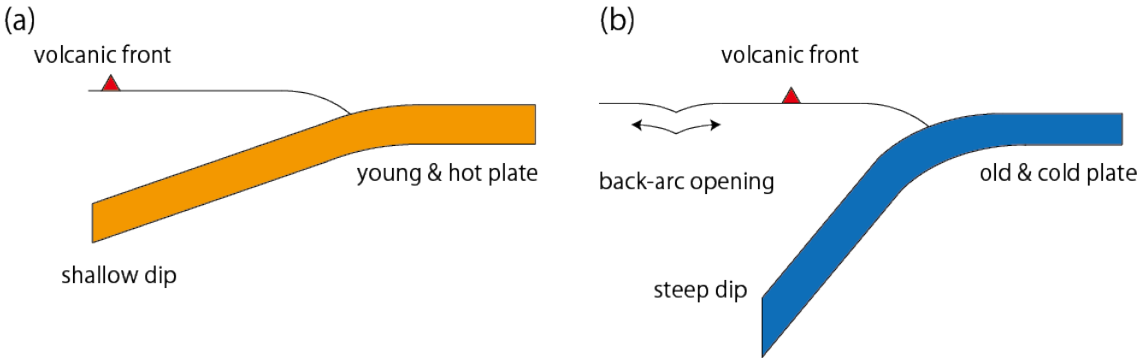

Figure 5.1: Schematic figure of (a) Chilean-type subduction zone and (b) Mariana-type subduction zone.

5.2.2. Revisit

After several giant earthquakes occurred around the Pacific, the classic comparative subductology has been revisited. Geodetic, geologic, and seismic information are updated, vanishing correlations among them observed by Ruff and Kanamori (1980) (Stein and Okal, 2007). Instead, it has been insisted that the maximum magnitude could be larger than M9 in all subduction zones (McCaffrey, 2008; Kagan and Jackson, 2013).

Giant earthquakes sometimes generate devastating tsunami, as human society experienced in 2004 Sumatra earthquake and 2011 Tohoku-oki earthquake. Such large tsunami leaves tsunami deposit on land, which is preserved in the geological formation. Hence, we can use tsunami deposit to reconstruct history of giant earthquakes (Atwater et al., 1995).

Filed observations of tsunami deposits clarified that the recurrence intervals of giant earthquakes are on the order of several hundreds years. Hence, now seismologists strongly realize that our record of giant earthquakes is not statistically complete because the period of our recordings spans at most a hundred years, which is much shorter than the timescale of giant-earthquake recurrences (McCaffrey, 2008). Therefore, discussions of the maximum earthquake size made by the classical comparative subductology are really difficult.

5.2.3. New era

It seems that the comparative subductology has been denied after several giant earthquakes. However, the differences in the seismicity actually exist among subduction zones, as is observed around Japan. In Figure 5.2, earthquakes recorded in the F-net catalog are shown for Tohoku and Nankai subduction zones. In Tohoku subduction zone along Japan Trench, various sizes of regular earthquakes from tiny one to 2011 M9 occur frequently on the plate interface. On the other hand, the plate interface of Nankai subduction zone is highly locked, and regular earthquakes rarely occur on the plate interface during an inter-seismic period of large (expected about M8) earthquakes (e.g., Ide, 2013). Such difference in the seismicity including smaller earthquakes should provide useful information to construct new comparative subductology.

Statistical parameters estimated by ETAS model are useful for this purpose. Ide (2013) revealed that background (declustered) seismicity rate estimated by ETAS model is proportional to the convergence rate. Because plate convergence accumulates strain on the fault, this result is very natural, though it has not quantitatively clarified so far. Furthermore, correlations between b-value and the plate age of subducted plate and between background seismicity rate and bending of subducted plate are shown by Nishikawa and Ide (2014, 2015). Such information will provide useful constraints on the physical mechanism connecting tectonic environments and earthquake genesis.

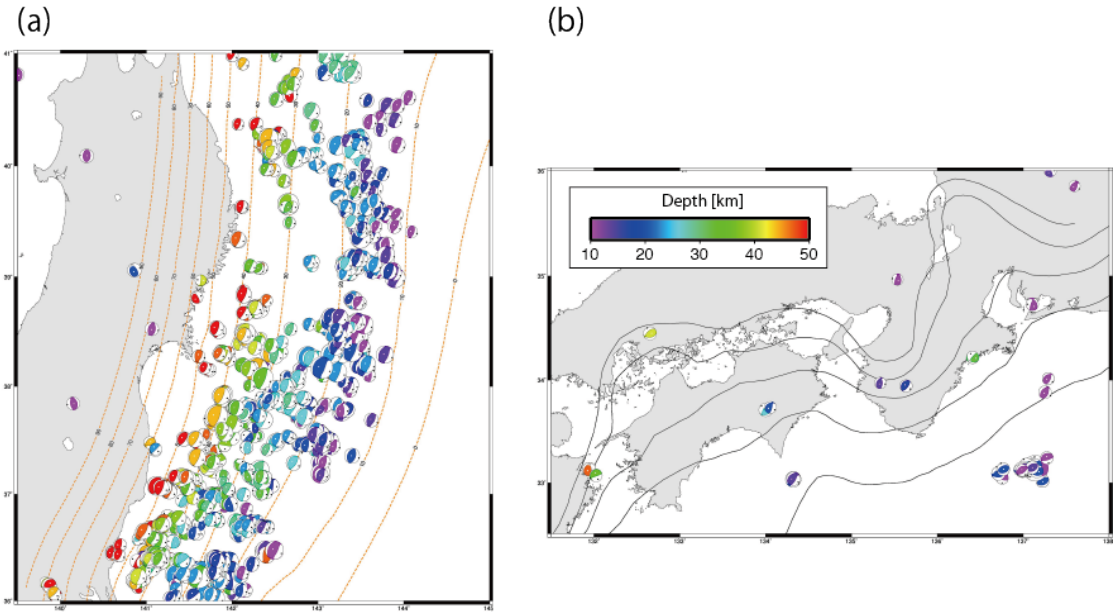

Figure 5.2: Seismicity recorded by F-net catalog in (a) Tohoku and (b) Nankai subduction zones. Earthquakes are selected between 1997/1/1-2011/3/11 (before M9 earthquake). Depth is confined between 10-50km. Fault plane of selected earthquake is strike: 170-220° (Tohoku) or 200-250° (Nankai), dip: 0-45°, and rake: 60-120°. Contours represent the depth of plate interface at every 10km interval (Baba et al., 2002; Nakajima and Hasegawa, 2006, 2007; Hirose et al., 2008a, 2008b; Nakajima et al., 2009; Kita et al, 2010).

Discovery of slow earthquakes in 21st century also provides new information to the comparative subductology. Now, slow earthquakes are widely observed in many subduction zones with diverse style. Active deep ETS has been observed in Nankai and Cascadia subduction zones (Rogers and Dragert, 2003; Obara et al., 2004). However, shallow ETS has been detected only in Nankai subduction zones (Obara and Ito, 2005). In Tohoku-Hokkaido subduction zone, SSEs with small regular earthquakes have been detected within the rupture area of M9 earthquakes (Ito et al., 2012; Kato et al., 2012). Shallow VLFs have been identified as well (Asano et al., 2008). Below Boso peninsula, SSEs with regular earthquakes have been identified as well (Ozawa et al., 2003). In Mexican subduction zones, deep tremor activities have been discovered widely along the strike, though

they are divided into clusters (Brudzinski et al., 2010; Ide, 2012; Maury et al., 2016), which is different from Nankai and Cascadia. Hikurangi subduction zone in New Zealand hosts large SSEs (Wallace and Beavan, 2010). However, deep tremor activities are very weak (Fry et al., 2011; Kim et al., 2011; Ide, 2012). Regular earthquakes synchronized with SSEs have been identified as well (Wallace et al., 2012). In Mariana subduction zone, swarms of regular earthquakes have been detected, which implies that SSEs occur in Mariana subduction zone as well (Holtkamp and Brudzinski, 2011). Slow earthquakes have been identified in various locations including Alaska (Ohta et al., 2006), Costa Rica (Brown et al., 2005), Chile (Ide, 2012), Taiwan (Peng and Chao, 2008), San Andreas Fault (Nadeau and Dolenc, 2005), and Alpine Fault (Wech et al., 2012) as well. Therefore, comparison of slow earthquake seismicity with tectonic environment should also provide useful information as well as the comparison of regular-earthquake seismicity.

This research project aims to construct a seismic source model, which can explain both regular seismicity and slow earthquake seismicity by different frictional heterogeneity. In other words, when the model is established, diverse seismic phenomena including regular earthquakes and slow earthquakes are characterized by a uniform index of the frictional heterogeneity. It will enable us to compare diverse seismic phenomena with tectonic environment in a unified manner (Figure 5.3).

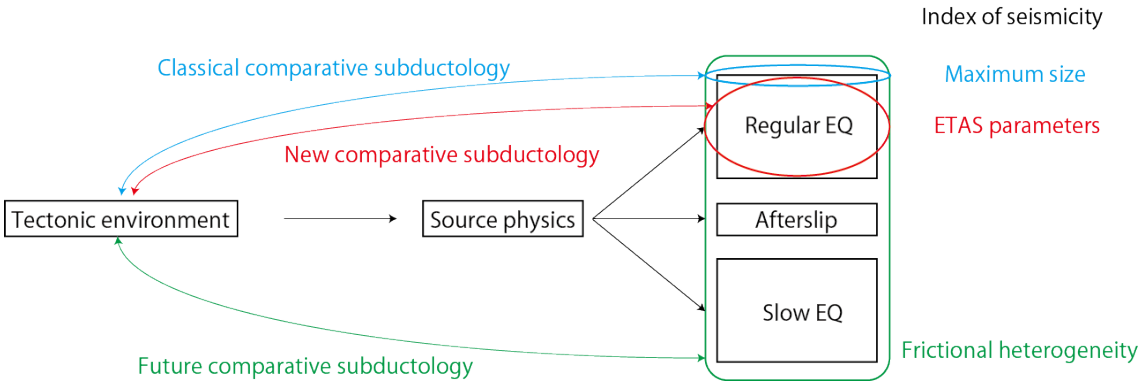

Figure 5.3: A schematic figure of the comparative subductology.

5.3. Future Studies

Finally, several topics are listed here, which should be addressed in future studies, in addition to the development of the frictionally heterogeneous fault model discussed in Chapter 4.

5.3.1. Deep slow earthquake vs Shallow slow earthquake

In Chapter 2, tremor activities of deep slow earthquake have been investigated. However, in some subduction zones, such Nankai and Costa Rica, slow earthquake exists at the up-dip part of plate interface (Obara and Ito, 2005; Dixon et al., 2014). As temperature is different between the source area of shallow and deep slow earthquake, it is very interesting to see whether there are any differences in slow earthquake activity. For this purpose, quantification of tremor activity as is done in Chapter 2 should be very useful. However, the observation of shallow slow earthquake is more difficult than that of deep slow earthquake because source area of shallow slow earthquake is usually located offshore. Hence, seismic signals of shallow tremors are recorded by ocean bottom seismometers (OBSs). Because OBS data sometimes have unique noise different from onshore data, such as water reverberations, careful analysis will be needed.

5.3.2. Triggering of slow earthquake in various frequencies

Tidal sensitivity of tectonic tremors has been investigated in Chapter 2. As discussed in Chapter 2, tidal sensitivity is expected to reflect frictional parameter on the plate interface because tidal sensitivity of tremors represents slip response of the fault to stress perturbations. By the way, the source of stress perturbations on the plate interface is not restricted to diurnal or semi-diurnal tidal stress. It has been already recognized that stress perturbations due to traveling surface wave can trigger tremors (Miyazawa and Mori, 2005; Miyazawa, 2012). Atmospheric pressure change at the ground surface can also perturb stress on the plate interface, and it is discussed that SSE was triggered by typhoon in Taiwan (Liu et al., 2009). Amplitudes of diurnal and semi-diurnal tidal stress are modulated by spring-neap tide with two-week and one-month periods. Seasonal variation

seems to be observed in tremor activity of an isolated Okayama cluster (Ide and Tanaka, 2014). Even longer tidal periods also exist (8.85 yr and 18.6 yr; e.g., Tanaka, 2014). Non-tidal modulation of ocean height perturbs stress on the plate interface as well (Tanaka et al., 2015). How tremor activity or slip on the fault reacts to those stress perturbations in different frequencies will provide us further information about frictional property on the plate interface. According to the analysis of a spring-block system, response of slip to stress perturbations changes with the frequency of stress perturbations (Ader et al., 2012). Hence comparisons of sensitivity in different frequencies will be helpful to constrain the frictional parameter on the fault.

5.3.3. Initial moment growth of slow earthquake

Scaling relation of slow earthquakes that the seismic moment is proportional to the duration of events (Ide et al., 2007b) is one of the most important characteristics of slow earthquake. However, there is possibility that this scaling relation is biased due to the noise in seismic observations (Ide, 2010b). Seismic moments can be estimated using seismograms as the low frequency limit of displacement spectrum. However, because LFEs are tiny signals at 2-8 Hz, lower frequency signals are buried below the noise. Instead, the amplitude of tectonic tremors is compared with regular earthquakes to empirically determine the seismic moment. However, because the shape of spectrum is different between slow earthquake and regular earthquake, estimated seismic moments of LFEs could be underestimations.

Mathematical models of Ide (2008, 2010b) and Ben-Zion (2012) predict the kink of scaling law for slow earthquakes. They predict that the seismic moment grows proportional to the square of the event duration when the seismic moment is relatively small. When it exceeds some threshold, the moment growth becomes linearly proportional to the duration. On the other hand, Gomberg et al. (2016) propose the common scaling law for regular earthquake and slow earthquake based on the assumption of constant stress drop. In their model, the seismic moment grows proportional to the cube of duration when the seismic rupture does not feel the boundary of fault. When

the rupture approaches the edge of rupture zone in the dip direction, the moment growth becomes linearly proportional to the duration. The difference in scaling law between regular earthquake and slow earthquake is the elongation of duration due to low stress drop and slow rupture propagation.

It is very important to clarify what kind of scaling law should be reproduced in the source model. Hence, the scaling law of slow earthquake for smaller seismic moments should be constrained through data analysis. When the seismic moment of slow earthquake is small, it is difficult to detect its signal in GNSS observations. Hence, combination analysis of seismic signals (short-period and long-period seismograms), and geodetic signals (strain, tilt, and GNSS) should be needed.

6. Summary

Dense and high-sensitivity observation networks in seismology and geodesy in the 21st century have revealed diverse style of fault slip on the plate interface of subduction zones, including regular earthquakes, afterslips, and slow earthquakes. The motivation of this thesis is to understand the physical mechanism of such slip diversity. Understanding physical mechanism of slip diversity is important to understand the whole seismic cycle in subduction zones, including the strain accumulation process of giant earthquakes and interactions between slow earthquake and regular earthquakes. The first half of this thesis has tried to constrain the physical mechanism of slow earthquake through data analysis of slow earthquake, which will facilitate the understanding of slip diversity. Then, it has shown that a result of data analysis is qualitatively consistent with the frictionally heterogeneous fault model. Hence, the slip behavior of a frictionally heterogeneous fault has been investigated in the latter half of this thesis. Although the model is still preliminary, and it cannot be compared with actual seismicity yet, it has been shown that the frictionally heterogeneous fault model has a potential to explain slip diversity on the plate interface.

As is the seismicity of regular earthquakes, the seismicity of slow earthquakes varies among subduction zones and even within an individual subduction zone. In Chapter 2, activities of tectonic tremor, which is high frequency component of slow earthquake, have been quantified in terms of tidal sensitivity in several subduction zones. Spatial variations of tidal sensitivity are compared with those of other characteristics (duration and amplitude), which have been quantified in a previous study. As a result, short-duration tremors tend to show higher tidal sensitivity. It has been also observed that tidal sensitivity increases after large-amplitude tremors occur, which are not sensitive to tidal stress. Because tidal sensitivity of tectonic tremor represents slip response to stress perturbations, it is expected to have information of frictional properties on the fault. An exponential relation between tremor rate and tidal stress implies the existence of rate and state friction law on the plate interface. Spatial variations of tidal sensitivity

imply spatial heterogeneities of frictional parameters. Correlations among tidal sensitivity, duration, and amplitude of tectonic tremors could be qualitatively interpreted with the frictionally heterogeneous fault model.

Based on the qualitative model proposed in Chapter 2, slip behavior of a linear fault with the simplest frictional heterogeneity governed by rate and state friction law has been investigated in Chapter 3. Shear slip behavior on the heterogeneous fault varies with the frictional heterogeneity. An analytical exploration has revealed that the spatial average of a-b value of rate and state friction law is important to determine the slip behavior on the frictionally heterogeneous fault. When the spatial average of a-b is positive, seismic slip is limited within the velocity-weakening zone where a-b is negative. On the other hand, when the spatial average of a-b is negative, the entire fault including velocity-strengthening zone, where the spatial average of a-b is positive, slips seismically. Complex interactions occur between seismic slip in velocity-weakening zone and aseismic slip in velocity-strengthening zone at this transition, where the spatial average of a-b is close to zero. Slower deformation dominates during seismic events, which may correspond to slow earthquakes. It has been also suggested that the scale dependency of fracture energy might be explained by hierarchical distributions of frictional parameters. In Chapter 4, some examples of numerical simulations with the frictional heterogeneity on a finite planar fault have been presented. It has been also discussed in Chapter 4 how the model should be developed to quantitatively reproduce statistical feature of slow earthquakes and regular earthquakes in the frictionally heterogeneous fault model.

In the 1970's and the 1980's, seismicity of regular earthquakes has been compared with tectonic environments of subduction zones, which is called the comparative subductology. Subduction zones have been categorized into Chilean type and Mariana type. In Chilean-type subduction zones, a young and hot oceanic plate is subducted with giant earthquakes. On the other hand, in Mariana-type subduction zones, where back-arc spreading is ongoing, an old and cold oceanic plate is subducted without giant earthquakes. Such comparisons have been criticized recently by

updating various information. Because the frequency of giant earthquakes is very low, our seismic catalogs of giant earthquakes are statistically incomplete. Now, uses of seismicity-statistics parameter have been suggested for the comparison between seismicity of regular earthquakes and tectonic environments because parameters of seismicity statistics can be evaluated more robustly using smaller earthquakes. Developments of the frictionally heterogeneous fault model as a unified seismic source model will provide us a new tool for such comparisons in the comparative subductology. The frictionally heterogeneous fault model can uniformly characterize diverse seismic phenomena, including regular earthquakes, afterslips, and slow earthquakes, in terms of the frictional heterogeneity. Hence, diverse seismic phenomena can be uniformly compared with tectonic environments with the frictionally heterogeneous fault model. Understanding physical mechanism of slip diversity will also contribute to the consideration of the possibility of earthquake forecasting.

Acknowledgements

First of all, I express my great appreciation to my advisor, Prof. Satoshi Ide. Since I started my research activity six years ago, he has provided various supports on my research, including discussions, inspirations, and research funding.

I would like to thank Dissertation Committee (Prof. Kazushige Obara, Prof. Shingo Yoshida, Ass. Prof. Hiroshi Tsuruoka, Ass. Prof. Nobuki Kame, Ass. Prof. Ryosuke Ando) for reviewing this thesis.

I am also grateful to my co-workers so far, Prof. Shoichi Yoshioka in Kobe University, Dr. Koki Idehara in PRRISM, Dr. Annemari Baltay in USGS, Prof. Gregory Beroza in Stanford University, Dr. Yoshiyuki Tanaka in Earthquake Research Institute, Prof. Kate Chen and Ms. Hsin-Ju Tai in National Taiwan Normal University, and Prof. Heidi Houston in Washington University. Discussions with them were very helpful for my research. Collaborations with various researchers have widened my research interests. I also thank to all researchers interacted with me so far for their discussions and advices.

All the seismic observation data used in this study has been downloaded from National Research Institute for Earth Science and Disaster Resilience, Incorporated Research Institutions for Seismology, and Canadian National Data Center. I appreciate the effort of all who maintains networks. For calculations, the computer system of the Earthquake and Volcano Information Center of the Earthquake Research Institute, the University of Tokyo has been utilized. GMT software (Wessel and Smith, 1998) is used to draw some figures.

My research projects have been supported by JSPS Institutional Program for Young Researcher Overseas Visits, JSPS KAKENHI (20340115, 23244090, and 14J08291) and by MEXT Japan (21107007, the Earthquake and Volcano Hazards Observation and Research Program, and the Program for Leading Graduate Schools). I am grateful to administrative stuffs in University of Tokyo as well.

Finally, I express my great appreciation to my wife, Moe, and family for their understanding, support, and kind cooperation.

Suguru Yabe

Tokyo, March 2016

References

Abercrombie, R. E., and J. R. Rice (2005), Can observations of earthquake scaling constrain slip weakening?, *Geophys. J. Int., 162*(2), 406–424, doi:10.1111/j.1365-246X.2005.02579.x.

Ader, T. J., J.-P. Ampuero, and J.-P. Avouac (2012), The role of velocity-neutral creep on the modulation of tectonic tremor activity by periodic loading, *Geophys. Res. Lett., 39*, L16310, doi:10.1029/2012GL052326.

Agnew, D. C. (2012), SPOTL: Some Programs for Ocean-Tide Loading, SIO Technical Report, Scripps Institution of Oceanography.

Aki, K. (1966), Generation and Propagation of G Waves from the Niigata Earthquake of June 16, 1964. : Part 2. Estimation of earthquake moment, released energy, and stress-strain drop from the G wave spectrum. *Bull. Earthquake Res. Inst., Tokyo Univ., 44*, 73-88.

Aki, K., and P. Richards (2002), Quantitative Seismology 2nd Ed., University Science Books, Sausalito, California.

Allis R.G., R. Funnell, and X. Zhan (1998), From basins to mountains and back again: NZ basin evolution since 10 Ma. Proceedings 9th International Symposium on Water-Rock Interaction, Taupo New Zealand, 3–7.

Allmann, B. P., and P. M. Shearer (2009), Global variations of stress drop for moderate to large earthquakes, *J. Geophys. Res., 114*, B01310, doi:10.1029/2008JB005821.

Ampuero, J.-P. (2002), Etude physique et numerique de la nucleation des seismes, Ph.D. thesis, Univ. Paris 7, Denis Diderot, Paris.

Ampuero, J.-P., and A. M. Rubin (2008), Earthquake nucleation on rate and state faults – Aging and slip laws, *J. Geophys. Res., 113*, B01302, doi:10.1029/2007JB005082.

Ando, R., and T. Yamashita (2007), Effects of mesoscopic-scale fault structure on dynamic earthquake ruptures: Dynamic formation of geometrical complexity of earthquake faults, *J. Geophys. Res., 112*,

B09303, doi:10.1029/2006JB004612.

Ando, R., R. Nakata, and T. Hori (2010), A slip pulse model with fault heterogeneity for low-frequency earthquakes and tremor along plate interfaces, *Geophys. Res. Lett., 37*, L10310, doi:10.1029/2010GL043056.

Ando, R., N. Takeda, and T. Yamashita (2012), Propagation dynamics of seismic and aseismic slip governed by fault heterogeneity and Newtonian rheology, *J. Geophys. Res., 117*, B11308, doi:10.1029/2012JB009532.

Andrews, D. J. (1976), Rupture velocity of plane strain shear cracks, *J. Geophys. Res., 81*(32), 5679–5687, doi:10.1029/JB081i032p05679.

Andrews, D. J. (2005), Rupture dynamics with energy loss outside the slip zone, *J. Geophys. Res., 110*, B01307, doi:10.1029/2004JB003191.

Archuleta, R. J. (1984), A faulting model for the 1979 Imperial Valley earthquake, *J. Geophys. Res., 89*(B6), 4559–4585, doi:10.1029/JB089iB06p04559.

Ariyoshi, K., T. Hori, J.-P. Ampuero , Y. Kaneda, T. Matsuzawa, R. Hino, and A. Hasegawa (2009) Influence of interaction between small asperities on various types of slow earthquakes in a 3-D simulation for a subduction plate boundary. *Gondwana Res., 16*(3-4), 534-544, doi:10.1016/j.gr.2009.03.006

Ariyoshi, K., T. Matsuzawa, J.-P. Ampuero, R. Nakata, T. Hori, Y. Kaneda, R. Hino, and A. Hasegawa (2012), Migration process of very low-frequency events based on a chain-reaction model and its application to the detection of preseismic slip for megathrust earthquakes, *Earth Planets Space, 64*(8), 693–702, doi:10.5047/eps.2010.09.003.

Asano, Y., K. Obara, and Y. Ito (2008), Spatiotemporal distribution of very-low frequency earthquakes in Tokachi-oki near the junction of the Kuril and Japan trenches revealed by using array signal processing, *Earth Planets Space, 60*(8), 871 – 875, doi:10.1186/BF03352839.

Aso, N., K. Ohta, and S. Ide (2013), Tectonic, volcanic, and semi-volcanic deep low-frequency earthquakes in western Japan, *Tectonophysics, 600,* 27–40, doi:10.1016/j.tecto.2012.12.015.

Atwater, B. F., A. R. Nelson, J. J. Clague, G. A. Carver, D. K. Yamaguchi, P. T. Bobrowsky, J. Bourgeois, M. E. Darienzo, W. C. Grant, E. Hemphill-Haley, H. M. Kelsey, G. C. Jacoby, S. P. Nishenko, S. P. Palmer, C. D. Peterson, and M. A. Reinhart (1995), Summary of coastal geologic evidence for past great earthquakes at the Cascadia subduction zone, *Earthquake Spectra, 11*(1), 1–18, doi:10.1193/1.1585800.

Audet, P., M. G. Bostock, N. I. Christensen, and S. M. Peacock (2009), Seismic evidence for overpressured subducted oceanic crust and megathrust fault sealing, *Nature, 457*, 76-78, doi:10.1038/nature07650.

Baba, T., Y. Tanioka, P. R. Cummins, and K. Uhira (2002), The slip distribution of the 1946 Nankai earthquake estimated from tsunami inversion using a new plate model, *Phys. Earth Planet. Inter., 132*(1-3), 59-73, doi:10.1016/S0031-9201(02)00044-4.

Barenblatt, G. I. (1959), The formation of equilibrium cracks during brittle fracture: General ideas and hypothesis: Axially symetric cracks. *J. Appl. Math. Mech., 23*(3), 622–636, doi:10.1016/0021-8928(59)90157-1.

Beeler, N. M., A. Thomas, R. Bürgmann, and D. Shelly (2013), Inferring fault rheology from low-frequency earthquakes on the San Andreas, *J. Geophys. Res., 118*, 5976–5990, doi:10.1002/2013JB010118.

Ben-Zion, Y. (2012), Episodic tremor and slip on a frictional interface with critical zero weakening in elastic solid. *Geophys. J. Int., 189*(2), 1159-1168, doi:10.1111/j.1365-246X.2012.05422.x.

Beroza, G., and P. Spudich (1988), Linearized inversion for fault rupture behavior: Application to the 1984 Morgan Hill, California, earthquake, *J. Geophys. Res., 93*(B6), 6275–6296, doi:10.1029/JB093iB06p06275.

Beroza, G. C., and S. Ide (2011), Slow earthquakes and nonvolcanic tremor, *Annu. Rev. Earth Planet. Sci., 39*, 271–296, doi:10.1146/annurev-earth-040809-152531.

Bilek, S. L., and T. Lay (2002), Tsunami earthquakes possibly widespread manifestations of frictional conditional stability, *Geophys. Res. Lett., 29*(14), doi:10.1029/2002GL015215.

Blanpied, M. L., D. A. Lockner, and J. D. Byedee (1991), Fault stability inferred from granite sliding experiments at hydrothermal conditions,

Geophys. Res. Lett., 18(4), 609-612, doi:10.1029/91GL00469.

Bostock, M. G., A. M. Thomas, G. Savard, L. Chuang, and A. M. Rubin (2015), Magnitudes and moment-duration scaling of low-frequency earthquakes beneath southern Vancouver Island, *J. Geophys. Res. Solid Earth, 120*, 6329-6350, doi:10.1002/2015JB012195.

Brown, K. M., M. D. Tryon, H. R. DeShon, L. M. Dorman, and S. Y. Schwartz (2005), Correlated transient fluid pulsing and seismic tremor in the Costa Rica subduction zone, *Earth Planet. Sci. Lett., 238*(1-2), 189 – 203, doi:10.1016/j.epsl.2005.06.055.

Brudzinski, M. R., H. R. Hinojosa-Prieto, K. M. Schlanser, E. Cabral-Cano, A. Arciniega-Ceballos, O. Diaz-Molina, and C. DeMets (2010), Nonvolcanic tremor along the Oaxaca segment of the Middle America subduction zone, *J. Geophys. Res., 115*, B00A23, doi:10.1029/2008JB006061.

Brune, J. N. (1970) Tectonic stress and spectra of seismic shear waves from earthquakes, *J. Geophys. Res., 75*(26), 4997–5009, doi:10.1029/JB075i026p04997.

Bucknam, R. C., G. Plafker, and R. V. Sharp (1978), Fault movement (afterslip) following the Guatemala earthquake of February 4, 1976, *Geology, 6*(3), 170–173, doi:10.1130/0091-7613(1978)6<170:FMAFTG>2.0CO;2.

Candela, T., F. Renard, Y. Klinger, K. Mair, J. Schmittbuhl, and E. E. Brodsky (2012), Roughness of fault surfaces over nine decades of length scales, *J. Geophys. Res., 117*, B08409, doi:10.1029/2011JB009041.

Chao, K., and K. Obara (2016), Triggered tectonic tremor in various types of fault systems of Japan following the 2012 Mw8.6 Sumatra earthquake, *J. Geophys. Res., 121*, 170-187, doi:10.1002/ 2015JB012566.

Christodouridis, D. C., D. E. Smith, R. Kolenkiewicz, S. M. Klosko, M. H. Torrence, and P. J. Dunn (1985), Observing tectonic plate motions and deformations from satellite laser ranging, *J. Geophys. Res., 90*(B11), 9249-9263, doi: 10.1029/JB090iB11p09249.

Cochran, E. S., J. E. Vidale, and S. Tanaka (2004), Earth tides can trigger shallow thrust fault earthquakes, *Science, 306*(5699), 1164–1166, doi:10.1126/science.1103961.

Dahlen, F. A. (1977), The balance of energy in earthquake faulting, *Geophys. J. Int., 48*(2), 239–261, doi:10.1111/j.1365-246X.1977.tb01298.x.

DeMets, C., R. G. Gordon, and D. F. Argus (2010), Geologically current plate motions, *Geophys. J. Int., 181*(1), 1–80, doi:10.1111/j.1365-246X.2009.04491.x.

Di Toro, G., D. L. Golbsby, and T. E. Tullis (2004), Friction falls toward zero in quartz rock as slip velocity approaches seismic rates, *Nature, 427*, 436–439, doi:10.1038/nature02249.

Dieterich, J. H. (1978). Time-dependent friction and the mechanics of stick-slip, *Pure Appl. Geophys. 116*(4), 790–806, doi:10.1007/BF00876539.

Dieterich, J. H. (1979), Modeling of rock friction: 1. Experimental results and constitutive equations, *J. Geophys. Res., 84*(B5), 2161–2168, doi:10.1029/JB084iB05p02161.

Dixon, T. H., Y. Jiang , R. Malservisi, R. McCaffrey, N. Voss, M. Protti, and V. Gonzalez (2014), Earthquake and tsunami forecasts: Relation of slow slip events to subsequent earthquake rupture, *Proc. Natl. Acad. Sci. U. S. A., 111*(48), 17039–17044, doi:10.1073/ pnas.1412299111.

Dragert, H., K. Wang, and T. S. James (2001), A silent slip event on the deeper Cascadia subduction interface, *Science, 292*(5521), 1525–1528, doi:10.1126/science.1060152.

Dublanchet, P., P. Bernard, and P. Favreau (2013), Interactions and triggering in a 3-D rate-and-state asperity model, *J. Geophys. Res., 118*, 2225–2245, doi:10.1002/jgrb.50187.

Dziewonski A. M, and A. Anderson (1981), Preliminary reference earth model, *Phys. Earth Planet. Inter., 25*(4), 297–356, doi:10.1016/0031-9201(81)90046-7.

Egbert, G. D., and S. Y. Erofeeva (2002), Efficient inverse modeling of barotropic ocean tides, *J. Atmos. Ocean. Tech., 19*, 183–204, doi:10.1175/1520-0426(2002)019<0183:EIMOBO>2.0.C0;2.

Eshelby, J. D. (1957). The determination of the elastic field of an ellipsoidal inclusion and related problems, *Proc. R. Soc. London, Ser. A., 241*(1226), 376–396, doi:10.1098/rspa.1957.0133.

Fagereng, Å., and R. H. Sibson (2010), Mélange rheology and seismic style,

Geology, 38(8), 751–754, doi:10.1130/G30868.1.

Fehlberg, E., (1969). Low-order classical Runge–Kutta formulas with step size control and their application to some heat transfer problems. *NASA Technical Report, 315*.

Fry B., K. Chao, S. Bannister, Z. Peng, L. Wallace (2011), Deep tremor in New Zealand triggered by the 2010 Mw8.8 Chile earthquake. *Geophys. Res. Lett., 38*, L15306, doi:10.1029/2011GL048319.

Ghosh, A., E. Huesca-Perez, E. E. Brodsky, and Y. Ito (2015), Very low frequency earthquakes (VLFEs) in Cascadia migrate with tremor, *Geophys. Res. Lett., 42*, 3228-3232, doi:10.1002/2015GL063286.

Gomberg, J., A. Wech, K. Creager, K. Obara, and D. Agnew (2016), Reconsidering earthquake scaling, *Geophys. Res. Lett., 43*, 6243-6251, doi:10.1002/ 2016GL069967.

Guo, X., S.M. Varlamov, and Y. Miyazawa (2010), Coastal Ocean Modeling by the Nesting Method, *Bull. Coast. Oceanogr., 47*(2), 113-123.

Gutenberg, B., and C. F. Richter (1944), Frequency of earthquakes in California. *Bull. Seismol. Soc. Am., 34*(4), 185-188.

Hacker, B. R., G. A. Abers, and S. M. Peacock (2003), Subduction factory, 1, Theoretical mineralogy, densities, seismic wave speeds, and H_2O contents, *J. Geophys. Res., 108*, 2029, doi:10.1029/2001JB001127.

Hawthorne, J. C., and A. M. Rubin (2010), Tidal modulation of slow slip in Cascadia, *J. Geophys. Res., 115*, B09406, doi:10.1029/2010JB007502.

Hawthorne, J. C., and A. M. Rubin (2013), Tidal modulation and back-propagating fronts in slow slip events simulated with a velocity-weakening to velocity-strengthening friction law, *J. Geophys. Res., 118*, 1216–1239, doi:10.1002/jgrb.50107.

Heaton, T. H. (1975), Tidal triggering of earthquakes, *Geophys. J. Int., 43*(2), 307–326, doi:10.1111/j.1365-246X.1975.tb00637.x.

Heuret, A., C. P. Conrad, F. Funiciello, S. Lallemand, and L. Sandri (2012), Relation between subduction megathrust earthquakes, trench sediment thickness and upper plate strain, *Geophys. Res. Lett., 39*, L05304, doi:10.1029/2011GL050712.

Hirose, H., and K. Obara (2010), Recurrence behavior of short-term slow slip

and correlated nonvolcanic tremor episodes in western Shikoku, southwest Japan, *J. Geophys. Res., 115*, B00A21, doi:10.1029/2008JB006050.

Hirose, F., J. Nakajima, and A. Hasegawa (2008a), Three-dimensional seismic velocity structure and configuration of the Philippine Sea slab in southwestern Japan estimated by double-difference tomography, *J. Geophys. Res., 113*, B09315, doi:10.1029/2007JB005274.

Hirose, F., J. Nakajima, and A. Hasegawa (2008b), Three-dimensional velocity structure and configuration of the Philippine Sea slab beneath Kanto district, central Japan, estimated by double-difference tomography, *Zishin, 60*(3), 123-138.

Holmes, A. (1931), XVIII. Radioactivity and Earth Movements. *Trans. Geol. Soc. Glasgow, 18*(3), 559-606.

Holtkamp, S. G., and M. R. Brudzinski (2011), Earthquake swarms in the circum-Pacific subduction zones, *Earth Planet. Sci. Lett., 305*(1-2), 215–225, doi:10.1016/j.epsl.2011.03.004.

Hori, T., and S. Miyazaki (2010), Hierarchical asperity model for multiscale characteristic earthquakes: A numerical study for the off-Kamaishi earthquake sequence in the NE Japan subduction zone, *Geophys. Res. Lett., 37*, L10304, doi:10.1029/2010GL042669.

Hori, T., N. Kato, K. Hirahara, T. Bada, and Y. Kaneda (2004), A numerical simulation of earthquake cycles along the Nankai trough, southwest Japan: Lateral variation in frictional property due to slab geometry controls the nucleation position, *Earth Planet. Sci. Lett., 228*(3-4), 215-226, doi:10.1016/ j.epsl.2004.09.033.

Houston, H. (2001), Influence of depth, focal mechanism, and tectonic setting on the shape and duration of earthquake source time functions, *J. Geophys. Res., 106*(B6), 11137-11150, doi:10.1029/2000JB900468.

Houston, H. (2015), Low friction and fault weakening revealed by rising sensitivity of tremor to tidal stress, *Nat. Geosci., 8*, 409–415, doi:10.1038/ngeo2419.

Houston, H., B. G. Delbridge, A. G. Wech, and K. C. Creager (2011), Rapid tremor reversals in Cascadia generated by a weakened plate interface,

Nat. Geosci., 4, 404–409, doi:10.1038/ngeo1157.

Hutchison, A. A., and A. Ghosh (2016), Very low frequency earthquakes spatiotemporally asynchronous with strong tremor during the 2014 episodic tremor and slip event in Cascadia. *Geophys. Res. Lett.*, *43*, 6876-6882, doi:10.1002/2016GL069750.

Ide, S. (2008), A Brownian walk model for slow earthquakes, *Geophys. Res. Lett., 35*, L17301, doi:10.1029/ 2008GL034821.

Ide, S. (2010a), Striations, duration, migration, and tidal response in deep tremor, *Nature, 466*, 356–359, doi:10.1038/nature09251.

Ide, S. (2010b), Quantifying the time function of nonvolcanic tremor based on a stochastic model, *J. Geophys. Res., 115*, B08313, doi:10.1029/2009JB000829.

Ide, S. (2012), Variety and spatial heterogeneity of tectonic tremor worldwide, *J. Geophys. Res., 117*, B03302, doi:10.1029/2011JB008840.

Ide, S. (2013), The proportionality between relative plate velocity and seismicity in subduction zones, *Nat. Geosci., 6*, 780–784, doi:10.1038/ngeo1901.

Ide, S. (2014), Modeling fast and slow earthquakes at various scales, *Proc. Jpn. Acad. Ser. B, 90*(8), 259–277, doi:10.2183/pjab.90.259.

Ide, S., and G. C. Beroza (2001), Does apparent stress vary with earthquake size?, *Geophys. Res. Lett., 28*(171), 3349–3352, doi:10.1029/2001GL013106.

Ide, S., and M. Takeo (1997), Determination of constitutive relations of fault slip based on seismic wave analysis, *J. Geophys. Res., 102*(B12), 27379–27392, doi:10.1029/97JB02675.

Ide, S., and H. Aochi (2005), Earthquakes as multiscale dynamic ruptures with heterogeneous fracture surface energy, *J. Geophys. Res., 110*, B11303, doi:10.1029/2004JB003591.

Ide, S., and H. Aochi (2014), Modeling earthquakes using fractal circular patch models with lessons from the 2011 Tohoku-Oki earthquake. *J. Disaster Res. 9*(3), 264–271.

Ide, S., and Y. Tanaka (2014), Controls on plate motion by oscillating tidal stress: Evidence from deep tremors in western Japan, *Geophys. Res.*

Lett., 41, 3842–3850, doi:10.1002/2014GL060035.

Ide, S., and S. Yabe (2014), Universality of slow earthquakes in the very low frequency band, *Geophys. Res. Lett., 41*, 2786–2793, doi:10.1002/2014GL059712.

Ide, S., G. C. Beroza, S. G. Prejean, and W. L. Ellsworth (2003), Apparent break in earthquake scaling due to path and site effects on deep borehole recordings, *J. Geophys. Res., 108*, 2271, doi:10.1029/2001JB001617.

Ide, S., D. R. Shelly, and G. C. Beroza (2007a), Mechanism of deep low frequency earthquakes: Further evidence that deep non-volcanic tremor is generated by shear slip on the plate interface, *Geophys. Res. Lett., 34*, L03308, doi:10.1029/2006GL028890.

Ide, S., G. C. Beroza, D. R. Shelly, and T. Uchide (2007b), A scaling law for slow earthquakes, *Nature, 447*, 76–79, doi:10.1038/nature05780.

Ide, S., K. Imanishi, Y. Yoshida, G. C. Beroza, and D. R. Shelly (2008), Bridging the gap between seismically and geodetically detected slow earthquakes, *Geophys. Res. Lett., 35*, L10305, doi:10.1029/2008GL034014.

Ide, S., K. Shiomi, K. Mochizuki, T. Tonegawa, and G. Kimura (2010), Split Philippine Sea Plate beneath Japan, *Geophys. Res. Lett., 37*, L21304, doi:10.1029/2010GL044585.

Ide, S., S. Yabe, H.-J. Tai, and K. H. Chen (2015), Thrust-type focal mechanisms of tectonic tremors in Taiwan: Evidence of subduction, *Geophys. Res. Lett., 42*, 3248-3256, doi:10.1002/2015GL063794.

Ide, S., S. Yabe, and Y. Tanaka (2016), Earthquake potential revealed by tidal influence on earthquake size-frequency statistics, *Nat. Geosci., 9*, 834-837, doi: 10.1038/NGEO2796.

Idehara, K., S. Yabe, and S. Ide (2014), Regional and global variations in the temporal clustering of tectonic tremor activity, *Earth Planets Space, 66*, 66, doi:10.1186/1880-5981-66-66.

Ishibashi, K., (1999), Great Tokai and Nankai, Japan, Earthquakes as revealed by historical seismology: 1. Review of the events until the mid-14th century. *J. Geogr., 108*(4), 399-423.

Ito, Y., K. Obara, K. Shiomi, S. Sekine, and H. Hirose (2007), Slow earthquakes coincident with episodic tremors and slow slip events, *Science, 315*(5811), 503-506, doi:10.1126/science.1134454.

Ito, Y., R. Hino, M. Kido, H. Fujimoto, Y. Osada, D. Inazu, Y. Ohta, T. Iinuma, M. Ohzono, S. Miura, M. Mishina, K. Suzuki, T. Tsuji, and J. Ahi, (2013) Episodic slow slip events in the Japan subduction zone before the 2011 Tohoku-Oki earthquake, *Tectonophysics, 600*, 14-26, doi:10.1016/j.tecto.2012.08.022.

Kagan, Y. Y. (1993), Statistics of characteristic earthquakes, *Bull. Seismol. Soc. Am., 83*, 7-24.

Kagan, Y. Y., and D. D. Jackson (2013), Tohoku earthquake: A surprise?, *Bull. Seismol. Soc. Am. 103*(28), 1181–1194, doi:10.1785/0120120110.

Kanamori, H., (1972) Mechanism of tsunami earthquakes, *Phys. Earth Planet Inter., 6*(5), 346-359, doi:10.1016/0031-9201(72)90058-1.

Kanamori, H. (1977), The energy release in great earthquakes, *J. Geophys. Res., 82*(20), 2981-2987, doi:10.1029/JB082i020p02981.

Kaneko, Y., J.-P. Avouav, and N. Lapusta (2010). Towards inferring earthquake patterns from geodetic observations of interseismic coupling, *Nature Geosci., 3*, 363-369, doi:10.1038/ngeo843.

Kano, Y., J. Mori, R. Fujio, H. Ito, T. Yanagidani, S. Nakao, and K.-F. Ma (2006), Heat signature on the Chelungpu fault associated with the 1999 Chi-Chi, Taiwan earthquake, *Geophys. Res. Lett., 33*, L14306, doi:10.1029/2006GL026733.

Kao, H., S.-J. Shan, H. Dragert, G. Rogers, J. F. Cassidy, and K. Ramachandran (2005), A wide depth distribution of seismic tremors along the northern Cascadia margin, *Nature, 436*, 841-844, doi:10.1038/nature03903.

Kato, N. (2003), Repeating slip events at a circular asperity: Numerical simulation with a rate- and state-dependent friction law, *Bull. Earthquake Res. Inst. Univ. Tokyo, 78*, 151–166.

Kato, N. (2004), Interaction of slip on asperities: Numerical simulation of seismic cycles on a two-dimensional planar fault with nonuniform frictional property, *J. Geophys. Res., 109*, B12306,

doi:10.1029/2004JB003001.

Kato, N. (2007), Expansion of aftershock areas caused by propagating post-seismic sliding, *Geophys. J. Int., 168*(2), 797–808, doi:10.1111/j.1365-246X.2006.03255.x.

Kato A., K. Obara, T. Igarashi, H. Tsuruoka, S. Nakagawa, and N. Hirata (2012), Propagation of slow slip leading up to the 2011 Mw 9.0 Tohoku-Oki earthquake, *Science, 335*(6069), 705-708, doi:10.1126/science.1215141.

Katsumata, A., and N. Kamaya (2003), Low-frequency continuous tremor around the Moho discontinuity away from volcanoes in the southwest Japan, *Geophys. Res. Lett., 30*(1), 1020, doi:10.1029/2002GL015981.

Kim, M. J., S. Y. Schwartz, and S. Bannister (2011), Non-volcanic tremor associated with the March 2010 Gisborne slow slip event at the Hikurangi subduction margin, New Zealand. *Geophys Res Lett 38*, L14301, doi:10.1029/2011GL048400

Kita, S., T. Okada, A. Hasegawa, J. Nakajima, and T. Matsuzawa (2010), Anomalous deepening of a seismic belt in the upper-plane of the double seismic zone in the Pacific slab beneath the Hokkaido corner: Possible evidence for thermal shielding caused by subducted forearc crust materials, *Earth Planet. Science Lett., 290*(3-4), 415-426, doi:10.1016/j.epsl.2009.12.038.

Klimes, L. (2002), Correlation functions of random media, *Pure Appl. Geophys., 159*(7), 1811–1831, doi:10.1007/s00024-002-8710-2.

Kostrov, B. V. (1974), Seismic moment and energy of earthquakes, and seismic flow of rock, *Izv. Acad. Sci. USSR Phys. Solid Earth, 1*, 23–40.

Kwiatek, G., K. Plenkers, M. Nakatani, Y. Yabe, and G. Dresen (2010), Frequency-magnitude characteristics down to magnitude –4.4 for induced seismicity recorded at Mponeng gold mine, South Africa, *Bull. Seismol. Soc. Am., 100*(3), 1165–1173, doi:10.1785/0120090277.

La Rocca, M., K. C. Creager, D. Galluzzo, S. D. Malone, J. E. Vidale, J. R. Sweet, and A. G. Wech (2009), Cascadia tremor located near plate interface constrained by S minus P wave times, *Science, 323*(5914), 620–623, doi:10.1126/science.116711.

Lay, T., and H. Kanamori (1981), An asperity model of large earthquake sequences, in Earthquake Prediction: An International Review, Maurice Ewing Ser., vol. 4, edited by D. W. Simpson and P. G. Richards, pp. 579 – 592, AGU, Washington, D. C, doi: 10.1029/ME004p0579.

Liu, Y. (2013), Numerical simulations on megathrust rupture stabilized under strong dilatancy strengthening in slow slip region, *Geophys. Res. Lett., 40*, 1311–1316, doi:10.1002/grl.50298.

Liu, Y., and J. R. Rice (2005), Aseismic slip transients emerge spontaneously in three-dimensional rate and state modeling of subduction earthquake sequences, *J. Geophys. Res., 110*, B08307, doi:10.1029/2004JB003424.

Liu, Y., and J. R. Rice (2007), Spontaneous and triggered aseismic deformation transients in a subduction fault model, *J. Geophys. Res., 112*, B09404, doi:10.1029/2007JB004930.

Liu, Y., and A. M. Rubin (2010), Role of fault gouge dilatancy on aseismic deformation transients, *J. Geophys. Res., 115*, B10414, doi:10.1029/2010JB007522.

Liu, C., A. T. Linde, and I. S. Sacks (2009). Slow earthquakes triggered by typhoons. *Nature, 459*, 833-836, doi: 10.1038/nature08042.

Maeda, T., and K. Obara (2009), Spatiotemporal distribution of seismic energy radiation from low-frequency tremor in western Shikoku, Japan, *J. Geophys. Res., 114*, B00A09, doi:10.1029/2008JB006043.

Mai, P. M., and G. C. Beroza (2000), Source scaling properties from finite-fault rupture models, *Bull. Seismol. Soc. Am., 90*(3), 605–614, doi:10.1785/0119990126.

Mai, P. M., and G. C. Beroza (2002), Aspatial random field model to characterize complexity in earthquake slip, *J. Geophys. Res., 107*(B11), 2308, doi:10.1029/2001JB000588.

Marone, C. (1998), Laboratory-derived friction laws and their application to seismic faulting. *Annu. Rev. Earth. Planet. Sci., 26*, 643-696, doi: 10.1146/annurev.earth.26.1.643.

Marone, C., and C. H. Scholz (1988), The depth of seismic faulting and the upper transition from stable to unstable slip regimes, *Geophys. Res. Lett., 15*(6), 621–624, doi:10.1029/GL015i006p00621.

Maruyama, T., (1963) On the force equivalent of dynamic elastic dislocations with reference to the earthquake mechanism, *Bull. Earthquake Res. Inst., Tokyo Univ., 41*(3), 467-486.

Matsumoto, K., T. Takanezawa, and M. Ooe (2000), Ocean tide models developed by assimilating Topex/Poseidon altimeter data into hydrodynamical model: a global model and a regional model around Japan, *J. Oceanogr., 56*(5), 567–581, doi:10.1023/A:1011157212596.

Maury, J., H. Aochi, and M. Radiguet (2014), Fault constitutive relations inferred from the 2009–2010 slow slip event in Guerrero, Mexico, *Geophys. Res. Lett., 41,* doi:10.1002/2014GL060691.

Maury, J., S. Ide, V. M. Cruz-Atienza, V. Kostoglodov, G. González-Molina, and X. Pérez-Campos (2016), Comparative study of tectonic tremor locations: Characterization of slow earthquakes in Guerrero, Mexico, *J. Geophys. Res. Solid Earth, 121*, 5136–5151, doi:10.1002/2016JB013027.

Mayeda, K., and W. R. Walter (1996), Moment, energy, stress drop, and source spectra of western U.S. earthquakes from regional coda envelopes, J. Geophys. Res., 101(B5), 11195–11208, doi:10.1029/96JB00112.

McCaffrey, R. (2008), Global frequency of magnitude 9 earthquakes, *Geology, 36*(3), 263–266, doi:10.1130/G24402A.1.

McCrory, P. A., J. L. Blair, F. Waldhauser, and D. H. Oppenheimer (2012), Juan de Fuca slab geometry and its relation to Wadati-Benioff zone seismicity, *J. Geophys. Res., 117*, B09306, doi:10.1029/2012JB009407.

Mitsui, Y. (2015), Interval modulation of recurrent slow slip events by two types of earthquake loading, *Earth Planet Space, 67*, 56, doi:10.1186/s40623-015-0230-2.

Mitsui, Y., and K. Hirahara (2011), Fault instability on a finite and planar fault related to early phase of nucleation, *J. Geophys. Res., 116*, B06301, doi:10.1029/2010JB007974.

Miyazaki, S., and K. Heki (2001), Crustal velocity field of southwest Japan: Subduction and arc-arc collision, *J. Geophys. Res., 106*(B3), 4305–4326, doi:10.1029/2000JB900312.

Miyazawa, M. (2012), Detection of seismic events triggered by P-waves from

the 2011 Tohoku-Oki earthquake, *Earth Planets Space, 64*, 1223–1229, doi:10.5047/eps.2012.07.003.

Miyazawa, M., and J. Mori (2005), Detection of triggered deep low-frequency events from the 2003 Tokachi-oki earthquake, *Geophys. Res. Lett., 32*, L10307, doi:10.1029/2005GL022539.

Mochizuki, K., T. Yamada, M. Shinohara, Y. Yamanaka, and T. Kanazawa (2008), Weak Interplate Coupling by Seamounts and Repeating M ~ 7 Earthquakes, *Science, 321*(5893), 1194–1197, doi:10.1126/science. 1160250.

Mogi, K. (1962), Magnitude-frequency relation for elastic shocks accompanying fractures of various materials and some related problems in earth- quakes (2nd paper). *Bull. Earthquake Res. Inst. 40*(4), 831–853.

Mogi, K. (1968), Development of aftershock areas of great earthquakes, *Bull. Earthq. Res. Inst. Univ. Tokyo, 46*, 175–203.

Muller, R. D., M. Sdrolias, C. Gaina, and W. R. Roest (2008), Age, spreading rates, and spreading asymmetry of the world's ocean crust, *Geochem. Geophys. Geosyst., 9*, Q04006, doi:10.1029/2007GC001743.

Nadeau, R. M., and T. V. McEvilly (1997), Seismological studies at Parkfield V: Characteristic microearthquake sequences as fault-zone drilling targets, *Bull. Seismol. Soc. Am., 87*(6), 1463 – 1472.

Nadeau, R. M., and L. R. Johnson (1998), Seismological studies at Parkfield VI: Moment release rates and estimates of source parameters for small repeating earthquakes, *Bull. Seismol. Soc. Am., 88*(3), 790–814.

Nadeau, R. M. and D. Dolenc (2005), Nonvolcanic tremors deep beneath the San Andreas fault, *Science, 307*(5708), 389, doi:10.1126/science.1107142.

Nadeau, R. M., and A. Guilhem (2009), Nonvolcanic tremor evolution and the San Simeon and Parkfield, California earthquakes, *Science, 325*(5937), 191-193, doi:10.1126/science.1174155.

Nakajima, J., and A. Hasegawa (2006), Anomalous low-velocity zone and linear alignment of seismicity along it in the subducted Pacific slab beneath Kanto, Japan: Reactivation of subducted fracture zone?,

Geophys. Res. Lett., 33, L16309, doi: 10.1029/2006GL026773.

Nakajima, J., and A. Hasegawa (2007), Subduction of the Philippine Sea plate beneath southwestern Japan: Slab geometry and its relationship to arc magmatism, *J. Geophys. Res., 112*, B08306, doi:10.1029/2006JB004770.

Nakajima, J., F. Hirose, and A. Hasegawa (2009), Seismotectonics beneath the Tokyo metropolitan area, Japan: Effect of slab-slab contact and overlap on seismicity, *J. Geophys. Res., 114*, B08309, doi:10.1029/2008JB006101.

Nagata, K., M. Nakatani, and S. Yoshida (2012), A revised rate- and state-dependent friction law obtained by constraining constitutive and evolution laws separately with laboratory data, *J. Geophys. Res., 117*, B02314, doi:10.1029/2011JB008818.

Nakata, R., N. Suda, and H. Tsuruoka (2008), Non-volcanic tremor resulting from the combined effect of earth tides and slow slip events, *Nat. Geosci., 1*, 676–678, doi:10.1038/ngeo288.

Nakata, R., R. Ando, T. Hori, and S. Ide (2011), Generation mechanism of slow earthquakes: Numerical analysis based on a dynamic model with brittle-ductile mixed fault heterogeneities, *J. Geophys. Res., 116*, B08308, doi:10.1029/2010JB008188.

Nakatani, M. (2001), Conceptual and physical clarification of rate and state friction: Frictional sliding as a thermally activated rheology, *J. Geophys. Res., 106*(B7), 13347–13380, doi: 10.1029/2000JB900453.

Nishikawa, T., and S. Ide (2014), Earthquake size distribution in subduc tion zones linked to slab bouyancy, *Nat. Geosci., 7*, 904-908, doi:10.1038/NGEO2279.

Nishikawa, T., and S. Ide (2015), Background seismicity rate at subduction zones linked to slab-bending-related hydration, *Geophys. Res. Lett., 42*, 7081–7089, doi:10.1002/2015GL064578.

Nishimura, T., T. Matsuzawa, and K. Obara (2013), Detection of short-term slow slip events along the Nankai Trough, southwest Japan, using GNSS data, *J. Geophys. Res. Solid Earth, 118*, 3112–3125, doi:10.1002/jgrb.50222.

Noda, H., and N. Lapusta (2013), Stable creeping fault segments can become destructive as a result of dynamic weakening, *Nature, 493*, 518-521, doi:10.1038/nature11703.

Noda, H., M., Nakatani, and T. Hori (2013), Large nucleation before large earthquakes is sometimes skipped due to cascade-up—Implications from a rate and state simulation of faults with hierarchical asperities, *J. Geophys. Res. Solid Earth, 118*, 2924–2952, doi:10.1002/jgrb.50211.

Obara, K. (2002), Nonvolcanic deep tremor associated with subduction in southwest Japan, *Science, 296*(5573), 1679–1681, doi:10.1126/science.1070378.

Obara, K. (2010), Phenomenology of deep slow earthquake family in southwest Japan: Spatiotemporal characteristics and segmentation, *J. Geophys. Res., 115*, B00A25, doi:10.1029/2008JB006048.

Obara, K. (2011), Characteristics and interactions between non-volcanic tremor and related slow earthquakes in the Nankai subduction zone, southwest Japan, *J. Geodyn., 52*(3-4), 229-248, doi:10.1016/j.jog.2011.04.002.

Obara, K., and Y. Ito (2005), Very low frequency earthquake excited by the 2004 off the Kii peninsula earthquake: A dynamic deformation process in the large accretionary prism, *Earth Planets Space, 57*, 321–326, doi:10.1186/BF03352570.

Obara, K., and A. Kato, (2016). Connecting slow earthquakes to huge earthquakes. *Science*, *353*(6296), 253-257, doi: 10.1126/science.aaf1512.

Obara, K., H. Hirose, F. Yamamizu, and K. Kasahara (2004), Episodic slow slip events accompanied by non-volcanic tremors in southwest Japan subduction zone, *Geophys. Res. Lett., 31*, L23602, doi: 10.1029/2004GL020848.

Obara, K., S. Tanaka, T. Maeda, and T. Matsuzawa (2010), Depth-dependent activity of non-volcanic tremor in south- west Japan, *Geophys. Res. Lett., 37*, L13306, doi:10.1029/ 2010GL043679.

Obara, K., T. Matsuzawa, S. Tanaka, T. Kimura, and T. Maeda (2011), Migration properties of non-volcanic tremor in Shikoku, southwest Japan, *Geophys. Res. Lett., 38*, L09311, doi:10.1029/2011GL047110.

Ogata, Y. (1988), Statistical models for earthquake occurrences and residual analysis for point processes, *J. Am. Stat. Assoc., 83*(401), 9–27, doi:10.1080/01621459.1988.10478560.

Ogata, Y. (1992), Detection of precursory relative quiescence before great earthquakes through a statistical model, *J. Geophys. Res., 97*(B13), 19845– 19871, doi:10.1029/92JB00708.

Ohnaka, M. (2003), A constitutive scaling law and a unified comprehension for frictional slip failure, shear fracture of intact rock, and earthquake rupture, *J. Geophys. Res., 108*, 2080, doi:10.1029/2000JB000123.

Ohta, Y., J. T. Freymueller, S. Hreinsdottir, and H. Suito (2006), A large slow slip event and the depth of the seismogenic zone in the south central Alaska subduction zone, *Earth Planet. Sci. Lett., 247*(1-2), 108-116, doi:10.1016/j.epsl.2006.05.013.

Okada, Y., K. Kasahara, S. Hori, K. Obara, S. Sekiguchi, H. Fujiwara, and A. Yamamoto (2004), Recent progress of seismic observation networks in Japan - Hi-net, F-net, K-NET and KiK-net -, *Earth Planets Space, 56*, xv-xxviii, doi:10.1186/BF03353076.

Okada, T., T. Yaginuma, N. Umino, T. Kono, T. Matsuzawa, S. Kita, and A. Hasegawa (2005), The 2005 M7. 2 MIYAGI-OKI earthquake, NE Japan: Possible rerupturing of one of asperities that caused the previous M7.4 earthquake, *Geophys. Res. Lett., 32*, L24302, doi:10.1029/2005GL024613.

Okubo, S. (1988), Asymptotic solutions to the static deformation of the Earth - I. Spheroidal mode, *Geophys. J. Int., 92*(1), 39-51, doi: 10.1111/j.1365-246X.1988.tb01119.x.

Okubo, S., and D. Tsuji (2001), Complex Green's function for diurnal/semidiurnal loading problems, *J. Geod. Soc. Jpn., 47*, 225-230, doi:10.11366/sokuchi1954.47.225.

Omori, F. (1894), Investigation of aftershocks. *Rep. Earthquake Inv. Comm., 2*, 103-139.

Ozawa, S., S. Miyazaki, Y. Hatanaka, T. Imakiire, M. Kaidzu, and M. Murakami (2003), Characteristic silent earthquakes in the eastern part of the Boso peninsula, Central Japan, *Geophys. Res. Lett., 30*, 1283,

doi:10.1029/ 2002GL016665.

Pardo, M., and G. Suarez (1995), Shape of the subducted Rivera and Coco plates in southern Mexico: Seismic and tectonic implications, *J. Geophys. Res., 100*(B7), 12357–12373, doi:10.1007/s004100050129.

Payero, J. S., V. Kostoglodov, N. Shapiro, T. Mikumo, A. Iglesias, X. Perez-Campos, and R. W. Clayton (2008), Nonvolcanic tremor observed in the Mexican subduction zone, *Geophys. Res. Lett., 35*, L07305, doi:10.1029/2007GL032877.

Peng, Z., and K. Chao (2008), Non-volcanic tremor beneath the Central Range in Taiwan triggered by the 2001 M_w7.8 Kunlun earthquake, *Geophys. J. Int., 175*(2), 825-829, doi:10.1111/j.1365-246X.2008.03886.x

Peng, Y., and A. M. Rubin (2016), High-resolution images of tremor migrations beneath the Olympic Peninsula from stacked array of arrays seismic data, *Geochem. Geophys. Geosyst., 17*, 587-601, doi:10.1002/2015GC006141.

Peng, Y., A. M. Rubin, M. G. Bostock, and J. G. Armbruster (2015), High-resolution imaging of rapid tremor migrations beneath southern Vancouver Island using cross-station cross correlations, *J. Geophys. Res. Solid Earth, 120,* 4317-4332, doi:10.1002/2015JB011892.

Pollack, H. N., S. J. Hurter, and J. R. Johnson (1993), Heat flow from the Earth's interior: analysis of the global data set, *Rev. Geophys., 31*(3), 267-280, doi:10.1029/93RG01249.

Rice, J. R. (1975), On the stability of dilatant hardening for saturated rock masses, *J. Geophys. Res., 80*(11), 1531–1536, doi:10.1029/JB080i011p01531.

Rice, J. R. (1993), Spatio-temporal complexity of slip on a fault, *J. Geophys. Res.*, *98*(B6), 9885-9907, doi:10.1029/93JB00191.

Rice, J. R., and A. L. Ruina (1983), Stability of steady frictional slipping, *J. Appl. Mech*, *50*(2), 343–349, doi:10.1115/1.3167042.

Rogers, G., and H. Dragert (2003), Episodic tremor and slip on the Cascadia subduction zone: The chatter of silent slip, *Science, 300*(5627), 1942–1943, doi:10.1126/science.1084783.

Royer, A. A., A. M. Thomas, and M. G. Bostock (2015), Tidal modulation and

triggering of low-frequency earthquakes in northern Cascadia, *J. Geophys. Res. Solid Earth, 120,* 384-405, doi:10.1002/2014JB011430.

Rubin, A. M. (2008), Episodic slow slip events and rate-and-state friction, *J. Geophys. Res., 113*, B11414, doi:10.1029/2008JB005642.

Rubin, A. M. (2011), Designer friction laws for bimodal slow slip propagation speeds, *Geochem. Geophys. Geosyst., 12*, Q04007, doi:10.1029/2010GC003386.

Rubin, A. M., and J.-P. Ampuero (2005), Earthquake nucleation on (aging) rate and state faults, *J. Geophys. Res., 110*, B11312, doi:10.1029/2005JB003686.

Rubinstein, J. L., J. E. Vidale, J. Gomberg, P. Bodin, K. C. Creager, and S. D. Malone (2007), Non-volcanic tremor driven by large transient shear stresses, *Nature, 448*, 579–582, doi:10.1038/nature06017.

Rubinstein, J. L., M. La Rocca, J. E. Vidale, K. C. Creager, and A. G. Wech (2008), Tidal modulation of nonvolcanic tremor, *Science, 319*(5860), 186-189, doi:10.1126/science.1150558.

Rudnicki, J. W., and L. B. Freund (1981), On energy radiation from seismic sources, *Bull. Seism. Soc. Am., 71*(3), 583-595.

Ruff, L., and H. Kanamori (1980), Seismicity and the subduction process, *Phys. Earth Planet. Inter., 23*(3), 240-252, doi:10.1016/0040-1951(83)90097-5.

Ruina, A. (1983), Slip instability and state variable friction laws, *J. Geophys. Res., 88*(B12), 10359-10370, doi:10.1029/JB088iB12p10359.

Sagiya, T. (2004), A decade of GEONET: 1994-2003 –The continuous GPS observation in Japan and its impact on earthquake studies–, *Earth Planets Space, 56*(8), xxix–xli, doi:10.1186/BF03353077.

Sagy, A., E. E. Brodsky, and G. J. Axen (2007), Evolution of fault-surface roughness with slip, *Geology, 35*(3), 283-286, doi:10.1130/G23235A.1.

Savage, J. C. (1983), A dislocation model of strain accumulation and release at a subduction zone, *J. Geophys. Res., 88*(B6), 4984-4996, doi:10.1029/JB088iB06p04984.

Savcenko, R., and W. Bosch (2012), EOT11a - Empirical Ocean Tide Model From Multi-Mission Satellite Altimetry, DGFI Report No. 89.

Sawai, M., A. R. Niemeijer, O. Plümper, T. Hirose, and C. J. Spiers (2016), Nucleation of frictional instability caused by fluid pressurization in subducted blueschist, *Geophys. Res. Lett., 43*, 2543-2551, doi:10.1002/2015GL067569.

Scholz, C. H. (2002), The Mechanics of Earthquake and Faulting, 2nd Ed., Cambridge Univ. Press, New York.

Schorlemmer, D., S. Wiemer, and M. Wyss (2005), Variations in earthquake-size distribution across different stress regimes, *Nature, 437*, 539 – 542, doi:10.1038/nature04094.

Schuster, A., (1897) On lunar and solar periodicities of earthquakes, *Proc. R. Soc. London*, 61, 455-465.

Schwartz, S. Y., and J. M. Rokosky (2007), Slow slip events and seismic tremor at circum-Pacific subduction zones, *Rev. Geophys., 45*, RG3004, doi:10.1029/2006RG000208.

Segall, P., A. M. Rubin, A. M. Bradley, and J. R. Rice (2010), Dilatant strengthening as a mechanism for slow slip events, *J. Geophys. Res., 115*, B12305, doi:10.1029/2010JB007449.

Shelly, D. R., G. C. Beroza, S. Ide, and S. Nakamula (2006), Low-frequency earthquakes in Shikoku, Japan, and their relationship to episodic tremor and slip, *Nature, 442*, 188-191, doi:10.1038/nature04931.

Shelly, D. R., G. C. Beroza, and S. Ide (2007a), Non-volcanic tremor and low-frequency earthquake swarms, *Nature, 446*, 305-307, doi:10.1038/nature05666.

Shelly, D. R., G. C. Beroza, and S. Ide (2007b), Complex evolution of transient slip derived from precise tremor locations in western Shikoku, Japan, *Geochem. Geophys. Geosyst., 8*, Q10014, doi:10.1029/2007GC001640.

Shibazaki, B., and Y. Iio (2003), On the physical mechanism of silent slip events along the deeper part of the seismogenic zone, *Geophys. Res. Lett., 30*, 1489, doi:10.1029/2003GL017047.

Shibazaki, B., and T. Shimamoto (2007), Modeling of short-interval silent slip events in deeper subduction interfaces considering the frictional properties at the unstable-stable transition regime, *Geophys. J. Int.,*

171(1), 191-205, doi:10.1111/j.1365-246.Z.2007.03434.x.

Shimamoto, T. (1986), Transition between frictional slip and ductile flow for halite shear zones at room temperature, *Science, 231*(4739), 711–714, doi:10.1126/science.231.4739.711.

Sibson, R. H. (1973), Interaction between temperature and pore-fluid pressure during earthquake faulting: A mechanism for partial or total stress relief, *Nature*, *243*, 66–68, doi:10.1038/physci243066a0.

Skarbek, R. M., A. W. Rempel, and D. A. Schmidt (2012), Geologic heterogeneity can produce aseismic slip transients, *Geophys. Res. Lett., 39*, L21306, doi:10.1029/ 2012GL053762.

Smith, S. W., and M. Wyss (1968), Displacement on the San Andreas Fault subsequent to the 1966 Parkfield earthquake, *Bull. Seismol. Soc. Am., 58*(6), 1955-1973.

Stein, S., and E. A. Okal (2007), Ultralong period seismic study of the December 2004 Indian Ocean earthquake and implications for regional tectonics and the subduction process, *Bull. Seismol. Soc. Am., 97*(1A), S279–S295, doi:10.1785/0120050617.

Suwa, Y., S. Miura, A. Hasegawa, T. Sato, and K. Tachibana (2006), Interplate coupling beneath NE Japan inferred from three-dimensional displacement field, *J. Geophys. Res., 111*, B04402, doi:10.1029/ 2004JB003203.

Suzuki, T., and T. Yamashita (2009), Dynamic modeling of slow earthquakes based on thermoporoelastic effects and inelastic generation of pores, *J. Geophys. Res., 114*, B00A04, doi:10.1029/2008JB006042.

Takeo, A., K. Idehara, R. Iritani, T. Tonegawa, Y. Nagaoka, K. Nishida, H. Kawakatsu, S. Tanaka, K. Miyakawa, T. Iidaka, M. Obayashi, H. Tsuruoka, K. Shiomi, and K. Obara (2010), Very broadband analysis of a swarm of very low frequency earthquakes and tremors beneath Kii Peninsula, SW Japan, *Geophys. Res. Lett., 37*, L06311, doi:10.1029/2010GL042586.

Takeuchi, H., and M. Saito (1972), Seismic surface waves, in Seismology: Surface Waves and Earth Oscillations, Methods in Comput. Phys., vol. 11, edited by B. A. Bolt, 217–295, Academic, New York.

Tamura, Y. (1987), A harmonic development of the tide-generating potential, Bull. Inf. Marées Terrestres, 99, 6813-6855.

Tanaka, S. (2010), Tidal triggering of earthquakes precursory to the recent Sumatra megathrust earthquakes of 26 December 2004 (M_w 9.0), 28 March 2005 (M_w 8.6), and 12 September 2007 (M_w 8.5), *Geophys. Res. Lett., 37*, L02301, doi:10.1029/2009GL041581.

Tanaka, S. (2012), Tidal triggering of earthquakes prior to the 2011 Tohoku-Oki earthquake (Mw 9.1), *Geophys. Res. Lett., 39*, L00G26, doi:10.1029/2012GL051179.

Tanaka, Y. (2014), An approximately 9-yr-period variation in seismicity and crustal deformation near the Japan Trench and a consideration of its origin, *Geophys. J. Int., 196*(2), 760-787, doi:10.1093/gji/ggt424.

Tanaka, S., M. Ohtake, and H. Sato (2002a), Spatio-temporal variation of the tidal triggering effect on earthquake occurrence associated with the 1982 South Tonga earthquake of M_w 7.5, *Geophys. Res. Lett., 29*(16), doi:10.1029/2002GL015386.

Tanaka, S., M. Ohtake, and H. Sato (2002b), Evidence for tidal triggering of earthquakes as revealed from statistical analysis of global data, *J. Geophys. Res., 107*(B10), 2211, doi:10.1029/2001JB001577.

Tanaka, S., H. Sato, S. Matsumura, and M. Ohtake (2006), Tidal triggering of earthquakes in the subducting Philippine Sea plate beneath the locked zone of the plate interface in the Tokai region, Japan, *Tectonophysics, 417*(1-2), 69-80, doi:10.1016/j.tecto.2005.09.013.

Tanaka, Y., S. Yabe, and S. Ide (2015), An estimate of tidal and non-tidal modulations of plate subduction speed in the transition zone in the Tokai district, *Earth Planets Space, 67*, 141, doi:10.1186/s40623-015-0311-2.

Tanioka, Y., L. Ruff, and K. Satake (1997), What controls the lateral variation of large earthquake occurrence along the Japan Trench, *Island Arc, 6*, 261-266, doi:10.1111/j.1440-1738.1997.tb00176.x.

Taylor, B. (2006), The single largest oceanic plateau: Ontong Java–Manihiki–Hikurangi, *Earth Planet. Sci. Lett., 241*(3-4), 372-380, doi:10.1016/j.epsl.2005.11.049.

Tchalenko, J. S., and M. Berberian (1975), Dasht-e-Bayaz fault, Iran: Earthquake and earlier related structures in bed rock, *Geol. Soc. Am. Bull.,* *86*(5), 703-709, doi:10.1130/0016-7606(1975)86<703:DBFIEA>2.0.CO;2.

Thomas, A. M., R. M. Nadeau, and R. Bürgmann (2009), Tremor-tide correlations and near-lithostatic pore pressure on the deep San Andreas fault, *Nature, 462*, 1048–1051, doi:10.1038/nature08654.

Thomas, A. M., R. Bürgmann, D. R. Shelly, N. M. Beeler, and M. L. Rudolph (2012), Tidal triggering of low frequency earthquakes near Parkfield, California: Implications for fault mechanics within the brittle-ductile transition, *J. Geophys. Res., 117*, B05301, doi:10.1029/2011JB009036.

Thomas, T. W., J. E. Vidale, H. Houston, K. C. Creager, J. R. Sweet, and A. Ghosh (2013), Evidence for tidal triggering of high-amplitude rapid tremor reversals and tremor streaks in northern Cascadia, *Geophys. Res. Lett., 40*, 4254-4259, doi:10.1002/grl.50832.

Thomas, M. Y., N. Lapusta, H. Noda, and J.-P. Avouac (2014), Quasi-dynamic versus fully dynamic simulations of earthquakes and aseismic slip with and without enhanced coseismic weakening, *J. Geophys. Res. Solid Earth, 119,* 1986-2004, doi:10.1002/2013JB010615.

Thomas, A. M., G. C. Beroza, and D. R. Shelly (2016), Constraints on the source parameters of low-frequency earthquakes on the San Andreas Fault, *Geophys. Res. Lett.*, 43, doi:10.1002/2015GL067173.

Torii, Y., and S. Yoshioka (2007), Physical conditions producing slab stagnation: constraints of the Clapeyron slope, mantle viscosity, trench retreat, and dip angles, *Tectonophysics, 445*(3-4), 200-209, doi:10.1016/j.tecto.2007.08.003

Townend, J. (1997), Estimates of conductive heat flow through bottom-simulating reflectors on the Hikurangi and southwest Fiordland continental margins, New Zealand, *Mar. Geol. 141*(1-4), 209-220, doi:10.1016/S0025-3227(97)00073-X

Tse, S., and J. R. Rice (1986), Crustal earthquake instability in relation to the depth variation of frictional slip properties, *J. Geophys. Res., 91*(B9), 9452–9472, doi:10.1029/JB091iB09p09452.

Tsuruoka, H., M. Ohtake, and H. Sato (1995), Statistical test of the tidal triggering of earthquakes: contribution of the ocean tide loading effect, *Geophys. J. Int. 122*(1), 183-194, doi:10.1111/j.1365-246X.1995.tb03546.x.

Tsutsumi, A., and T. Shimamoto (1997), High-velocity frictional properties of gabbro, *Geophys. Res. Lett.*, *24*(6), 699-702, doi:10.1029/97GL00503.

Turcotte, D. L., and G. Schubert (2002). Geodynamics, Cambridge Univ. Press, Cambridge, UK.

Uchide, T., and S. Ide (2010), Scaling of earthquake rupture growth in the Parkfield area: Self-similar growth and suppression by the finite seismogenic layer, *J. Geophys. Res., 115*, B11302, doi:10.1029/2009JB007122.

Uhlenbeck, G. E., and L. S. Ornstein (1930), On the theory of the Brownian motion, *Phys. Rev., 36*, 823–841, doi:10.1103/PhysRev.36.823.

Utsu, T. (1970), Aftershocks and earthquake statistics (1): Some parameters which characterize an aftershock sequence and their interrelations, *J. Fac. Sci., Hokkaido Univ., Ser. VII (Geophysics), 3*(3), 129–195.

Uyeda, S., and H. Kanamori (1979), Back-arc opening and the mode of subduction, *J. Geophys. Res., 84*(B3), 1049-1061, doi:10.1029/JB084iB03p01049.

Vidale, J. E., D. C. Agnew, M. J. S. Johnston, and D. H. Oppenheimer, (1998) Absence of earthquake correlation with Earth tides: An indication of high preseismic fault stress rate, *J. Geophys. Res., 103*(B10), 24567-24572, doi:10.1029/98JB00594.

Wadati, K. (1935), On the activity of deep-focus earthquakes in the Japan Island and neighbourhoods, *Geophys. Mag. 8*(3-4), 305-326.

Walker, J. C. G., P. B. Heys and J. F. Kasting (1981), A negative feedback mechanism for the long-term stabilization of the Earth's surface temperature, *J. Geophys. Res., 86*(C10), 9776-9782, doi:10.1029/JC086iC10p09776.

Wallace, L. M., and J. Beavan (2010), Diverse slow slip behavior at the Hikurangi subduction margin, New Zealand, *J. Geophys. Res., 115*, B12402, doi:10.1029/2010JB007717.

Wallace, L. M., J. Beavan, S. Bannister, and C. Williams (2012), Simultaneous long-term and short-term slow slip events at the Hikurangi subduction margin, New Zealand: Implications for processes that control slow slip event occurrence, duration, and migration, *J. Geophys. Res., 117*, B11402, doi:10.1029/2012JB009489.

Wallace, L. M., S. V. Webb, Y. Ito, K. Mochizuki, R. Hino, S. Henrys, S. Y. Schwartz, and A. F., Sheehan (2016), Slow slip near the trench at the Hikurangi subduction zone, New Zealand, *Science, 353*(6286), 701-704, doi:10.1126/science.aaf2349.

Wang, K., and S. L. Bilek (2014), Invited review paper: Fault creep caused by subduction of rough seafloor relief, *Tectonophysics, 610*, 1–24, doi:10.1016/j.tecto.2013.11.024.

Watanabe, T., Y. Hiramatsu, and K. Obara (2007), Scaling relationship between the duration and the amplitude of non-volcanic deep low-frequency tremors, *Geophys. Res. Lett., 34*, L07305, doi:10.1029/2007GL029391.

Wech, A. G., and K. C. Creager (2011), A continuum of stress, strength and slip in the Cascadia subduction zone, *Nat. Geosci., 4*, 624-628, doi:10.1038/ngeo1215.

Wech, A. G., K. C. Creager, H. Houston, and J. E. Vidale (2010), An earthquake-like magnitude-frequency distribution of slow slip in northern Cascadia, *Geophys. Res. Lett., 37*, L22310, doi:10.1029/2010GL044881.

Wech, A. G., C. M. Boese, T. A. Stern, and J. Townend (2012), Tectonic tremor and deep slow slip on the Alpine Fault, *Geophys. Res. Lett., 39*, L10303, doi:10.1029/2012GL051751.

Wessel, P., and W. H. F. Smith (1998), New, improved version of generic mapping tools released, *Eos Trans. AGU, 79*(47), 579, doi:10.1029/98EO00426.

Yabe, S., and S. Ide (2013), Repeating deep tremors on the plate interface beneath Kyushu, southwest Japan, *Earth Planets Space, 65*, 17–23, doi:10.5047/eps.2012.06.001.

Yabe, S., and S. Ide (2014), Spatial distribution of seismic energy rate of

tectonic tremors in subduction zones, *J. Geophys. Res. Solid Earth, 119*, 8171–8185, doi:10.1002/2014JB011383.

Yabe, S., and S. Ide (2017), Slip-behavior transitions of a heterogeneous linear fault, *J. Geophys. Res. Solid Earth, accepted*, doi:10.1002/2016JB013132.

Yabe, S., Ide, S. and Yoshioka, S., (2014a). Along-strike variations in temperature and tectonic tremor activity along the Hikurangi subduction zone, New Zealand, *Earth Planets Space, 66*, 142, doi:10.1186/s40623-014-0142-6.

Yabe, S., A. Baltay, S. Ide, and G. Beroza (2014b), Seismic wave attenuation determined from tectonic tremor in multiple subduction zones, *Bull. Seismol. Soc. Am., 104*(4), 2043-2059, doi:10.1785/0120140032.

Yabe, S., Y. Tanaka, H. Houston, and S. Ide (2015), Tidal sensitivity of tectonic tremors in Nankai and Cascadia subduction zones, *J. Geophys. Res. Solid Earth, 120*, 7587–7605, doi:10.1002/ 2015JB012250.

Yagi, Y. and M. Kikuchi (2003), Partitioning between seismogenic and aseismic slip as highlighted from slow slip events in Hyuga-nada, Japan, *Geophys. Res. Lett.,* 30**,** 1087, doi:10.1029/2002GL015664.

Yamanaka, Y., and M. Kikuchi (2004), Asperity map along the subduction zone in northeastern Japan inferred from regional seismic data, *J. Geophys. Res., 109*, B07307, doi:10.1029/2003JB002683.

Yamashita, T., and T. Suzuki (2011), Dynamic modeling of slow slip coupled with tremor, *J. Geophys. Res., 116*, B05301, doi:10.1029/2010JB008136.

Yoshioka, S., and H. Sanshadokoro (2002), Numerical simulations of deformation and dynamics of horizontally lying slabs, *Geophys. J. Int., 151*(1), 69-82, doi:10.1046/ j.1365-246X.2002.01735.x

Zhang, J., P. Gerstoft, P. M. Shearer, H. Yao, J. E. Vidale, H. Houston, and A. Ghosh (2011), Cascadia tremor spectra: Low corner frequencies and earthquake-like high-frequency falloff, *Geochem. Geophys. Geosyst., 12*, Q10007, doi:10.1029/2011GC003759.

Ziv, A., and A. M. Rubin (2003), Implications of rate-and-state friction for properties of aftershock sequence: Quasi-static inherently discrete simulations, *J. Geophys. Res., 108*, 2051, doi:10.1029/2001JB001219.